Computational Modelling of A_2BO_4 Materials for Solid Oxide Fuel Cells

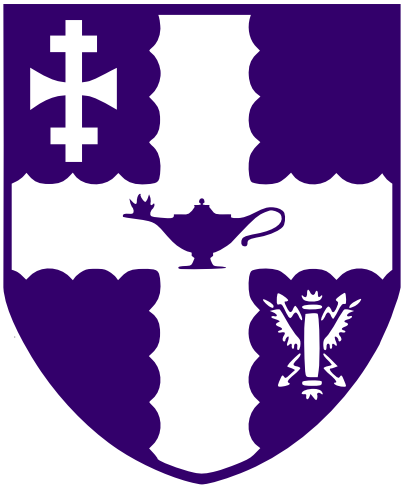

Adam Joseph McSloy

Loughborough University

Doctoral Thesis

2017

A thesis submitted in partial fulfillment of
the requirements for the award of
Doctor of Philosophy
at Loughborough
University
2017

Abstract

Solid oxide fuel cells are a clean, attractive and highly efficient alternative to traditional methods of power generation. However, their high operating temperature prevents their widespread use, as it makes them prohibitively expensive and causes stability issues. In response to this, new materials which exhibit fast oxide ion conduction at low-intermediate temperatures have gained considerable research interest.

In this thesis, atomic scale computational modelling techniques have been employed to investigate defects, dopants and oxide ion conductivity in the A_2BO_4 materials; Cd_2GeO_4 and Ba_2TiO_4. Calculations suggest that these materials' parent structures are poor oxide ion conductors due to their highly unfavourable intrinsic defect formation energies of 3.00-10.56 eV defect^{-1}. Results also indicate that oxide ion interstitials can be formed in Cd_2GeO_4 through trivalent doping of the Cd sites. In Ba_2TiO_4, monovalent and trivalent doping of its Ba and Ti sites respectively induces the formation of oxide ion vacancies. In both materials, strong dopant-oxide ion defect associations are present. Interestingly, only Cd_2GeO_4 shows enhanced oxide ion migration upon doping, the defects in Ba_2TiO_4 being effectively immobile. This suggest that the oxide ion vacancies are more intensely associated with their causal dopant ions. With an average migration barrier of $\sim$0.79 eV, oxide ions diffuse in Cd_2GeO_4 *via* a "knock-on" mechanism down the *a*-axis and a stepwise mechanism along the *c*-axis. Despite this, defect trapping confines the interstitials to the dopant rich regions of the cell, resulting in poor oxide ion diffusion on the order of 1×10^{-8} cm^2 s^{-1} at 1273 K.

Generally, defects are found to be more stable in the α'-phase of Ba_2TiO_4, suggesting, in agreement with experiment, that they are likely to stabilise the α'-phase at reduced temperatures. Subsequent investigations, also in accord with experiment, reveal carbonate impurities are likely to be common in pristine and doped Ba_2TiO_4 systems alike, and that their presence will stabilise the α'-phase. The hydroxide type defects formed upon water incorporation are shown to be low in energy in Ba_2TiO_4 systems containing oxide ion vacancies or interstitials. Both carbonate and hydroxide type defects are shown to bind aggressively to any oxide ion defects present, reducing their mobility.

Acknowledgements

First and foremost, I would like to express my sincerest gratitude to my supervisor, Dr. Pooja Panchmatia, for her invaluable knowledge and unwavering support throughout my studies.

I would also like to extend my thanks to our experimental collaborators in Birmingham, in particular Professor Peter Slater for his invaluable input regarding the materials investigated, and to Dr David Cooke of Huddersfield for his helpful discussions at the beginning of my studies. Furthermore, I would also like to thank Dr. David Case, Dr. Stephen Yeandel and Paul Mouratidis for both their advice and comradery towards the end of my studies. Finally, I would like to thank my family, without whom none of this would have been possible.

Contents

List of Figures

List of Tables

List of Abbreviations

AFC	Alkaline fuel cell
CCSD(T)	Coupled cluster with single, double and "triple" excitations
CGO	Gadolinia-stabilised ceria
CHP	Combined heat and power
DMFC	Direct methanol fuel cell
DSC	Differential scanning calorimetry
IT-SOFC	Intermediate temperature solid oxide fuel cell
KVN	Kröger-Vink notation
LSCF	Lanthanum strontium cobalt ferrite
LSGM	Lanthanum strontium gallate magnesite
LSM	Lanthanum strontium manganite
LT-SOFC	Low temperature solid oxide fuel cell
MCFC	Molten carbonate fuel cell
MD	Molecular dynamics
MIEC	Mixed ionic electronic conductor
MSD	Mean squared displacement
ORR	Oxygen reduction reaction
PAFC	Phosphoric acid fuel cell
PBC	Periodic boundary conditions
PEM	Proton exchange membrane fuel cell
RDF	Radial distribution function
SOFC	Solid oxide fuel cell
SSZ	Scandia-stabilised zirconia
TEC	Thermal expansion coefficient
TPB	Triple phase boundary (region)
YSZ	Yttria-stabilised zirconia

Presentations and Publications

Published Papers

Sep. 2016: A. J. McSloy, P. F. Kelly, P. R. Slater, and P. M. Panchmatia, "A computational study of doped olivine structured Cd_2GeO_4: local defect trapping of interstitial oxide ions." *Phys. Chem. Chem. Phys.*, 2016, **18**, 26284-26290.

Oral Presentations

Jun. 2014: Annual Northern Regional Dalton Meeting, Huddersfield
Computational Studies of Barium Orthotitanate

Feb. 2015: RSC Energy Sector Early Career Chemists' Symposium, Derby
Computational Studies of Ba_2TiO_4

Dec. 2016: RSC Solid State Chemistry Group Meeting, Loughborough
Defects, Dopants and Ionic Conductivity in Cd_2GeO_4

Poster Presentations

Jun. 2014: Annual Northern Regional Dalton Meeting, Huddersfield
Computational Studies of Barium Orthotitanate

Sep. 2014: CCP5 Annual Meeting, Harper Adams
Computational Studies of Ba_2TiO_4 for Use in SOFCs

Dec. 2014: RSC Solid State Chemistry Group Meeting, Bath
Computational Studies of Doped Ba_2TiO_4 for Use in SOFCs

Feb. 2015: RSC Energy Sector Early Career Chemists' Symposium, Derby
Computational Studies of Ba_2TiO_4 (prize)

Sep. 2015: CCP5 Annual Meeting, Lancaster
Computational Studies of Doped Ba_2TiO_4 for Use in SOFCs

Dec. 2015: RSC Solid State Chemistry Group Meeting, Kent
Defects and Dopants in Cd_2GeO_4

Sep. 2016: CCP5 Annual Meeting, Harper Adams
Defects, Dopants and Ionic Conductivity in Cd_2GeO_4

Dec. 2016: RSC Solid State Chemistry Group Meeting, Loughborough
Defects, Dopants and Ionic Conductivity in Cd_2GeO_4

This page is intentionally left blank.

Chapter 1

Introduction

Due to continuous population growth and industrialisation there is an ever increasing demand for energy across the globe. With the current global focus on environmental protection, there has been a shift in the developmental drive towards finding not only more efficient means of producing power but "cleaner" ones.

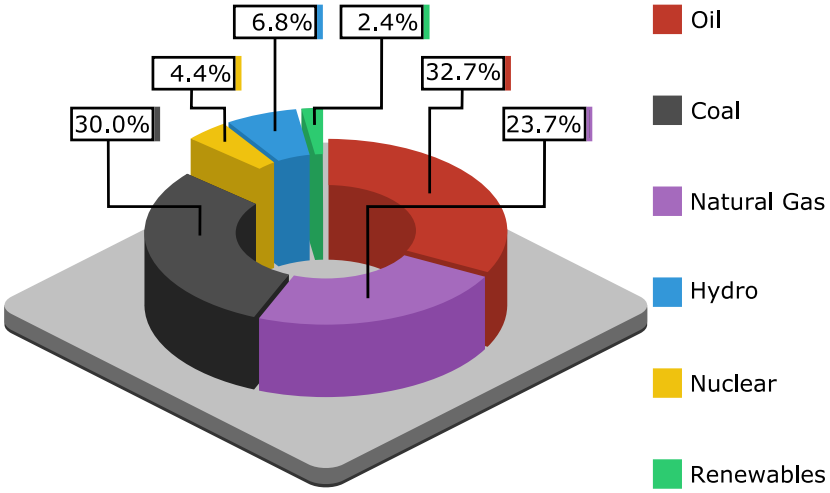

Figure 1.1: Primary energy consumption by fuel in 2015.[1]

A breakdown of the current primary energy sources and their shares are shown in figure 1.1.[1] From this it can be seen that more than 80% of the power generated globally comes from the burning of fossil fuels. Although considerable reserves of fossil fuels still remain, such reserves are of a finite and limited size and will therefore become exhausted. Current estimates suggest that if modern consumption rates are maintained, both oil and natural gas reserves will be depleted by around 2045 and coal by 2112.[2] However, reserves could be exhausted much sooner if consumption rates continue to rise. Clearly there exists a need to develop and encourage alternative methods of generating power which do not require fossil fuels.

Another, and perhaps more pressing reason behind the fervent research of alternative energy is due to the environmental impact that fossil fuels have.[3] The burning of fossil fuels generates substantial quantities of environmentally harmful pollutants and greenhouse gases such as CO_2.[4] This issue is only further exacerbated by the low overall efficiently of fossil fuel burning power stations. In an effort to tackle this, many governments have introduced legislation and regulations, such as CO_2 penalties, to encourage the usage and development of alternative power.[5]

The global dependence on fossil fuels and the environmental impacts they have can be reduced in one of several ways. In the most radical approach, fossil fuels could be completely purged from our economy. This would require gas and coal fired power stations to be replaced with nuclear, hydroelectric or other alternatives, and internal combustion engines in motor-vehicles with their electric counterparts. A less radical and somewhat more feasible approach would be to increase the overall efficiency of the power generating process, thereby increasing the amount of energy produced per unit of fuel, and ultimately decreasing the amount of fuel required per year. As a consequence of this, the amount of pollution generated per year would also decrease and would help in reducing environmental damage. Carbon capture has also been proposed to help combat the negative environmental impact of increasing CO_2. This involves capturing and storing the CO_2 gases produced by power plants during operation.[6–8] The sequestered carbon may then be stored in geological formations or utilised elsewhere.[9,10]

One alternative which may fill the gap of traditional fossil fuels is renewable biofuels. Biofuels can be solid, liquid or gas and are generally combusted in a manner similar to fossil fuels to produce power. They are so similar in fact that they are able to make use of the already existing infrastructures, allowing them a smoother transition into the economy. Although lower than that of fossil fuels, biofuels still produce notable quantities of carbon emissions.[11,12] The many issues presently associated with biofuel production has made their widespread use somewhat impractical e.g. large land requirements, high costs and, in some cases, the potential to cause food shortages.[13,14] Veering away from direct combustion methods brings cleaner, more environmentally friendly and therefore more attractive methods of generating power. Currently, hydroelectric power stations are the single largest source of clean renewable energy, figure 1.1. However, their development has been stunted due to environmental concerns, high initial costs, specific

site requirements and their effects on the local population.[7] Although geothermal plants would make an excellent alternative, most locations do not meet the strict geological conditions required for their operation.

In recent times there has been a steady and continuous growth in the number of solar and wind farms in operation.[15] These differ from those discussed in the previous paragraph in that they are larger arrays rather than single structures and their operation is more conditionally dependent.[7] This is to say, solar and wind farms will only operate so long as the required weather conditions are met. Such farms are both environmentally friendly and highly renewable. Despite being good supplementary power sources, they are not yet ready to be relied upon to fulfil national power gird requirements. This is due to the intermittency with which they operate and the difficulty and costs associated with power storage and distribution. Reducing the costs and increasing the efficiencies and service lives of these technologies would enable more developed use. It is possible that battery arrays could be used to store excess energy generated by the solar and wind farms for use later.[7] Fuel cells, which are somewhat related to batteries, have also featured prominently in the search for new power generating technologies due to their many desirable attributes. Fuel cells come in many different types, each with their own advantages, disadvantages and target applications. Specifics on the construction and operation of fuel cells are discussed in the sections to follow.

1.1 Fuel Cells

Fuel cells are energy conversion devices that, like batteries, directly convert chemical energy into electrical energy *via* an electrochemical reaction.[16,17] Unlike batteries, fuel cells are designed to generate rather than store energy and so require fuel rather than recharging, and will operate continuously so long as both fuel and oxidiser are provided. Conventional power systems employ heat engines to convert the chemical energy of a fuel to electrical energy, and so their total system efficiency is effectively restricted by the Carnot cycle.[18] As fuel cells directly convert the chemical energy of a fuel into electrical energy, without an intermediary combustion step, they are not subject to the same limitations and so are able to achieve much higher efficiencies.[19] A fuel cell, if using hydrogen and oxygen as reactants, can be considered a zero emission power source as water is the only by-product. Fuel cells are an attractive alternative to conventional methods of power generation due to their simplistic design, silent operation, high efficiency and low levels of pollutive emissions. While several different classes of fuel cells exist, see section 1.1.2, they all operate and are constructed in a similar manner.[20]

1.1.1 Fuel Cell Construction and Operation

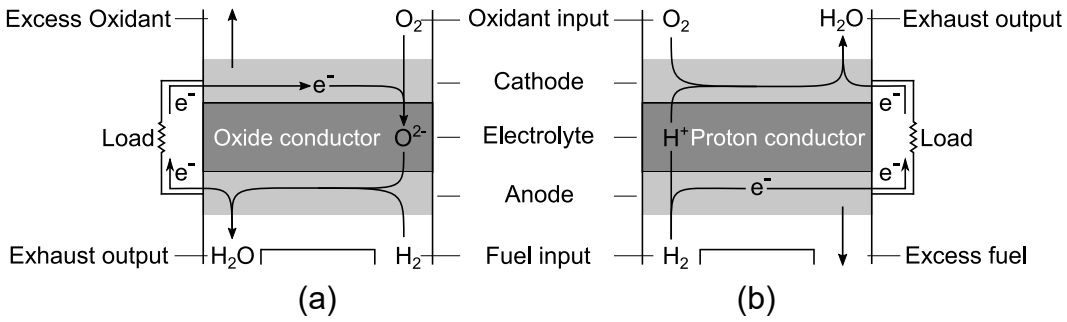

Figure 1.2: Basic components and operating principles of fuel cells with a) oxide ion and b) proton conducting electrolytes. Adapted from [21] and [22].

A single fuel cell unit consists of a pair of porous electrodes, known as the cathode and anode, separated by an electrolyte, as depicted in figure 1.2.[23] During operation, fuel and oxidant are continuously fed into the anodic and cathode sides of the cell respectively. The mixing and direct combustion of the reactant gasses is prevented by the electrolyte which only permits the transport of selected ions across it. The overall chemical reaction for a cell utilising hydrogen and oxygen as reactants is given in equation 1.3.[24] The exact nature of the two constituent half-cell reactions depends on the electrolyte material selected. For fuel cells which employ proton conducting electrolytes, such as PEM* cells, the mobile species, H^+, is generated by the oxidation of H_2 to protons and free electrons at the anode, as shown in equation 1.1. The protons and electrons then travel to the cathode where they recombine with oxygen to form water, as shown in equation 1.2.[24] While protons can transverse the electrolyte to reach the cathode, electrons must travel around an external circuit, where they are used to perform work. A depiction of this process is given in figure 1.2b. As the direct transfer of electrons between the electrodes would result in a short circuit the electrolyte material must be electrically insulating.

Anodic: $$H_2 \rightarrow 2H^+ + 2e^- \tag{1.1}$$

Cathodic: $$2H^+ + 2e^- + \frac{1}{2}O_2 \rightarrow H_2O \tag{1.2}$$

Overall: $$H_2 + \frac{1}{2}O_2 \rightarrow H_2O \tag{1.3}$$

*PEM = proton exchange membrane fuel cell.

An oxide ion conducting electrolyte fuel cell is shown in figure 1.2a, in this, oxygen is adsorbed, dissociated and reduced at the cathode surface following equation 1.4.[25] Following the oxygen reduction reaction (ORR) the oxide ions are absorbed and transported through the electrolyte to the anode where they react with hydrogen to form water, coupled with the release of electrons, equation 1.5.[26]

Cathodic: $$\frac{1}{2}O_2 + 2e^- \rightarrow O^{2-} \tag{1.4}$$

Anodic: $$O^{2-} + H_2 \rightarrow H_2O + 2e^- \tag{1.5}$$

Each class of fuel cell is defined primarily by the type of electrolyte used in its fabrication and by the reactants it uses during operation. Each class has its own advantages, disadvantages and target applications. A detailed discussion of each fuel cell class is beyond the scope of this review. However, comprehensive reviews on this topic can been found elsewhere.[23,27–29] For comparative purposes, an overview of the six main fuel cell classes is given in table 1.1.

Table 1.1: Comparison of the six main fuel cell classes and their properties.[23,27,29,30]

Fuel cell type	Operating Temp. (°C)	Electrical Efficiency (%)	CHP[a] Efficiency (%)
Alkaline (AFC)[31]	90–100	60	>80
Phosphoric Acid (PAFC)	150–200	∼40	>85
Solid Oxide (SOFC)	600–1000	40–60	<90
Molten Carbonate (MCFC)	600–700	45–47	>80
Proton Exchange Membrane (PEM)	50–100	40–60	70–90
Direct methanol (DMFC)	60–200	40	80

[a] CHP = combined heat and power.

Proton exchange membrane fuel cells (PEM) are one of the more notable classes of fuel cells.[24,32] Currently undergoing large-scale trials in public transport around the world, PEM cells are designed with low temperature operation and mobility in mind.[33] Therefore PEM cells are aimed mainly, but not exclusively, at the transport industries. Solid oxide fuel cells (SOFC) are another class of note which, and in contrast to PEM cells, are intended for static and co-power generation. SOFCs offer several advantages over other fuel cell devices: they are not limited to the use of pure H_2 as their only source of fuel but are able to use light hydrocarbons; they do not require expensive catalytic materials (i.e. noble metals) for their anode and cathodes; they have the highest potential efficiency of any fuel cell; and they are less susceptible to poisoning.[34] The specific advantages and disadvantages of SOFCs are discussed in the section below.

1.1.2 Solid Oxide Fuel Cells

Solid oxide fuel cells (SOFC) are a class of high temperature fuel cell constructed entirely from solid ceramic components.[35] Solid oxide fuel cells are one of the most promising classes of fuel cell and are reported to be one of the most efficient† electrical generators currently in development.[36] With electrical efficiencies in the region of 60-70%, and a further 20% recoverable from heat, such cells present remarkable total system efficiencies (∼90%).[21,23,29,35–39] The fuel flexibility of such cells, owed to their high operating temperatures, allows them to utilise a variety of fuels such as hydrogen, carbon monoxide, natural gas and other various light hydrocarbons without the need for an external reformer.[35,40,41] Larger hydrocarbons such as diesel can be used if coupled with an external fuel reformer.[42,43] The ability to utilise fuels derived from both renewable and fossil sources enables for an almost effortless transition into the market. High operating temperatures also removes the need for expensive catalysts, such as platinum.[37,44] Other positive aspects include low noise pollution, low levels of chemical pollution, high quality heat by-product, conversion of CO exhaust gas into CO_2 at high temperatures, enhanced mechanical stability, the absence of liquid electrolytes and reduced susceptibility to poisoning to name but a few.[27,29,39] These attributes make SOFCs ideal candidates for use as combined heat and power units in housing, as large static power generation units or as portable generators for disaster and emergency situations.[45,46] However, the shortcomings associated with such cells, discussed later, must be overcome to enable their widespread deployment.

Solid oxide fuel cells primarily use oxide ion conducting electrolytes, the mechanisms for which were discussed in the previous section. Although proton conducting electrolytes permit faster ion conduction, at reduced temperatures, they are more susceptible to poisoning and suffer from stability issues.[47,48] High operating temperatures, 800-1000 °C, are required for the electrolyte to exhibit adequate oxide ion conduction rates and are conducive to fast reaction kinetics. Insufficient operating temperatures can significantly affect cell efficiency. As previously discussed the cell's high operating temperature enables higher reactant activity. However, it also poses a notable safety risk and leads to increased material degradation rates.[49,50] Other disadvantages stemming from high temperature operation include high material costs and long start up times. Despite these shortcomings the fuel flexibility and remarkable efficiencies that such cells can achieve makes them a highly desirable technology, giving reason to their continued and fervent research.[41] There exists a need to reduce the operating temperature of SOFCs to a safer

†Efficiency considered in terms of fuel in to electrical output.

and more manageable level of around 500-700 °C, while simultaneously maintaining the fast ion transport speeds and efficiencies associated with such cells.[22,39,51] Such a reduction would create a safer and more cost effective cell with a longer service life which would enable SOFCs to be more readily implemented.

1.2 Materials for Solid Oxide Fuel Cells

Considerable demands are placed upon materials intended for use in solid oxide fuel cells. Each component material is required not only to perform its intended function during operation, but to remain stable while doing so. This is no small feat, given that these materials will be exposed to reducing and or oxidising conditions at high temperatures for prolonged periods of time. Furthermore, the materials must be both stable and compatible with respect to one another.[52] The matching of thermal expansion coefficients (TEC) is required to avert cell degradation arising from thermally induced mechanical stress.[20,35,36,38,53] It is highly desirable for, although not strictly a requirement of, the materials to be low-cost, easy to manufacture, non-toxic and sustainable. The general and specific requirements of the primary SOFC component materials are discussed below in their relevant sections.

1.2.1 Electrolyte Materials

In addition to the previously discussed requirements of a fuel cell material, a good electrolyte should have: 1) high ionic conductivity ($\sigma = \sim 0.1$ S cm^{-1}) to permit ion transport between the electrodes, 2) low electrical conductivity to prevent short circuiting, 3) high density and low porosity to prevent reactant gas mixing and 4) good thermal and chemical stability in high temperature oxidising and reducing environments.[20,54,55] The polarisation resistances associated with ion transport across the material are the primary source of Ohmic loss in the electrolyte, and the second greatest source of loss in the cell as a whole.[56] Ohmic losses can be reduced by either increasing ionic conductivity or reducing the thickness of the electrolyte. Doing so would not only improve the electrolyte's efficiency, but also help it maintain better efficiency as the operating temperature of the cell is reduced. The ionic conductivities of a selection of common and advanced electrolyte materials have been plotted as a function of temperature in figure 1.3.

In general, oxide ion conductivity tends to increase with the number of oxide anion defects.[57] Therefore, oxygen non-stoichiometric materials often exhibit greater ionic conducting abilities than their stoichiometric counterparts.[58,59] While some materials naturally contain oxide defects, others require doping in order to form them. However, increasing the number of defects beyond a certain point may in fact diminish conductivity due to defect ordering effects.[57,60] Further information on defect chemistry, specific defect forms and migration mechanisms can be found in section 2.5.

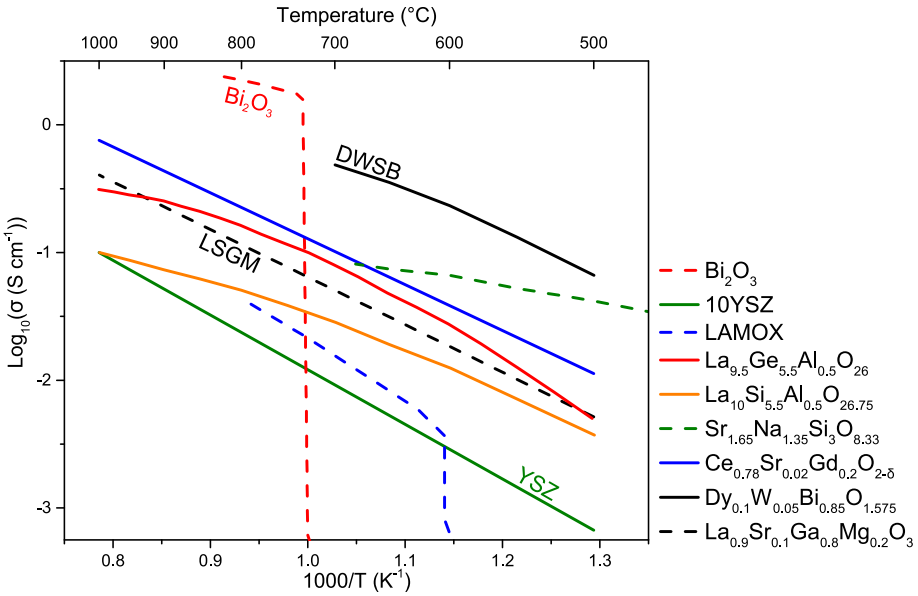

Figure 1.3: Ionic conductivities of common and advanced electrolytes as a function of temperature, note some series have been extrapolated forward or backwards to permit comparison.[61–69]

A great many materials have been investigated in the search for new and improved SOFC electrolytes. However, most are found to be unsuitable due to stability issues, electronic conducting behaviour or poor ionic conductivity. Commonly, the materials investigated fall into one of three structural categories: fluorite, perovskite or apatite.[21] These represent the three most prominent class of oxide ion conductors, as such they will be discussed in the most detail. In this section, both common and advanced SOFC electrolyte materials will be reviewed. The fluorites, perovskites and apatites along with related materials will be discussed, after which less common materials will be covered.

Fluorites

Many fast oxide ion conductors adopt the fluorite-type MO_2 structure, where M is a large tetravalent cation. This structure, shown in figure 1.4, is a face centred cubic array of cations with anions occupying the tetrahedral sites. While some fluorite-type structures, such as δ-Bi_2O_3, naturally possess the oxygen (vacancy) defects required for oxide ion conduction, most require M^{3+}/M^{2+} doping to achieve this.[22,62] The key feature of these materials is their large open structure which permits the accommodation of large dopant concentrations, often without significant structural distortion.[70] This enables them to achieve high degrees of oxygen non-stoichiometry, making them excellent oxide ion conductors. In such structures, oxide ion conduction occurs *via* the stepwise vacancy mechanism described in section 2.8.1.

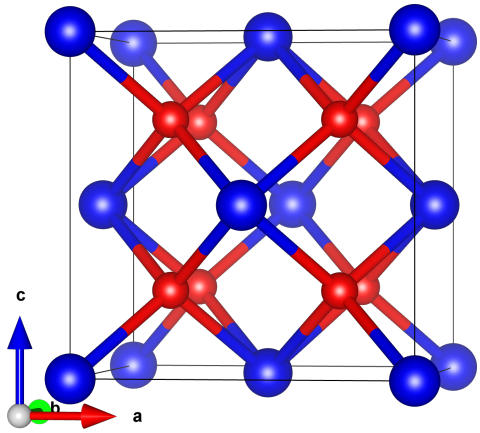

Figure 1.4: MO_2 fluorite structure with M and O ions coloured blue and red respectively.‡

Zirconia (ZrO_2) based fluorites make excellent electrolytes. However, subvalent doping is required to stabilise the cubic-fluorite phase below 2340 °C, and to introduce oxide ion vacancies.[22,35,55,72] Those doped with Y^{3+}, known as yttria-stabilised zirconia (YSZ), present ionic conductivities (σ) of ~0.1 S cm^{-1} at 1000 °C and are the standard to which all electrolytes are compared.[38,61] Typically Y^{3+} contents of 8-10% are used, as higher concentrations actually reduce conductivity due to defect clustering.[35,60] Temperatures of 800-1000 °C are required for YSZ to operate satisfactory. This places further stress on other components in the cell which negatively effects the cell's stability and longevity. As YSZ's operational temperature fails to meet the 500-700 °C target range, alternatives must be considered. Higher conductivities are reached by scandia-stabilised zirconia

‡Crystal structure images in this work have been drawn using the program VESTA.[71]

(SSZ), this is because Sc^{3+} is a better size match for Zr^{4+} which reduces the strain its substitution induces.[48,73] However, high scandium costs and long term stability issues currently bar its use.[21,39]

Ceria (CeO_2) is another promising fluorite, which, like zirconia, requires doping to promote fast ion conduction. The highest conductivities in ceria are achieved when doped with Gd^{3+} (CGO), Sm^{3+} or Gd^{3+} and Sr^{2+}.[64,74] At 800 °C 15% doped CGO displays ionic conductivities comparable to YSZ at 1000 °C.[74,75] Although figure 1.3 shows these to be superb ionic conductors, they are unfit for use above 600 °C, as Ce^{4+} starts to reduce to Ce^{3+} causing the material to degrade and become electrically conducting.[48,55] However, they are still viable for low temperature SOFC applications.

The best oxide ion conductors to date are those based on δ-Bi_2O_3.[21] The δ-Bi_2O_3 structure is effectively an oxygen deficient fluorite where one in four of the normal fluorite anion sites are vacant.[26] Pure Bi_2O_3 manifests in a monoclinic α-phase below 730 °C and a cubic δ-phase up to its melting point at 804 °C.[76] While only the latter is conductive, it can be stabilised to room temperature by dopants such as Y^{3+} and La^{3+}.[62] However, these materials have poor mechanical strength, are prone to corrosion, tend reduce to bismuth metal under reducing conditions, have significant TECs and suffer from Bi_2O_3 volatilization.[21,77] Similar issues are also encountered in the related γ-$Bi_2VO_{5.5}$ based materials.[21] More recent investigations showed that the stability and suitability of bismuth(III) oxide could be increased by codoping [§] with Dy^3 and W^{6+}.[63] The codoped $(DyO_{1.5})_x(WO_3)_y(BiO_{1.5})_{1-x-y}$ (DWSB) bismuth(III) oxides show some of the best stabilities and oxide ionic conductivities of the doped bismuth family, $\sigma = 0.098$ S cm^{-1} at 500 °C in 8D4WSB.[78] A σ value of 0.0068 S cm^{-1} can be stably maintained for more than 500 h in 25D5WSB at 500 °C without significant loss.[63] While further work is still required, these materials are still potential candidates for SOFC applications.

Numerous other fluorite type electrolyte materials have been examined, many of which exhibit excellent oxide ion conducting abilities. However, most are found to be too unstable or expensive for realistic use. More comprehensive literature on fluorite oxide electrolytes and their ionic conducting abilities are listed in the following references.[21,22,26,70,73,79–81]

[§]The act of doping with more than one dopant species.

Perovskites

Perovskite structured oxides are another common and well investigated family of ionic conductors. These follow the form ABO_3, where the sum of the cations' charges is equal to six. The 12-coordinate A-sites are typically occupied by large cations such as La^{3+} or Sr^{2+}, and the 6-coordinate B-sites by smaller, higher valence cations like Ga^{3+} or Ti^{4+}, figure 1.5. Perovskites are very versatile as they can accommodate a broad range of cation sizes and valences. This allows for high oxide ion vacancy concentrations to be achieved, with minimal distortion to the lattice, resulting in high ionic conductivities.[70,82,83] To reduce structural strain and reduce defect trapping, dopants similar in size to the A/B-cations are generally selected. By carefully selecting the A and B-site cations, and by doping at one or both sites, the perovskite's structure and its properties can be tuned to the desired specifications.[21]

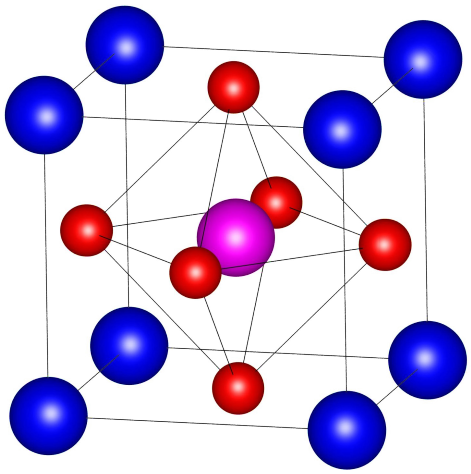

Figure 1.5: Ideal cubic structure of the ABO_3 perovskite, where the A, B and O sites are represented by blue, purple and red spheres respectively.

Lanthanum gallate ($LaGaO_3$) is one of the most studied perovskite-structured oxides to date.[84] It is commonly codoped with Sr^{2+} and Mg^{2+} to produce lanthanum strontium gallate magnesite (LSGM, $La_{1-x}Sr_xGa_{1-y}Mg_yO_{3-\delta}$).[83] LSGM is a good ionic conductor which displays σ values of around 0.17 S cm^{-1} at 800 °C.[26,85] This is comparable to CeO_2 based fluorites, but has the added advantage in that it does not undergo reduction. While LSGM shows high reactivity towards common electrode martials, Morales *et al.* suggests this can be mitigated by introducing an electrode-electrolyte interface.[84] The same report also demonstrate methods of reducing the synthesis temperature, which improves material stability. Although $LnBO_3$ based perovskites, where B = Al^{3+}, In^{3+}, Sc^{3+} or Y^{3+}, are generally more stable, they often present poorer ionic conductivities or high electrical conductivities.[21]

Other promising perovskite based materials are starting to emerge, such as those based on the $A_{0.5}A'_{0.5}BO_3$ material $Na_{0.5}Bi_{0.5}TiO_3$. These are of interest as they are the first to show that small changes in A-site stoichiometry of undoped perovskites can induce high levels of oxide ion conduction, equivalent to those in LSGM.[86] A detailed survey of perovskite materials and their properties is provided in a review by Vasala *et al.*[87]

Brownmillerites

Related to the perovskites are brownmillerites, e.g. $Ba_2In_2O_5$, which are an oxygen deficient form of the perovskite. At room temperature, the oxide ion vacancies order in rows resulting in the formation of alternating layers of InO_6 octahedra and InO_4 tetrahedra, stacked orthogonal to the vacancy rows, as shown in figure 1.6.[88] This ordering traps the oxide ion vacancies, preventing fast ion conduction.[22] However, when heated above 930 °C this ordering effect dissipates and $Ba_2In_2O_5$ becomes a good oxide ion conductor.[89] The highly conductive phase of $Ba_2In_2O_5$ can be stabilised at lower temperatures by doping at one or both of the cation sites. Some brownmillerites such as $(Ba_{0.3}Sr_{0.2}La_{0.5})_2In_2O_{5.5}$ present σ values greater than YSZ, 0.12 S cm^{-1} at 800 °C.[90] However, these materials tend to be sensitive to H_2O, CO_2 and oxidising environments.

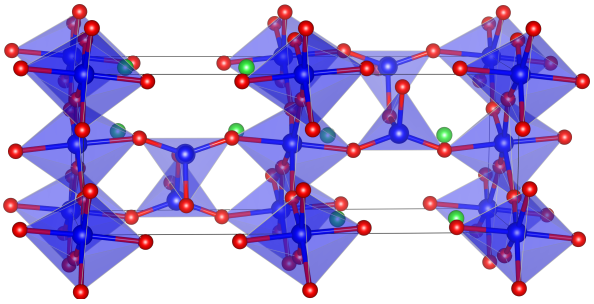

Figure 1.6: Ordered *Ibm2* brownmillerite structure with Ba, In and O represented by green, blue and red spheres respectively and InO_x polyhedra in blue.

Apatites

Oxyapatites are a more recent addition to the list of fast ion conductors being considered for SOFC applications. These have the general formula $A_{10-x}(BO_4)_6O_{2\pm\delta}$ where A is an alkaline or rare earth metal cation, often La^{3+}, and B is a p-block element like Si^{4+} or Ge^{4+}. The degrees of cation and oxygen non-stoichiometry are indicated by x and δ respectively. This non-stoichiometric nature allows oxyapatites to display good conductivities, even prior to doping.[91] Oxyapatites have open structures with hexagonal, or occasionally triclinic, symmetry. As shown in figure 1.7, they are comprised of isolated BO_4 tetrahedra with A-cation and O-anion channels running along the c-axis.

Investigations have been conducted into a range of $La_{9.33+x}(SiO_4)_6O_{2+3x/2}$ based materials. The results of which show non-stoichiometric systems, e.g. $La_{9.33}(SiO_4)_6O_2$, are better ionic conductors than fully stoichiometric systems like $La_8Ba_2(SiO_4)_6O_2$ and oxygen excess systems like $La_{9.67}(SiO_4)_6O_{2.5}$ are better still.[92] These differ from previous materials as they facilitate oxide ion conduction, in oxygen excess systems, *via* an interstitial mechanism.[59,93,94] In silicate systems, interstitials diffuse following a "sinusoidal" path down the *c*-axial oxide channels.[59] In the germanate systems, interstitials migrate down the *c*-axis through continued destruction and reformation of bridged "Ge_2O_9" units.[95] The high conductivities of these materials is, in part, a result of this interstitial mechanism, as discussed in section 2.8.2. Whilst σ increases with x, the undoped Si and Ge systems are only stable up to $x = 0.34$ and 0.42 respectively.[96] Beyond this, impurity phases start to form. Like perovskites, a diverse array of dopants can be substituted onto both the A and B cation sites.[96,97] Nevertheless, oxyapatites in which A = La^{3+} and B = Si^{4+}/Ge^{4+} are currently the best in their family.

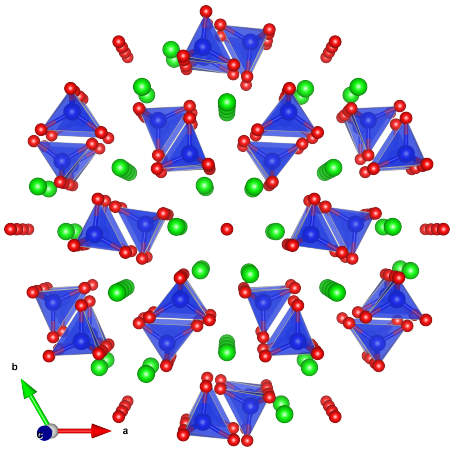

Figure 1.7: Hexagonal $A_{10}(BO_4)_6O_2$ apatite structure, green, blue and red spheres represent A, B and O sites respectively, and blue polyhedra - BO_4 tetrahedra.

Silicate oxyapatites are generally superior ionic conductors to YSZ. For example, at 500 °C $La_{9.67}(SiO_4)_6O_{2.5}$ reaches $\sigma = 1.1\times10^{-3}$ S cm^{-1}.[91] This increases to 3.7×10^{-3} S cm^{-1} when doped with Al^{3+} to form $La_{10}(SiO_4)_{5.5}(AlO_4)_{0.5}O_{2.75}$.[69,98] In contrast to the silicates, the oxygen excess germanates present poor σ values at low temperatures.[99,100] This is because they transition from hexagonal to triclinic symmetry below ~650 °C.[22,99] However, this can be prevented by Y^{3+} or Al^{3+} doping, for example $La_{9.5}(GeO_4)_{5.5}(AlO_4)_{0.5}O_2$ displays a σ value of 5×10^{-3} S cm^{-1} at 500 °C.[22,66] While germanate-apatites tend to be better oxide ion conductors than their silicate analogues above 500-600 °C, they are worse below, are more expensive and suffer from volatility and glass formation issues.[21,92] Thus, the silicates are generally preferred.

Other Electrolyte Materials

Many comparisons can be drawn between δ-Bi_2O_3 and $La_2Mo_2O_9$ based materials. Like the former, $La_2Mo_2O_9$ contains vacant "oxide sites" resulting from the lone pair effect.[101] As such, the pure material presents a σ value of $\sim 6\times10^{-2}$ S cm^{-1} at 800 °C.[67] Similarly, it undergoes transformation to a non-conductive phase below 580 °C . The conductive phase can be stabilised to room temperature, without significant detriment to its conductivity, by doping the La^{3+} sites with Y^{3+} or Ga^{3+}.[102] Doped $La_2Mo_2O_9$ systems are referred to as LAMOX. The volatility and reducibility of Mo^{6+} makes LAMOX somewhat unstable. It is therefore more beneficial to dope at the Mo^{6+} site with ions like W^{6+}, this stabilises the conductive phase, helps supress electrical conductivity and bolsters overall stability.[103] However, this also reduces its low temperature conductivity. The high thermal expansion coefficients of these materials and their reactivity towards current electrode materials present a further barrier to their use.[103,104]

Recently, fast oxide-ion conduction has been reported in 2D layered materials of composition $Sr_{1-x}A_xBO_{3-0.5x}$, where A = Na^+, K^+ and B = Si^{4+} and/or Ge^{4+}.[105,106] Such structures are comprised of layers of isolated B_3O_9 units, which in turn are formed of three corner sharing BO_4 tetrahedra. These layers are separated from one another by planes of close packed Sr^{2+} ions. The doping of Sr^{2+} sites with K^+ or Na^+ induces oxide ion vacancy formation which enhances ionic conductivity. It is reported that, at 500 °C, the composition $Sr_{0.55}Na_{0.45}SiO_{2.775}$ has an oxide ion conductivity of $> 10^{-2}$ S cm^{-1} which is a substantial improvement over LSGM and YSZ type materials.[68] These materials are highly promising as they present some of the highest reported conductivity values of any known chemically stable electrolyte material.[107] However, others have been unable to reproduce the reported results.[108] They instead suggest that the high conductivity values reported are not related to oxide ion migration, but rather some other effect. Therefore, further investigations must be conducted to resolve the origins of the reported conductivities before further progress can be made.

Fast oxide and proton conduction in also observed in $LaBaGaO_4$ based materials.[109,110] These adopt orthorhombic β-K_2SO_4 type structures with isolated GaO_4 tetrahedra and alternating La and Ba cation layers. For satisfactory ion conduction levels to be reached doping must be employed to promote oxide ion vacancy formation. To accommodate these vacancies, pairs of neighbouring GaO_4 tetrahedra bind together to form "Ga_2O_7" units. It is the repeated making and breaking of these units which facilitates oxide ion conduction. These materials bear a strong resemblance to those investigated herein.

1.3 Electrode Materials

In addition to the general requirements discussed in section 1.2, an electrode material must be sufficiently porous to permit the diffusion of reactant gasses, present high electronic conductivities (preferably > 100 S cm^{-1}) and show a good catalytic ability to reduce/oxidise oxidant/fuel at the cathode/anode.[21,53,111,112] Furthermore, it is highly advantageous for electrode materials to be good ionic conductors, the reasons for which will be discussed in section 1.3.2. The basics of electrode construction and operation will now be discussed alongside a review of pertinent materials. However, only a cursory review of the anode is given as it shares many attributes with the cathode, and is less relevant to this study.

1.3.1 Anode Materials

The reducing conditions present at the anode permits metals such as nickel or cobalt to be used. Nickel has the advantage of being cheap and chemically stable while showing good catalytic ability towards fuel oxidation and reformation. However, nickel has a much higher TEC than the most common electrolyte materials and displays low porosity due to its tendency to sinter at high temperatures. By combining nickel with YSZ, a Ni/YSZ cermet anode can be produced. The cermet presents significantly better porosity and compatibility with common electrolytes, and has the added advantage of increasing the electrochemically active area of the anode. This cermet is currently the SOFC anode material of choice. However, anode materials development is still an ongoing process as Ni/YSZ has its drawbacks. These include, but are not limited to, susceptibility to sulphur poisoning and anode degradation through carbon deposition.[21,113] Improvements to the cermet have been made by replacing YSZ with another more conductive electrolyte or by adding small amounts of iron (10%) to the nickel.[114] To resolve the stability and fuel flexibility issues, investigations have shifted more towards the development of solid oxide based anodes.[114,115] Some of these solid oxides, such as $Sr_{1.6}K_{0.4}FeMnO_{6-\delta}$, are found to show enhanced anodic performance.[116]

While only a brief review of anode materials has been given, more in-depth reviews of current and novel anode materials can be found in the following references.[21,113–115,117] Furthermore, the operation, features and material requirements of SOFC anodes are similar to those of a cathode, which will now be discussed.

1.3.2 Cathode Materials

The cathode's primary role in oxide ion conducting SOFCs is to facilitate the oxygen reduction reaction (ORR), as detailed in equation 1.4. To do this, a cathode must have the ability to catalytically adsorb, dissociate and reduce oxygen, whilst remaining stable in a highly oxidising environment. With slow kinetics and high activation energy, the ORR, and so the cathode, is a major cause of efficiency loss at reduced temperatures.[25,52,118] As the choice of cathode material can profoundly affect the cell's overall performance it must be selected with care. For this reason, considerable emphasis has been placed on developing higher performance cathodes for intermediate to low temperature applications. It is therefore important to understand basic cathode construction and operation as it will aid discussion of the cathode materials currently being developed.

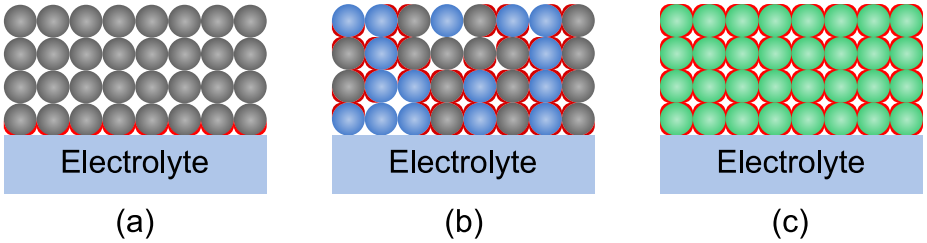

Figure 1.8: Triple phase boundaries (red) in a) electronic conducting (grey), b) dual-phase composite (grey/blue) and c) mixed conducting (green) cathodes.

For the ORR to take place, electrons, molecular oxygen and a drain for the reduced ions must to be present simultaneously. These electrochemically active regions occur at locations where an electronic conductor, an ionic conductor and gaseous oxygen all come into contact with one another. Such locations are often referred to as triple phase boundary regions (TPB). In purely electronic conducting cathodes, such as lanthanum strontium manganite (LSM), the TPB regions appear along the cathode-electrolyte interface where gaseous oxygen is found, shown schematically in figure 1.8a. By combining LSM with an ionic conductor, such as YSZ, the TPB can be extended to regions beyond the cathode-electrolyte interface. This allows ORRs to occur in the cathode where electronic and ionic conducting grains are in contact with one another and the gas phase, as shown in figure 1.8b. Such cathodes, which are comprised of a mix of electronic and ionic conducting materials, are known as composite cathodes, the most common of which is LSM/YSZ. The TPB region can be extended even further through the use of mixed ionic-electronic conducting materials (MIEC) like lanthanum strontium cobalt ferrite.[113,119] In mixed conductor cathodes the ORR can take place at any point where the cathode's surface is in contact with the gas phase, as depicted in figure 1.8c.

MIEC materials have also been used in composite-type cathodes. This offers a larger electrochemically active surface which reduces cathodic polarisation and aids retention of cell efficiency as the temperature is decreased.[120]

Further, improvements to both stability and activity can reliably be achieved through surface modification methods, such as fabrication by impregnation.[121] These methods offer a means to create next-generation cathodes using only current-generation materials. Impregnation involves the deposition of an electrochemically active material as a thin film coating, or as discrete particles, onto a porous electrode backbone. The porous backbone structure can be either functional or purely skeletal in nature. An example of the former can be seen when impregnating the MIEC material $La_xSr_{1-x}Co_yFe_{1-y}O_{3-\delta}$ (LSCF) with $Sm_{0.5}Sr_{0.5}CoO_{3-\delta}$. This decreases polarisation resistance by 80%, increases power density by about 22% and enhances the cathode's long term stability by suppressing strontium segregation.[122] In the latter, an ionic conductfing backbone is used, which is often just an extension of the electrolyte. This effectively creates a nanostructured composite cathode with an increased TPB region and enhanced ionic transport properties, often with increased stability. In general, these techniques are extremely powerful and offer a viable means towards the creation of cathodes for intermediate temperature solid oxide fuel cells.

Current cathode materials possess high stability, matched TEC with common electrolyte materials and good electrical conductivity. However, the large cathodic polarisation resistances encountered at temperatures below 700 °C prevents their use in low and intermediate temperature applications. Therefore, new cathode materials are required for the development of low and intermediate temperature SOFCs. A selection of the most common and promising cathode materials are reviewed below, starting with the perovskites.

Perovskites

The perovskite based oxides, described previously in section 1.2.1, are of great research interest for SOFC cathode applications.[114,119,123,124] Perovskites designed for cathodic applications usually have B-sites occupied by reducible transition metal cations such as Mn, Fe or Co (multivalent).[53] This is due to the enhanced catalytic abilities and electronic conductivities they offer. Material property enhancements are commonly made through aliovalent A-site doping or isovalent doping of the B-site. While the previously discussed perovskites compensated charge imbalances through the formation of oxide ion vacancies (ionic compensation), some of these materials compensate through shifts in

their B-site valencies such as Mn^{3+} to Mn^{4+} (electronic compensation).[123] This increases the electron defect concentration and so enhances electrical conductivity. Perovskites with highly reducible B-site cations, such as $LaMnO_3$, tend to prefer electronic forms of charge compensation and so are generally good electronic conductors but poor ionic conductors. Partially doping the B-site with less reducible ions decreases the amount of reducible species available for electronic charge compensation, leading to increased levels of ionic charge compensation. This effectively increases the materials ionic conductivity at the expense of its electrical conductivity.

Lanthanum strontium manganite (LSM), $La_{1-x}Sr_xMnO_{3-\delta}$ (where x is the level of doping), is a popular SOFC cathode material due to its high electronic conductivity, electrocatalytic activity and matching TEC with existing SOFC materials. Sr^{2+} is usually the dopant of choice for $LaMnO_3$ as it is similar in size to La^{3+}. Doping with Sr^{2+} not only enhances ionic conductivity but increase compatibility with YSZ. Undoped $LaMnO_3$ reacts with YSZ to form the insulating material $La_2Zr_2O_7$ at the cathode-electrolyte interface. However, Sr^{2+} doping inhibits this reaction. A maximum doping limit is reached at around 30 mol. %, beyond which LSM starts to react with YSZ to form $SrZrO_3$. Despite its other abilities, LSM is a poor ionic conductor, which limits its use at reduced temperatures.[118,125] To combat the increasing polarisation resistances encountered at lower temperatures, LSM is often coupled with a fast ion conductor, such as YSZ, to form a composite cathode with improved lower temperature functionality.[118,126] Further enhancements to the low temperature functionality of LSM/YSZ composites can be made by impregnating them with materials such as $Ce_{0.8}Ge_{0.2}O_{2-\delta}$.[127]

Lanthanum strontium cobalt ferrite (LSCF), $La_{1-x}Sr_xCo_{1-y}Fe_yO_{3-\delta}$, is another prominent member of the perovskite family. Unlike LSM, which is a pure electronic conductor, LSCF is a mixed ionic-electronic conductor, and so displays superior ionic conductivity over the former.[119] While LSCF is a good mixed conductor, it displays poor activity towards the ORR, due in part to Sr^{2+} segregation, and suffers from long term stability issues.[53,128,129] However, the catalytic activity and long term stability of LSCF based cathodes can be significantly improved by impregnating them with a thin catalytic layer.[121,130] As it stands, LSCF based materials are currently one of the most promising SOFC cathode materials for intermediate temperatures. $Ba_{1-x}Sr_xCo_{1-y}Fe_yO_{3-\delta}$ (BSCF) based materials displays higher MIECs and lower polarisation resistances at low temperature than other perovskite materials. However, they tend to have large TEC and react with CO_2, SO_2 and H_2O at temperatures below 800 °C.[53,114]

Other Cathode Materials

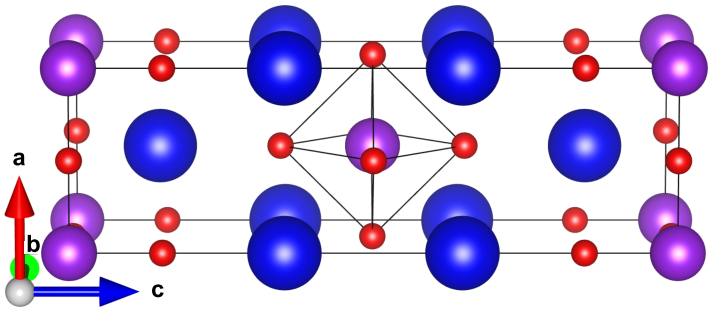

Figure 1.9: Structure of n=1 type $(AO)(ABO_3)_n$ Ruddleston-Popper phase with A, B and O represented as blue, purple and red spheres respectively.

Although perovskites have been the material of choice for a long time, other hybrid-perovskite and non-perovskite structures are starting to gain interest. Related to the perovskites are the Ruddleston-Popper (RP) phases. Based on the K_2NiF_4 structure, these materials consist of alternating perovskite and rock salt layers, as shown in figure 1.9. Ruddleston-Popper oxides follow the generic formula $(AO)(ABO_3)_n$ where n is the number of perovskite units per layer. Most investigations commonly focus on RP materials in which A = La^{3+}, Nd^{3+} or Pr^{3+} and B = $Cu^{2+/3+}$, $Ni^{2+/3+}$ or $Co^{2+/3+}$.[131] Undoped materials like $La_2NiO_{4+\delta}$ generally display high degrees of oxygen hyperstoichiometry, the extent of which depends on the A and B species, A and B-site doping, oxygen partial pressure and the temperature. The highest oxygen concentrations are normally encountered in materials where B = Ni^{2+}. Within $Ln_2NiO_{4+\delta}$ materials, there exists an inherent structural strain due to the mismatch in size of the perovskite and rock salt sub-lattices.[132] By incorporating oxide ion interstitials into the rock salt layers, the size mismatch, and therefore the strain, can be decreased. This decrease can be explained by the increased Ln-O bond distances, caused by greater La^{3+} coordination numbers, and the decreased Ni-O bond distances, caused by Ni-oxidation.[132] The extent of oxygen hyperstoichiometry is generally greater in $Nd_2NiO_{4+\delta}$ and $Pr_2NiO_{4+\delta}$ than $La_2NiO_{4+\delta}$, this is due to the additional inter-layer strain caused by the smaller ionic radii of Nd^{3+} and Pr^{3+}. These materials tend to be good MIEC due to their oxygen hyperstoichiometry and mixed valence states. Reports suggest these materials present good oxide ion diffusion rates, and that diffusion proceeds *via* an interstitial mechanism.[53,133–135] Some investigations have found the oxide ion conductivity of $Ln_2NiO_{4+\delta}$ materials to be of the same order of magnitude as 8YSZ (8% doping).[136] However, these materials, when $n = 1$, generally tend to be poor electronic conductors compared to other perovskite related compounds.[114] Nevertheless, these materials are of interest as they naturally have a low polarisation resistance and a high oxide defect concentration, and so do not necessarily require doping.[137] Opposite to other

perovskites, Sr^{2+} doping actually reduces ionic conductivity as it decreases the oxide ion interstitial content.[133] However, Sr^{2+} is reported to increase electrical conductivity and enhance phase stability.[138,139] Many investigations have probed the effects of various dopants on cathodic ability and, particularly, electrical conductivity.[133,136,140,141] An advantage of these materials is the similarity of their TECs to those of common electrolyte materials. Furthermore, Ni^{2+} is commonly use in place of Co^{2+}, which removes the need for special recycling protocols. An alternative approach to improving the electrical conducting abilities of these materials, other than doping, is to combine the $n = 1$ material with its $n = 3$ counterpart.[142] While the $n = 1$ materials are generally good ionic conductors the $n = 3$ counterparts are good electronic conductors. The resulting composite yields improved MIECs over either parent bulk material. Like the previously discussed materials, these can be further enhanced through composite-impregnation methods.[143]

Other more exotic materials are also being investigated. One such example is the Swedenborgite-type oxide family, these materials have the general formula $RBa(Co,M)_4O_{7+\delta}$ where R = Y^{3+}, In^{3+} or Ca^{2+} and M = $Co^{2+/3+}$, $Fe^{2+/3+}$, Zn^{2+}, Al^{3+} or Ga^{3+}. They have been shown to have acceptable thermal expansion coefficients and favourable electrochemical performance properties at reduced temperatures.[144,145] However, such materials are generally not stable over long time periods (e.g. 120 h) at common SOFC operating temperatures (600-800 °C). More recent work, such as that conducted by West *et al.*, has shown that material stabilisation is achievable through the selection of suitable R and M site dopants.[146] Whilst the perovskite based materials are promising, it can be seen that it is still important to investigate other materials. It is possible that other material classes possess cathodic abilities greater than or equal those of the perovskites. Furthermore, by investigating and cataloguing the abilities of other materials, a better understanding of cathodic materials in general can be gained, which may aid further investigations. It is this exploration of alternative materials that is the focus of this thesis.

1.4 Investigation of A_2BO_4 Oxometallates

The general formula A_2BO_4 represents a diverse group of oxometallates with over 50 known crystal structures.[147] Members of this group include the spinels, olivines and some of the Ruddlesden-Popper phases. The structures found within this group can vary from one another, and shifts in chemical composition can also yield structural diversity within each of the crystal structures. This group therefore offers a wide spectrum of ma-

terials with a plethora of properties and, perhaps more importantly, structural tunability. By measuring and correlating the abilities of these materials to their structures, it may be possible to conduct material investigations in a more targeted manner. Recently, A_2BO_4 materials have been the focus of an increased number of studies, some yielding promising results in terms of ionic conducting abilities.[136,138,148–151] This suggests that other good oxide ion conductors, which have not yet been assessed, may still be found within the A_2BO_4 group. Interstitial oxide ion conductors, such as apatites and melilites, tend to exhibit excellent ionic conductivities.[58,148,152] Such conductors often, but not always, contain flexible tetrahedral networks. Many materials containing either isolated or linked tetrahedral frameworks can be found within the A_2BO_4 group.[147,153] Therefore, it is possible that many potential fast oxide ion conductors can also be found within the A_2BO_4 group. It is from this diverse group that the materials to be investigated are selected.

In this thesis, a selection of possible fast oxide ion conducting A_2BO_4 materials are to be investigated, and the viability of their use in solid oxide fuel cells assessed. Using the computational methods discussed in chapter 2, the defect chemistry and oxide ion conducting properties of selected materials are investigated. Through an atomic level understanding of the role of defects and dopants on ion transport, the ionic conducting abilities of these materials may be optimised. A very brief description of the materials selected for investigation will now be given below.

The first material selected for investigation in this study is the olivine-structured material cadmium orthogermanate (Cd_2GeO_4). Some olivines, such as lithium iron phosphate, have shown promise as cathodes in lithium ion batteries.[154] However, little is known about their applicability in SOFCs. This material was selected based on its relatively short inter-tetrahedral distances (3.96 Å) in comparison to Ba_2TiO_4. The second material selected is barium orthotitanate (Ba_2TiO_4). This material is isostructural with β-Ca_2SiO_4 and is one of only a handful of materials in which Ti^{4+} occupies a 4 coordinate tetrahedral site. The unusual tetrahedral geometry in Ba_2TiO_4 gives the structure an additional degree of coordinational flexibility, which could aid in the formation of oxide defects. Finally, barium orthogermanate (Ba_2GeO_4) was also selected for investigation to assess the effects of differing B site cation on ionic conduction. This material is comparable to Ba_2TiO_4 in terms of its structure, but with a higher degree of symmetry. Comprehensive structural descriptions of Cd_2GeO_4, Ba_2TiO_4 and Ba_2GeO_4 can be found in chapters 3, 4 and 5 respectively, along with their results and discussions. However, only preliminary results have been presented for Ba_2GeO_4 in this work.

Chapter 2

Methodology

2.1 Introduction

Computational chemistry, as the name would suggest, is a means of investigation the properties and behaviours of a system through computational simulations of numerical models. Such methods are becoming ever more prevalent in modern scientific investigations. This is due, in part, to recent technological advances which have enabled wider availability of access to high performance computing systems. Molecular modelling, as a scientific means of investigation, is a powerful tool, especially when used in conjunction with experiment. Such methods can be used to complement experimental results and more importantly to probe properties that are difficult to see experimentally. Computational methods can simulate samples or environments that are normally too expensive, time consuming, dangerous or otherwise infeasible to investigate through non-simulatory means with comparative ease.

Many different methods exist for representing and simulating atomistic systems, each with varying orders of approximation, ranging from *ab-initio* quantum and semi-empirical techniques to molecular mechanics. The methods of investigation are dictated by the properties of interest, system size, the system itself and the level accuracy required. For the most part, the decision often comes down to a trade-off between accuracy and efficiency in the form of computational expense.

Two main computational methods are employed in this work, both of which utilise interatomic based potentials. The first is static lattice energy minimisation as implemented in the general utility lattice program (GULP).[155–157] This, as detailed in section 2.3, is used not only to verify and refine the interatomic potential model but to understand the crystal structure and defects within it. Molecular dynamics simulations, as described in

section 2.9, are then performed on this model, using the program DL_POLY classic, to extract time averaged information about system behaviour at known temperatures and pressures.[158,159] The interatomic potential model will be discussed first as it is what the calculations in this work will be based on.

2.2 The Interatomic Potential Model

In recent times, computational simulations based on the Born model have been used with great success to gain atomic level insights into a diverse range of solid ionic materials. All of the atomistic calculations conducted in this work have been based upon the Born model for ionic solids.[160] This model treats the crystal lattice as an infinite and periodic array of charged, spherical ions.

Within the crystal lattice, all ions interact with all other ions in a complex and interdependent fashion. These interactions can be expressed as a series expansion of all n-body interactions, ranging from simple two-body interactions to high order many-body interactions. The sum of this series, equation 2.1, yields the system's lattice energy.

$$U_{Latt} = \sum_{ij} \Phi_{ij}\left(r_{ij}\right) + \sum_{ijk} \Phi_{ijk}\left(r_{ijk}\right) + ... \sum_{i \to n} \Phi_{i \to n}\left(r_{i \to n}\right) \tag{2.1}$$

Where U_{Latt} is the lattice energy, Φ_{ij} is the total potential energy of all two-body interactions, Φ_{ijk} of all three-body interactions and so on. In the majority of cases involving ionic solids, the two-body terms contribute significantly more to the lattice energy then all of the other terms. This is due to the highly ordered nature of most crystal structures. Therefore, the Born model truncates this series at the two-body term, this is known as the pairwise approximation.[161] Furthermore, any contributions from the other n-body terms will generally be incorporated into the two-body potentials during the fitting process. The remaining pairwise interactions are then partitioned into their long range coulombic and short range constituents as shown below:

$$U_{Latt} = \sum_{ij} \frac{q_i q_j}{4\pi\epsilon_0 r_{ij}} + \sum_{ij} \Phi_{ij}^{Short}\left(r_{ij}\right) \tag{2.2}$$

Or more simplistically as just:

$$U_{Latt} = \Phi_{ij}^{Long} + \Phi_{ij}^{Short} \tag{2.3}$$

The first and second terms in the above equations are the long range coulombic and short range interaction terms respectively, both of which are described in full in the next few sections.

2.2.1 Long-Range Interactions

At large interatomic separation distances ($r_{ij} > 12$ Å) the short range term Φ_{ij}^{Short} is negligibly small and all interactions can be considered to be entirely coulombic in nature. Such interactions can be either attractive or repulsive depending on the comparative charge of the ions involved. The strength of the interaction is dependent on both the magnitude of the ion's charges and the distance between them. The potential energy for this long range pairwise coulombic interaction is given in equation 2.4.

$$\Phi_{ij}^{Long}(r_{ij}) = \frac{1}{4\pi\epsilon_0}\frac{q_i q_j}{r_{ij}} \tag{2.4}$$

Where Φ_{ij}^{Long} is the energy arising from the long range coulombic interaction of ions i and j with charges q_i and q_j respectively over a distance of r_{ij}, and ϵ_0 is the permittivity of free space. Although simple in definition the coulombic interaction is extremely expensive to calculate explicitly. While the strength of each coulombic interaction decreases with distance, the number of interactions increases. Meaning that even at large distances such interactions can be non-trivial, leading to slow convergence. However, a method developed by Ewald, known as the Ewald sum, helps to overcome this barrier.[162]

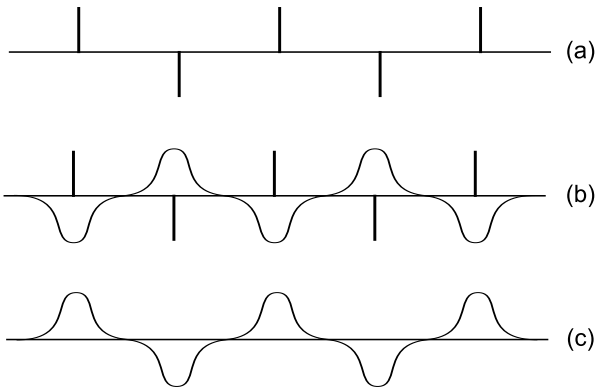

Figure 2.1: Illustration of Ewald summation showing a) point charges, b) screened point charges and c) compensating charges.

The Ewald sum method works by splitting the coulombic interaction into a short-range real-space component and a long-range reciprocal-space component, both of which converge rapidly. To evaluate the short-range component each point charge is screened with a diffuse Gaussian charge of equal magnitude but opposite sign, as shown in figure 2.1b. This causes the net charge, and therefore the interaction, to rapidly zero out with increasing distance. How quickly the charges drop to zero is defined by the width of the Gaussian. To compensate for the original screening charge, a second Gaussian charge distribution of equal magnitude and sign to original point charges is now applied,

as shown in figure 2.1c. The long-range component is then evaluated in reciprocal-space. These two components are then summed to return the full coulombic interaction. However, such methods are only valid for charge neutral cells. More comprehensive reviews of the Ewald summation can be found in the following references.[163–165]

2.2.2 Short-Range Interactions

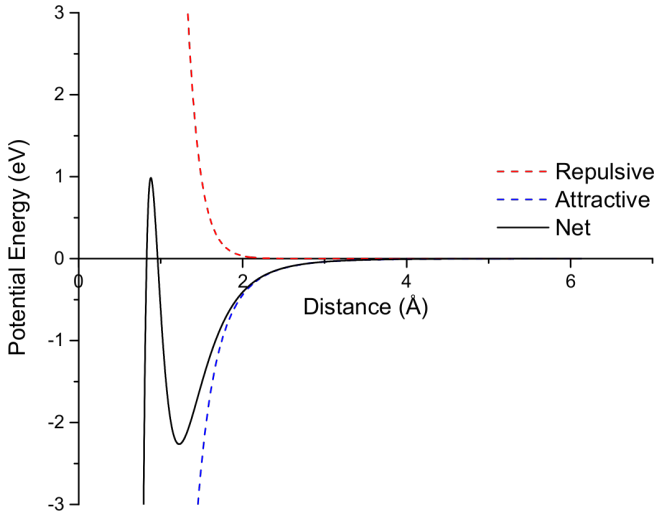

Figure 2.2: The short range Buckingham interaction as a function of distance alongside its attractive an repulsive components.

The treatment of ions as simple point charges interacting with one another electrostatically holds well for large distances. However, this approximation breaks down with reducing interatomic separation. As such, an additional short-range term is included to model the more complex behaviour which emerges at such distance. These interactions can act as an exclusively repulsive force or a combination of attractive and repulsive forces, where the extent and type of force is dependent on the ion pair. There are a variety of different expressions which can be used to model the behaviour of short-range interactions, such as the Lennard-Jones potential. Perhaps one of the most popular and successfully applied potential forms for ionic solids is the Buckingham potential:[166]

$$\Phi_{ij}^{Short}\left(r_{ij}\right) = A\exp\left(-\frac{r_{ij}}{\rho}\right) - \frac{C}{r_{ij}^{6}} \tag{2.5}$$

Where A, ρ and C are the adjustable parameters unique to each ion pair which must be modified in order to accurately reproduce the experimental crystal structure. The Buckingham potential can be split into two parts, a repulsive and an attractive term.

The first term, containing parameters A and ρ, was developed by Born and Mayer and accounts for the short range repulsive interactions which occur at small separation distances. As the distance between a pair of ions decreases their electron clouds start to overlap with one another. This results in the emergence strong short range repulsive forces. Such behaviour is a product of the Pauli exclusion principle and the increased nuclear-nuclear interactions. The repulsive component of the Buckingham potential is shown in figure 2.2 as a dashed red line.

Reappropriated from the Lennard-Jones equation, the second part of the Buckingham potential, which includes the C parameter, details the attractive and comparatively longer range dispersive van der Waals–London interactions. This attractive component is also shown in figure 2.2 as the dashed blue line. The dispersive forces experienced are due to the instantaneous dipoles formed as a result of density fluctuations in an ion's electron cloud. The newly formed dipoles can then go on to induce dipole formation in neighbouring ions, resulting in an attraction. These types of interactions are highly dependent on the polarisability of the ion's electron cloud. Greater values are typically seen in highly polarisable species such as large anions.

The short-range nature of these Buckingham interactions means that they quickly become trivial with increasing distance. As such, there is no tangible advantage to calculating them beyond a certain distance. Therefore, a cutoff of 12 Å is usually employed, beyond which they are not calculated. Truncating the short-range interactions in such a manner helps reduce the computational expense of subsequent calculations. The Buckingham potential has been extensively used since its conception due to the accuracy and efficiently it provides. However, care must be taken when calculating interactions at short distances, as when r_{ij} tends towards 0, the attractive component $-C/r_{ij}^6$, and indeed the interaction as a whole, rapidly approaches $-\infty$. The consequence of this is that at small separation distances the ions may become unphysically attracted and bonded to one another.

Before an interatomic potential based investigation can be carried out, a suitable set of interatomic potentials must be identified. The general process by which interatomic potential models were empirically fitted in this work is shown in figure 2.3. The first stage of this process consists of scanning combinations of known interatomic potentials from literature to identify a suitable starting model. The interatomic potential terms are then iteratively adjusted, either manually or using a genetic algorithm, to improve the

fit, as determined by the least square difference between calculated and experimental values. Adjustments which improve the model are kept and those which dont are not. This adjustment loop continues until the specified convergence criteria are met i.e. calculated parameter values are with a few percent of the experimental values.

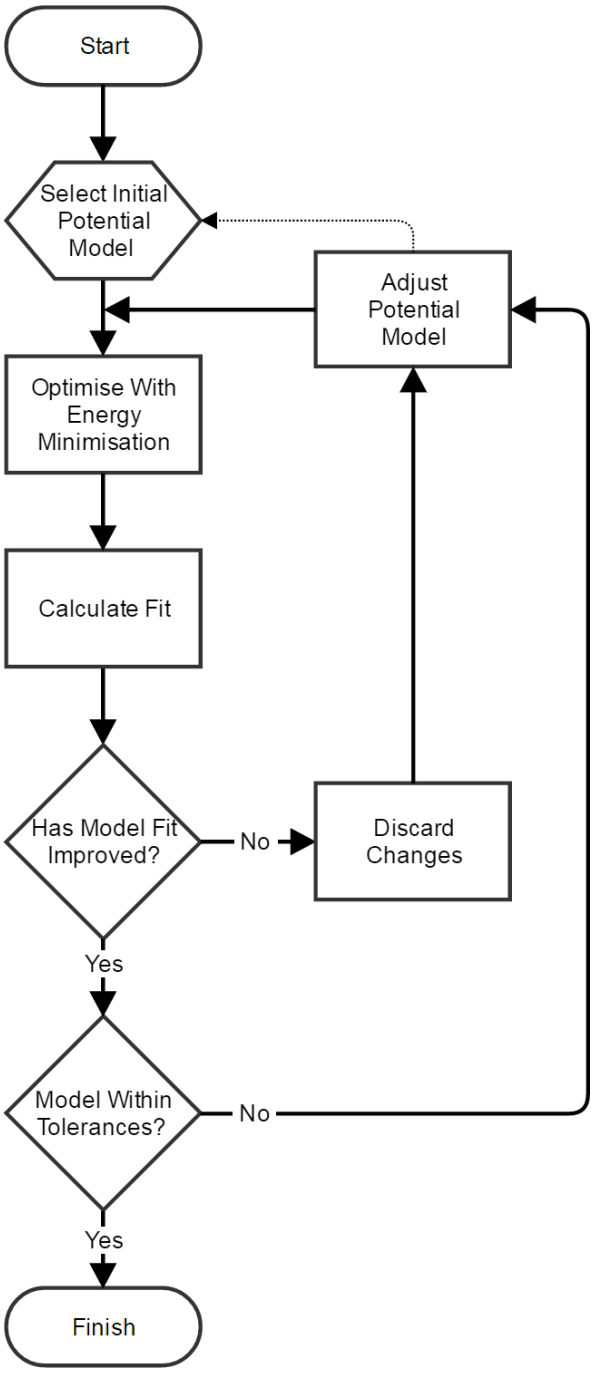

Figure 2.3: Flow chart representation of the generalised process for the empirical fitting of an interatomic potential model.

2.2.3 Bonding Interactions

Morse potentials were employed for calculations involving covalently bonded molecules such as H_2O or CO_3^{2-}.[167] These potentials are more suited to describing covalent interactions than those discussed previously. The classic Morse potential takes the form:

$$\Phi_{ij}\left(r_{ij}\right) = D_e[(1 - exp^{-a(r_{ij}-r_0)})^2 - 1] \tag{2.6}$$

Where D_e and a are depth and width of the potential well respectively and r_0 is the equilibrium bond distance. The well depth is equivalent to the sum of the bonds dissociation and zero point energies. The potential well depth is commonly subtracted so that the interaction becomes zero at infinite separation. Furthermore, the coulombic interactions between ions of the same molecule were also subtracted to negate its effects.

Three-body terms were also included in the model to maintain the CO_3^{2-} group's 120° bond angle. This potential is shown in equation 2.7 and is controlled through the specification of an equilibrium bond angle θ_0 and a force constant k_2.

$$\Phi_{ijk}\left(\theta_{ijk}\right) = \frac{1}{2}k_2(\theta_{ijk} - \theta_0)^2 \tag{2.7}$$

A four-body torsional term, shown in equation 2.8, was also included to model the potential energy associated with the out-of-plane bending of the carbonate group. In the torsional potential the terms k_4, θ_0 and n represent the force constant, equilibrium torsion angle and number of stable minima respectively.

$$\Phi_{ijjl}\left(\theta_{ijjl}\right) = k_4(1 - cos(n\theta_{ijkl} - \theta_0)) \tag{2.8}$$

2.2.4 Polarisation

When subjected to an electric field, the electron cloud encompassing an ion shifts producing a net field response. This effect, known as polarisation, is particularly important when studying large ions, which polarise easily, or charged defects which aggressively polarise surrounding ions. Furthermore, polarisation can play an important role in defining the properties and behaviours of a system. Neglecting polarisability is likely to result in non-representative behaviour. It is therefore important to include electronic polarisability in the model to ensure that the systems under investigation and their defective states are modelled accurately. One of the first and simplest methods of introducing electronic polarisability into model systems is through the use of the point

polarisable ion model. This method assigns each ion a linear polarisability constant. The dipole resulting from an electric field is expressed as $\mu = \alpha E$. Where μ is the dipole moment resulting from an electric field E acting upon an ion of polarisability α. However this model fails to take into account the dynamic and environmentally dependent nature of polarisation resulting from short range repulsion-polarisation coupling and so often produces unsatisfactory results.

As an ion is polarised its electron cloud is distorted creating regions of high electron density, because such regions are unfavourable an opposing force, known as the polarisation resistance, is generated which acts to dampen further polarisation. The extent of polarisation resistance is dependent on the current level of polarisation. Which is to say that the more polarised an ion is, the harder it becomes to further polarise. As such, further terms must be introduced to enable a more comprehensive description which takes into account the non-linear nature of polarisation.

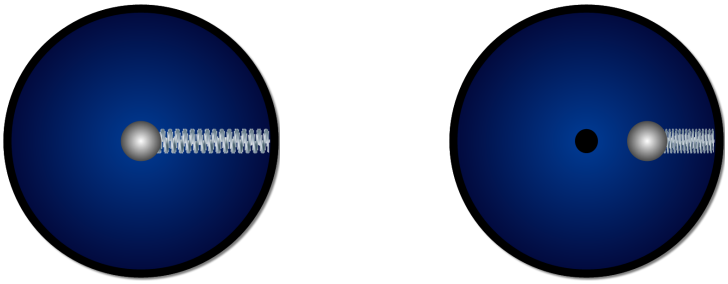

(a) (b)

Figure 2.4: Representations of (a) unpolarised and (b) polarised shells, with grey, blue and black representing the core, shell and the shell's centre respectively.

The shell model developed by Dick and Overhauser[168] treats ions as multicomponent entities, each ion consisting of a massive core of charge X and a spherical, often massless, shell of charge Y, where $X+Y$ is equal to the formal valence charge of the ion. The core is then bound to its shell by means of a mechanical spring of harmonic force constant k. The extent of polarisation, α, of an ion can be expressed as:

$$\alpha = \frac{Y^2}{k} \tag{2.9}$$

When the shell is relaxed, it occupies the same Cartesian centre point as its core and the ion is said to be in a non-polarised state, as shown in figure 2.4a. If an external force field, such as a Buckingham potential, acts upon the ion then its shell is shifted away from its norm and the ion is said to be polarised, as shown in figure 2.4b. The

degree of polarisation is determined by the extent to which the shell is displaced from its core. It is worth noting that the shell should not be considered representative of an ion's valence electrons as it can be positively charged. This model offers a simplistic and mechanically representable means of modelling polarisation in an ionic system. In order to achieve short–range–polarisation coupling the short–range potentials are assumed to interact only between shells, when present. In some cases, such as molecular dynamics, the shell is not massless, instead the adiabatic shell model is used, this entails placing a small portion of an ion's mass on to its shell.

2.3 Energy Minimisation

As previously discussed, a system's potential energy can be expressed as the sum of all energies which arise due to the interatomic interactions. The interaction between a given ion pair is, in turn, dependent solely on the distance separating them. Therefore, the interactions, their energies and subsequently the system's potential energy are dependent on the atomic coordinates. Thus, a system's potential energy can be considered to be a complex multidimensional function of its coordinates, as described in equation 2.10.

$$U_{Latt} = f(\vec{x}_i) \tag{2.10}$$

Where U_{Latt} is the lattice energy associated with a system when its atoms are in the coordinates defined by the vector $\vec{x}_i$. The implication of this being that as the coordinates of a system change there is a corresponding shift in its energy. As such, it is possible to consider the relationship between a system's energy and its coordinates as a surface with a high level of dimensionality. This is more commonly referred to as a potential energy surface. For a given system, each point on its energy surface represents a particular spatial arrangement of its atoms and the energy associated with that arrangement.

To fully describe an N atom system, 3N Cartesian coordinates are required. Therefore, the energy surface of a 5 atom system is 16 dimensional (15 coordinates + energy), and so cannot be graphically represented with ease. From this, it is also clear to see that for all but the simplest systems the investigation of an energy surface is not a trivial matter. An insight into this complexity can be gleamed by the fact that roughly 10^{25} calculations would be required to sample the energy surface of an a=b=c=5 Å cell containing 5 atoms with a 0.1 Å resolution. Despite its complex nature, an energy surface can provide a wealth of information about the system it represents.

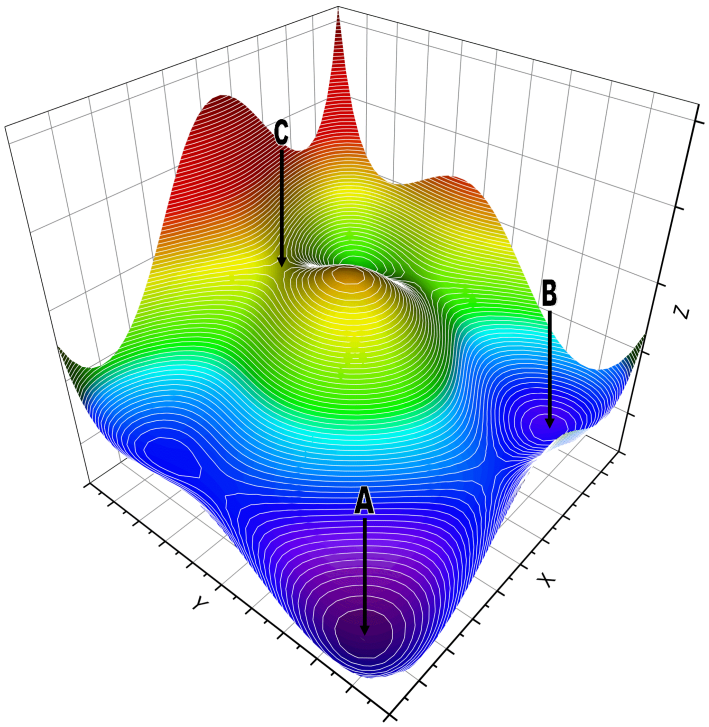

Figure 2.5: Simplified representation of an energy surface with labels indicating the locations of A) a global minimum, B) local minimum and C) saddle point.

A simplified plot of an energy surface is given in figure 2.5. In this, several features which correspond to local energy minima (wells A+B) and saddle points (bridges C) have been labelled. The energy minima (A+B) correspond to the systems stable conformations, the lowest of which is known as the global minimum (A) and represents the systems lowest possible energy conformation. Saddle points (C) indicate transition state structural conformations. The former is of particular interest as it represents a systems equilibrium state(s). The numerical process of finding energy minimised states, from a higher initial point, is known as energy minimisation.

Given the number of variables and the complexity of 3N dimensional systems the act of finding local energy minima is no simple task. For most systems this task cannot be done analytically so alternative iterative means must be employed. Many various techniques and algorithms exist for probing energy surfaces, each with their own intended applications. The methods discussed in this section are minimisation techniques which are exclusively designed to locate the nearest energy minimum and are only capable of travelling "downhill" on the energy surface.

The majority of energy minimisation techniques are based on the same fundamental process by which the coordinates are iteratively adjusted in the apparent direction of the minimum by the addition of some correction factor, as follows:

$$\vec{x}_{i+1} = \vec{x}_i + \vec{\varsigma} \tag{2.11}$$

Where $\vec{x}_{i+1}$ is the updated coordinate set, $\vec{x}_i$ is previous coordinate set and $\vec{\varsigma}$ is the correction factor which consists of a vector specifying the magnitude and direction in which the coordinates are to be adjusted. Following each adjustment step the conformation is checked against a set of criteria to tested if a minimum has been reached yet. The various techniques to be discussed differ primarily in how the correction factor is determined and can be broken up into two main categories. Which are first order techniques such as "steepest descent" and "conjugate gradient" and second order techniques such as "Newton-Raphson".

2.3.1 Steepest Descent

The steepest descent method, also known as gradient descent, is the most simplistic of the first order energy minimisation techniques.[164] This method is generally most appropriate when far from a minimum. In this method the atomic coordinates of the system are quickly and iteratively adjusted so that they, and the systems energy, follow the direction of steepest descent. The direction of steepest descent, $\vec{r}$, for an initial point $\vec{x}_i$ on the energy surface can be represented as the negative vector of the gradient of the function around that point:

$$\vec{r} = -\nabla f(\vec{x}_i) \tag{2.12}$$

Therefore the procedure used to update the coordinates during a descent step can be expressed as:

$$\vec{x}_{i+1} = \vec{x}_i + \lambda_i \vec{r} \tag{2.13}$$

Where $\vec{x}_{i+1}$ is the updated coordinates after a step of size λ_i in direction $\vec{r}$ has been taken. The vector of form $\lambda_i \vec{r}$ is identical to $\vec{\varsigma}$ seen in equation 2.11. The magnitude of the step to be taken, λ_i, is often specified using either arbitrary step or line search methods as discussed below.

Using line search methods, the minimum point along the line of direction $\vec{r}$ is located, and the magnitude λ_i is the distance required to reach the it. The minima can be located through the use of an iterative "bracketing method" or a more economic three-point quadratic. The details of these methods are beyond the scope of this discussion but comprehensive descriptions can be found in the reference work authored by A. R. Leach.[164] Alternatively, the arbitrary step method can be employed which, in direct contrast to line search methods, takes many small sub-steps towards the minimum, the size of which is determined by a scaler value.

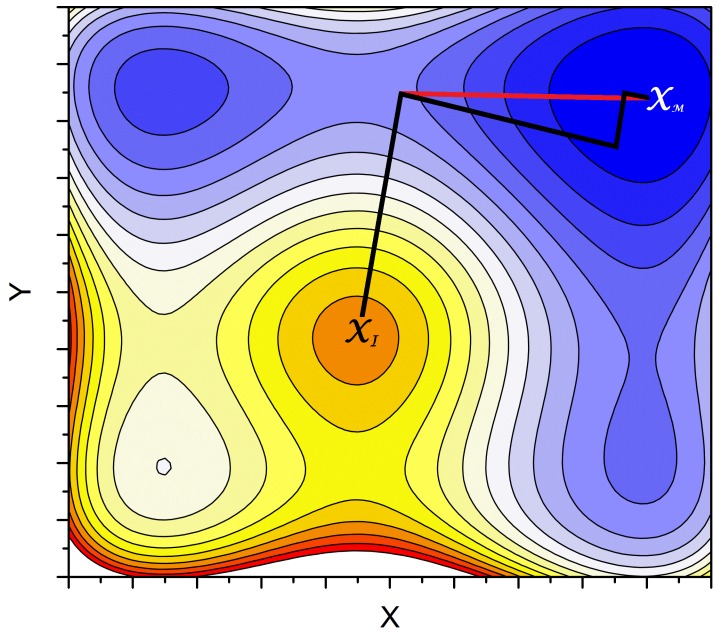

Figure 2.6: Contour representation of figure 2.5, X_I and X_M are the initial and final energy minimised locations respectively. Black lines show the steepest descent path to X_M and red lines where the conjugate gradient path differs.

Each step taken will invariably terminate at the lowest accessible point along the line of direction $\vec{r}$. As such, any further movement in that direction would result in increased energy, violating the constrains of energy minimisation. Therefore, the direction of travel of the following step must be directly orthogonal to that of the former. The black line in figure 2.6 demonstrates the way in which the steepest descent method approaches the minimum. This orthogonal movement results in the same directions repeatedly being scanned, which can be an inefficient means of approaching the minimum. The oscillatory nature of this method can lead to the propagation of errors through overcorrection and low efficiency, especially when traversing certain landscapes such as valleys.

2.3.2 Conjugate Gradient

The conjugate gradient method offers a means to avoid the pitfalls and insufficiencies associated with the oscillatory motion of the steepest descent method.[164] While the first step taken in each method is identical, the conjugate gradient then stores information about each step for use in calculating the next step. In the conjugate gradient method, the direction of travel for the current step i is augmented by the addition of some portion of the previous direction $i-1$ so that each successive step is conjugate to its predecessor. The direction of travel, $\vec{r}$, can be expressed loosely as:

$$\vec{r} \cong -\nabla f(\vec{x}_i) - \nabla f(\vec{x}_{i-1})P \tag{2.14}$$

Where P is some weighting factor, usually determined using either the Fletcher-Reeves or Polak-Ribière method. At first, the conjugate gradient and steepest descent methods converge at equal rates, but the rates diverge quickly as the minimum is approached. The conjugate gradient method allows for a more direct approach to the minimum to be taken, and so allowing for faster convergence, while the steepest descent method will tend to oscillates about the minimum. A comparison of the steepest descent (black) and conjugate gradient (red) methods is shown in figure 2.6.

2.3.3 Newton-Raphson

The Newton-Raphson method is the most computationally expensive of the three methods discussed here.[164] This is due to it requiring the repeated calculation of not only the first but also the second derivatives as well. While the first derivative gives the slope the second derivative gives information about the function‘s curvature. The use of second derivative information ensures a faster and more accurate convergence than that normally provided by first derivative methods. However, faster convergence times not directly translate into faster computing time. In fact, the handling of second derivative information is very time consuming, especially when large systems are in play. The update process for the Newton-Raphson method is specified below:

$$\vec{x}_{i+1} = \vec{x}_i - \frac{f'(\vec{x}_i)}{f''(\vec{x}_i)} \tag{2.15}$$

Where $f''(\vec{x}_i)$ represents the second derivatives of the vectors. This makes the assumption that the energy surface is of the form of a quadratic and that the second derivative data is the same everywhere. Whilst first derivative methods are better when staring far from the energy minimum, second derivative methods are more useful when starting at locations already close to a minima or when accuracy of convergence is paramount.

2.4 Bulk Lattice Calculations

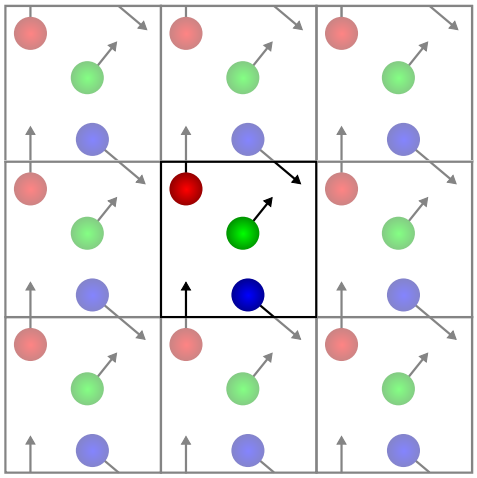

Figure 2.7: Two dimensional representation of periodic boundary conditions.

For simulations conducted on multi-atom systems the computational expense increases rapidly with the number of atoms. As such it is generally more pragmatic to model systems of smaller size, thus reducing the overall cost. However, one is often most interested in studying the bulk properties of a material as they are usually what defines its behaviour. To accurately model this, a large number of atoms would be required to satisfy all long range interactions and fully negate any surface or edge phenomena that may occur. In order to overcome the problems associated with small system sizes, and the expense of larger systems, periodic boundary conditions (PBC) are implemented. Periodic boundary conditions effectively wraps a cell by surrounding it, in all directions, with identical replicas known as images, a two dimensional representation of this is shown in figure 2.7. If an atom in the central master cell crosses into an adjacent image cell then an identical atom from the opposite image cell simultaneously enters the master cell to preserve the system. This method allows for the representation of a system as an infinite body with no surface or edge effects. However, if desired, periodic boundary conditions can be applied to only one or two dimensions to allow for surface control.

The nature of periodic boundary conditions means that a defect present in the master cell will be infinitely replicated in all images cells. Thus a defect will interact with itself over periodic boundaries. In some cases, this may be undesirable. However, such an effect can be minimised by increasing the size of the master cell or completely eliminated using the Mott-Littleton method described in section 2.5.

2.5 Point Defect Calculations

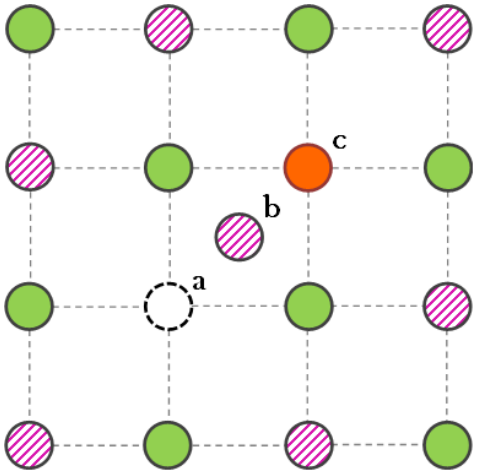

Figure 2.8: Point defects, a) Vacancy b) Interstitial c) Substitution site

The most interesting properties of a material are rarely exclusively dependent on its pristine character, but rather its defective states, or a combination thereof. Through the diligent investigation and careful regulation of such defects the behaviours of a system can be understood and, perhaps more importantly, controlled. Although many forms of defects exists the three main types of point defects, as shown in figure 2.8, are vacancies, interstitials and substitutions. Vacancies are unoccupied lattice sites, interstitials are atoms which are located at non-lattice sites and substitutions are where a lattice atom is replaced with a dissimilar atom.

Generally, there is a formation energy associated with the creation of a point defect due to the bonds cleaved and lattice distortions induced upon its formation. However, the introduction of a defect into an otherwise perfect lattice results in an increase in entropy. This gain in entropy acts to offset the endothermic nature of the formation process. At any given temperature, the approximate number of defects present is given by equation 2.16.

$$n_d \approx N \cdot exp\left(\frac{-Q_d}{k_B T}\right) \tag{2.16}$$

Where n_d is the number of defects, N the number of possible defect formation sites, Q_d defect formation energy, k_B the Boltzmann constant and T the temperature. From this equation, it can be seen that the defect concentration is proportional to the temperature, the number of possible formation sites and the energy required to form the defect.

The introduction of a defect into a pristine lattice provokes local structural distortions which radiate out into the bulk with decreasing intensity. Special treatment is often required as defects, particularly those with non-zero charge, can lead to long range perturbations. As the distance from the defect increases its effect on the structure diminishes until such a point where its effects can be considered negligible. This allows for the surrounding lattice to be segmented into a series of concentric regions each of which is treated more approximately than the previous. The multi-region approach, also known as the Mott-Littleton method, is advantageous as it enables the efficient treatment of charged point defects at the limits of infinite dilution.

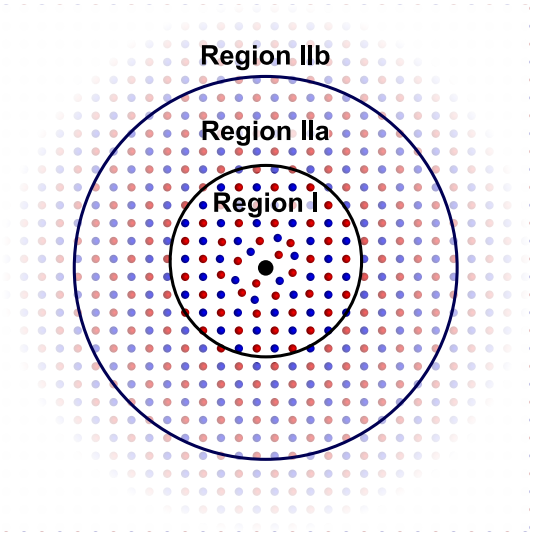

Figure 2.9: Schematic depiction of the three Mott-Littleton regions.

In the Mott-Littleton approach the lattice is partitioned into two spherical regions, both of which are centred on the defect as shown in figure 2.9. The inner region, referred to as region-I, contains the defect and all the surrounding ions which fall within a specified cut-off distance. All of the ions within this region, and their interactions, are treated explicitly and are relaxed to minimal force. Region-II, which extends to infinity, is sub-divided into two further regions known as region-IIa and region-IIb. Much like region-I, the ions in region-IIa are treated explicitly and are allowed to relax. However the forces on these ions are calculated using the Mott-Littleton approximation.[169] Region-IIa acts as a buffer for region-IIb which, unlike the other regions, does not have explicit ions and makes the assumption that the defect only affects a change in polarisation. Typically, the size of region-I and the difference between region-I and region-IIa should be greater than or equal to the short range potential cut-off. Mott-Littleton region-I and region-IIa sizes of 12.0 and 24.0 Å respectively were employed in this work. However, it should be noted that larger region sizes were employed when studying defect clusters.

2.6 Kröger-Vink Defect Notation

Kröger-Vink notation (KVN) is a set of conventions that is capable of describing point defect reactions in a more meaningful way than standard chemical notation.[170] In KVN, a species is represented as A_x^q where A corresponds to the ion itself or V if a vacancy. The subscript, x, represents the species' lattice site and if its site is an interstitial one then the symbol i is used. The superscript q is the species' effective electronic charge relative to the lattice site it occupies. Positive charges are represented by dots $\bullet$, negative charges by primes $\prime$ and no charge by a times symbol $\times$.

Using NaCl as an example:

- $Na_{Na}^{\times}$ is a sodium (Na) on its lattice site ($_{Na}$) with an excess site charge of 0 ($^{\times}$)
- $Na_{Cl}^{\bullet\bullet}$ is an antisite defect with sodium (Na) on a chlorine lattice site ($_{\mathrm{Cl}}$) causing an excess site charge of +2 ($^{\bullet\bullet}$)
- $V_{Na}^{\prime}$ is a vacancy (V) at a sodium site ($_{\mathrm{Na}}$), resulting in a site charge of -1 ($^{\prime}$)
- $Cl_i^{\prime}$ is a chlorine (Cl) interstitial site ($_{\mathrm{i}}$) with a site charge of -1 ($^{\prime}$)

2.7 Defect Clustering

In the Mott-Littleton method, defects are modelled as infinitely separated non-interacting species. While such treatment of a defect is often convenient, and even aids in its understanding, it can, in some circumstances, lead to deviations from reality. At non-trivial concentrations defects are no longer isolated from one another and as such cannot be considered so. Therefore, defect-defect interactions, and the effects thereof, must be investigated. This is of particular importance when one considers the potential effects that dopant-oxygen defect interactions may have on ionic conduction.[60,171] It is known that defects, particularly those of opposite charge, tend to associate with one another.[172] These interactions are a result of complex lattice relaxation interactions and coulombic forces. Such interactions can significantly restrict or event trap the defects concerned, leading to diminished ionic conductivities.[22] An understanding of defect-dopant clustering behaviour is therefore vital to the selection of a suitable dopant for the enhancement of ionic conductivity and offers insight into the extent and possible effects of defect clustering. The exact method and process by which defect clustering is investigated depends strongly on the system under investigation and the types of defects involved. Therefore only a general overview of the basics of defect clustering is given below. However, specifics can be found in relevant sections of the results and discussion.

Within the context of this work the, term "*defect clustering*" is used in specific reference to the tendency of oxide defects to associate and bind to one or more dopant cations.

When considering the formation of defect clusters it is important to determine which configurations are most stable. A measure of the stability of a particular cluster conformation can be determined from its binding energy ($E_{Binding}$). This, as shown in equation 2.17 below, is simply the difference in energy between the cluster ($E_{Cluster}$) and the sum of that clusters constituent point defects (E_{Defect}).

$$E_{Binding} = E_{Cluster} - \sum E_{Defect} \tag{2.17}$$

For example, the binding energy of a cluster comprised of two dopants and a single oxide ion interstitial ($2Nd^{\bullet}_{Cd}O''_i$) would be calculated following equation 2.18. Where the values for $E(O''_i)$ and $E(Nd^{\bullet}_{Cd})$ are the isolated point defect energy values calculated using the Mott-Littleton method.

$$E_{Binding} = E(2Nd^{\bullet}_{Cd}O''_i) - E(O''_i) - 2E(Nd^{\bullet}_{Cd}) \tag{2.18}$$

A negative binding energy would indicate that a cluster is bound, and is more favourable compared to the defects at infinite separation. As a rule, clusters with large negative binding energies can be considered more stable than those with smaller negative binding energies. It is also worth noting that these binding energies have uses beyond simply defining cluster stability. These values can also be used as correction terms for the dopant incorporation (solution) energies which traditionally neglect defect-defect interaction energies. It should be noted that the terms "uncorrected" and "corrected" are used to indicate solution energy values before and after the binding energy correction term has been applied. It is important to consider not only the absolute binding energy values but also their normalised forms. By normalising all of the the binding energies of a particular cluster to their lowest value a better insight into defect trapping can be gained. A cluster which presents multiple conformations of similar energy is more likely to permit the transfer of its oxide defect to a neighbouring cluster and so is less likely to trap. This is to say that a dopant which presents multiple conformations with similar, but large, binding energies may in fact be less likely to trap than another dopant which presents only a single low binding energy conformation.

Conducting defect cluster analysis on ever larger clusters yields much information concerning defect behaviour, defect trapping and material stability. However the total number of possible conformational permutations per cluster, and therefore the total number of calculations required for complete analysis, scales exponentially with cluster size. This makes extensive investigations of large clusters computationally expensive. Therefore, clustering analysis in this work primarily focus on the investigation of small charge neutral clusters.

Although binding energies are an approximate indicator of the extent to which an oxygen defect may become trapped by a dopant it is often more appropriate to consider the defect separation energy. This represents the energy required to remove an oxygen defect, such as a vacancy or interstitial, from it host cluster to infinity. As opposed to binding energy which is representative of the energy required to dismantle the whole cluster. The separation energy can be calculated as the difference in binding energy between a cluster with and without its oxide ion interstitial/vacancy.

2.8 Ionic Transport

Diffusion is the process by which ions, atoms or molecules flow through a surrounding medium. Several mechanisms exist by which ions may diffuse within a solid crystal lattice. However, only the interstitial and vacancy type migration mechanisms, as described below, are relevant to the current investigation. Both mechanisms are dependent on the presence of specific types of defects, without which they cannot occur. As such, ion diffusion will only be observed in materials containing, or able to form, such defects.

2.8.1 Vacancy Transport

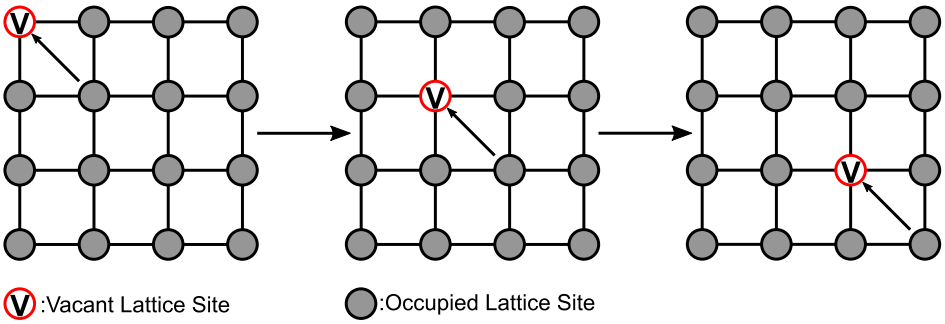

Figure 2.10: Schematic representation of the vacancy site hopping mechanism.

The vacancy mechanism, shown in figure 2.10, is perhaps the most well-known and studied defect migration mechanism. This mechanism consists of a series of migratory hops between pairs of occupied and unoccupied lattice sites. As an ion migrates from its current site to the unoccupied vacant sites it leaves behind a vacancy into which another ion can migrate. This results in the movement of a vacancy defect in one direction and an ion in the opposite direction. Generally speaking, the act of vacancy "hopping" is fundamentally a reactive and stepwise process in which one migratory event can only occur upon completion of the previous. Oxide ion conduction in the majority of electrolyte materials occurs through this mechanism, the most notable examples of which are the fluorite and perovskite type materials, see section 1.2.1 for further details.[73] However, the vacancy migration mechanism has two main drawbacks

compared to the interstitial mechanism. Firstly, there are generally many more sites to which an interstitial may jump than a vacancy. Secondly, the bonding of the interstitial to the surrounding lattice ions is generally weaker.

2.8.2 Interstitial Transport

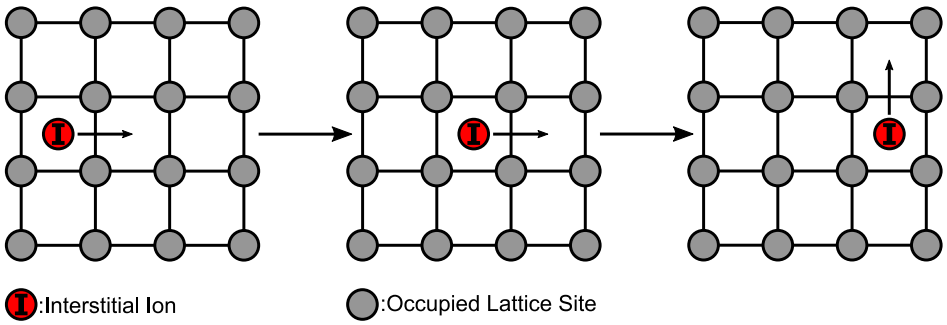

Figure 2.11: Schematic representation of direct interstitial migration mechanism.

In recent times, several new classes of materials have been identified which exhibit excellent fast ion conducting abilities.[92,96,148,173–175] These materials differ from the majority of previously known oxide ion conductors in that they conduct oxide ions *via* an interstitial mechanism, rather than the more common vacancy mechanism. Interstitial diffusion can occur *via* either a direct or indirect mechanism. In the direct mechanism, shown in figure 2.11, the interstitial ion moves directly from one interstitial site to another. However, in the indirect mechanism shown in figure 2.12, the interstitial jumps from an interstitial site to a normally occupied lattice site, ejecting the previous occupant in the process. This indirect "knock-on" mechanism, commonly referred to as interstitialcy diffusion, has the added advantage in that it can theoretically project down the structure in a concerted manner. That is to say that as the first ion starts to displace the second ion, the second ion is already starting to displace the third and so on. However the extent and occurrence of such propagation would depend heavily on the lattice structure.

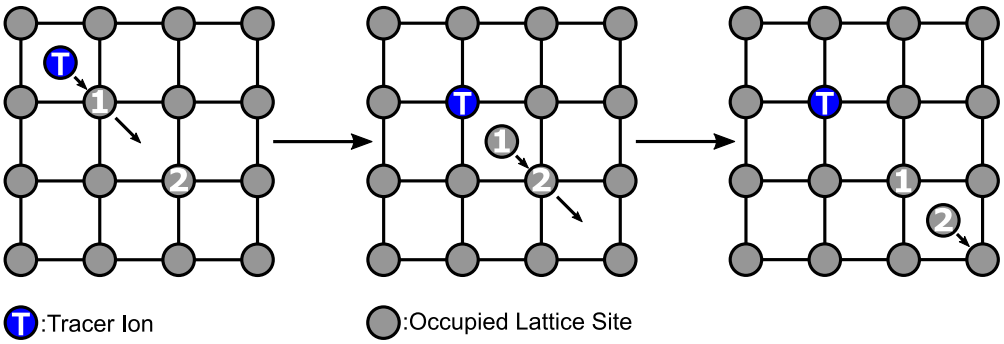

Figure 2.12: Schematic representation of indirect interstitialcy migration mechanism.

2.9 Molecular Dynamics

Molecular dynamics (MD) differs from the previously discussed methods in that it is designed to model large dynamic systems in an emergent and time dependent manner. While invaluable, the information provided by energy minimisation calculations is somewhat limited. They're focused solely on identifying and modelling the closest minimum energy configuration, and so often fail to accurately model any states which might deviate from this. MD simulations, on the other hand, take into account kinetic energy contributions, which are omitted in static lattice energy minimisation calculations. The inclusion of kinetic energy results in the potential for an ion to possess enough energy to overcome the energetic barriers associated with its confinement. The upshot of this is that it allows for less restrained movement about the energy surface, and gives access to states previously unreachable through static lattice methods. The kinetic component is introduced through the use of Newtonian momentum, in accordance with Newton's laws of motion. Each particle is assigned a vector describing its momentum, which is continually and repeatedly updated in a time dependant fashion. This allows for time-dependent and time-averaged information about a system to be extracted. This information can be either quantitative, such as ionic diffusion coefficients, or qualitative in nature, such as the description of a migration pathway and its corresponding mechanism. Furthermore, temperature dependant information can also be extracted as the collective momentum of all the ions corresponds to a specific temperature.

The basic working principle of molecular dynamics is as follows. If the positions, r, of the ions at time t are known then the forces which act upon them at time t, due to the interatomic pair potentials, are also known. The accelerations of the of the ions can then be worked out from Newton's second law of motion:

$$F = ma \tag{2.19}$$

Where F, m and a are the force, mass and acceleration of the ion. If the velocities of the ions at time t (v_t) are also known, then the positions and velocities of the ions at time $t + \delta t$ can be calculated using equations 2.20 and 2.21 respectively.

$$r_{(t+\delta t)} = r_t + v_t \delta t + \tfrac{1}{2} a_t \delta t^2 \tag{2.20}$$

$$v_{(t+\delta t)} = v_t + a_t \delta t \tag{2.21}$$

However, this is based on the assumption that acceleration remains constant. While such an assumption holds well for the very smallest values of δt, it is found to be a significant source of error over longer more statistically relevant time periods. It is therefore important to take into account the fact that acceleration changes over time.

2.9.1 Integration Algorithms

Many different integration algorithms exist to handle the time dependent progression of a system's coordinates during simulation, however all are based on the same fundamental principles. Each integration algorithm partitions the simulation into a series of frames representing the time evolution of the system at δt intervals. At each and every time frame the total force exerted upon each ion by its interactions with all the other ions is calculated and from these their accelerations. Following this, the updated positions and velocities of each ion are then calculated. During each step the forces acting on each ion is calculated once and is assumed to remain constant, along with the accelerations, but only for the duration of a single time frame. All algorithms assume that the time dependent properties of a system can be approximated by a Taylor series expansion, the most fundamental form of this is shown below:

$$r_{t+\Delta t} = r_t + v_t\Delta t + a_t\frac{1}{2}\Delta t^2 + j_t\frac{1}{6}\Delta t^3 + h_t\frac{1}{24}\Delta t^4 .... x_t\frac{1}{n!}\Delta t^n \tag{2.22}$$

Where r, v, a and j are the position, velocity, acceleration and jerk values respectively which represent the zeroth, first, second and third positional derivatives with respect to time. The other derivative values can be determined by a suitable restatement of the above expansion with respect to its derivative order, e.g:

$$v_{t+\Delta t} = v_t + a_t\Delta t + j_t\frac{1}{2}\Delta t^2 + h_t\frac{1}{6}\Delta t^3 .... x_t\frac{1}{n!}\Delta t^n \tag{2.23}$$

While many different integration algorithms exist, molecular dynamic simulations commonly employ one of two integrators, the leapfrog-Verlet or the velocity-Verlet. Both of which are based on the original Verlet algorithm in which the Taylor series is truncated following the third derivative.[176] These methods are generally used due to their simplicity and stability. An in-depth explanation of the various integration algorithms is beyond the scope of this discussion, however specific details on both can be found in the following references.[158,164] In this investigation the leapfrog-Verlet integrator was employed to update the systems coordinates. In this method the velocities are calculated first, at time $t+\delta t/2$, and are then used to calculated the positions, r, at time $t+\delta t$.

The choice of the time-step value δt has a profound effect on the stability, accuracy and efficiency of the simulation. It is therefore critical to ensure that a suitable value is selected. If the step size is too small, then the simulation will progress slowly and fail to simulate a meaningful timespan leading to high inefficiencies. Too large, and the approximation that the forces remain constant over the time step will start to fail,

leading to a reduction in accuracy. Additionally, if even more unsuitably large time-steps are used then the likelihood of simulation failure due to unphysical collisions will be dramatically increased. So a balance must be struck between the stability, accuracy and efficiency of the simulation. In this work, all molecular dynamic simulations adopted a fixed time-step size value of 0.5 fs.

2.9.2 Ensembles

A statistical ensemble is a collection of all the possible microstates which fall within the bounds of a given set of macroscopic constraints. Within the context of molecular dynamics, each ensemble is defined by the constraints it imposes on the system. The main ensembles employed in this work, and the reason for their use, are discussed below.

It is important to ensure that the system under investigation has been sufficiently optimised prior to the start of any other molecular dynamic simulations. It is possible that the introduction of defects, or the act of scaling the system from a simple unit-cell to a supercell may introduce excess energy. This can act as a possible source of error and instability. Therefore, larges systems are subjected to zero Kelvin energy minimisations prior to starting the thermodynamical simulations.[158] In this method a simulation is conducted at ∼1 Kelvin and the atoms move in the direction of the forces which act on them. However, they are not allowed to acquire velocities larger than that which corresponds to a temperature of 1 Kelvin. Although this is not strictly an ensemble in the standard sense it is closest to the NVE ensemble.

In the NVE-microcanonical ensemble the total number of atoms (N), volume (V) and energy (E) of the system are kept constant. As energy cannot move between the system and its environment it is considered to be isolated. However, energetic exchanges between the internal kinetic and potential components of the system are permitted. Systems under NVE conditions are often prone to large fluctuations in both temperature and pressure.

The NPT-isobaric-isothermal ensemble simulates systems with a constant number of atoms (N), pressure (P) and temperature (T). This allows for the control of both the temperature and pressure at which the simulation is conducted. Such conditions are very useful for bringing the system up to, and equilibrating it at, the desired temperatures, whilst allowing for volume changes. Neglecting the thermal expansion could result in the use of a system that is non-representative of the temperature at which it is being simulated. An alternative to this is the NST ensemble, this keeps both the stress (S)

and the temperature (T) of the system constant. The NST ensemble has the added advantage in that it permits the lattice angles of the cell to change. This is of particular importance when investigating systems known to undergo phase transformations.

Once a system has been optimised and brought up to the required thermal state, it is ready for its final production run. In this work the final production run is carried out under the conditions specified by the NVT-canonical ensemble. When under NVT conditions the number of atoms (N) along with the volume (V) and temperature (T) of the system is kept constant. This simulates the behaviour of a system over time at a fixed temperature.

The general procedure used for simulating systems using molecular dynamics is summarised using a flow chart in figure 2.13.

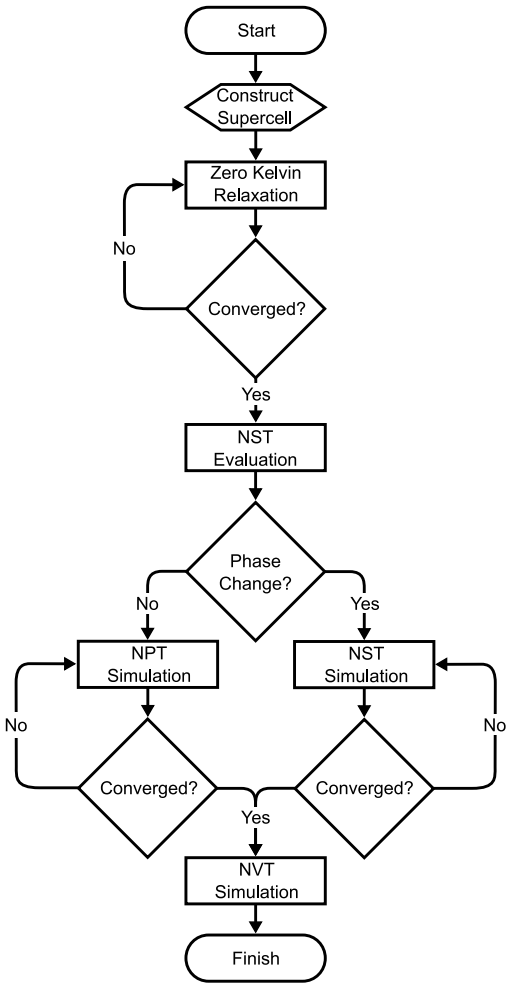

Figure 2.13: Flow chart of the molecular dynamics simulation process.

2.9.3 Thermostats

Although a systems temperature is constrained when under NPT, NST and NVT conditions, it is not actually fixed. Rather, its temperature is allowed to fluctuate about a mean value. The systems are coupled to heat baths which ensure that the average temperature of the system is maintained while still allowing for thermal fluctuation. This is done because the act of implicitly fixing a systems temperature and preventing its fluctuation would be unphysical and would not represent reality. Heat baths are regulated and coupled to the system through the use of mathematical thermostats. The strength of coupling between the heat bath and the system is controlled by means of a coupling constant. Very large coupling values result in minimal thermal coupling, meaning that the temperature of the system would effectively be unconstrained. In contrast to this, very small values would result in intense coupling which would prevent any thermal fluctuation from occurring.

In this work two different thermostats were used, the Berendsen and the Nosè-Hoover.[177,178] The Berendsen thermostat was employed during NPT and NST simulations as it excels at relaxing a system to the target temperature in a quick and efficient manner. However, once the desired temperature has been reached it is perhaps more appropriate to switch to Nosè-Hoover thermostat. This is because the Berendsen thermostat cannot truly maintain a canonical ensemble, making it less reliable during equilibrium simulation, in comparison to other thermostats. Therefore, the Nosè-Hoover thermostat is employed during NVT simulations, as it better captures system fluctuations. Coupling constant values of 0.2 and 0.5 ps were selected for the Berendsen and Nosè-Hoover thermostats respectively. These values are in line with those typically employed in molecular dynamic simulations of condensed phase materials.[158,179]

2.9.4 Molecular Dynamic Analysis

Much information regarding a system and its time dependent behaviours can be extracted from a molecular dynamic simulation. Such information is invaluable as it can provide an insight into the materials ionic conducting abilities, which is the focus of this work. The methods employed to extract and distil this information are discussed below.

Diffusion

Within liquid and gaseous systems, the position of a particle is in a constant state of flux, as such it can migrate through its system in a process known as diffusion. The same effect also occurs, albeit to a lesser degree, in solid state systems where lattice or interstitial ions may diffuse. See section 2.8 for a more in-depth description of diffusion in solids. Information about the extent to which a particle diffuses through a given medium can be extracted from its mean squared displacements (MSD). The mean squared displacement of a particle is a measure of the distance that particle will travel within a given amount of time and is expressed as:

$$\Delta r^2(t) = \frac{1}{N}\sum_{i=1}^{N}[r_i(t) - r_i(0)]^2 \tag{2.24}$$

Where Δr^2 is the MSD at time t averaged over N ions with $r_i(t)$ representing the current and $r_i(0)$ the initial positions of ion i. It should be noted that Δr^2 is often recalculated using different values of $r_i(0)$ so that Δr^2 can be further averaged over different starting frames. More qualitative information about the diffusion process can be extracted by plotting $\Delta r^2(t)$ as a function of t and inspecting the resulting curve. For example, a linear curve with a consistent slope would indicate uninterrupted motion, whereas a curve with negative curvature would indicate confined/caged diffusion.

Generally, the diffusion rate of a particular ion in a given system is quantified by its diffusion coefficient. The Einstein relation, shown in equation 2.25, relates the mean squared displacements of an ion to its diffusion coefficient.

$$D = \frac{\Delta r^2(t)}{t v_i} \tag{2.25}$$

Where D is the diffusion coefficient and v_i a variable which depends on the dimensionality of the diffusion, $v_i = 2$, 4 or 6 for 1, 2 and 3 dimensional diffusion respectively. Therefore, the diffusion coefficient can be calculated from the first derivative of the mean squared displacements with respect to time over six. Ionic conductivity, σ, can then be calculated from the diffusion coefficient using the Nernst-Einstein equation:

$$\sigma = \frac{D q_i^2 N}{H_r k_b T} \tag{2.26}$$

Where N is the concentration of diffusible ions per unit volume, q_i is the charge of those ions, T the temperature, k_b the Boltzmann constant and H_r the Haven ratio. The Haven ratio is a material specific non-negative value which is less than or equal to 1. In short the Haven ratio is the ratio between the tracer diffusion coefficient and the

charge diffusion coefficient and acts as a correctional term.[180] In solids, the temperature dependency of the diffusion coefficient is found to follow an Arrhenius relation. This makes it possible to extract the average activation energy for the diffusion process. The form of this relationship is expressed in equation 2.27 where k_B is the Boltzmann constant and $-E_a/k_B$ is the slope of a plot of $Ln(D)$ against T^{-1}.

$$Ln(D) = \frac{-E_a}{k_B}\frac{1}{T} + Ln(A) \tag{2.27}$$

Defect Tracking

As the name would suggest, defect tracking is the act of physically tracking the location of a defect, or a defective state, throughout the duration of a simulation. The act of tracking a substitutional defect is rather simple as the location of the defect corresponds to that of the dopant ion itself. However, tracking becomes considerably more complex when dealing with vacancy or interstitial defects as their locations often do not correspond directly to that of a single ion or even an ion at all. The crudest approach to tackling this is to identify defective polyhedra i.e. a tetrahedra with only 3 ions coordinated to it would likely indicate the presence of a vacancy. Although more specific methods must be employed to further narrow down the location of the defect and to be able to differentiate between one defect and another.

Defect tracking offers a means ascertain whether or not a particular defect is mobile in its host system. The diffusion coefficients calculated from the mean squared displacements are purely quantitative in nature. As such, they are unable to differentiate between true migratory diffusion and say large thermal oscillations in short simulations. This means that, in some systems, non-trivial diffusion coefficients may still be measured regardless of whether or not true migratory diffusion is actually taking place. As only true migratory diffusion is pertinent to ionic conduction, such a situation would result in the overestimation of the materials ion conducting ability. Increasing the duration of the simulation can help to alleviate this issue, but only at the cost of increased computational expense. Defect tracking can also aid in identifying the main diffusion mechanisms, finding out which defects are trapped and calculating defect residence times.

Radial Distribution Functions

Radial pair distribution functions (RDF) offer a means to investigate the way in which the atoms of a system are packed around one another. They describe how the average atomic density varies as function of the distance to a reference atom. This can be thought of as a measure of the probability of finding an atom at a particular distance from another atom. Such information is particularly useful when trying to gauge a measure of the disorder of a structure, probing for defect clustering or simply investigating defect structures.

To calculate a RDF, the area which surrounds each atom is segmented into a series of concentric spherical shells of width Δr. An illustrative representation of this is shown in figure 2.14. The number of atoms found in each shell is calculated and average over the simulation. This is then divided by the shells volume to get its density and then by the average density of the entire system to produce a fraction. The RDF can be expressed mathematically as:

$$g(r) = \frac{n(r)}{4\pi r^2 \rho \Delta r} \tag{2.28}$$

Where $g(r)$ is the RDF, $n(r)$ is the average number of atoms in a shell of width Δr at a distance of r and ρ is the average density of the system as a whole. By comparing the radial pair distribution functions of a dopant atom to that of a natural lattice atom an insight into the extent of clustering around the dopant can be gleamed. This particularly useful when testing for defect trapping.

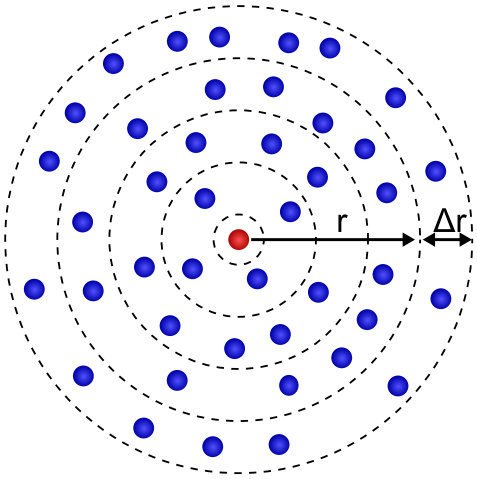

Figure 2.14: Illustrative representation of a radial pair distribution function of blue atoms around red atoms in a disordered system, labels for r and Δr have been included.

Chapter 3

Cadmium Orthogermanate

Cadmium orthogermanate (Cd_2GeO_4) crystallises with an orthorhombic olivine type *Pmcn* structure, as shown in figure 3.1.[181,182] Like apatites, Cd_2GeO_4 contains an isolated tetrahedral framework that, if flexible enough, may be conducive to fast interstitial oxide ion conduction.[95,152] Its olivine structure, detailed in section 3.1, is also of interest since Li-containing olivines have been shown to be good ionic conductors.[154] This introduction will discuss the reasons for studying Cd_2GeO_4, findings from previous investigations and will describe the interatomic potential model selection process. After which, details of the Cd_2GeO_4 structure and the interatomic potential model will be given. This will then be followed by a discussion of intrinsic defects, dopants and defect clustering. Finally, the process by which oxide ions diffuse in Cd_2GeO_4 will be elucidated, and the main findings of this work summarised.

To date, there is no literature on the applicability of Cd_2GeO_4 as a SOFC material, however Whipple *et al.* reported on the semiconducting properties of Cd_2GeO_4 in the 80's.[183] They showed that when prepared under vacuum, Cd_2GeO_4 is electrically conducting (~ 0.8 S cm^{-1}), and that doping with trivalent metal ions could enhance electrical conductivity when still prepared under vacuum ($\sim$100 S cm^{-1}). It is suggested that electrons originate from shallow donor defects and that their mobility is determined by a combination of large polaron formation and impurity scattering.[183] They also report a substantial, but reversible, drop in electrical conductivity is observed upon exposure to oxygen. This is thought to originate from the reversible chemisorption of oxygen on to the surface of the Cd_2GeO_4 grains. Although the bulk material would, in theory, remain electronically conductive the adsorbed oxygen, in the form of O^{2-}, would deplete the electrons below the surface, causing the observed insulating behaviour.

Similar behaviours have been observed in other polycrystalline oxides such as In_2O_3 and ZnO.[184–186] This theoretical ability to naturally chemisorb and reduce oxygen is interesting when considering possible SOFC cathode applications.

The local tetrahedral ordering in Cd_2GeO_4 is relatively similar to that found in the K_2SO_4-structured material Ba_2TiO_4. However, the neighbouring tetrahedra are ∼0.7 Å closer in Cd_2GeO_4. In Cd_2GeO_4 its likely that oxygen defects will be accommodated as bridged-tetrahedra structures such as "Ge_2O_9" or "Ge_2O_7". Such defect structures are seen in other similarly structured oxide ion conductors, like $La_{9.67}(GeO_4)_6O_{2.5}$ and $La_{0.8}Ba_{1.2}GaO_{3.9}$.[109,187] The formation of tetrahedrally bridged defects should profoundly affect defect chemistry and oxygen diffusion in Cd_2GeO_4. As such, Cd_2GeO_4 makes for an interesting comparison point to Ba_2TiO_4. Of the possible olivine materials, Cd_2GeO_4 was selected for modelling based on: the reduced inter-tetrahedral distance it offers, which may aid oxide migration; its GeO_4 tetrahedra, which are more likely to form bridged defects[187]; its possible ability to facilitate the ORR, which would be advantageous in cathodic applications[183]; and because Cd is one of the closest ions in size to Ba^{2+} that will form a stable olivine structure. Furthermore, the large mass and size of the Cd^{2+} ion (0.95 Å) may assist in suppressing cation migration and aid structural stability.[188]

To enable the computational investigation of Cd_2GeO_4 an interatomic potential model was derived from existing experimental crystal structure data.[181] The first stage of this process involved a scan of existing interatomic pair potentials, which had originally been derived for binary oxides and other solid oxide materials. The best combination was then further refined using a semi trial and error approach until the lattice parameters, interatomic distances, angles and tetrahedral positions were within a few percent of the experimental crystal structure.[181] The interatomic potentials were then further verified in binary oxides. The finial interatomic potential model is listed in table 3.1. Such a fitting process is a non-trivial task for complex structures involving isolated tetrahedral units and multiple cation/anion sites. However, the derivation of a reliable interatomic potential model is crucial as interatomic potential model based methods allow larger systems to be studied which is key when characterising defects and defect migration. The principles of interatomic pair potentials and defect characterisation have been previously addressed in sections 2.2 and 2.5 of the methodology chapter. These methods have been employed to investigate Cd_2GeO_4, the results of which are given in the remainder of this chapter.

3.1 Structural Modelling

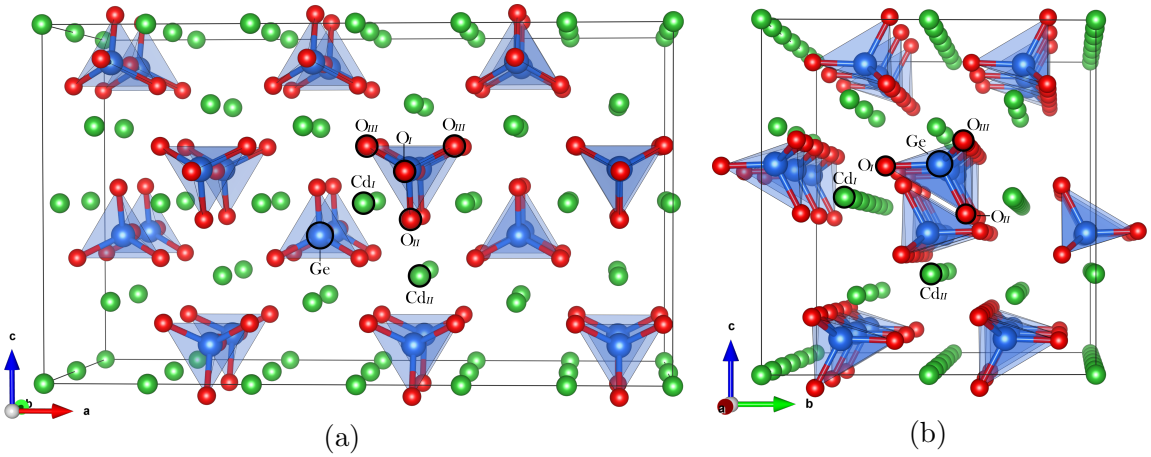

(a) (b)

Figure 3.1: Crystal structure of Cd_2GeO_4 (3×2×1 supercell) viewed down the a) *b*-axis and b) *a*-axis, with Ge, Cd and O ions represented as blue, green and red spheres respectively, and GeO_4 tetrahedra as blue polyhedra.

Cd_2GeO_4 crystallises with an orthorhombic olivine structure of space group *Pmcn*, as shown in figure 3.1. In this structure, the cadmium ions occupy two distinct lattice sites and the oxygen ions three, the latter of which coordinates octahedrally around the cadmium ions and tetrahedrally around the germanium ions. From the interatomic distances, shown in table 3.3, and bond valence sum calculations, the Cd^{2+} and Ge^{4+} cation sites can be unambiguously defined as six and four coordinate respectively.[189,190] In Cd_2GeO_4 the GeO_4 tetrahedra are isolated from one another, but are linked by corner and edge sharing cadmium octahedra, and align to form columns down the *b*-axis, see figure 3.1a. Cd_2GeO_4 differs to the other A_2BO_4 materials investigated in this work (e.g. Ba_2TiO_4) in that it crystallises with an olivine rather than K_2SO_4-type structure. This is due to the comparatively small size of its divalent cation.

Table 3.1: Final Buckingham interatomic potentials and shell model parameters used in this work for Cd_2GeO_4.

Interaction	A (eV)	ρ (Å)	C (eV Å^6)	Y(e)	k(eV Å^{-2})
Cd^{2+}- O^{2-}	1207.7	0.3271	0.00	2.00	r
Ge^{4+}- O^{2-} [187]	1497.4	0.3256	16.00	4.00	r
O^{2-}- O^{2-} [97]	22764.3	0.1490	27.89	-2.86	74.92

Where r indicates rigid ion model (i.e. no polarisable shell model).

The interatomic pair potentials used to model Cd_2GeO_4 in this work are given in table 3.1, along with the shell model parameters where applicable. A comparison of the experimental and calculated lattice parameters, table 3.2, indicates a good fit to within 1 %.[181] The interatomic cation-oxygen distances, given in table 3.3, are also found to be in reasonable agreement with the experimental data. Most notably the tetrahedral GeO_4 unit, which plays an important role in determining the defect behaviour of the system, was successfully reproduced. In general, the model is found to satisfactorily reproduce the experimentally reported structure. This helps to support the validity of the interatomic potential model employed in this work and the accuracy of the defect calculations which follow.

Table 3.2: Comparison of calculated and experimental Cd_2GeO_4 lattice parameters, with the experimental standard deviations in parenthesise.[181]

Parameter	Calc.	Expt.	Difference (%)
a (Å)	6.528	6.584(3)	-0.056 (-0.86)
b (Å)	5.262	5.211(2)	0.051 (0.98)
c (Å)	11.178	11.160(4)	0.018 (0.16)
$\alpha = \beta = \gamma$ (°)	90.000	90.000	0.000 (0.00)

Table 3.3: Comparison of calculated and experimentally determined cation-oxide ion interatomic distances within Cd_2GeO_4.[181]

Cation	Oxygen	Count*	Expt. (Å)	Calc. (Å)	Difference (%)
Cd_I	O_{II}	2	2.292	2.297	0.004 (0.19)
	O_I	2	2.298	2.258	-0.039 (-1.72)
	O_{III}	2	2.365	2.401	0.037 (1.53)
Cd_{II}	O_{II}	1	2.254	2.229	-0.026 (-1.14)
	O_{III}	2	2.279	2.253	-0.026 (-1.15)
	O_I	1	2.360	2.435	0.076 (3.15)
	O_{III}	2	2.429	2.487	0.058 (2.34)
Ge	O_I	1	1.756	1.728	-0.029 (-1.65)
	O_{III}	2	1.758	1.749	-0.010 (-0.55)
	O_{II}	1	1.771	1.773	0.002 (0.12)

* Count indicates the number of equivalent Cation-Oxygen "bonds".

3.2 Intrinsic Point Defects

With the previously discussed interatomic potential model, the intrinsic defect properties of Cd_2GeO_4 are investigated. Using the Mott Littleton method described in section 2.5, the vacancy and interstitial defect energies for all native ions were calculated. These energies were then combined to calculate the Schottky and Frenkel defect energies, which are presented alongside their Kröger-Vink mechanisms in table 3.4. In materials such as $Ba_2In_2O_5$ the oxygen defects, pivotal to oxide ion conduction, form naturally through oxygen Frenkels.[53,191] However, the formation of Frenkel and Schottky defects in Cd_2GeO_4 is found to be energetically unfavourable. Therefore, the concentration of these defects will be negligibly small, even at high temperatures. This is consistent with other olivine materials which also show Schottky and Frenkel defects to be energetically unfavourable.[192,193] As the spontaneous formation of oxygen defects in pristine Cd_2GeO_4 is unfavourable, doping must be employed to induce their formation. While experimental investigations have demonstrated the viability of doping Cd_2GeO_4 with monovalent and trivalent dopants, such investigations have focused primarily on the resulting changes to the materials electrical and photoelectric properties.[183,194] The next section will therefore focus on the doping of Cd_2GeO_4.

Table 3.4: Calculated Cd_2GeO_4 Frenkel and Schottky intrinsic defect energies.

Type	Defect equation	Energy (eV)[a]
Cd Frenkel	$Cd_{Cd}^{\times} \rightarrow V_{Cd}'' + Cd_i^{\bullet\bullet}$	3.00
Ge Frenkel	$Ge_{Ge}^{\times} \rightarrow V_{Ge}'''' + Ge_i^{\bullet\bullet\bullet\bullet}$	9.65
O Frenkel	$O_O^{\times} \rightarrow V_O^{\bullet\bullet} + O_i''$	3.12
Schottky	$2Cd_{Cd}^{\times}+Ge_{Ge}^{\times}+4O_O^{\times} \rightarrow 2V_{Cd}''+V_{Ge}''''+4V_O^{\bullet\bullet}+Cd_2GeO_4$	4.57

a Energy values are quoted per-defect.

3.3 Dopants

As identified in the previous section, the oxygen defects crucial to oxide-ion conduction will not naturally form in any significant quantity in Cd_2GeO_4. However, aliovalent doping is a well-known method of promoting oxygen defect formation in such oxide materials.[21,73] When selecting a suitable dopant to enhance ionic conductivity it's important to consider not only the dopant's ability to promote oxygen defect formation, but the favourability of its incorporation and the extent to which it may then trap the oxygen defect. While the first two considerations are examined here, the trapping of defects is addressed later in section 3.3.5.

The relative favourability of a particular dopant and its incorporation mechanism can be established from its solution energy, which is calculated from its constituent isolated point defect energies and relevant lattice energies. All calculated solution energies for the doping of Cd_2GeO_4 can be found in tables A.2, A.3, A.4 and A.5 of the appendix. It should be noted that the solution energies are calculated at infinite dilution using the Mott-Littleton method. In this investigation, a broad range of mono, di, tri and tetravalent dopant ions on both of the cation sites were investigated. Considering both constant-cation and constant-oxygen based methods of charge-compensation. In constant-cation mechanisms, such as equation 3.1, charge-compensation is achieved through the formation of oxide ion interstitials or vacancies. While constant-oxygen mechanisms are charge balanced by cation vacancies or interstitials, as seen in equation 3.2. Aliovalent doping schemes are investigated as a possible means of inducting the formation of oxygen defects. While isovalent doping is unlikely to offer a direct pathway towards oxygen defect formation, it does offer a means of tuning the structural properties of Cd_2GeO_4 and makes for a more diverse study.

For each of the four dopant regimes, M^+, M^{2+}, M^{3+} and M^{4+}, the different incorporation mechanisms were compared by plotting their calculated solution energies as a function of dopant radius. However, it should be noted that six coordinate radii have been used in all such plots to aid comparison, and that radii for high-spin states have been used where applicable.[188] To ensure consistent results, the interatomic potential for each dopant was selected based on its compatibility with the oxygen potential used. Where the compatibility of a dopant's interatomic potential is defined by the accuracy with which it, and the oxygen interatomic potential, can stably reproduce the dopant's binary oxide. References for each of the dopant interatomic potentials, along with their relevant defect energies, can be found in table A.1 of the appendix.

3.3.1 Monovalent Dopants

Monovalent doping represents one of the possible ways in which oxygen defects might be introduced to the Cd_2GeO_4 structure. The alkali metal cations Li^+, Na^+, K^+ and Rb^+ were selected for investigation based on their cost, availability, stability and indications that such dopants can be readily incorporated in similar materials such as apatites.[97,195] Furthermore, experimental investigations have shown that Na^+ doping of Cd_2GeO_4 is viable.[183]

The four monovalent doping mechanisms considered in this work are shown in equations 3.1 - 3.4. Where the first two mechanisms represent monovalent substitution at the Cd^{2+} sites, and the latter two, the Ge^{4+} sites. In the constant-cation mechanisms, equations 3.1 and 3.3, charge compensation is maintained through the formation of oxide ion vacancies. Whereas charge compensating cation interstitials form in the constant-oxygen mechanisms shown in equations 3.2 and 3.4.

Cd Site:
$$\frac{1}{2}M_2O + Cd_{Cd}^{\times} + \frac{1}{2}O_O^{\times} \rightarrow M'_{Cd} + \frac{1}{2}V_O^{\bullet\bullet} + CdO \tag{3.1}$$
$$\frac{1}{2}M_2O + Cd_{Cd}^{\times} \rightarrow M'_{Cd} + \frac{1}{2}Cd_i^{\bullet\bullet} + \frac{1}{2}CdO \tag{3.2}$$

Ge Site:
$$\frac{1}{2}M_2O + Ge_{Ge}^{\times} + \frac{3}{2}O_O^{\times} \rightarrow M'''_{Ge} + \frac{3}{2}V_O^{\bullet\bullet} + GeO_2 \tag{3.3}$$
$$\frac{1}{2}M_2O + Ge_{Ge}^{\times} \rightarrow M'''_{Ge} + \frac{3}{4}Ge_i^{\bullet\bullet\bullet\bullet} + \frac{1}{4}GeO_2 \tag{3.4}$$

The calculated solution energies for monovalent doping of Cd_2GeO_4 at the Cd_I^{2+} and Ge^{4+} sites following mechanisms 3.1 - 3.4, are plotted against dopant radius in figure 3.2. Examination reveals a strong preference for monovalent ions to substitute at the Cd^{2+}, rather than Ge^{4+}, sites. This is to be expected given that the monovalent ions are much closer in size and charge to Cd^{2+} than they are Ge^{4+}. Solution energies for the Cd_{II}^{2+} sites have not been included as they are found to be ~ 0.5 eV higher in energy. Results also show that constant-oxygen stoichiometry is around 0.35 eV lower than constant-cation stoichiometry. This suggests that charge compensation will be achieved *via* the formation cation interstitials ($Cd_i^{\bullet\bullet}$) rather than oxide ion vacancies ($V_O^{\bullet\bullet}$).

In summary, monovalent dopant ions are found to prefer Cd_I^{2+} site substitution and constant-oxygen stoichiometry, making mechanism 3.2 the most likely. Of the ions considered, Na^+ was found to be the most favourable due to its similarity in size to the native Cd^{2+} ion. However, as constant-oxygen stoichiometry is favoured, cation interstitials are likely to be formed in preference to oxide ion vacancies. Therefore, it is unlikely that monovalent doping will offer a viable means of increasing the oxygen defect concentration or significantly enhancing the oxide ion conducting abilities of Cd_2GeO_4.

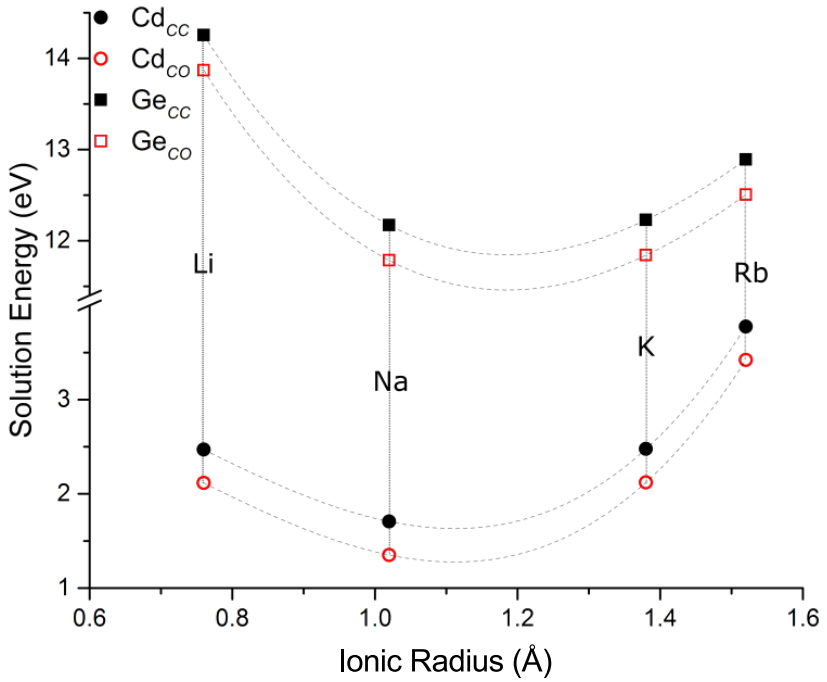

Figure 3.2: Solution energies for monovalent doping of the Cd_I^{2+} & Ge^{4+} sites *via* the mechanisms shown in equations 3.1 (Cd_{CC}), 3.2 (Cd_{CO}), 3.3 (Ge_{CC}) and 3.4 (Ge_{CO}), where cc-constant cation and co-constant oxygen.

3.3.2 Divalent Dopants

Divalent dopant ions can either substitute isovalently onto the Cd^{2+} sites, as shown in equation 3.5, or aliovalently onto the Ge^{4+} sites following the constant-cation and constant-oxygen mechanisms shown in equations 3.6 and 3.7 respectively. Many cathode materials, such as perovskites, are doped with reducible transition metal ions such as Mn, Ni, Co and Fe (multivalent) to improve their electrical conductivity and, in some instances, aid the formation of oxygen defects.[53] Additionally, such dopants are able to catalyse the cathodic oxygen reduction and incorporation reactions.[196] Since the transition metals' oxidation states are not static, the solution energies for these dopants at different oxidation states have been calculated, and are compared in section 3.3.3. The larger dopants Ba^{2+}, Sr^{2+} and Ca^{2+} were included due to their large radii which is likely to make them more favourable dopants for the Cd^{2+} sites. Investigation into the divalent doping of Cd_2GeO_4 will yield information on the materials stability and possible ways in which it can be modified.

The three divalent incorporation mechanisms, mentioned in the previous paragraph, are shown below in equations 3.5, 3.6 and 3.7. In the first mechanism, the dopants substitute isovalently onto the Cd^{2+} sites, and therefore do not require charge compensating defects. In the second and third mechanisms, the dopants substitute onto the Ge^{4+} sites where

they form oxide ion vacancy and Ge interstitial charge compensating defects respectively. The calculated solution energies for the Cd^{2+} site substitution mechanism are plotted in figure 3.3a and those of the Ge^{4+} mechanisms in figure 3.3b.

$$\text{Cd Site:} \qquad MO + Cd_{Cd}^{\times} \rightarrow M_{Cd}^{\times} + CdO \tag{3.5}$$

$$\text{Ge Site:} \qquad MO + Ge_{Ge}^{\times} + O_{O}^{\times} \rightarrow M_{Ge}'' + V_{O}^{\bullet\bullet} + GeO_2 \tag{3.6}$$

$$MO + Ge_{Ge}^{\times} \rightarrow M_{Ge}'' + \frac{1}{2}Ge_{i}^{\bullet\bullet} + \frac{1}{2}GeO_2 \tag{3.7}$$

Like monovalent dopants, results suggest the divalent dopants prefer to substitute at the larger and comparably charged Cd^{2+} sites compared to the smaller and differently charged Ge^{4+} sites. Due to their comparatively large radii, divalent cations are often found in octahedral geometries and tend to prefer coordination numbers greater than or equal to six. This preference can be noted from the cation/anion size ratios (Pauling's first rule). From figure 3.3a it can be seen that of the two Cd^{2+} sites, the larger divalent dopant ions, i.e. Ca^{2+}, Sr^{2+} and Ba^{2+}, prefer the Cd_{II}^{2+} site and the smaller ions, such as Mn^{2+}, Zn^{2+} and Co^{2+}, prefer to reside on the Cd_{I}^{2+} sites. Currently no experimental investigations concerning divalent doping of Cd_2GeO_4 have been conducted. However, studies into the doped-forsterite (Mg_2SiO_4) olivine systems offer a comparison point.[197] The study suggests that larger cations generally tend to prefer M_{II}^{2+} sites, and smaller ions the M_{I}^{2+} sites. This is in agreement with the findings herein, which suggest that the larger Cd_{II}^{2+} sites are able to better accommodate the large dopant ions without as much structural distortion. The study also suggests that charge, electronic configuration, crystal field and electronegativity can play a role in determining site preference.

Results show that the isovalent Cd^{2+} site substitution mechanism shown in equation 3.5 is preferred by all divalent dopant ions tested, and that dopants closer in size to Cd^{2+} are more favourable. The results also suggest substitution is energetically favourable for the dopants Ca^{2+} and Sr^{2+}. However, as the primary incorporation mechanism is isovalent in nature it will not directly induce the formation of oxide defects. While dopants, such as Sr^{2+}, are only likely to affect the materials structure, dopants like Mn^{2+} and Fe^{2+} may offer a means to change the materials electronic behaviour or even induce defect formation *via* a redox reaction. Furthermore, the favourability of Sr^{2+} incorporation may make Cd_2GeO_4 incompatible with cathode materials such as LSCF which tend to leach Sr^{2+}.[129] In summary, while divalent doping may not offer a direct means of inducing oxide defect formation in Cd_2GeO_4, it does offer a potential means of subtly tuning its structural and material properties.

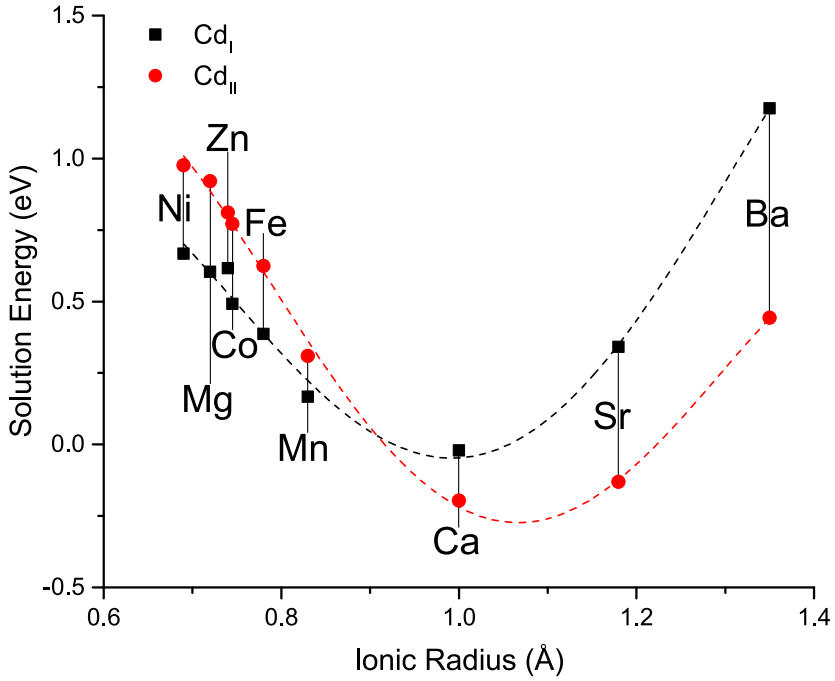

(a)

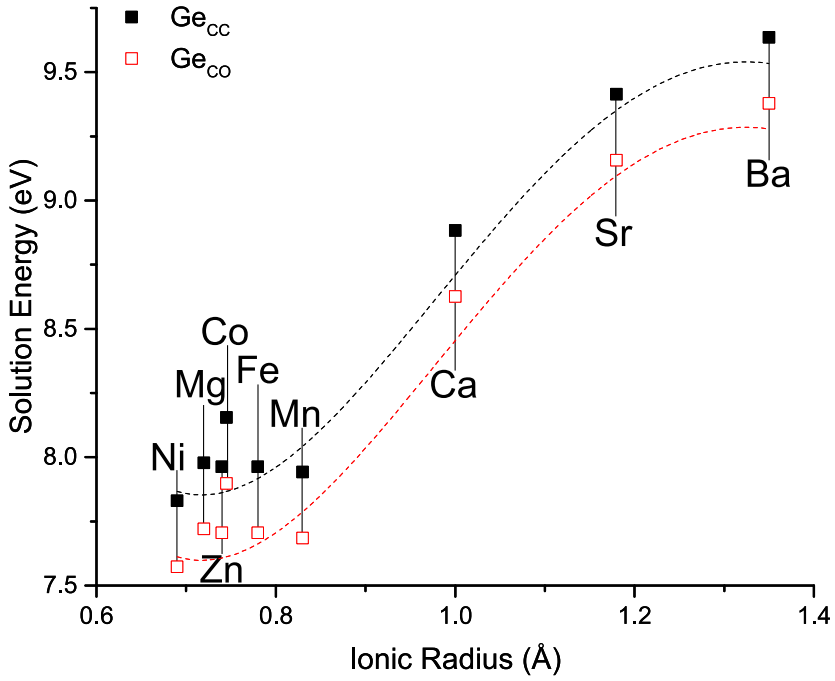

(b)

Figure 3.3: Solution energies for divalent doping of the a) Cd^{2+} sites *via* equation 3.5 and b) Ge^{4+} sites *via* equations 3.6 (Ge_{CC}) and 3.7 (Ge_{CO}), cc/co = constant cation/oxygen.

3.3.3 Trivalent Dopants

The trivalent doping regime is more flexible than the other doping regimes considered in this work. This is because trivalent ions can present in a broad range of sizes e.g. La^{3+} and Al^{3+} which have ionic radii of 1.0 and 0.5 Å respectively.[188]* The diverse nature of these ions allows for them to reside in both octahedral and tetrahedral geometries. This makes trivalent doping a promising pathway for encouraging oxygen defect formation. The dopants selected for investigation were primarily chosen based on the similarity of their ionic radii to those of either Ge^{4+} or Cd^{2+}, experimental precedence or their common usage in other similar materials.[183,194] Dopants of intermediary sizes were also included to help elucidate site selectivity.

In this work four different trivalent doping mechanisms were considered. The first two represent trivalent doping of the Cd^{2+} sites ($M^{\bullet}_{Cd}$), with the charges in equation 3.8 compensated for by O interstitials (O''_i) and in equation 3.9 by Cd vacancies (V''_{Cd}). Equations 3.10 and 3.11 represent Ge^{4+} site doping (M'_{Ge}) with O vacancy ($V^{\bullet\bullet}_{O}$) and Ge interstitial ($Ge^{\bullet\bullet\bullet\bullet}_i$) charge compensation respectively.

Cd Site:

$$\frac{1}{2}M_2O_3 + Cd^{\times}_{Cd} \rightarrow M^{\bullet}_{Cd} + \frac{1}{2}O''_i + CdO \tag{3.8}$$

$$\frac{1}{2}M_2O_3 + \frac{3}{2}Cd^{\times}_{Cd} \rightarrow M^{\bullet}_{Cd} + \frac{1}{2}V''_{Cd} + \frac{3}{2}CdO \tag{3.9}$$

Ge Site:

$$\frac{1}{2}M_2O_3 + Ge^{\times}_{Ge} + \frac{1}{2}O^{\times}_{O} \rightarrow M'_{Ge} + \frac{1}{2}V^{\bullet\bullet}_{O} + GeO_2 \tag{3.10}$$

$$\frac{1}{2}M_2O_3 + Ge^{\times}_{Ge} \rightarrow M'_{Ge} + \frac{1}{4}Ge^{\bullet\bullet\bullet\bullet}_i + \frac{3}{4}GeO_2 \tag{3.11}$$

The calculated solution energies for the trivalent doping of Cd_2GeO_4 at the Cd^{2+}_{II} and Ge^{4+} sites, following equations 3.8 - 3.11, are plotted in figure 3.4 as a function of dopant ionic radii. Results show Cd^{2+}, specifically Cd^{2+}_{II}, site substitution mechanisms are favoured by all but the smallest trivalent dopant ion tested (Al^{3+}). The solution energies for Cd^{2+} site substitutions decrease with increasing dopant size, indicating larger dopant ions to be more favourable on the Cd^{2+} sites. This is consistent with experimental suggestions, and is to be expected from dopant-site size trends.[183,194] It can be seen from table A.1, in the appendix, that the majority of dopants favour the larger of the two Cd^{2+} sites (Cd^{2+}_{II}). Results also show that the Ga^{3+} ions prefer the octahedral Cd sites as well, as opposed to the smaller Ge^{4+} sites. These sites are similar to those found in α-Ga_2O_3 and show only a 1.6% difference in average Ga-O bond distance.[198] Calculations suggest

*Ionic radii quoted are for six coordinated ions.

that Ge^{4+} based substitutions are generally unfavourable, with high defect solution energies. Substitutions on the Cd^{2+} sites are much more favourable, with a small (0.23 eV) preference for the constant-cation mechanism in which oxide ion interstitials form to compensate for the charge imbalance. These promising results suggest that trivalent doping offers a potential method of promoting the formation oxide ion interstitial defects.

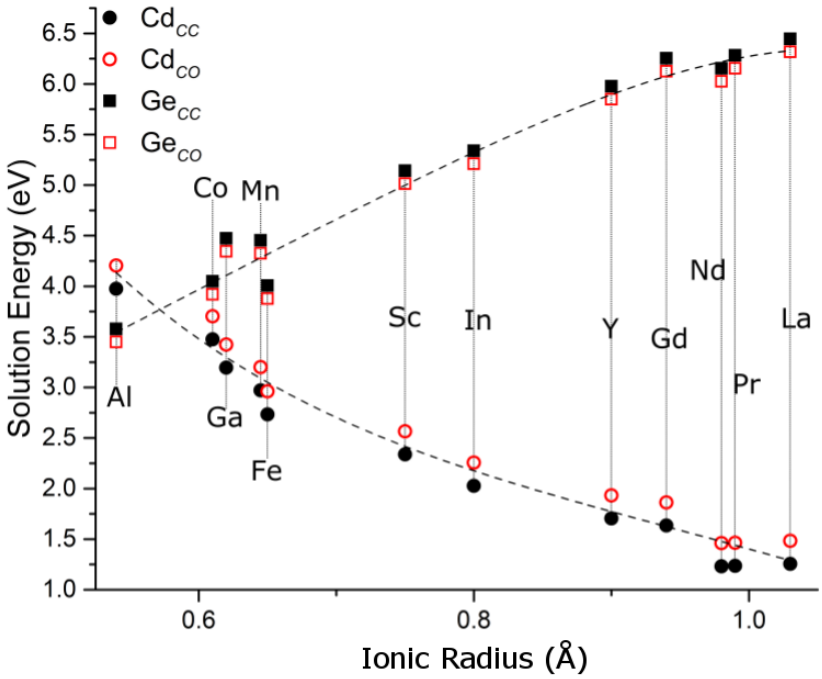

Figure 3.4: Solution energies for the trivalent doping of the Cd^{2+}_{II} & Ge^{4+} sites *via* the mechanisms shown in equations 3.8 (Cd_{CC}), 3.9 (Cd_{CO}), 3.10 (Ge_{CC}) and 3.11 (Ge_{CO}), where cc-constant cation and co-constant oxygen.

As discussed in section 3.3.2, reducible transition metal ions such as Mn, Co and Fe are often incorporated into cathodic materials. Comparing the solution energies of the trivalent dopant ions to their reduced forms shows that the M^{2+} species are around 2.5 eV lower in energy than their M^{3+} counterparts. This suggest that on the Cd sites M^{3+} dopants may be unstable with respect to their reduced M^{2+} states, and could therefore reduce to their M^{2+} states, losing an oxygen defect in the process to maintain charge compensation. This preference could be explained as a result of the reduced state's closer match in terms of ionic radii and charge to the Cd^{2+} site. Again, similar behaviour has been predicted to occur in related materials.[97] The comparatively higher incorporation energies and potential to undergo reduction, coupled with oxygen defect loss, makes reducible trivalent dopants, such as Fe^{3+}, a substandard choice for the promotion of oxygen defect formation.

In review, the lowest incorporation energies were seen when Cd_{II}^{2+} sites were doped with rare earth cations and charge balanced by oxide ion interstitials, *via* the mechanism shown in equation 3.8. These results suggest that oxide ion interstitial defects are likely to form in Cd_2GeO_4 when doped with large trivalent rare earth ions, such as La^{3+}. This may subsequently result in increased oxide ion conductivity, as seen in other oxide ion conductors. The effect of trivalent doping on oxide ion conduction/mobility in Cd_2GeO_4 is investigated further in section 3.4 using molecular dynamic simulations.

3.3.4 Tetravalent Dopants

The tetravalent series was the final doping regime considered in the investigation of Cd_2GeO_4. Again, a selection of dopants with range of different radii were selected, and both Cd^{2+} and Ge^{4+} site substitution mechanisms considered.

Three tetravalent doping mechanisms were considered during the course of the investigation. Equations 3.12 and 3.13 are the mechanisms for Cd^{2+} site substitutions ($M_{Cd}^{\bullet\bullet}$) with charge compensation achieved through formation of O interstitials (O_i'') in the former, and Cd vacancies (V_{Cd}'') in the latter. While equation 3.14 represents the isovalent Ge^{4+} site substitution mechanism ($M_{Ge}^{\times}$). The calculated solution energies for all three doping mechanisms are plotted in figure 3.5.

Cd Site:
$$MO_2 + Cd_{Cd}^{\times} \rightarrow M_{Cd}^{\bullet\bullet} + O_i'' + CdO \tag{3.12}$$
$$MO_2 + 2Cd_{Cd}^{\times} \rightarrow M_{Cd}^{\bullet\bullet} + V_{Cd}'' + 2CdO \tag{3.13}$$

Ge Site:
$$MO_2 + Ge_{Ge}^{\times} \rightarrow M_{Ge}^{\times} + GeO_2 \tag{3.14}$$

The results show that all of the tetravalent dopants examined prefer to substitute isovalently onto the smaller and similarly charged Ge^{4+} sites, and suggests that isovalent substitution occurs favourably for both the Si^{4+} and Ti^{4+} dopants. Interestingly, the solution energy for Mn^{4+} doping is found to be higher than one might expect from the trends. This may be due to tetravalent manganese's strong preference for higher coordination numbers. However, the same is generally said for Ti^{4+}, whose incorporation is suggested to be favourable in Cd_2GeO_4. Isovalent doping, shown in equation 3.14 for tetravalent dopants, will not result in oxygen defect formation. However, the favourable solution energies found for the Si^{4+} and Ti^{4+} substitutions suggests that systems with mixed $(Ge/Si/Ti)O_4$ tetrahedral units may be possible. This has been observed in both olivine and apatite systems, where Si^{4+} doping is employed in the latter case to increase material stability and by extension enhancing ionic conductivity.[58,92,199]

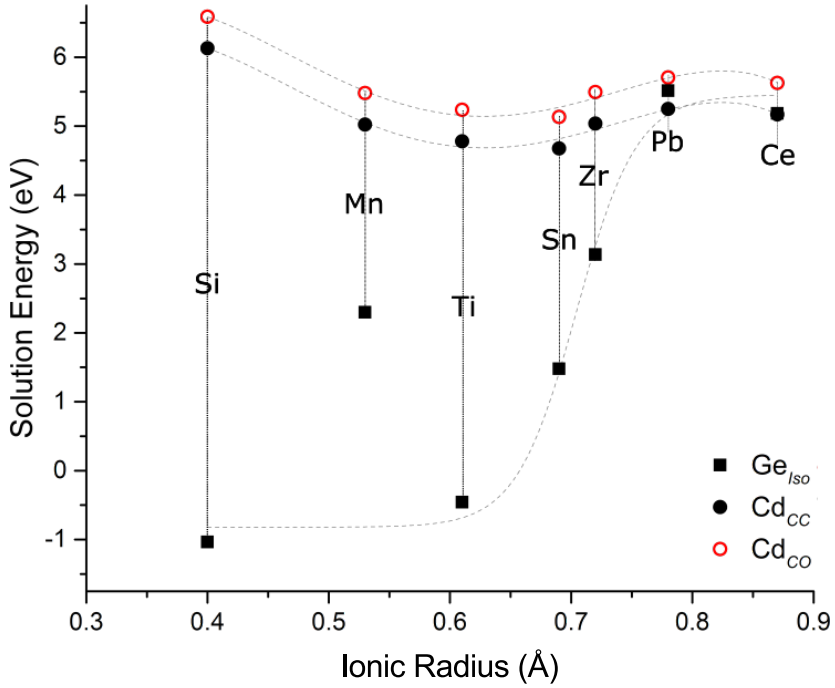

Figure 3.5: Solution energies for the tetravalent doping of the Cd_{II}^{2+} & Ge^{4+} sites *via* the mechanisms shown in equations 3.12 (Cd_{CC}), 3.13 (Cd_{CO}) and 3.14 (Ge_{Iso}), where cc-constant cation, co-constant oxygen and iso-isovalent.

In summary, a broad range of doping regimes and mechanisms were investigated. Results suggest that trivalent doping, particularly with large lanthanide ions, offers a possible means of inducing the formation of oxide ion interstitial defects. Thus far, calculations have only considered defects as isolated entities.† However, it is known that the interactions between defects, and the effects such interactions have, can be substantial. These interactions are therefore considered in the next section.

3.3.5 Defect Clustering

In the previous calculations, defects were treated as isolated species which did not interact with one another. However, it is known that defects, particularly those of opposite charge, generally tend to associate with one another.[172] These defect-defect interactions, which are determined by coulombic forces and lattice relaxations, can significantly affect defect mobility and could result in ion trapping.[60,171] Therefore, an understanding of defect clustering behaviour will be important to the selection of a suitable dopant for the enhancement of ionic conductivity. For this, $2M_{Cd}^{\bullet}{:}O_i''$ defect clusters, where M = Sc^{3+}, Y^{3+}, Nd^{3+}, Pr^{3+} and La^{3+}, were examined. The lanthanides were considered due to their large size and low incorporation energies. The

†With isolated indicating that no defect interacts with any other defect.

two comparatively smaller dopants Y^{3+} and Sc^{3+} were also included to elucidate the effects of dopant size on defect clustering, and due to existence experimental data for the former.[183] The methods employed to study defect clustering in Cd_2GeO_4 have been discussed in further detail in section 2.7 of the methodology.

As previously discussed, an oxide ion interstitial is formed for every two dopants in order to maintain charge neutrality (equation 3.8). Therefore, the simplest charge neutral defect cluster would consist of a single oxide ion interstitial and a pair of neighbouring dopant ions ($2M^{\bullet}_{Cd}{:}O''_i$). The investigation of small $2M^{\bullet}_{Cd}{:}O''_i$ clusters can be conducted with relative ease due to the limited number of possible permutations ($\sim$4000). The complex nature of defect clustering means that behaviours may differ in larger clusters. However, investigation of larger clusters quickly becomes infeasible due to the vast number of possible conformations associated with them ($> 1{\times}10^7$ for $4M^{\bullet}_{Cd}{:}2O''_i$ systems). As such, investigations have been restricted to $2M^{\bullet}_{Cd}{:}O''_i$ clusters. Any effects which may arise from further clustering will be captured during the molecular dynamics simulations, discussed in section 3.4, where the random placement of clusters leads to some being in proximity to one another.

A variety of different dopant-dopant-oxide ion interstitial starting configurations were generated and relaxed. The stability of each cluster is determined from its binding energy $E_{Binding}$, which is the difference in energy between the cluster $E_{Cluster}$ and the sum of its constituent point defects E_{Defect}, as shown in equation 3.15.

$$E_{Binding} = E_{Cluster} - \sum E_{Defect} \tag{3.15}$$

For example, the binding energy of a $2Nd^{\bullet}_{Cd}{:}O''_i$ cluster is calculated following equation 3.16.

$$E_{Binding} = E(2Nd^{\bullet}_{Cd}O''_i) - E(O''_i) - 2E(Nd^{\bullet}_{Cd}) \tag{3.16}$$

Where a negative binding energy would indicate that the cluster is bound, and, is more favourable compared to the defects at infinite separation. It is found that conformations are more favourable than infinite separation when their oxide ion interstitial neighbours one or both of their dopants. However, of all the structurally inequivalent cluster conformations one was generally found to be at least 0.20 eV more favourable than the others.

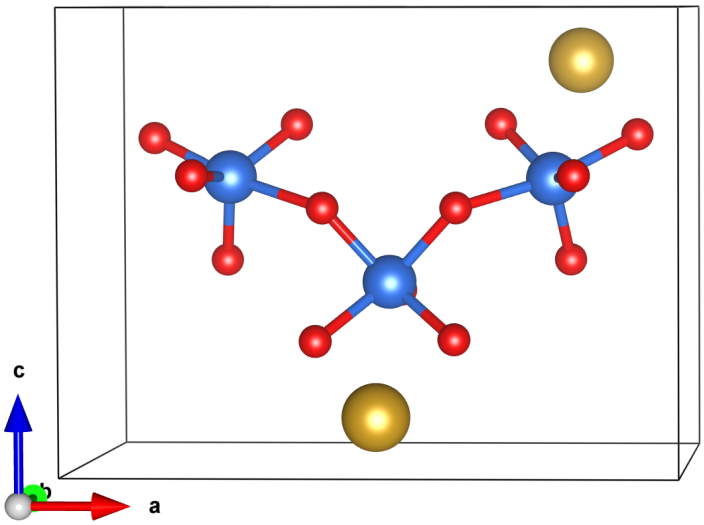

(a)

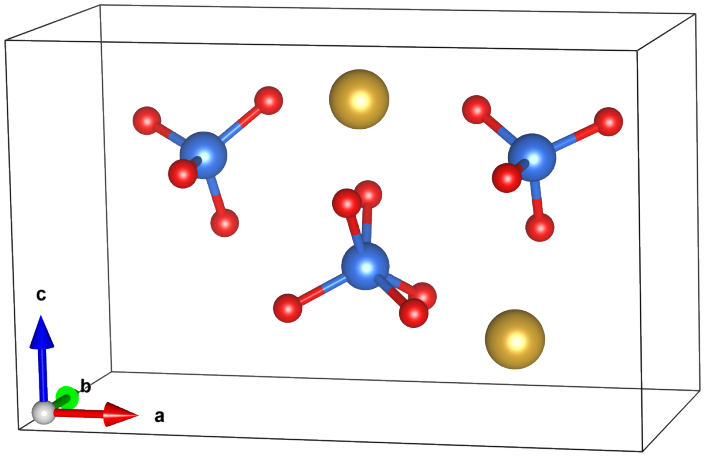

(b)

Figure 3.6: a) "Ge_3O_{13}" and b) "GeO_5" $2M^{\bullet}_{Cd}{:}O''_i$ clusters in Cd_2GeO_4, with O, Ge and M^{3+} ions represented as red, blue and gold spheres respectively. Surrounding ions have been omitted for clarity.

With the exception of Y^{3+}, each dopant is found to present only a single most stable $2M^{\bullet}_{Cd}{:}O''_i$ cluster conformation. The Sc^{3+} and Y^{3+} based clusters adopt "Ge_3O_{13}" based defect structures, as shown in figure 3.6a, in which the dopants, like the natural Cd^{2+} ions, are six coordinate and are on 13^{th} nearest neighbouring sites to one another. However, the "GeO_5" structure shown in figure 3.6b is favoured by the three larger dopants, Nd^{3+}, Pr^{3+} and La^{3+}, as it affords them a more preferable seven coordinate environment, and are on 3^{rd} nearest neighbouring sites to one another. This is achieved by the coordination of what would have been the bridging oxygens in a "Ge_3O_{13}" group directly to the dopants. The Y^{3+} doped clusters were also found to be equally stable in a similar seven coordinate cluster conformation.

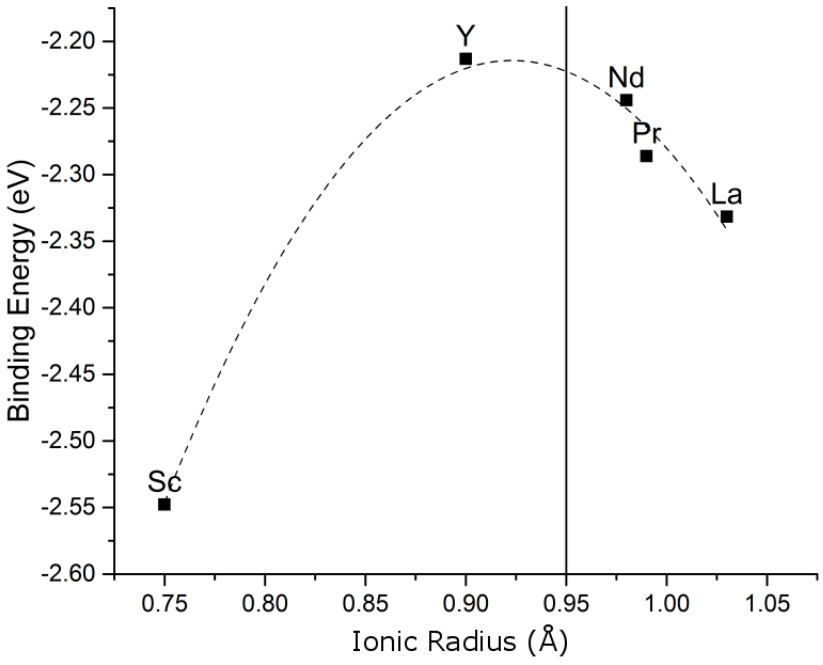

(a)

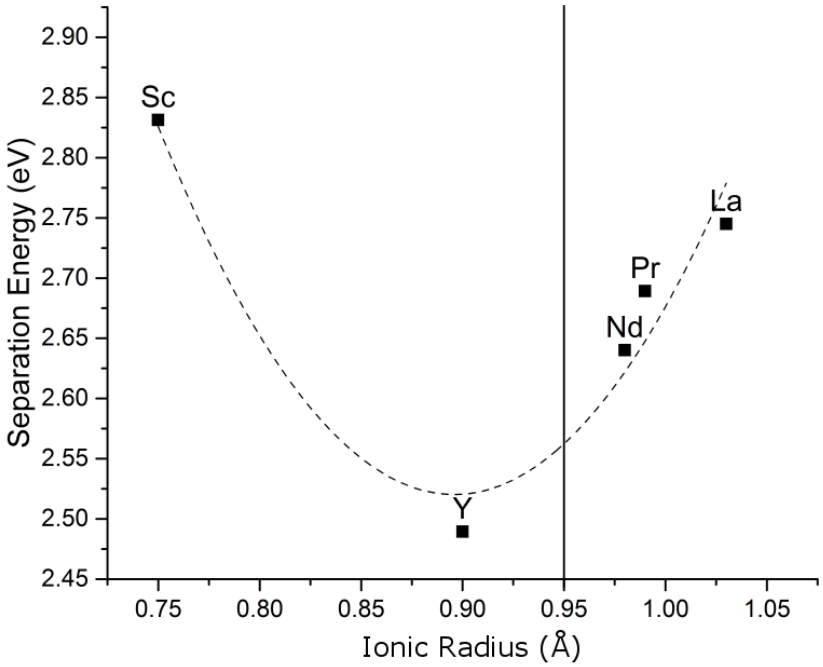

(b)

Figure 3.7: a) Binding and b) interstitial separation energies of $2M^{\bullet}_{Cd}{:}O''_i$ clusters as a function of dopant radius with Cd's ionic radius indicated by the solid black line, trend line include as a guide only.

Table 3.5: Binding and interstitial separation energies of stable $2M^{\bullet}_{Cd}{:}O''_i$ clusters and dopant radii.

Cluster	Radius (Å)	$E_{Binding}$ (eV)	$E_{Separation}$ (eV)
$2Sc^{\bullet}_{Cd}{:}O''_i$	0.75	-2.55	2.83
$2Y^{\bullet}_{Cd}{:}O''_i$ †	0.90	-2.21	2.49
$2Nd^{\bullet}_{Cd}{:}O''_i$	0.98	-2.24	2.64
$2Pr^{\bullet}_{Cd}{:}O''_i$	0.99	-2.29	2.69
$2La^{\bullet}_{Cd}{:}O''_i$	1.03	-2.33	2.74

† Note a second, similarly structured, $2Y^{\bullet}_{Cd}{:}O''_i$ cluster also identified (-2.16 eV).

The calculated binding energies for the stable $2M^{\bullet}_{Cd}{:}O''_i$ defect clusters are reported in table 3.5 and are plotted against dopant size in figure 3.7a. Examination of these results reveals this defect clustering is a highly favourable process. Therefore, the existence of isolated defects, particularly at non-trivial defect concentrations, is unlikely. Furthermore, the binding energy generally decreases as the dopant's radius deviates from the native Cd^{2+} ion's (0.95 Å), which is due to the dopant size dependency of the lattice relaxation interactions (discussed later).

Table 3.6: Corrected and uncorrected solution energies for the trivalent doping of Cd_2GeO_4 *via* the mechanism in equation 3.8.

Dopant	Radii (Å)	Solution Energy (eV)	
		Uncorrected	Corrected
Sc^{3+}	0.75	2.34	1.06
Y^{3+}	0.90	1.70	0.60
Nd^{3+}	0.98	1.23	0.11
Pr^{3+}	0.99	1.24	0.09
La^{3+}	1.03	1.26	0.09

As the previously discussed solution energies were calculated assuming infinite dilution, they failed to take into account the additional stabilisation energy which arises from defect-defect interactions. This results in an overestimation of the solution energies due to the non-trivial nature of such interactions. However, this can be corrected for by simply adding the binding energy to the solution energy. It can be seen from table 3.6 that the dopant incorporation energies are much more favourable once defect-defect stabilisation energies are factored in.

Although binding energies are an approximate indicator of the extent to which an oxide ion interstitial may become trapped, it is more appropriate to consider the interstitial separation energy. This represents the energy required to remove an oxide ion interstitial from its cluster to infinity. The separation energy is calculated as the difference in binding energy between a cluster with and without its oxide ion interstitial. The calculated interstitial separation energies for the $2M^{\bullet}_{Cd}{:}O''_i$ clusters are presented in table 3.5 and figure 3.7b. Again, this shows increased separation energies for dopants notably larger or smaller than Cd^{2+}. The larger the dopant ion, the greater its preference for the seven coordinate environment provided by the oxide ion interstitial. Small dopants, such as Sc^{3+}, are a poor fit for the native Cd^{2+} site. However, interstitial defects allow the oxide ions to relax around to dopant to accommodate it better. As such, the energetic penalty for the movement of an oxide ion interstitial away from its $2M^{\bullet}_{Cd}{:}O''_i$ cluster is likely to be greater for dopants notably larger or smaller then Cd^{2+}. This suggests that ions closer in size to Cd^{2+} are generally more appropriate dopants as their lower trapping capability suggests increased oxide defect mobility. However, this is not conclusive as it fails to provide information on the short to medium range defect interactions. Further to this, molecular dynamic simulations were carried out to elucidate interstitial defect trapping at higher temperatures. This being said, the large binding and separation energies clearly show that interstitial diffusion will be heavily restricted by the dopants, with a high trapping probability.

3.4 Oxide Ion Migration

Previous calculations suggested that pristine Cd_2GeO_4 is likely to be a poor oxide ion conductor due to its high intrinsic defect formation energies. However, the results also suggested that the formation oxide ion interstitial defects could be induced through trivalent doping, leading to enhanced ionic conductivities. In this section, the impacts of doping on oxide ion conduction, and the mechanisms by which oxide ions migrate, in Cd_2GeO_4 have been investigated using molecular dynamics (MD). Molecular dynamics simulations were carried out on both pristine and 10% doped Cd_2GeO_4. Yttrium was selected as the primary dopant due to its reduced binding and separation energies. However, neodymium doped systems were also studied for comparison. Details regarding the set up and execution of these simulations are given below, after which the diffusion of oxide ions in Cd_2GeO_4 will be discussed.

Molecular dynamic simulations were performed on 5×5×5 supercells, containing approximately 3500 ions, at four temperatures 873, 1073, 1273 and 1473 K. The doped systems were generated by introducing 25 randomly placed $2M^{\bullet}_{Cd}{:}O''_i$ clusters in the supercell. Two configurations were run for each system to help mitigate the effects of starting configuration on the final results. Systems were equilibrated at zero kelvin before simulating for a further 3 ns under NPT conditions. NPT conditions were employed as preliminary NST simulations showed no indications of phase transformations. Final production runs were carried out under NVT conditions for 3 ns, with a time step 0.5 fs. Oxygen shells with a mass of 1.6 amu were included using the adiabatic model. The results from the final production runs were then analysed using the methods described in section 2.9.

The mean squared displacements (MSD) of the oxide ions, plotted in figure 3.8, clearly shows that oxygen diffusion is only significant in the doped systems. Over the course of the simulation, no oxygen defects were found to form in pristine Cd_2GeO_4. This accounts for the observed absence of migratory diffusion in the pristine system, and agrees well with the static lattice calculations; which show oxygen Frenkel formation to be unfavourable. Oxygen density maps are provided in figures A.1, A.2 and A.3 of the appendix to enable a more visual representation of oxygen mobility in these systems. The calculated diffusion coefficients for oxygen in $Cd_{1.9}Y_{0.1}GeO_{4.05}$ and $Cd_{1.9}Nd_{0.1}GeO_{4.05}$ are presented in figure 3.9 and in table A.6 of the appendix. Results suggest that, although mobile, the oxide ion interstitial defects generally tend to reside in the dopant rich regions of the cell. This effect can be seen in figure 3.10 which compares the O^{2-}-Y^{3+} and O^{2-}-Cd^{2+}_{II} radial distribution functions. The defect tracking map displayed in figure A.4 also demonstrates this caging effect. This supports the earlier defect clustering analysis which indicated the trapping of interstitials by dopants to be highly favourable.

As discussed in the previous section, $2Y^{\bullet}_{Cd}{:}O''_i$ based clusters assume "Ge_3O_{13}" type structures while larger ions such as Nd^{3+} prefer to adopt "GeO_5" type clusters (figures 3.6a and b). Therefore, Nd^{3+} doped systems were also simulated to enable the effects of differing defect cluster structure on oxide ion diffusion in Cd_2GeO_4 to be probed. From these simulations, it was found that the oxygen diffusion coefficients of Nd^{3+} doped systems were comparable to those of the Y^{3+} doped systems, figure 3.9. This suggests that the difference in trapping of oxide ion interstitials in the Y^{3+} and Nd^{3+} doped systems, calculated at high temperature, is negligible compared to their overall binding energies, which were calculated at zero kelvin.

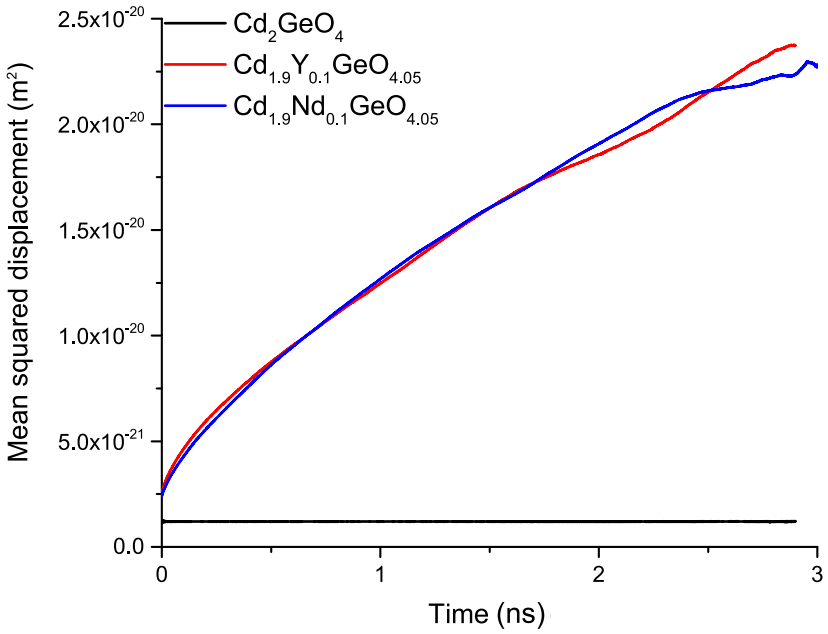

Figure 3.8: Mean squared displacements for oxygen in Cd_2GeO_4 (black), $Cd_{1.9}Y_{0.1}GeO_{4.05}$ (red) and $Cd_{1.9}Nd_{0.1}GeO_{4.05}$ (blue) at 1273 K.

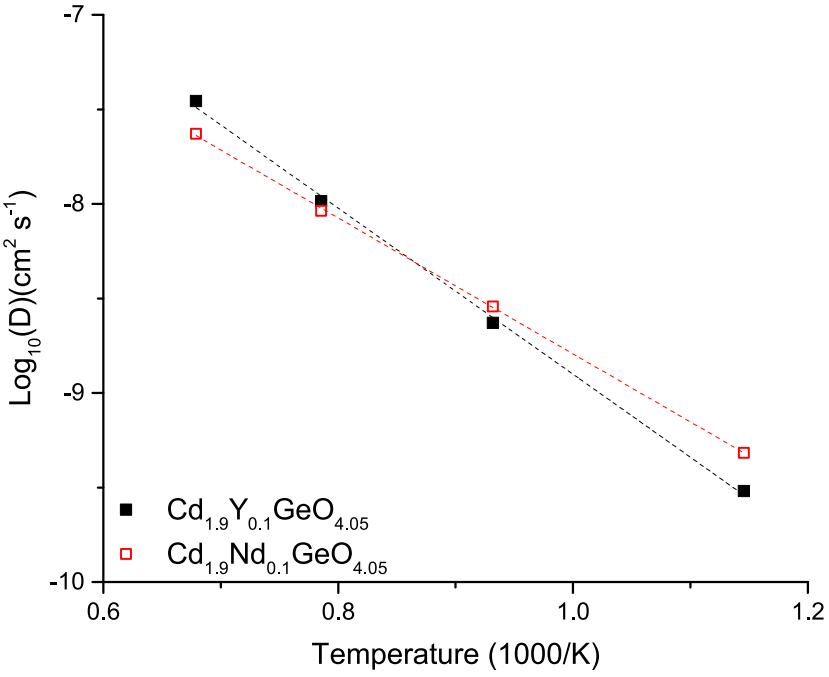

Figure 3.9: Plot showing the temperature dependency of the oxygen diffusion coefficient (D) in $Cd_{1.9}Y_{0.1}GeO_{4.05}$ and $Cd_{1.9}Nd_{0.1}GeO_{4.05}$.

The calculated diffusion coefficients of the doped Cd_2GeO_4 systems, figure 3.9, are found to be several orders of magnitude higher than those of the common cathode material LSM-20, and on a par with composite cathode materials such as YSZ-40 wt.% LSM which, at 1073 K, have diffusion coefficients of 1.3×10^{-12} and 1.0×10^{-9} cm^2 s^{-1} respectively.[118] However, many common electrolyte or advanced electrode materials present significantly higher diffusion coefficients, for example yttria stabilized zirconia (2.6×10^{-7} cm^2 s^{-1} at 1273 K) and lanthanum strontium cobalt ferrite (2.6×10^{-9} cm^2 s^{-1} at 773 K).[53,60]

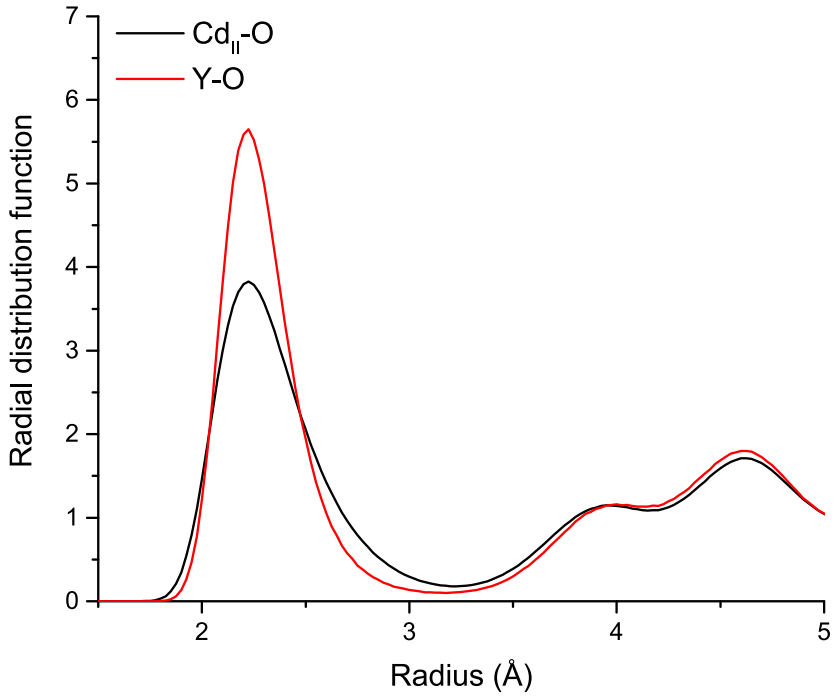

Figure 3.10: Radial distribution functions for oxide ions around $Cd_{II}^{\times}$ sites and $Y_{Cd_{II}}^{\bullet}$ sites in $Cd_{1.9}Y_{0.1}GeO_{4.05}$ at 1473 K.

More qualitative information about the diffusion process can be extracted from the mean squared displacement by calculating its axial components individually. This, shown in figure 3.11, suggests that the oxide ions diffuse primarily along the *ac*-plane. Furthermore, like the apatite germanates, all of the oxide ions are found to be mobile, suggesting that migration does not take place *via* a direct interstitial mechanism.[95] Average activation energies of 0.87 and 0.71 eV were calculated for oxygen migration in the Y^{3+} and Nd^{3+} doped systems respectively. As these energies are independent of temperature, it is unlikely that the migration mechanisms vary significantly over the simulated temperature range.

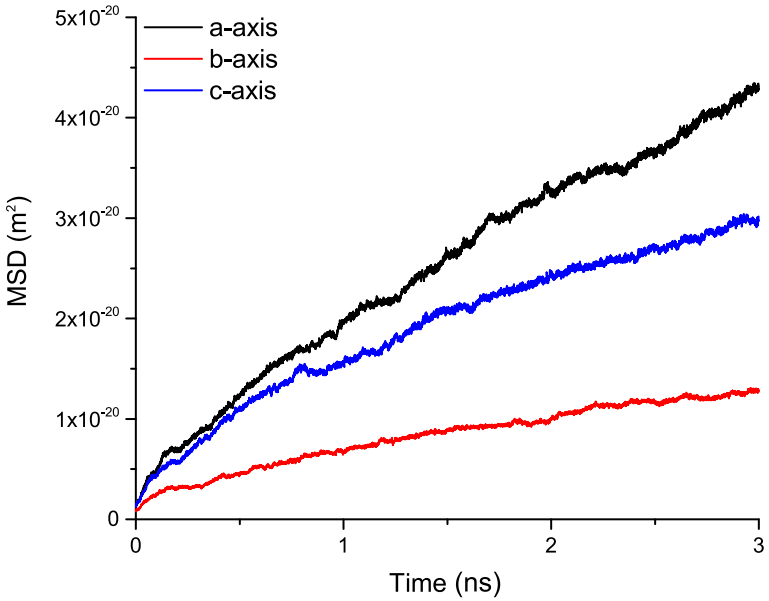

Figure 3.11: Axial MSDs for oxide ions in $Cd_{1.9}Y_{0.1}GeO_{4.05}$ at 1473 K.

Defect tracking was employed to identify the main oxide ion migration pathways, a visualisation of these results are given in figure A.4. In $Cd_{1.9}Y_{0.1}GeO_{4.05}$, the oxide ion defects diffuse down the a-axis through the sequential formation of "Ge_3O_{13}" and intermediary "Ge_2O_9" defects between neighbouring tetrahedra in a "knock-on" type mechanism. This mechanism, which is depicted in figure 3.12, forms wave-like diffusion channels along the a-axis, as represented in figure 3.13.

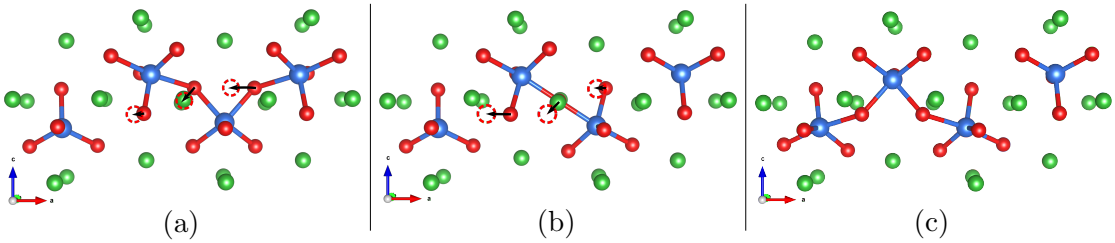

(a) (b) (c)

Figure 3.12: Schematic representation of oxygen migration in $Cd_{1.9}Y_{0.1}GeO_{4.05}$ along the a-axis *via* the making and breaking of intermediary "Ge_2O_9" groups. With Ge, Cd and O ions represented as blue, green and red spheres respectively.

This bears a striking resemblance to the oxide ion vacancy diffusion mechanism reported in $La_{1-x}Ba_{1+x}GaO_{4-x/2}$.[109] Movement between these a-axial channels are permitted by means of a c-axial diffusion mechanism. This mechanism differs from the former in that it is more stepwise in nature, and as oxide ions must unbind from their tetrahedra, traverse the Cd^{2+}_{II} channel and rebind with another tetrahedra. The exact pathway of the latter mechanism depends strongly on the local environment, specifically the presence of dopant or other interstitial ions. However, it was found, particularly at high temperatures, that oxygen defects could become trapped within Cd^{2+}_{II} channels as

isolated oxide ion interstitials or heavily distorted "GeO_5" units. Diffusion mechanisms in the Nd^{3+} systems are very similar, however isolated "GeO_5" groups are more commonly seen to precede "Ge_2O_9" formation. Several parallels can be drawn between oxygen diffusion in Cd_2GeO_4 and true olivine. Similar anisotropic diffusivity is predicted, *via* static lattice methods, for olivine (Mg_2SiO_4) itself. Such work reports *a*-axial diffusion is also favoured, with an activation energy of 0.97 eV.[192] The oxide ion diffusion pathways in Cd_2GeO_4 bear a strong resemblance to those of lithium ions in the olivine phosphate material $LiFePO_4$.[200] However, the migration pathway in $LiFePO_4$ is shifted away from the tetrahedra in comparison to Cd_2GeO_4 and proceeds *via* a vacancy mechanism.

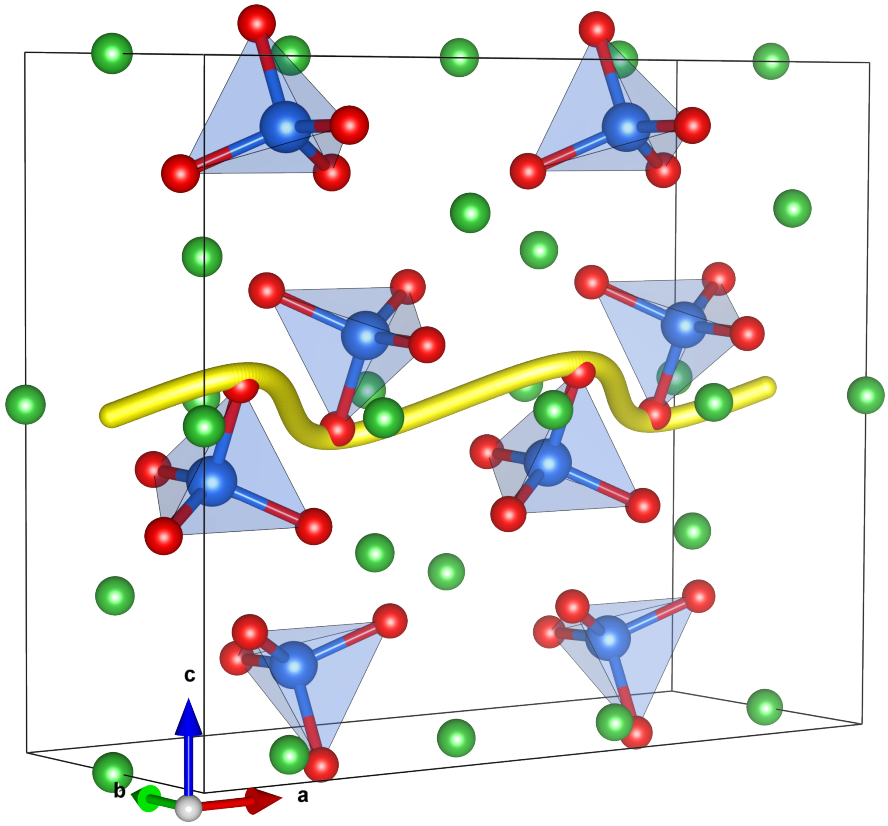

Figure 3.13: Depiction of the *a*-axial diffusion pathway (yellow) extracted from 1273 K simulations of $Cd_{1.9}Y_{0.1}GeO_{4.05}$. With Ge, Cd and O ions represented as blue, green and red spheres respectively.

To summarise, molecular dynamics simulations suggest that the oxide ion conducting abilities of Cd_2GeO_4 can be enhanced through trivalent doping. However, the calculated diffusion coefficients of both the Y^{3+} and Nd^{3+} doped systems are found to be lower than common fast oxide ion conductors, due to defect trapping. Simulations have also suggested that oxide ion diffusion occurs primarily along the *ac*-plane *via* a "knock-on" type mechanism, forming wave-like diffusion pathways.

3.5 Summary and Conclusions

In this chapter, computational methods have been employed to study defects, dopants and oxide ion migration in Cd_2GeO_4 at an atomic level. The main findings of this investigation have been summarised below.

A stable interatomic potential model capable of accurately reproducing the complex Cd_2GeO_4 structure has been successfully derived. This showed the formation of all intrinsic Frenkel and Schottky defects to be energetically unfavourable, thus indicating poor ionic conductivity. However, trivalently doped systems showed oxide ion interstitial defect formation and therefore enhanced ionic conductivities. Although mobile, defect trapping effects are found to confine these interstitial defects to the dopant rich regions of the cell, reducing their mobility. This effect, even at high temperatures, significantly reduces the materials ionic conducting ability. The oxide ions diffused primarily along the *ac*-plane; *via* an interstitial "knock-on" mechanism along the *a*-axis and a stepwise mechanism along the *c*-axis. Finally, migration barriers of 0.87 and 0.71 eV were calculated for the Y^{3+} and Nd^{3+} doped systems respectively. From this information, the applicability of Cd_2GeO_4 as a SOFC material can be evaluated.

As a single phase material, Cd_2GeO_4 offers no tangible advantage over current cathode or current electrolyte SOFC materials. This is due to its comparatively low oxide ion conducting ability even at higher temperatures, and its electrically insulating nature in oxygen containing environments. However, an investigation by Whipple *et al.* suggest that Cd_2GeO_4 might be a possible intermediate-low temperature catalyst for the cathodic oxygen reduction reaction.[183] Therefore, impregnating common cathode materials with Cd_2GeO_4 may offer a way to improve cell efficiency at reduced temperatures, but further work would be required to assess this. Suggestions for further work into the Cd_2GeO_4 system are discussed in chapter 6. In addition to its relevance in the oxide ion conductor field, this work is also interest in the Li-ion battery field, given the large interest in olivine-type material $LiFePO_4$. Finally, this work has been successfully published in Physical Chemistry Chemical Physics, and a copy of the publication has been attached as an appendix on page 153.

Chapter 4

Barium Orthotitanate

Numerous compounds exist within the BaO-TiO_2 system, some of which are found to be good electroceramics.[201,202] Of these compounds, only barium orthotitanate (Ba_2TiO_4) is both barium-rich and stable.[203,204] This material has a high melting point of 1860 °C and is somewhat unusual as it has Ti^{4+} ions that are tetrahedrally coordinated, rather than octahedrally coordinated, to oxygen.[205,206] Ba_2TiO_4 has been the focus of a number of studies due to its CO_2 sorption properties which make it a potential candidate for carbon capture applications.[207–211] Two crystalline phases of Ba_2TiO_4 are known to exist, a low temperature monoclinic β-phase and a high temperature orthorhombic α′-phase.[206,212] Like many other barium titanates, Ba_2TiO_4 is predicted to be a wide-gap insulator (4.5 eV).[213] In this introductory section, barium orthotitanate's structure, phase behaviour, stability and other various properties will be detailed. After which, the results of the computational investigations will be reported and discussed.

The Ba_2TiO_4 structure can be described as a series of isolated TiO_4 tetrahedra separated by Ba^{2+} ions. The isolated nature of these tetrahedra coupled with the open structure provided by the Ba^{2+} ions may afford these tetrahedra a degree of flexibility. Furthermore, this structure is unusual in that it presents tetrahedrally, rather than octahedrally, coordinated Ti^{4+} ions. This unusual coordination geometry may give the tetrahedra an additional degree of coordinational flexibility. It is conceivable that such flexibilities, if present, would make Ba_2TiO_4 a good interstitial oxide ion conductor worthy of investigation.

The low temperature monoclinic β-phase of Ba_2TiO_4 has a $P2_1/n$ space group and is isostructural with β-Ca_2SiO_4.[214] At high temperatures an orthorhombic $P2_1nb$ α′-phase is adopted, this is a tripled b-axis superstructure of the former and has a distorted β-K_2SO_4-type structure.[212] It has been shown that the α′-phase can be stabilised to room temperature by the addition of various dopants.[215,216] It is evident from literature (see Chen *et al.*[215] and Lee *et al.*[216]) that the exact temperature of the β to α′-phase transformation depends on both the method of synthesis and the sample's history.

In an investigation conducted by Lee *et al.*[216], dilatometry and DSC* methods were employed to identify the temperature at which the phase transformation occurred in Ba_2TiO_4. They reported an observed transformation at 710 °C. However, using non-ambient X-ray powder diffraction, Chen *et al.*[215] showed that complete conversion to the orthorhombic phase was achieved by 200 °C. Such a discrepancy is non-trivial, especially when considering that the transformation is martensitic (diffusionless) and should not have a large energetic barrier associated with it. A plausible reason for this discrepancy can be found in report by Ahmad and Ganguli[217] which also investigates the phase behaviour of Ba_2TiO_4. They show, following an 800 °C synthesis, that the as prepared Ba_2TiO_4 samples contain only 30% β-phase. Sintering the samples at 900 °C increases the β-phase content to 80%. However, after further sintering the sample at 1000 °C only the α′-phase is found to remain. They suggest that the high temperature α′-phase can be retained at room temperature if the grain size is small enough, and that α′-phase content should decrease with increasing grain size. This is somewhat supported by the increasing preference of higher symmetry phases with decreasing grain sizes.[218] However, this alone does not necessarily account for the observation of pure α′-phase following sintering at 1000 °C. Differences in the lattice parameters of the α′ and β phases means that strains will be present at the interfaces between them. This interfacial strain is likely to hinder phase transformation in Ba_2TiO_4 and will be more pronounced in grains of larger size, suggesting that the effective energy barrier to phase transformation will depend not only on grain size but also on the relative concentrations of α′ and β phases at that time.[215] This is further supported by Marks *et al.*[219] who shows that larger grains become stuck in the high temperature phase, while the smaller ones easily convert to the low temperature phase. Furthermore, it can be concluded that, barring any impurity effects, the results from the investigation by Chen *et al.*[215] are closest to what might be considered the unhindered phase transformation temperature of 100-200 °C which would be observed in small single crystals. This is because samples were mechanically ground prior to use, which helped to negate grain size effects.[215]

*DSC = differential scanning calorimetry.

The material Ba_2TiO_4, particularly its orthorhombic modification, is found to be chemically unstable under ambient conditions and will decompose slowly on contact with air.[220–222] At temperatures above 750 °C, Ba_2TiO_4 is stable, below this, it reacts with CO_2 forming $BaTiO_3$ and $BaCO_3$.[215,223] As this degradation occurs with minimal swelling, Ba_2TiO_4 can potentially be used in carbon capture applications.[208] Although CO_2 induced degradation of Ba_2TiO_4 is found to proceed slowly below 300 °C, it can be accelerated by the presence of water.[203,215,221]

4.1 Structural Modelling

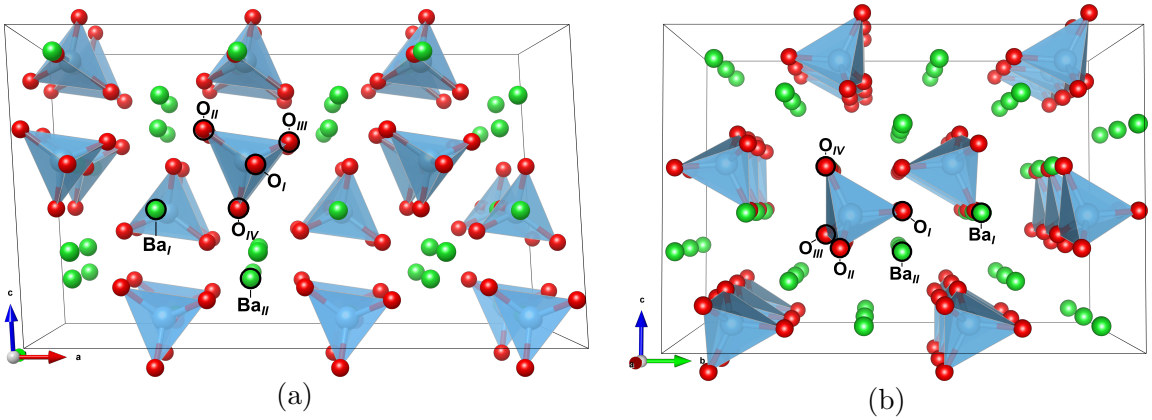

Figure 4.1: Crystal structure of β-Ba_2TiO_4 (3×2×1 supercell) as viewed down the a) *b*-axis and b) *a*-axis, with the Ti, Ba and O ions represented as blue, green and red spheres respectively, and TiO_4 tetrahedra as blue polyhedra.

At room temperature, Ba_2TiO_4 crystallises in its monoclinic $P2_1/n$ β-phase. This structure, shown in figure 4.1, is isostructural with β-Ca_2SiO_4 and is comprised of four distinct O^{2-} sites, two Ba^{2+} sites and one Ti^{4+} site. The two divalent barium sites Ba_I^{2+} and Ba_{II}^{2+} are coordinated to seven and eight O^{2-} ions respectively.[214,224] While the Ba_I^{2+} sites are less coordinated than the Ba_{II}^{2+} sites, they are larger. Each Ti^{4+} ion is coordinated to four O^{2-} ions in a tetrahedral arrangement. Within the isolated TiO_4 tetrahedra, Ti-$^{4+}O_I^{2-}$ distances are reportedly shorter than other Ti^{4+}-O_x^{2-} distances, this is because the O_I^{2-} site are coordinated to only three Ba^{2+} ions while the others to four. The tetrahedra alternate with Ba_I sites to form TiO_4-Ba_I^{2+} channels down the *b*-axis, and are linked to one another through the Ba_{II}^{2+} only channels which separate them. The high temperature orthorhombic $P2_1nb$ α′-phase, as shown in figure 4.2, is a tripled *b*-axis superstructure of the β-phase. It therefore shares the same basic, if less

ordered, general structure as the β-phase. It should be noted that while the α′-phase contains six symmetrically inequivalent Ba^{2+} sites, the sites Ba_I^{2+}-Ba_{III}^{2+} and Ba_{IV}^{2+}-Ba_{VI}^{2+} are comparable to the Ba_I^{2+} and Ba_{II} sites of the β-phase respectively, but with slight variations in their Ba-O lengths, the only exception to this is the α′-Ba_I^{2+} site which is closer to a six coordinate geometry. Likewise, the three unique TiO_4 tetrahedra found in the α′-phase are similar to those in the β-phase but with slightly different orientations. During the course of investigation, both the high and low temperature phase structures were modelled.

Table 4.1: Refined Buckingham interatomic potentials and shell model parameters used in this work for Ba_2TiO_4.[97,225,226]

Interaction	A (eV)	ρ (Å)	C (eV Å^6)	Y (e)	k (eV Å^{-2})
Ba^{2+}- O^{2-}	4939.2	0.3074	0.00	2.00	r
Ti^{4+}- O^{2-}	1946.9	0.3020	9.22	4.00	r
O^{2-}- O^{2-}	22764.3	0.1490	28.33	-2.91	49.53

Where r indicates rigid ion model (i.e no polarisable shell model).

To identify a suitable interatomic potential model for Ba_2TiO_4, a selection of potentials from literature were scanned. Those which provided the best stable fit were then used as the base from which the final model was derived.[97,225,226] This was done by iteratively fitting the interatomic potential parameters to the experimentally determined structure.[214] To ensure consistency, interatomic potentials were selected based on their ability to model both the β and α′ phases of Ba_2TiO_4. The interatomic potentials were further verified using their respective binary oxide materials. The final interatomic pair potentials used to model Ba_2TiO_4 in this work are given in table 4.1, along with the shell model parameters where applicable.

The comparison of the calculated and experimental lattice parameters of both the β and α′-phases of Ba_2TiO_4, given in table 4.2, indicates a good fit to within 1%.[212,214] The calculated and experimental cation-oxygen distances, given for the β-phase in table 4.3, are also found to be in reasonable agreement with one another. A similar fit was obtained for the α′-phase using the same interatomic potential model, however slightly higher errors in the Ba-O distances were encountered. While the deviation in the Ti-O bond distances are slightly higher than desired, they are still within acceptable limits, especially when considering the titanium ions unusual environment. Now that an adequate interatomic potential model for Ba_2TiO_4 has been identified, investigations into its defect properties can be conducted.

Table 4.2: Comparison of calculated and experimental lattice parameters of the (a) β and (b) α′ phases of Ba_2TiO_4, with the experimental standard deviations in parenthesise.

(a) Lattice parameters of β-Ba_2TiO_4			
Parameter	Expt.[214]	Calc.	Difference (%)
a (Å)	6.096(4)	6.100	0.004 (0.06)
b (Å)	7.681(6)	7.676	-0.005 (-0.07)
c (Å)	10.545(9)	10.488	-0.057 (-0.54)
α=γ(°)	90.000	90.000	0.000 (0.00)
β(°)	92.990(6)	93.425	0.435 (0.47)
(b) Lattice parameters of α′-Ba_2TiO_4			
Parameter	Expt.[212]	Calc.	Difference (%)
a (Å)	6.107(8)	6.118	0.011 (0.18)
b (Å)	22.952(4)	22.969	0.017 (0.08)
c (Å)	10.540(2)	10.476	-0.064 (-0.61)
α=β=γ(°)	90.000	90.000	0.000 (0.00)

Table 4.3: Comparison of calculated and experimentally determined cation-oxygen distances in β-Ba_2TiO_4.

Cation	Oxygen	Expt.[214] (Å)	Calc (Å)	Difference (%)
Ba_I	O_I	2.573	2.562	-0.011 (-0.43)
	O_{IV}	2.696	2.762	0.066 (2.42)
	O_{III}	2.760	2.814	0.054 (1.94)
	O_{II}	2.897	2.881	-0.016 (-0.55)
	O_{III}	2.987	2.947	-0.040 (-1.35)
	O_{IV}	3.072	3.058	-0.014 (-0.46)
	O_{II}	3.229	3.182	-0.047 (-1.47)
Ba_{II}	O_{II}	2.692	2.684	-0.008 (-0.30)
	O_{III}	2.697	2.676	-0.021 (-0.78)
	O_{II}	2.699	2.710	0.011 (0.41)
	O_{IV}	2.802	2.789	-0.013 (-0.47)
	O_I	2.824	2.832	0.008 (0.28)
	O_{IV}	2.869	2.924	0.055 (1.90)
	O_{III}	2.918	2.988	0.070 (2.37)
	O_I	2.982	2.924	-0.058 (-1.96)
Ti	O_I	1.766	1.755	-0.011 (-0.62)
	O_{II}	1.811	1.774	-0.037 (-2.06)
	O_{III}	1.817	1.781	-0.036 (-2.00)
	O_{IV}	1.834	1.787	-0.047 (-2.60)

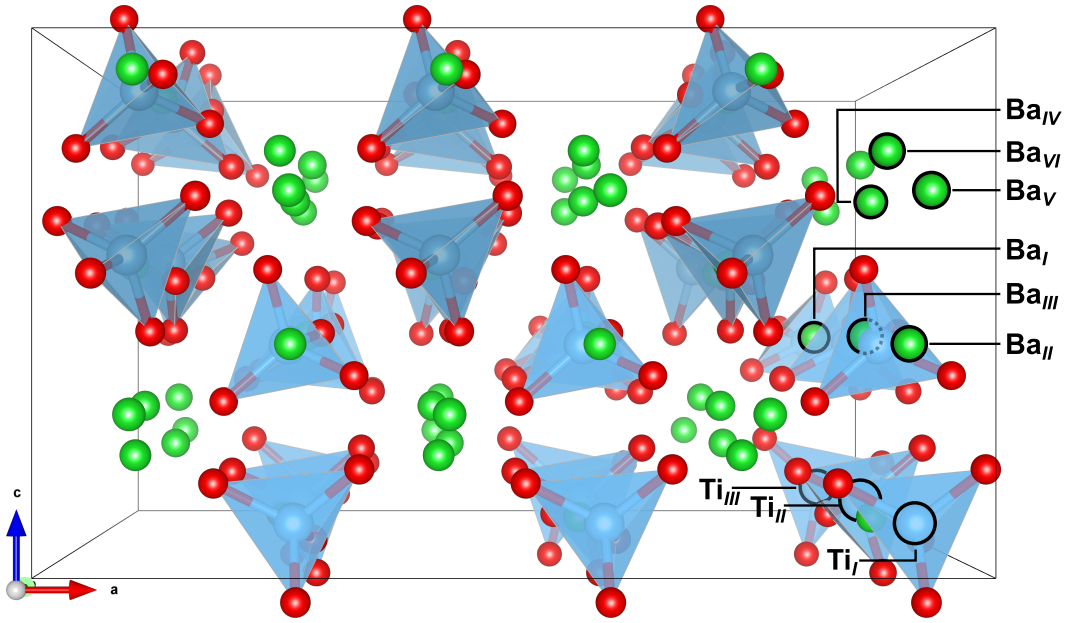

Figure 4.2: Crystal structure of α′-Ba_2TiO_4 (3×1×1 supercell) as viewed down the *b*-axis, see figure 4.1 for the image key.

4.2 Intrinsic Point Defects

Using the Mott Littleton method described in section 2.5, the vacancy and interstitial point defect energies for all native ions are calculated. These are combined to calculate the Schottky and Frenkel defect energies, which are presented alongside their Kröger-Vink mechanisms in table 4.4. It is worth noting that these calculations show that intrinsic defect formation energies are lower in the α′-phase of Ba_2TiO_4. In materials such as $Ba_2In_2O_5$ oxygen defects, which are pivotal to oxide ion conduction, form naturally through oxygen Frenkels.[53,191] However, the formation of Frenkel and Schottky defects in β and α′-phase Ba_2TiO_4 are found to be energetically unfavourable, as seen in table 4.4. Therefore, the concentration of these defects will be negligibly small, even at high temperatures. As the spontaneous formation of oxygen defects in pristine Ba_2TiO_4 is unfavourable, doping must be employed to induce their formation. While experimental investigations have demonstrated the viability of doping Ba_2TiO_4 with divalent and trivalent ions, most have done so purely as means of stabilising the high temperature α′-phase at room temperature.[215,216] Therefore doping of Ba_2TiO_4 will be investigated computationally, in section 4.4, as a means of inducing oxygen defect formation.

Table 4.4: Calculated Frenkel and Schottky defect energies[a] (eV) for Ba_2TiO_4.

Type	Defect equation	β	α′
Ba Frenkel	$Ba_{Ba}^{\times} \rightarrow V_{Ba}'' + Ba_i^{\bullet\bullet}$	4.78	4.26
Ti Frenkel	$Ti_{Ti}^{\times} \rightarrow V_{Ti}'''' + Ti_i^{\bullet\bullet\bullet\bullet}$	10.56	10.16
O Frenkel	$O_O^{\times} \rightarrow V_O^{\bullet\bullet} + O_i''$	3.48	3.35
Schottky	$2Ba_{Ba}^{\times}+Ti_{Ti}^{\times}+4O_O^{\times} \rightarrow 2V_{Ba}''+V_{Ti}''''+4V_O^{\bullet\bullet}+Ba_2TiO_4$	4.26	4.05

a Energy values are quoted per-defect.

4.3 Impurity Defects

As discussed in the introduction, barium orthotitanate is both hygroscopic and highly reactive towards CO_2.[215,227] Therefore, it is feasible that the incorporation CO_2 and H_2O based defects are favourable. If so, the likelihood of contamination is high given that both CO_2 and H_2O are often present during synthesis or when stored under ambient conditions. Such defects warrant investigation as they may interfere with those required for oxide ion conduction. In the sections which follow, both CO_2 and H_2O based defects are investigated and their possible impacts on oxide ion formation considered.

4.3.1 Water Incorporation

In perovskite based ionic conductors, the most common defects present are oxide ion vacancies. Such defects form the foundation of the material's oxide ion conducting ability. This is also true of proton conducting perovskites, in which the oxide ion vacancies react with water, *via* mechanism 4.1, leading to the incorporation of protonic defects, albeit as hydroxide groups ($OH_O^{\bullet}$).[228]

$$H_2O + V_O^{\bullet\bullet} + O_O^{\times} \rightarrow 2OH_O^{\bullet} \tag{4.1}$$

However, the elimination of oxide ion vacancies generally tends to reduce oxide ion conductivity, as it is replaced by proton conductivity. The incorporation of water into solid oxide systems, often as a pair of hydroxyl groups, is widely known in literature.[22,187,192] As previously discussed, Ba_2TiO_4 is known to be reactive to atmospheric water, which is present in most environments and during synthesis.[217,221,227] As water incorporation can have a profound impact on oxide ion conductivity it is vital to investigate its effects on Ba_2TiO_4 based systems.

Table 4.5: Buckingham and Morse potentials for modelling OH^- [187]

(a) Intermolecular Buckingham			
Interaction	A (eV)	ρ (Å)	C (eV Å^6)
O-H	311.97	0.25	0.000
(b) Intramolecular Morse			
Interaction	D (eV)	β (Å^{-1})	r_0 (Å)
O-H	7.0525	2.1986	0.9485

As before, a suitable interatomic potential model for OH^- must be identified. Several different interatomic potential models were evaluated, the selected intermolecular Buckingham and the intramolecular Morse potentials are presented in table 4.5. In accordance with the study by Panchmatia *et al.*[187], partial charges of -1.4263 and 0.4263 were placed on the O and H species respectively to model the dipole moment of the hydroxyl group. Using the Mott-Littleton method, the isolated point defect energies of interstitial (OH_i') and substitutional ($OH_O^\bullet$) hydroxy defects were calculated. Combining these values following the equations given in table 4.6, discussed later, yields the final water incorporation energies, also shown in table 4.6. E_{PT} is the energy of the gas phase proton transfer reaction $H_2O+O^{2-} \rightarrow 2OH^-$ (-9.74 eV).[229] While an E_{PT} value of -9.74 eV was chosen in this work, other values around -11.77 eV have also been used successfully elsewhere.[187] Negative water incorporation energies indicate a favourable process, while positive values an unfavourable process.

The first two, of the four, water incorporation mechanisms to be considered for Ba_2TiO_4 are shown below in equations 4.2 and 4.3.

$$H_2O + 2O_O^x \rightarrow 2OH_O^\bullet + O_i'' \tag{4.2}$$

$$H_2O + O_O^x \rightarrow OH_O^\bullet + OH_i' \tag{4.3}$$

These two water incorporation mechanisms are common to the pristine and doped systems alike. The first mechanism, equation 4.2, involves the formation of two hydroxide groups ($OH_O^\bullet$) on native oxygen sites coupled with the formation of a single oxide ion interstitial (O_i). Increasing the interstitial defect concentrations in this manner is known to improve the oxide ion conducting abilities of some interstitial conductors.[187] In the second of the two mechanisms, equation 4.3, one substitutional hydroxide group and one interstitial hydroxide group are formed (OH_i'). However, such a mechanism may not directly enhance oxide ion conductivity.

$$H_2O + O_i'' \rightarrow 2OH_i' \tag{4.4}$$

The final two water incorporation mechanisms considered in this work are shown in equations 4.1 and 4.4. These are unique to the oxygen deficient and oxygen excess systems respectively. This is due to the fact that they require the presence of specific oxide defects. As these mechanisms would eliminate any oxygen defects present in the material, e.g. those formed through doping, their occurrence would most likely result in diminished oxide ion conduction.

Table 4.6: Water incorporation energies (eV) for Ba_2TiO_4.

Equation	β-phase	α′-phase
4.1: $E_{H_2O} = 2OH_O^{\bullet} - V_O^{\bullet\bullet} + E_{PT}$	0.83	0.47
4.2: $E_{H_2O} = 2OH_O^{\bullet} + O_i'' + E_{PT}$	7.80	7.17
4.3: $E_{H_2O} = OH_O^{\bullet} + OH_i' + E_{PT}$	4.32	3.96
4.4: $E_{H_2O} = 2OH_i' - O_i'' + E_{PT}$	0.85	0.75

It can be seen from the large positive water incorporation energies in table 4.6 that water incorporation *via* mechanisms 4.2 and 4.3 is energetically unfavourable. This suggests that water inclusions are unlikely to be found in the bulk of pristine Ba_2TiO_4 in any significant quantity. However, it is possible that interactions with CO_2 based defects, discussed in the section which follows, may shift the favourability of water incorporation.[215] That being said, Ba_2TiO_4 is a hygroscopic material known to be unstable in humid environments. Any contact with water, such as that in air, would result in decomposition with swelling *via* equations 4.5 and 4.6.[221,230]

$$Ba_2TiO_4 + H_2O \longrightarrow BaTiO_3 + Ba(OH)_2 \tag{4.5}$$

$$BaTiO_3 + H_2O \longrightarrow TiO_2 + Ba(OH)_2 \tag{4.6}$$

Water incorporation *via* the oxide defect interaction mechanisms 4.1 and 4.4 is found to be significantly lower in energy, and can be considered favourable within the error of the model and the E_{PT} value. This suggests that oxide ion defects formed in Ba_2TiO_4 as a result of doping may be supplanted by hydroxide defects during synthesis or when exposed to humid environments, resulting in reduced oxide ion conductivities. However, it is likely that some measure of proton conduction would be observed in samples with water inclusions. The presence of proton conduction in water containing Ba_2TiO_4 samples could be confirmed, or disproved, using the hydrogen isotope effect which has been successfully used with many other materials.[231,232]

4.3.2 Carbon Dioxide Defects

Other possible impurity defects that may interfere with the stability or oxide ion conductivity of Ba_2TiO_4 based materials may result from CO_2 incorporation. While many experimental investigations into the reaction of Ba_2TiO_4 with CO_2 have been conducted, all have focused on macroscopic effects, such as reaction temperatures and cycling speeds, rather than atomistic effects.[207,208,215,219,223] As stated in the introduction to this chapter, CO_2 is known to degrade Ba_2TiO_4. However, what is not known is the local structural effects of small concentrations of CO_2 and the defects that such molecules may form. It is possible that CO_2 based defects may, like H_2O, retard oxide ion conduction. Since Ba_2TiO_4 is commonly synthesised *via* the carbonate route it is likely that carbonate defects, if favourable, will form during synthesis. This section will be divided into three parts; the first will review what is already known about the CO_2-Ba_2TiO_4 reaction, the second will cover the procedures and investigative techniques use to study CO_2 based defects, and the third will discuss the findings of the computational investigations.

Above 450 °C, Ba_2TiO_4 reacts with CO_2, *via* mechanism 4.7, to produce barium carbonate ($BaCO_3$) and barium titanate ($BaTiO_3$).[208,215,223]

$$Ba_2TiO_4 + CO_2 \rightarrow BaCO_3 + BaTiO_3 \tag{4.7}$$

At 600 °C the reaction speeds up dramatically and conversion to $BaCO_3$ and $BaTiO_3$ is almost complete. This reaction is found to be reversible above 750 °C, where Ba_2TiO_4 reforms and is stable.[215] The reaction generally occurs at the material surface, which requires oxygen and barium ions to diffuse towards the surfaces.[219] Interestingly, Saito and Sakabe[208] report that this interconversion occurs with lesser volume change than other materials. Although reaction with CO_2 does occur between 300 and 400 °C, it is found to be relatively slow, with no measurable degradation found within 24 hours.[215] However, between 150 and 300 °C the reaction once again proceeds at a reasonable speed. Chen *et al.*[215] attributes this low temperature catalyzation to water absorbed at the powder's surface. Below 150 °C, Ba_2TiO_4 is once again found to be (relatively) stable as there is insufficient thermal energy for the reaction to occur. However, if kept under ambient conditions for long enough, the sample eventually degrades into $BaCO_3$ and $BaTiO_3$.[220]

Following their incorporation into Ba_2TiO_4, carbon dioxide molecules (CO_2) could react with either interstitial or lattice oxygens to form carbonate groups (CO_3^{2-}). These carbonate groups are known to exist both naturally and as impurity defects in many materials.[233–235] A series of calculations were carried out to study the possible effects of small carbon dioxide inclusions on oxide ion defects. However, several issues were encountered during the initial modelling stages.

It was found that common interatomic potential models for carbonate groups were unable to accurately model carbonate molecules in Ba_2TiO_4. The use of common non-rigid body interatomic potentials from literature resulted in unrealistic out of plane bending angles of up to 114° in CO_3^{2-}.[233,236–238] Rigid body potentials also proved unsuitable as they did not permit the relaxation of CO_3^{2-} molecules.[239] The CO_3^{2-} interatomic potentials were therefore revisited, in particular the four body torsional potential was refined. Seven *ab initio* CCSD(T) calculations were conducted to calculate the energy of the CO_3^{2-} molecule with out of plane torsion angles ranging from 0 to 30° at intervals of 5°. The torsional k term was then fitted to the resulting energy curve.† No extreme out of plane bending behaviour was observed when using the newly derived torsional term. The final interatomic potential model selected for CO_3^{2-} is shown in table 4.7, and was based upon that by Archer *et al.*[236]. It should be noted that all intramolecular interactions act between oxygen cores, rather than their shells. Furthermore, all other interactions are the same as those in the standard Ba_2TiO_4 model. All carbonate calculations were carried out using the supercell method (4×3×2 supercell) and neutralising background charges were applied to maintain charge neutrality where required.‡

To correctly calculate carbonate incorporation energies, a reaction term similar to that of the water incorporation's proton transfer term (E_{PT}) was included. This value, herein referred to as E_{OT}, represents the energy of the reaction $CO_2 + O^{2-} \rightarrow CO_3^{2-}$. Currently, no value exists in literature for E_{OT}, and the derivation of such a value was a non-trivial process. This is due to the rarity of the terms required to derive such a value, and ambiguity of such terms. An example of such ambiguity can be seen in the reported first electron affinity values for CO_3 which range from 2.69 to 6.76 eV.[188,240] In this work a value of -14.37 eV was derived for E_{OT}. The E_{OT} derivation process has been included in section B.1 of the appendix.

†Contributions from other interatomic potentials to total energy were subtracted prior to fitting.
‡Compatibility issues were encountered with GULP's Mott-Littleton code and the CO_3^{2-} potentials.

Table 4.7: Intramolecular CO_3^{2-} potential parameters.

Functional	Interaction		Parameters		Cutoffs (Å)	
Buckingham		A (eV)	ρ (Å)	C (eV Å^6)	Min	Max
	O_c-O_c	4030.3	0.245497	0.000	0.000	12.000
	O-C* [241]	435.0	0.340000	0.000	0.000	12.000
Morse	C-O_c	D (eV)	A (Å^{-1})	r_0 (Å)	Min	Max
		5.000	2.5155	1.20246	0.000	2.000
Three-body	C-O_c-O_c	k_2 (eV rad^{-2})	θ_0 (°)		O_c-C	O_c-O_c
		1.7887	120		2.000	3.464
Torsional	O_c-O_c-C-O_c	k (eV)	ϕ_0 (°)		O_c-O_c	O_c-C
		1.10	0.00		3.464	2.000
Spring	O_c	k_2 (eV Å^2)	k_4 (eVÅ^4)			
		20.67	1000			
Charges		Charge (e)				
	O_c core	0.23				
	O_c shell	-1.38				
	C core	1.45				

Note that all interactions, except for that marked with *, are intramolecular.

In this work, five carbonate incorporation mechanisms were considered. The first and simplest of which is described in equation 4.8 using Kröger-Vink notation. In this mechanism, the carbon dioxide molecule ($CO_{2(g)}$) reacts with a native lattice oxide ion ($O_O^\times$) to form an interstitial carbonate defect clustered with an oxide ion vacancy ($[(CO_3)_i''+V_O^{\bullet\bullet}]$). Since CO_2 is a charge neutral molecule, no charge compensation occurs as a result of its incorporation. It should be noted that square brackets denote clustered defects, and therefore includes the presence an additional binding energy term which has been omitted to aid visual clarity.

$$CO_{2(g)} + O_O^\times \rightarrow [(CO_3)_i''+V_O^{\bullet\bullet}] \tag{4.8}$$

It can be seen, from table 4.8, that energy of carbonate defect formation in pristine α′-Ba_2TiO_4 *via* mechanism 4.8 is favourable (-0.05 eV), suggesting that such defects are a likely occurrence in α′-Ba_2TiO_4 base materials that have been exposed to CO_2. It is perhaps interesting to note that during these calculations the introduction of a carbonate defect to a β-phase supercell commonly resulted in a shift to α′-phase geometry. Furthermore, from table 4.8 it can be seen that these carbonate defects are 0.40 eV lower in energy in the α′-phase. This suggests that low levels of carbonate defects may help stabilise the α′-phase at reduced temperatures. Rather than forming a joint tetrahedra-carbonate like defect similar to those seen in "$YAlO_3$", the CO_3^{2-} groups prefer to remain isolated, but clustered with the oxygen deficient "Ti_2O_7" units

which form as a result of the oxide ion vacancy.[235] Images of these defect structures can be found in figure B.1 of the appendix. The carbonate defect formed in equation 4.8 effectively rips an oxide ion from a proximal TiO_4 tetrahedra creating an oxide ion vacancy, albeit a highly clustered one. It is possible that this pseudo-vacancy could accommodate H_2O based defects more favourably than a pristine Ba_2TiO_4 lattice, as hinted by equation 4.1, however further calculations are required to confirm this.[215]

$$CO_{2(g)} + O_O^{\times} \rightarrow V_O^{\bullet\bullet} + (CO_3)_i'' \tag{4.9}$$

The second mechanism, shown in equation 4.9, is a variant on the first in which the carbonate interstitial and the oxide ion vacancy defects are unclustered. The comparably high energy of this mechanism (4.3 eV table 4.8) shows that a significant clustering force exists between the $V_O^{\bullet\bullet}$ and $(CO_3)_i''$, suggests that both will be trapped and fairly immobile. Having established the primary mechanism by which carbonate defects will react with the pristine Ba_2TiO_4 lattice (equation 4.8), attention can be turned to their interactions with oxide defects.

$$CO_{2(g)} + O_i'' \rightarrow (CO_3)_i'' \tag{4.10}$$

The first of the CO_2-oxygen defect interaction mechanisms is shown in equation 4.10. This represents the formation of carbonate interstitial defect ($(CO_3)_i''$) from the merging of an absorbed CO_2 molecule with an oxide ion interstitial. With an energy of -2.47 eV, mechanism 4.10 is highly favourable. From this, it can be suggested that any oxide ion interstitial defects present in Ba_2TiO_4, such as those induced through doping, could readily be annihilated by carbonate defect formation. As the oxide ion interstitial would be replaced by a much larger defect of similar charge, it is highly likely that ionic conductivity would be decreased. Like before, carbonate defects are found to be significantly more stable in the α'-phase of Ba_2TiO_4 (by $\sim$0.5 eV). The structure of the $(CO_3)_i''$ defect is shown in figure B.2 of the appendix. Interestingly the local arrangement of the Ba ions around the $(CO_3)_i''$ defect is an almost perfect match for the $BaCO_3$ structure, which is one of the by-products of the Ba_2TiO_4-CO_2 reaction.

$$CO_{2(g)} + O_O^{\times} + V_O^{\bullet\bullet} \rightarrow [(CO_3)_i'' + 2V_O^{\bullet\bullet}] \tag{4.11}$$

Interactions between oxide ion vacancies and carbonate defects were also considered. However, due to its nature, the interaction between an oxide ion vacancy and a carbonate group will be associative rather than a direct reaction. Mechanism 4.11 represents formation and further clustering of a $(CO_3)_i''$ defect to an oxide ion vacancy, such as that created through doping. This is analogous to mechanism 4.8 with a second oxide

ion vacancy clustering augment. It can be seen from the energy of this mechanism, -3.24 eV, that the presence of oxide ion vacancies will dramatically increase the favourability of carbon dioxide incorporation and subsequent carbonate defect formation. Taking the difference of mechanism 4.8 and 4.11 gives a clustering energy of -3.19 eV. This suggests that oxide ion vacancies formed through doping could become strongly bound to carbonate impurity defects, if present. This is the most energetically favourable of the carbonate incorporation mechanisms considered. It can be seen from figure 4.5 that the presence of such a defect causes significant structural distortions to the Ba_2TiO_4 lattice.

$$2CO_{2(g)} + 2O_O^{\times} \rightarrow [(CO_3)_i'' + 2V_O^{\bullet\bullet}] + (CO_3)_i'' \tag{4.12}$$

The final incorporation mechanism considered was the carbonate induced oxygen Frenkel defect formation reaction. This, shown in equation 4.12, represents the formation of an oxygen Frenkel defect pair in which the oxide ion vacancy and interstitial defects form carbonate defects *via* mechanisms 4.11 and 4.10 respectively. The carbonate induced oxygen Frenkel defect formation (0.49 eV) is found to be much lower in energy than the pure oxygen Frenkel defect pathway (6.70 eV). Suggesting that carbonate defects may reduce the energy required for further defect formation.

Table 4.8: Carbonate defect incorporation energies.

Equation	Formula	Defect Energy (eV)	
		α′-phase	β-phase
4.8	$[(CO_3)_i'' + V_O^{\bullet\bullet}] + E_{OT}$	-0.05	0.35
4.9	$(CO_3)_i'' + E_{OT} + V_O^{\bullet\bullet}$	4.23	4.99
4.10	$(CO_3)_i'' + E_{OT}$ - O_i''	-2.47	-1.97
4.11	$[(CO_3)_i'' + 2V_O^{\bullet\bullet}] + E_{OT}$ - $V_O^{\bullet\bullet}$	-3.24	-3.08
4.12	$\frac{1}{2}[(CO_3)_i'' + 2V_O^{\bullet\bullet}] + E_{OT} + \frac{1}{2}(CO_3)_i''$	0.49	0.96

Experimental investigations into the effects of carbonate defects on the phase stability of Ba_2TiO_4 were conducted by Trussov, Jarvis and Slater[242], the findings of which are now summarised. It was shown that the XRD diffraction patterns of β-Ba_2TiO_4 samples slowly cooled from 950 °C at 0.5 °C min^{-1} in N_2 remained unchanged, while similar heat treatment in air lead to a change from monoclinic to orthorhombic. However, such heat treatment in air resulted in large $BaCO_3$ and $BaTiO_3$ impurities, see figure 4.3. Samples heated in air at 450 °C for 8 hours also showed conversion to the orthorhombic phase, but with minimal $BaCO_3$ and $BaTiO_3$ impurity formation, figure 4.3.

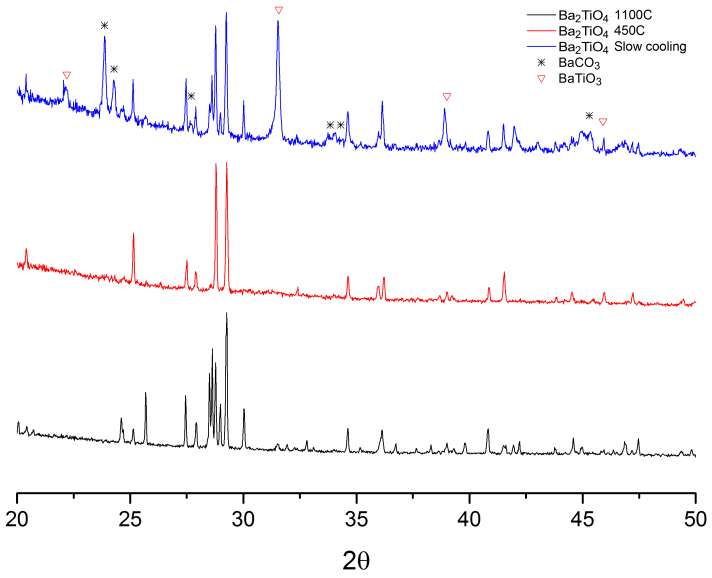

Figure 4.3: X-Ray diffraction patterns of Ba_2TiO_4 samples cooled from 950 °C at 30 °C min^{-1} to room temperature (blue), annealed at 450 °C for 8 hours in air (Red) and as prepared at 1100 °C in air and furnace cooled (Black).[242] Image used with the permission of experimental collaborator, Prof. Peter R. Slater, School of Chemistry, The University of Birmingham, Birmingham, UK.

Thermogravimetric analysis mass spectrometry, TG-MS, (under N_2) of the latter sample showed a small mass loss at 880 °C (figure 4.4a). Mass spectrometry identified the emission as CO_2, and suggested a composition of $Ba_2TiO_4{\cdot}0.09CO_2$ ($Ba_2TiO_{3.91}(CO_3)_{0.09}$). The second, much smaller, mass loss peak at 1040 °C was attributed to the partial decomposition of Ba_2TiO_4 to $BaCO_3$ and $BaTiO_3$ which reacted at the higher temperature to form Ba_2TiO_4 and CO_2. Following completion of the TG-MS run, the sample, now devoid of carbonate defects, returned to the monoclinic phase. TG-MS analysis of the sample slowly cooled from 950 °C in air (figure 4.4b) showed only a single mass loss peak in the high temperature region, primarily associated with the formation of Ba_2TiO_4 and CO_2 from $BaCO_3$ and $BaTiO_3$ impurities.[242]

In summary, the results presented in table 4.8 suggests that CO_2 incorporation is a favourable process in both pristine and doped Ba_2TiO_4. This suggests that carbonates are likely to be a common impurity defect in Ba_2TiO_4 based materials, especially those synthesised by the carbonate route. Furthermore, these results have also shown that oxide ion interstitial and vacancy defects are highly susceptible to carbonate based trapping. Therefore it is highly likely that carbonate defects, if present, will reduce the mobility of any oxide ion defects. However, care must be taken, as the E_{OT} term may be a non-trivial source of error. Finally, because carbonate defects are more stable in the α'-phase than the β-phase (table 4.8), the α'-phase may be stabilised by the presence of small concentrations of carbonate impurities, as supported by experimental work.[242]

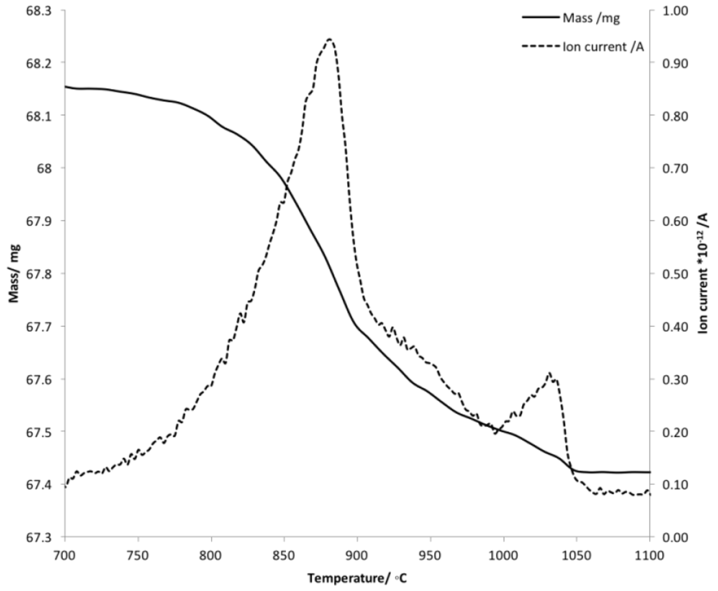

(a)

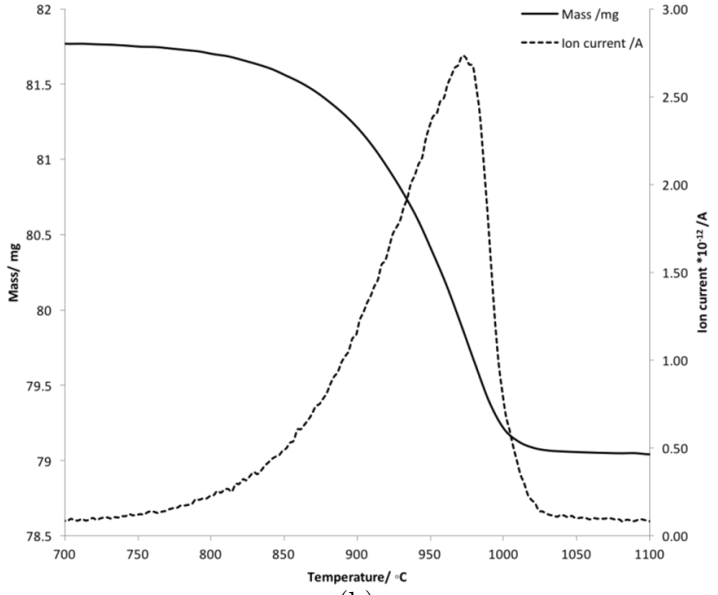

(b)

Figure 4.4: Thermogravimetric mass spectrometry analysis of a) α′-Ba_2TiO_4 prepared by annealing β-Ba_2TiO_4 at 450 °C for 8 hours in air and b) sample of Ba_2TiO_4 cooled from 950 °C at 30 °C min^{-1} to room temperature.[242] Image used with the permission of experimental collaborator, Prof. Peter R. Slater, School of Chemistry, The University of Birmingham, Birmingham, UK.

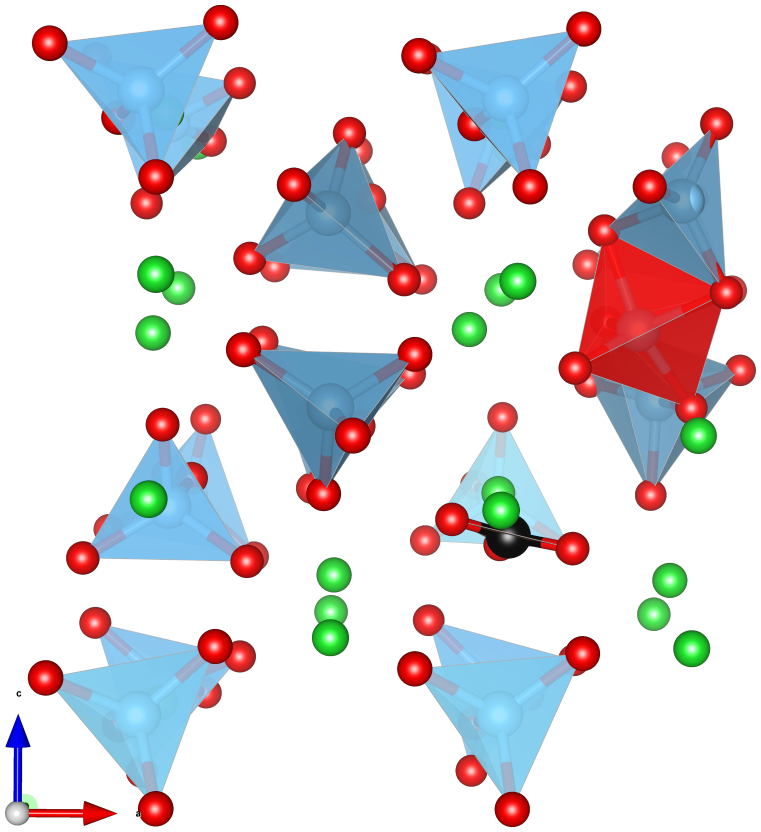

(a)

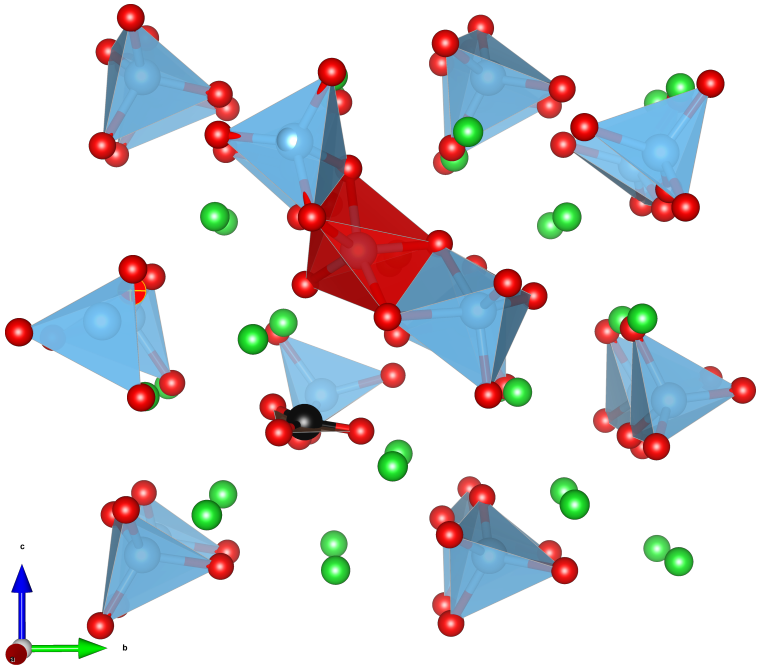

(b)

Figure 4.5: $[(CO_3)_i'' + 2V_O^{\bullet\bullet}]$ defect pair in α'-Ba_2TiO_4 viewed down the a) *b*-axis and b) *a*-axis. Green, blue, red and black spheres represent Ba, Ti, O and C respectively, and blue, red and brown polyhedra represent TiO_4, "TiO_3" and CO_3 units respectively.

4.4 Dopants

As evident from the numerous material discussions in chapter 1, aliovalent doping is a well-known, and commonly employed method for promoting the formation of defects in solid oxide materials. By applying these methods to Ba_2TiO_4, it may be possible to induce the formation oxygen defects. In this section, the abilities of mono- and trivalent dopants to promote the formation of oxygen defects in Ba_2TiO_4 will be assessed, the most likely incorporation mechanisms identified and their energies evaluated.

The relative favourability of a particular dopant and its incorporation mechanism can be established from its solution energy, which is calculated from its constituent isolated point defect energies and relevant lattice energies. It should be noted that the solution energies are calculated at infinite dilution using the Mott-Littleton method, and as such do not take into account defect-defect interactions. The implications of this assumption are discussed later in section 4.4.3. During the course of investigation, a broad range of mono and trivalent dopant ions on both of the cation sites and in both phases of Ba_2TiO_4 were investigated. Considering both constant-cation and constant-oxygen based methods of charge-compensation. In constant-cation mechanisms, such as equation 4.13, charge-compensation is achieved through the formation of oxide ion interstitials or vacancies. While constant-oxygen mechanisms are charge balanced by cation vacancies or interstitials, as seen in equation 4.14. Isovalent doping schemes were not considered as they did not offer a viable means to induce the formation of oxygen defects. All calculated solution energies can be found in tables B.1 to B.4 of the appendix.

For each of the two dopant regimes, M^+ and M^{3+}, different incorporation mechanisms were compared by plotting their calculated solution energies as a function of dopant radius. However, it should be noted that, unless specifically stated otherwise, six coordinate radii have been used in all such plots to aid comparison, and that radii for high-spin states have been used where applicable.[188] To improve the reliability of the calculations, interatomic potentials for each dopant were selected based on their compatibility with the oxygen interatomic potential and, when possible, were selected from the same reference sources to aid consistency. The compatibility of a dopant's interatomic potential was defined by the accuracy with which it could stably reproduce the dopant's binary oxide. References for each of the dopant interatomic potentials have been listed in table B.5 of the appendix.

4.4.1 Monovalent Dopants

Monovalent doping represents one of the possible ways in which oxygen defects might be introduced to the Ba_2TiO_4 structure. Monovalent substitution at either the Ba^{2+} or Ti^{4+} sites may result in the formation of charge balancing oxide ion vacancy defects, as shown in equations 4.13 and 4.15 respectively. However, it is also possible that the constant-oxygen mechanisms shown in equations 4.14 and 4.16 may be favoured instead. If so, cation interstitials, rather than oxide ion vacancies, would be formed to balance the charge.

Ba Site:

$$\frac{1}{2}M_2O + Ba_{Ba}^{\times} + \frac{1}{2}O_O^{\times} \rightarrow M'_{Ba} + \frac{1}{2}V_O^{\bullet\bullet} + BaO \tag{4.13}$$

$$\frac{1}{2}M_2O + Ba_{Ba}^{\times} \rightarrow M'_{Ba} + \frac{1}{2}Ba_i^{\bullet\bullet} + \frac{1}{2}BaO \tag{4.14}$$

Ti Site:

$$\frac{1}{2}M_2O + Ti_{Ti}^{\times} + \frac{3}{2}O_O^{\times} \rightarrow M'''_{Ti} + \frac{3}{2}V_O^{\bullet\bullet} + TiO_2 \tag{4.15}$$

$$\frac{1}{2}M_2O + Ti_{Ti}^{\times} \rightarrow M'''_{Ti} + \frac{3}{4}Ti_i^{\bullet\bullet\bullet\bullet} + \frac{1}{4}TiO_2 \tag{4.16}$$

The alkali metal cations Li^+, Na^+, K^+ and Rb^+ were selected for investigation based on size, cost, stability or availability considerations. The calculated solution energies for the substitution of these dopants onto the Ba_I^{2+} and Ti^{4+} sites of β-Ba_2TiO_4 following equations 4.13 to 4.16 are plotted against dopant radius in figure 4.6.

Examination of this plot clearly shows that there is a substantial energetic preference (> 10 eV) for Ba^{2+}, over Ti^{4+}, site substitution mechanisms. This is to be expected given that monovalent ions are considerably closer in both ionic radii and charge to Ba^{2+} than they are Ti^{4+}. Results also suggest that constant-cation stoichiometry is favoured by ∼1.5 eV, indicating that oxide ion vacancies are likely to form as a result of monovalent doping. Of the two β-Ba_2TiO_4 Ba^{2+} sites, substitution at the larger seven coordinate Ba_I^{2+} site was favoured by all four monovalent dopants (by 0.5-0.7 eV). Furthermore, it is seen that the favourability of incorporation increases as the dopant's radii approaches that of Ba_I^{2+}. The lowest solution energy for monovalent doping of the Ba_I^{2+} site is found for K^+. This is due to its similarity in size (1.46 Å) to the Ba_I^{2+} site (1.38 Å).[243] Both the proposed mechanism and site selectivity of the dopants agrees well with analogous investigations of the isostructural material β-Ca_2SiO_4.[224]

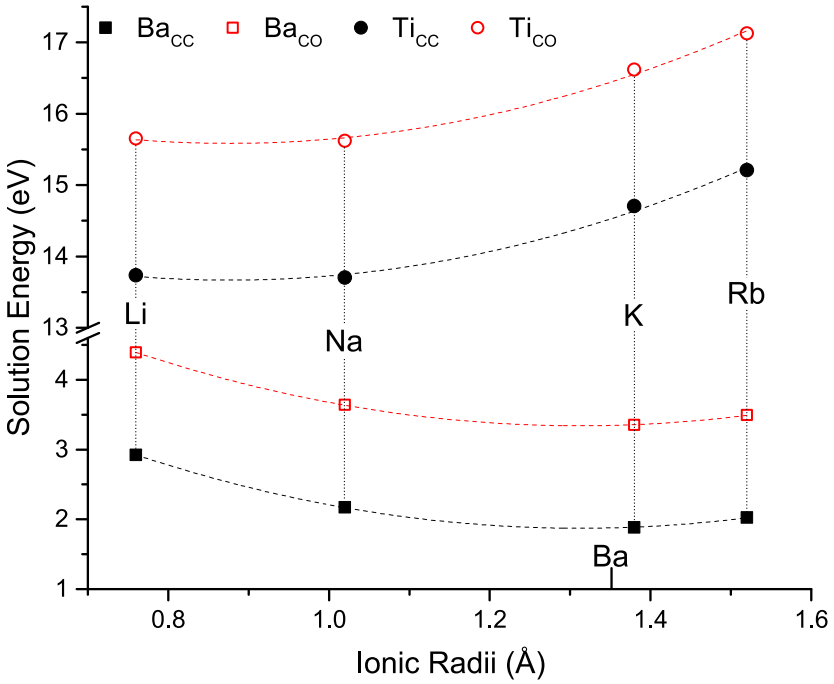

Figure 4.6: Solution energies for M^+ doping of Ba_I & Ti sites in β-Ba_2TiO_4 *via* mechanisms 4.13 (Ba_{CC}), 4.14 (Ba_{CO}), 4.15 (Ti_{CC}) and 4.16 (Ti_{CO}), additional tick indicates Ba's radius.

Repeating this process for the α′-phase of Ba_2TiO_4 yields identical results in terms of site and mechanistic selectivity. However, constant-cation substitutions for the ions Na^+, K^+ and Rb^+ are found to be 0.14, 0.24 and 0.30 eV more favourable respectively, for the Ba^{2+}_{III} site. The increased ease with these ions can be incorporated is due to the larger size of the β-Ba^{2+}_I like Ba^{2+}_{III} sites of the α′-phase. This suggests that doping Ba_2TiO_4 with such ions may act to stabilise the α′-phase down to room temperature.

The above results tend to suggest that monovalent doping of Ba_2TiO_4 is not only feasible, but will result in the formation of oxide ion vacancy defects. However, experimental attempts by Chen *et al.*[215] to synthesise Na^+ doped Ba_2TiO_4 were met with limited success. They suggest that rather than entering the Ba_2TiO_4 lattice, Na_2O sublimates, as its melting point (1134 °C) is lower than the synthesis temperature (1250 °C). This effect would only be compounded for K^+, as its binary oxide has a significantly lower melting point of 740 °C.[188] However, synthesis of K^+ doped Ba_2TiO_4 may be achievable through the use of K_2TiO_3, which has a significantly higher melting point of 1515 °C, and so may be less prone to loss of reactant.[188] Alternative low temperature synthesis routes, such as the reverse-micellar route, may also offer a viable solution.[217]

4.4.2 Trivalent Dopants

Of those considered, the trivalent doping regime is the most flexible series of dopants for Ba_2TiO_4. This regime's flexibility stems from the diverse nature of its ions, whose ionic radii range in size from 0.5 (Al^{3+}) to 1.0 Å (La^{3+}). This means that trivalent ions may be accommodated at either native cation site. Therefore, trivalent doping potentially offers multiple routes towards oxygen defect formation, and so warrants investigation.

The substitution of a diverse range of trivalent ions on both the Ba^{2+} and Ti^{4+} sites of Ba_2TiO_4 were considered. Larger ions, such as La^{3+}, were selected as they are likely to favour the Ba^{2+} sites. Likewise, smaller ions, such as Al^{3+}, were selected for Ti^{4+} site substitutions. The mechanisms by which these substitutions occur are detailed below.

The first mechanism, shown in equation 4.17, represents the constant-cation trivalent doping of a Ba^{2+} site ($M^{\bullet}_{Ba}$) coupled with the formation of a charge compensating oxide ion interstitial defect (O''_i). The second, shown in equation 4.18, is the constant-oxygen stoichiometry variant in which charge compensating cation vacancies (V''_{Ba}) form instead. Equations 4.19 and 4.20 represent the constant-cation and constant-oxygen Ti^{4+} site (M'_{Ti}) substitution mechanisms respectively. In the former, charge compensating oxide ion vacancies ($V^{\bullet\bullet}_{O}$) form, and in the latter, cation interstitials ($Ti^{\bullet\bullet\bullet\bullet}_i$).

Ba Site:

$$\frac{1}{2}M_2O_3 + Ba^{\times}_{Ba} \rightarrow M^{\bullet}_{Ba} + \frac{1}{2}O''_i + BaO \tag{4.17}$$

$$\frac{1}{2}M_2O_3 + \frac{3}{2}Ba^{\times}_{Ba} \rightarrow M^{\bullet}_{Ba} + \frac{1}{2}V''_{Ba} + \frac{3}{2}BaO \tag{4.18}$$

Ti Site:

$$\frac{1}{2}M_2O_3 + Ti^{\times}_{Ti} + \frac{1}{2}O^{\times}_{O} \rightarrow M'_{Ti} + \frac{1}{2}V^{\bullet\bullet}_{O} + TiO_2 \tag{4.19}$$

$$\frac{1}{2}M_2O_3 + Ti^{\times}_{Ti} \rightarrow M'_{Ti} + \frac{1}{4}Ti^{\bullet\bullet\bullet\bullet}_i + \frac{3}{4}TiO_2 \tag{4.20}$$

The calculated solution energies for the trivalent doping of β-Ba_2TiO_4 *via* the mechanisms shown in equations 4.17 - 4.20 are plotted in figures 4.7 and 4.8 against ionic radii. As expected, ions greater than or equal in size to In^{3+} prefer to substitute at the Ba^{2+} site, while those that are smaller favour Ti^{4+} site substitutions. Due to their size, the dopants Al^{3+} and La^{3+} are found to yield the lowest solution energies for the Ti^{4+} and Ba^{2+} site substitution mechanisms respectively. Of the two Ba^{2+} sites in β-Ba_2TiO_4, the trivalent ions favour the smaller Ba^{2+}_{II} sites, by ∼0.3 eV, in which they are able to attain an almost regular octahedral geometry, similar observations have been made by Guo *et al.*[224] for trivalent dopants in the isostructural material β-Ca_2SiO_4. Calculations

show that Ti^{4+} site substitutions favour constant-cation stoichiometry by 0.6 eV, and Ba^{2+} site substitutions favour constant-oxygen stoichiometry by 0.2 eV. This suggests that trivalent doping of the Ti^{4+} sites will result in the formation of O-vacancies, while doping of the Ba^{2+} sites will form Ba-vacancies, in accord the with behaviour reported for the isostructural material β-Ca_2SiO_4 where interstitial defects are reported to be high in energy.[224] Specific details regarding the trivalent doping of the Ba^{2+} and Ti^{4+} sites will now be discussed in turn below.

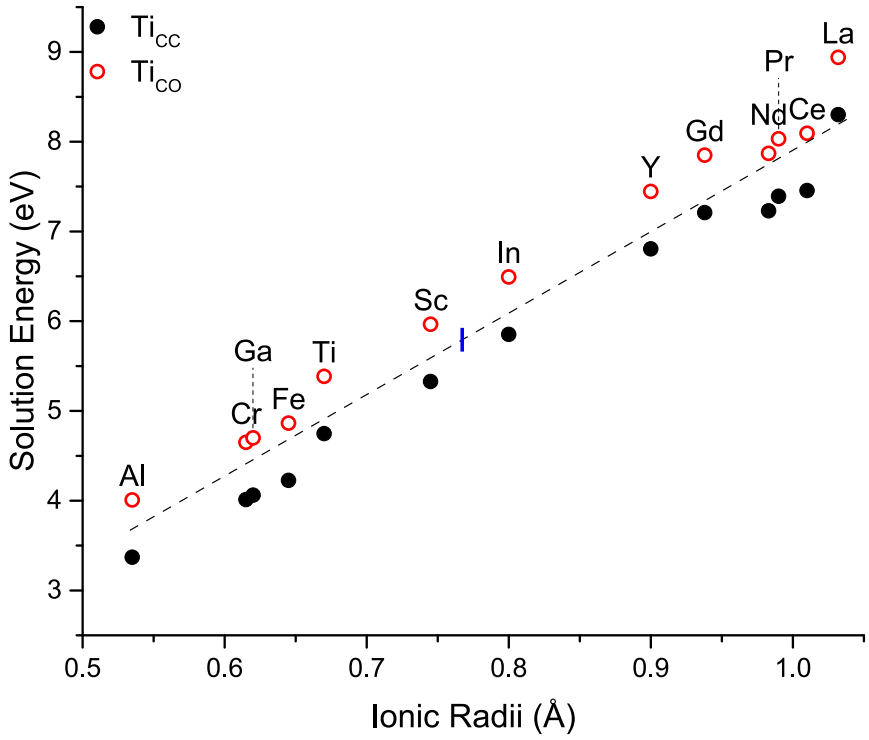

Figure 4.7: Solution energies for the trivalent Ti site doping of β-Ba_2TiO_4 *via* mechanisms 4.19 (Ti_{CC}) and 4.20 (Ti_{CO}). Blue bar indicates the crossover point of the trend-lines in figures 4.7 and 4.8.

It has been shown from the above discussion that doping of the Ti^{4+} sites with small trivalent ions, such as Al^{3+}, offers a possible route towards oxide ion vacancy defect formation and therefore the enhancement of oxide ion conductivity. However, previous discussions suggested that oxide ion vacancy defects may not be mobile in the Ba_2TiO_4 lattice, as they may become trapped by carbonate impurities. Furthermore, small trivalent dopants on the α′-phase Ti^{4+} sites were found to be only 0.04 eV lower in energy that those in the β-phase. It is therefore unlikely that such dopants will significantly favour the stabilisation of one phase over the other.

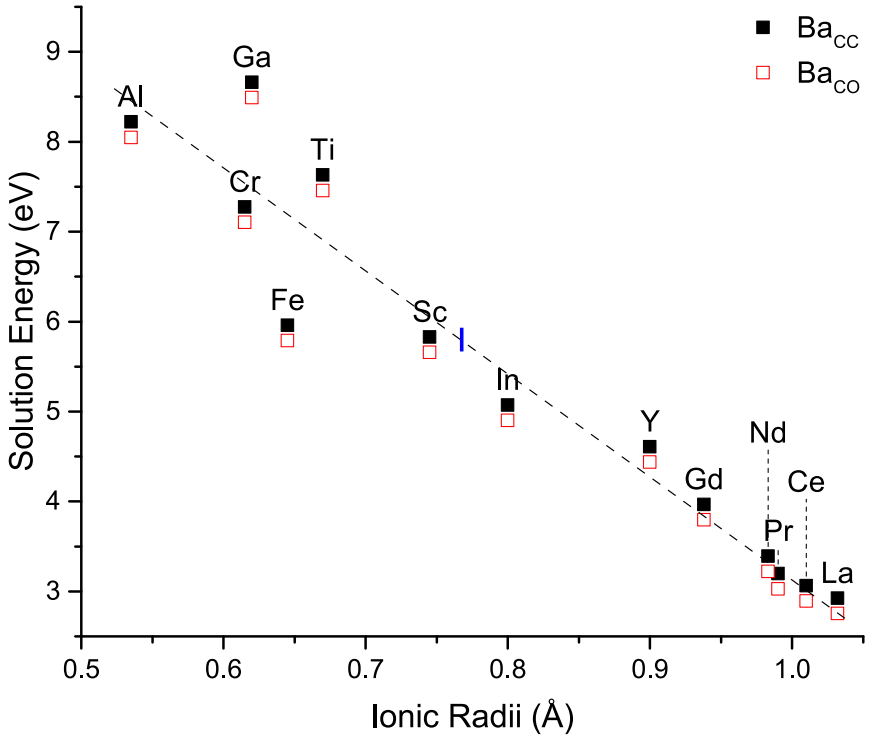

Figure 4.8: Solution energies for the trivalent Ba_{II} site doping of β-Ba_2TiO_4 *via* mechanisms 4.17 (Ba_{CC}) and 4.18 (Ba_{CO}). Blue bar indicates the crossover point of the trend-lines in figures 4.7 and 4.8.

In contrast to the Ti^{4+} site substitutions, the Ba^{2+} site substitutions are found to be much more stable in the α′-phase than the β-phase, with solution energy differences of ∼0.5 eV, suggesting that the α′-phase may be stabilised over the β-phase at lower temperatures by the presence large trivalent dopants. This agrees well with the experimental work conducted by Chen *et al.*[215], which showed even small levels of Nd^{3+} doping (0.75% Ba site substitution) stabilises the α′-phase down to room temperature. They also reported that the solubility and long term stability of Nd^{3+} in Ba_2TiO_4 is quite low and that such ions tend to drop out of solution. Furthermore, it is unlikely that significant quantities of oxygen defects will be formed as a result of Ba^{2+} site substitutions as constant-oxygen stoichiometry is energetically favoured. If CO_2 is present, then a carbonate defect could form in place of the oxide ion interstitial in mechanism 4.17. Although this would lower the solution energy by 1.4 eV it would result in the interstitial becoming trapped within a carbonate group. Finally, charge compensation through the reduction of Ti^{4+} to Ti^{3+} was also considered, however, such mechanisms were found to be high in energy and so were not considered further.

To summarise, large trivalent ions such as La^{3+} prefer Ba site substitutions and favour the α'-phase, while smaller ions like Al^{3+} prefer Ti^{4+} site substitutions, but have no phase preference. Results also suggest that only Ti^{4+} site substitutions are likely to form oxygen defects, whereas Ba^{2+} site substitutions form cation vacancies to compensate charge. Therefore, trivalent doping of the Ti^{4+} sites with small ions such as Al^{3+} is suggested to be a likely route towards oxide ion vacancy defect formation.

4.4.3 Defect Clustering

In the previous calculations, defects were treated as isolated species and did not interact with one another. However, it is known that defects, particularly those of opposite charge, generally tend to associate with one another.[172] These defect-defect interactions, which are determined by coulombic forces and lattice relaxations, can significantly affect defect mobility and could result in ion trapping.[60,171] Therefore, an understanding of defect clustering behaviour will be important when selecting a suitable dopant for the enhancement of ionic conductivity. In discussions which follow, the methods described in section 2.7 will be employed to investigate the clustering of monovalent and trivalent dopants to oxide ion vacancy defects in Ba_2TiO_4. Discussions regarding defect clustering behaviour will focus on the trivalently doped systems first due to their diminished complexity, before moving on to the monovalently doped systems.

Trivalent Clusters

In section 4.4.2 it was shown that small trivalent dopants are likely to substitute aliovalently onto the Ti^{4+} sites of the Ba_2TiO_4 lattice, resulting in the formation of charge compensating oxide ion vacancy defects. Of those examined, the dopants Al^{3+}, Cr^{3+} and Ga^{3+} present the lowest solution energies due to their similarity in size to Ti^{4+}. Both Al^{3+} and Ga^{3+} were selected for investigation due to their low solution energies, known existence in tetrahedral environments, experimental precedence in the similarly structured material Ba_2GeO_4 and to elucidate the effects of size on defect clustering behaviour.[244]

As detailed in equation 4.19, one oxide ion vacancy ($V_O^{\bullet\bullet}$) is formed for every two trivalent dopants (M'_{Ti}) to maintain charge neutrality. Therefore, the simplest charge neutral defect cluster would consist of a single oxide ion vacancy and a pair of neighbouring dopant ions ($2M'_{Ti}{:}V_O^{\bullet\bullet}$). A sequence of such clusters were generated by introducing two dopants and an oxide ion vacancy to random Ti^{4+} and O^{2-} sites respectively, in a β-Ba_2TiO_4 cell. The clusters were then relaxed using the Mott-Littleton method, their binding energies calculated and the most stable of them identified.[§] Before further examining and comparing the clustering behaviours of the two dopant systems, a brief description of their most stable cluster structure will be given. When positioned on nearest neighbouring sites to one another the dopant ions form "M_2O_7" like defect groups. The oxygen bridged "M_2O_7" defect structure, shown in figure 4.9, is formed as a result of the oxygen deficient "MO_3" "tetrahedra" migrating out of its channel towards its nearest MO_4 unit.

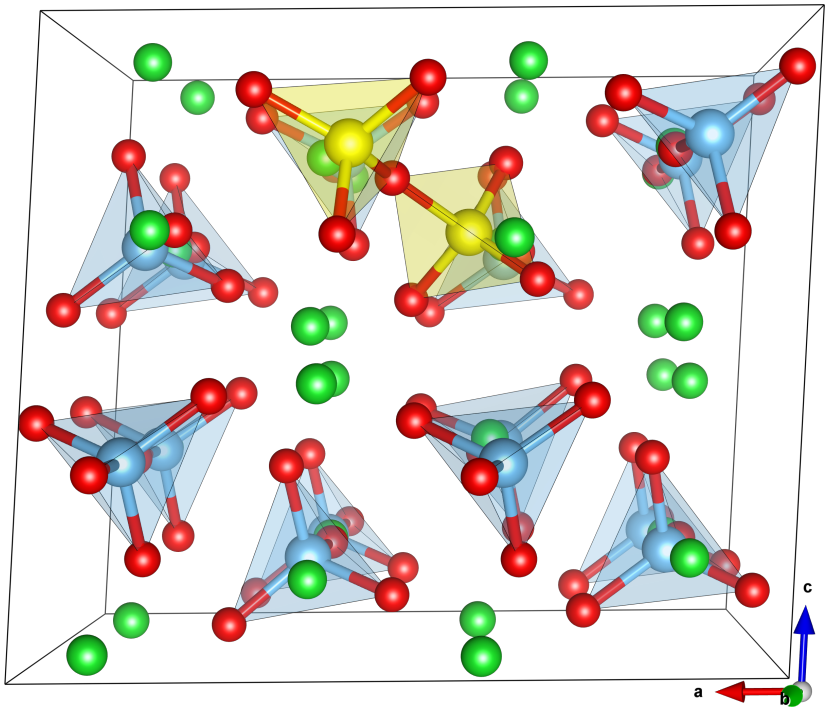

Figure 4.9: β-Ba_2TiO_4 containing the most stable $2Al'_{Ti}{:}V_O^{\bullet\bullet}$ cluster: blue, green, red and yellow spheres represent Ti, Ba, O and Al ions respectively, blue and yellow polyhedra correspond to TiO_4 and "Al_2O_7" units respectively.

[§]Using Mott-Littleton region *a* and *b* sizes of 17 and 29 Å respectively.

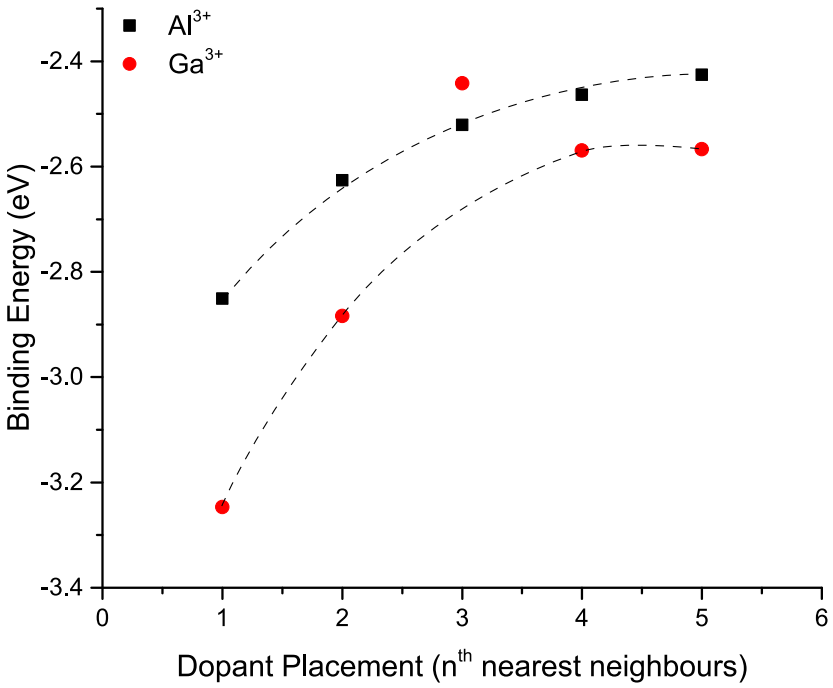

(a)

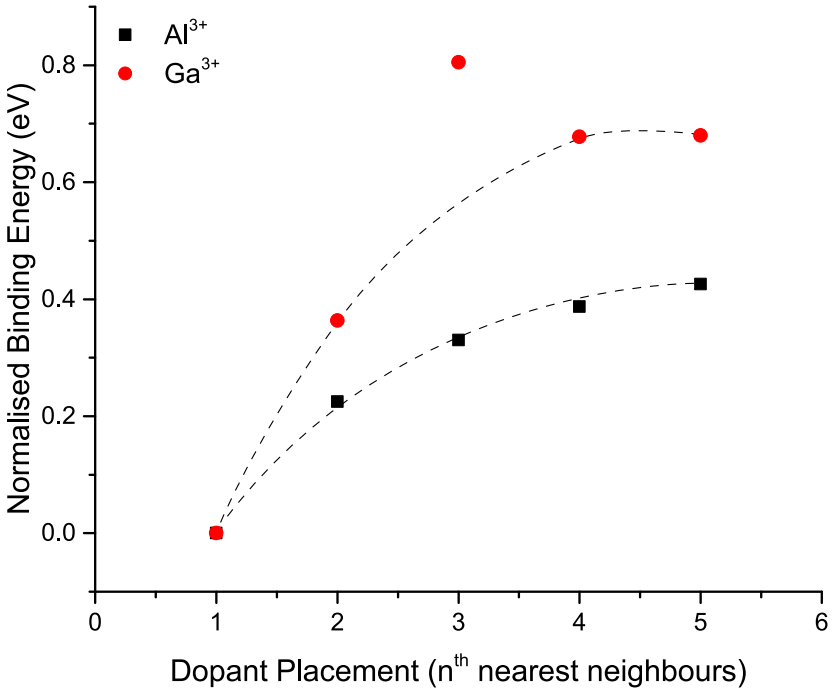

(b)

Figure 4.10: The a) defect binding energies of $2M'_{Ti}$:$V_O^{\bullet\bullet}$ clusters as a function of dopant separation, b) the same points normalised to the lowest energy value. $V_O^{\bullet\bullet}$ is located in one of the doped tetrahedra in each instance, this represents the lowest energy structure attainable for a given dopant separation distance.

The binding energies of the five most clustered conformations, as defined by dopant-dopant separation distance, are plotted in figure 4.10a and listed in table B.6 of the appendix. Binding energies were found to be lowest when the dopants resided on nearest neighbouring sites to one another and generally tended to increase with dopant separation distance. Furthermore, conformations with large or infinite dopant-oxide ion vacancy separation distances always exhibited comparatively large, and often positive, binding energies. Binding energies of -2.85 and -3.25 eV are calculated for the most favourable Al^{3+} and Ga^{3+} based defect clusters structures respectively. The sign and magnitude of these values strongly suggests that oxide ion vacancies and dopants will aggressively cluster together. It is therefore unlikely that such defects will exist as isolated species in the Ba_2TiO_4 lattice, particularly at high defect concentrations. Calculated binding energies for the Ga^{3+} based defect clusters are generally found to be lower in energy than their Al^{3+} based counterparts. This suggests that the drive towards defect clustering is greater in Ga^{3+} doped systems. Furthermore, the normalised binding energies, plotted in figure 4.10b, show that more energy is required in the Ga^{3+} based systems to transition from the most clustered conformation to a less clustered one. This suggests that defect movement might be more constrained in Ga^{3+} doped Ba_2TiO_4 systems.

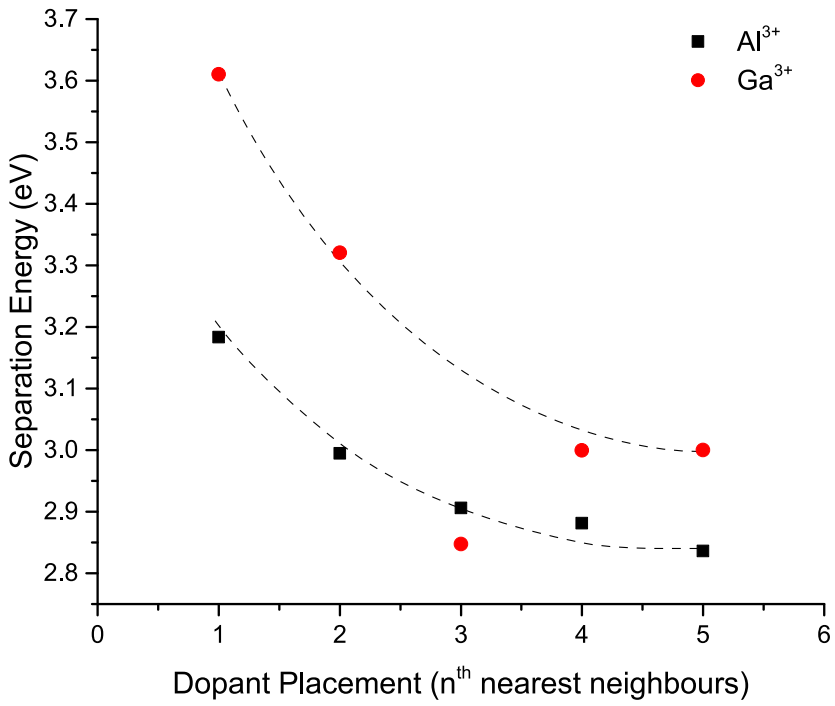

Figure 4.11: Oxide ion vacancy separation energies for the most stable Al^{3+} and Ga^{3+} $2M'_{Ti}{:}V^{\bullet\bullet}_{O}$ clusters plotted as a function of dopant separation.

Although binding energies are an approximate indicator of the extent to which an oxide ion vacancy may become trapped, it is more appropriate to consider the vacancy separation energy. This represents the energy required to remove an oxide ion vacancy from its cluster to infinity. The separation energy is calculated as the difference in binding energy between a cluster with and without its oxide ion vacancy. The calculated vacancy separation energies for the $2M'_{Ti}{:}V^{\bullet\bullet}_{O}$ clusters are presented in figure 4.11. This shows that oxide ion vacancy defects are strongly bound to their respective clusters, and that binding is greater in the Ga^{3+} based clusters. This, coupled with the above findings suggests that oxygen defect mobility, and therefore oxide ion conductivity, is likely to be lower in the Ga^{3+} doped systems.

As the previously discussed dopant solution energies were calculated assuming infinite dilution they do not take into account the additional stabilisation energy arising from defect-defect interactions. This results in an overestimation of the solution energies due to the non-trivial nature of such interactions. To correct for this, the binding energies were added to their respective solution energies. Following the addition of the relevant binding energies, the dopant solution energies for Al^{3+} (3.33 eV) and Ga^{3} (4.03 eV) drop to more favourable values of 1.90 and 2.41 eV respectively.

In summary, clustering between small trivalent dopants and oxide ion vacancy defects has been found to be a highly favourable process. The favourability of this process acts to lower the solution energies of small trivalent dopant ions. However, the large binding and separation energies suggest that trapping of the oxygen defects by the trivalent dopants is highly likely. Of the two trivalent dopants considered, calculations revealed Al^{3+} to be the most suitable, due to its less aggressive defect trapping behaviour.

Monovalent Clusters

The calculations detailed in section 4.4.1 suggests monovalent doping is another route by which oxide ion vacancy defects can be formed. However, unlike the small trivalent ions discussed above, the monovalent ions substitute onto the Ba^{2+}_{I} sites rather than the tetrahedral Ti^{4+} sites, shown in figure 4.6. As such, they will cluster differently. The monovalent dopants Na^{+}, K^{+} and Rb^{+} were selected for defect clustering analysis as they showed the most favourable solution energies.

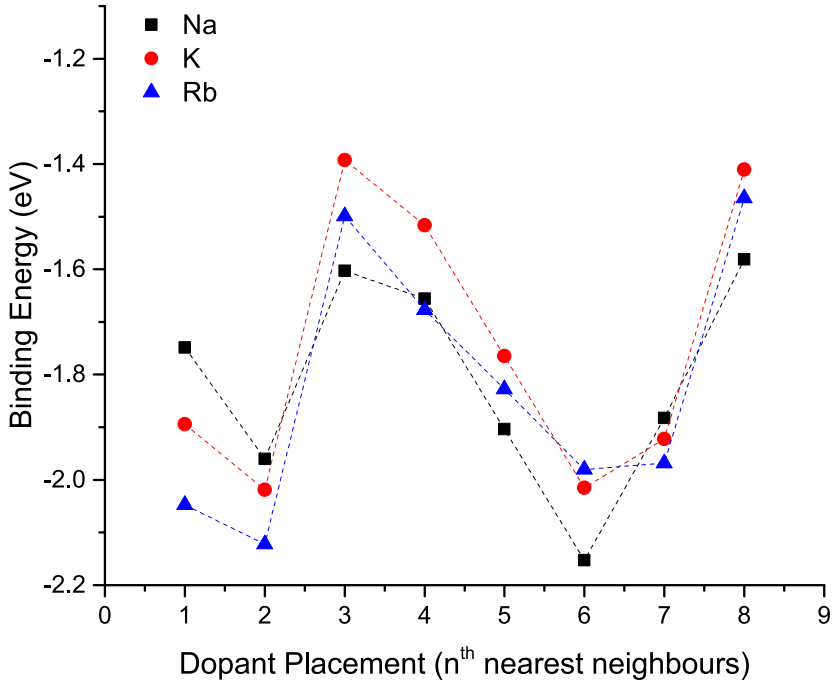

(a)

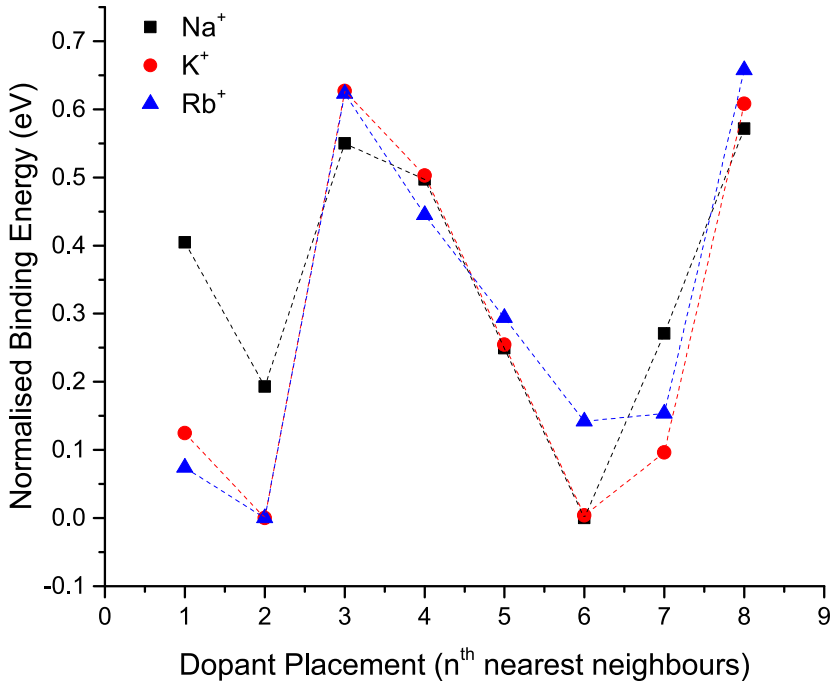

(b)

Figure 4.12: The a) defect binding energies of $2M'_{Ba_I}$:$V_O^{\bullet\bullet}$ clusters as a function of dopant separation, b) the same points normalised to the lowest energy value of each series. $V_O^{\bullet\bullet}$ relaxed to its lowest energy position in each cluster, commonly close to one or both dopants.

In a method similar to that used for the trivalent ions, calculations were carried out on defect clusters comprised of two monovalent dopants and a single oxide ion vacancy ($2M'_{Ba_I}{:}V^{\bullet\bullet}_{O}$). These represent the smallest charge neutral defect clusters in accordance with equation 4.13. Eight defect clusters were generated in which the two dopants were placed on nearest neighbouring Ba_I^{2+} sites, 2^{nd} nearest neighbouring Ba_I^{2+} sites, 3^{rd} nearest neighbouring Ba_I^{2+} sites and so on. The oxide ion vacancy was then trialled at different sites to identify its optimal position within the cluster. The calculated binding energies for these clusters are plotted in figure 4.12, are listed in table B.7 of the appendix and discussed in the paragraphs to follow. It should be noted that in this context the phrases "(1^{st}) nearest neighbouring", "2^{nd} nearest neighbouring", "3^{rd} nearest neighbouring" and so on are used to indicate "dopant-A on the closest possible site to dopant-B", "dopant-A on the second closest site to dopant-B" and "dopant-A on the third closest site to dopant-B" respectively. Unless explicitly stated otherwise it should be assumed that the conformation reported for a particular dopant - dopant arrangement is that which presented the lowest energy of all oxide ion vacancy sub-configurations tested. It should also be assumed that the oxide ion vacancy is located near one or both dopants in all such cases.

Firstly, calculations conducted on conformations with oxide ion vacancies proximal to their dopants were always found to be lower in energy than those with distant or isolated oxide ion vacancies. From plot 4.12a it can be seen that monovalent defect clustering is a highly favourable process. However, it is also immediately clear that the binding energies do not correlate particularly well with dopant-dopant site separation. This is because the density of the cluster does not necessarily correspond directly to dopant-dopant separation distance. In all conformations, oxide ion vacancy defects were accommodated through the formation of asymmetrical "Ti_2O_7" groups between pairs of nearest neighbouring $TiO_{4/3}$ units. In order for this to form, the oxygen deficient "TiO_3" "tetrahedra" is require to migrate away from its natural lattice site and towards the nearest neighbouring oxygen stoichiometric TiO_4 tetrahedra. This creates a large pocket of reduced oxygen density around the original site of the migratory "TiO_3" unit, and a second much smaller one near the natural O_I lattice site of the nearest neighbouring TiO_4 unit, which has undergone slight reorientation to accommodate "Ti_2O_7" formation. Therefore, what might be considered the most clustered conformation is likely to be one in which the dopants reside on the sites closest to the pockets of reduced oxygen density.

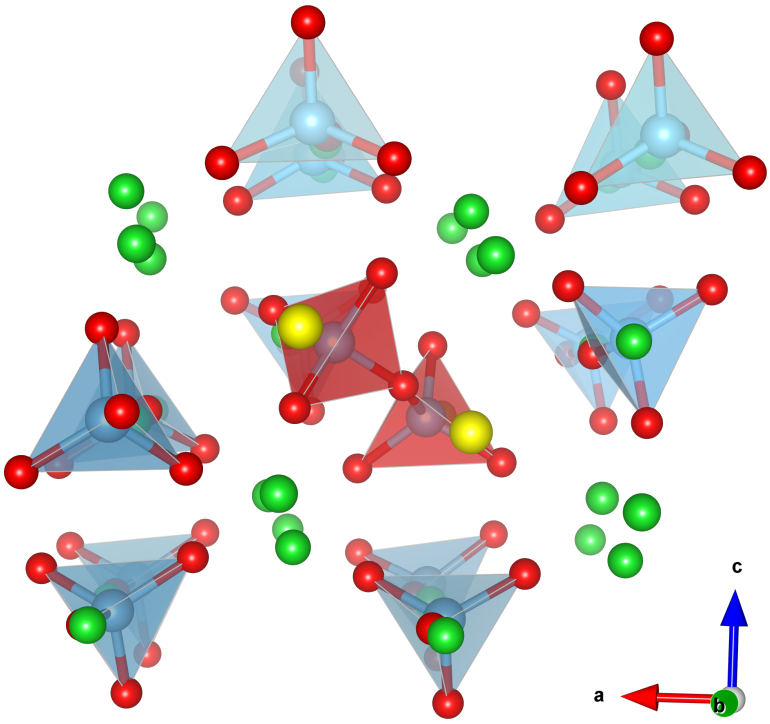

Figure 4.13: β-Ba_2TiO_4 containing the most stable $2Rb'_{Ba_I}$:$V^{\bullet\bullet}_O$ cluster with dopants on 2^{nd} nearest neighbouring sites: blue, green, red and yellow spheres represent Ti, Ba, O and Rb ions respectively, blue and red polyhedra correspond to TiO_4 and "Ti_2O_7" units respectively.

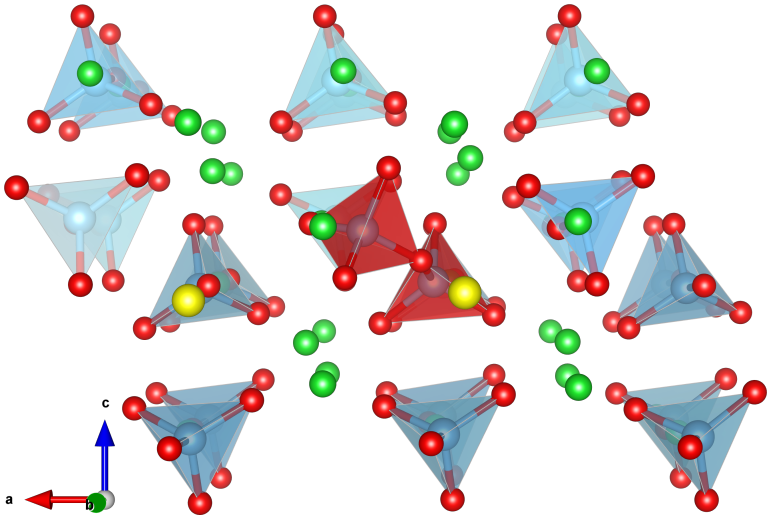

Figure 4.14: β-Ba_2TiO_4 containing the most stable $2Na'_{Ba_I}$:$V^{\bullet\bullet}_O$ cluster with dopants on 6^{th} nearest neighbouring sites: blue, green, red and yellow spheres represent Ti, Ba, O and Na ions respectively, blue and red polyhedra correspond to TiO_4 and Ti_2O_7 units respectively.

The structure of the most energetically favourable Rb^+ based defect cluster is shown in figure 4.13. In this conformation the dopants reside on 2^{nd} nearest neighbouring sites to one another, which allows them to occupy sites close to the pockets of reduced oxygen density and therefore close to the oxide ion vacancy. While such sites are electrostatically favourable, one is highly distorted due to its diminished coordination sphere. Although these distorted sites can accommodate, and even prefer the larger Rb^+ ions over the native Ba^{2+} ions, the same cannot be said for the smaller Na^+ ions. The smaller Na^+ ions prefer the conformation shown in figure 4.14 where the dopants reside on 6^{th} nearest neighbouring sites with respect to one another. On the other hand, K^+, being similar in size to Ba^{2+} , is equally stable in both 2^{nd} and 6^{th} nearest neighbouring configurations, these being the joint most favourable configuration. Such multi-configurational stability could suggest increased structural flexibility and perhaps defect mobility.

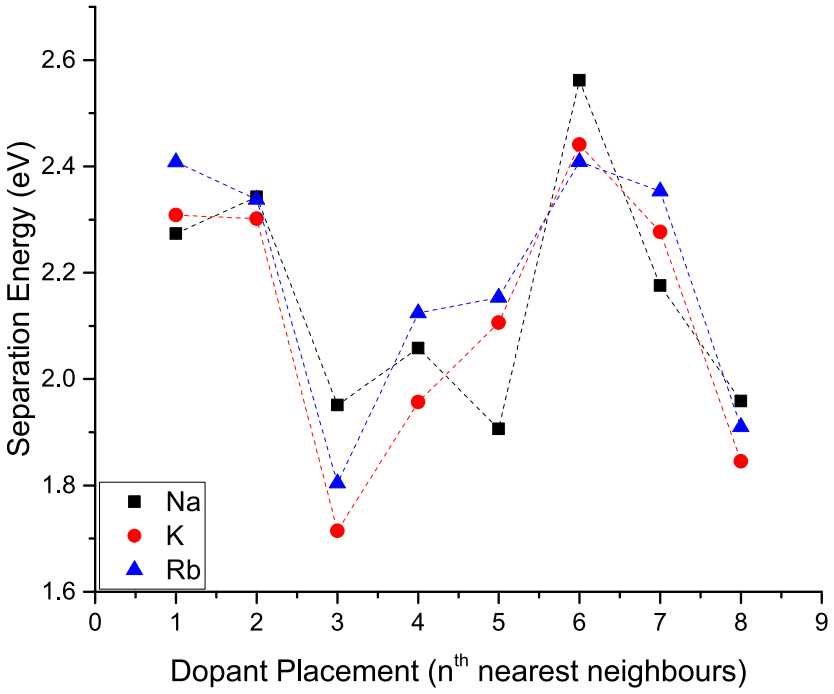

Figure 4.15: Oxide ion vacancy separation energies for $2M'_{Ba_{II}}{:}V^{\bullet\bullet}_{O}$ clusters plotted as a function of dopant separation.

While the binding energies suggest that the drive towards defect clustering will be less in systems doped with K^+ than those with Na^+ or Rb^+, the overall drive will still be significant. Unlike those for the small trivalent ions, the normalised binding energies, displayed in figure 4.12b, do not suggest that oxide ions are likely to be significantly more mobile in one doped system than the others. The oxide ion vacancy separation energies for the monovalent clusters are plotted in figure 4.15. These values are calculated to

be 2.56, 2.37 and 2.34 eV for the most stable Na^+, K^+ and Rb^+ clusters respectively (K^+ value = average of the two best sites). Although slightly higher for Na^+, these values are all non-trivial and suggest that clustering effects will significantly reduce the mobility of oxide defects possibly leading to their trapping.

As previously discussed, binding energies can be used as correctional terms for the dopant incorporation energies. Corrected solution energy values of 0.96, 0.63 and 0.66 eV were calculated for the monovalent substituents Na^+, K^+ and Rb^+ respectively. This corresponds to a ∼1.00 eV increase in favourability, and supports the viability of such dopants.

The above results have shown that defect clustering is a highly favourable process in both monovalently and trivalently doped Ba_2TiO_4 systems. While this reduces the energy required for defect incorporation it also increases the likelihood of ion trapping. The magnitude of the calculated oxide ion vacancy separation energies suggests the mobility of such defects will be low and the probability of their trapping high. Of the those examined, results suggest Al^{3+} and K^+ to be the most suitable of the trivalent and monovalent dopants respectively. Furthermore, the oxide ion defects are likely to be more mobile in the monovalently doped systems as their separation energies are more than 0.80 eV smaller than their trivalent counterparts. These findings have been verified and further expanded on using molecular dynamics simulations, discussed henceforth.

4.5 Oxide Ion Migration

The high intrinsic defect formation energies, calculated in section 4.2, strongly suggests that pristine Ba_2TiO_4 is likely to be a poor oxide ion conductor. However, it was also suggested that the formation of oxide ion vacancy defects could be brought about through monovalent or trivalent doping. In this section, molecular dynamics simulations have been employed to assess the impacts of 10% monovalent and 10% trivalent doping on oxide ion conduction in Ba_2TiO_4. The dopants selected for investigation are based on those used in the defect clustering analyses, Al^{3+}, Ga^{3+}, Na^+ and K^+. However, Rb^+ was omitted as its likely to undergo sublimation during synthesis due to the low melting point of its binary oxide.[188,215] Key simulation details will now be given and will be followed by discussions of the results.

Molecular dynamic simulations were performed on 6×5×4 supercells (3360 ions) at the temperature range 873 - 1473 K in steps of 100 K. The doped systems were generated by introducing 24 randomly placed $2M'_{Ti/Ba_I}:V^{\bullet\bullet}_O$ defect clusters per supercell. Two random configurations were run for each system to help mitigate the bias of the starting configuration on the final results. Systems were equilibrated at zero kelvin before simulating for a further 3 ns under NST conditions to allow for thermal expansion of the cell. Oxygen shells, with a mass of 1.6 amu, were included using the adiabatic model. The final production runs were carried out under NVT conditions for 6 ns with a 0.5 fs time step. The results of these simulations were then analysed using the methods described in section 2.9. These results of these simulations are detailed and discussed below.

Before discussing oxide ion migration, the molecular dynamic observations made regarding Ba_2TiO_4's phase behaviour will be discussed and compared to experiment. As previously stated, Ba_2TiO_4 has two phases, a low temperature β-phase and a high temperature α′-phase. As these are monoclinic and orthorhombic respectively the phase of the material during simulation can easily be identified from the β-angle, which is ∼93° for the former and 90° for the latter.[212,214] A plot of the β-angle for pristine Ba_2TiO_4 at different temperatures, figure 4.16a, suggests the transformation from low to high temperature phase occurs at 373-398 K. This is in reasonable agreement with the X-ray powder diffraction measurements conducted by Chen *et al.* who reports a phase transformation temperature range of 373-473 K, as indicated by the grey region in figure 4.16a.[215] In difference to this, Lee *et al.* reported the transformation to occur at 983 K.[216] However, the -0.5% volumetric shift they measure using dilatometry during heating and cooling, and report to indicate phase transformation, is not observed in the these simulations, figure 4.16b. Due to the grain size effect discussed in the introduction to Ba_2TiO_4, discrepancies in the experimental phase transformation temperatures are not unexpected.[215,217] As the simulated systems studied are small compared to experiment such effects are not likely to be significant. The simulated results are in good agreement with those by Chen *et al.*, suggesting their results are more likely closer to what might be expected from a small single crystal than those by Lee *et al.*, whose high values may be a consequence of the grain size effect. However, if this were the case transformation on cooling would be unlikely, suggesting other impurity effects may also be partly responsible for the high temperature changes.

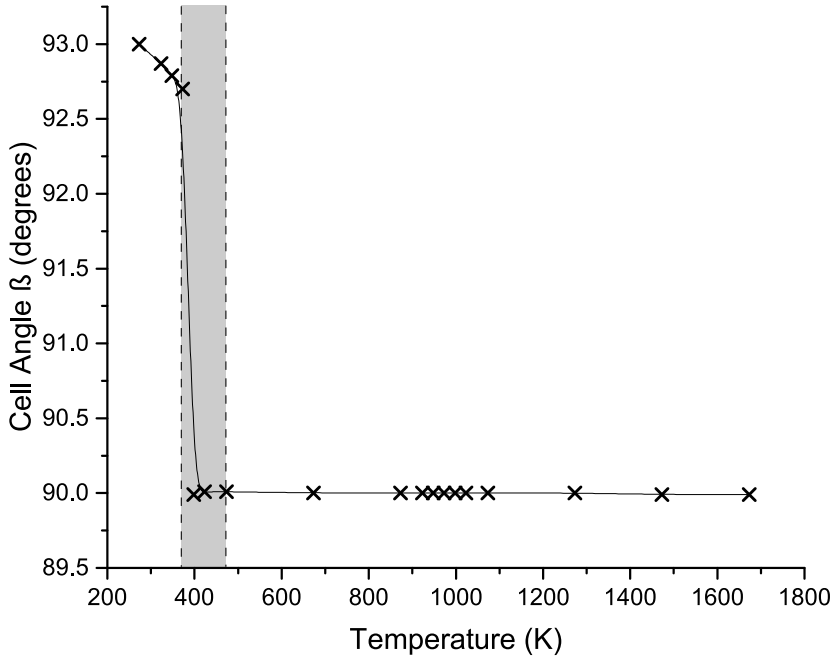

(a)

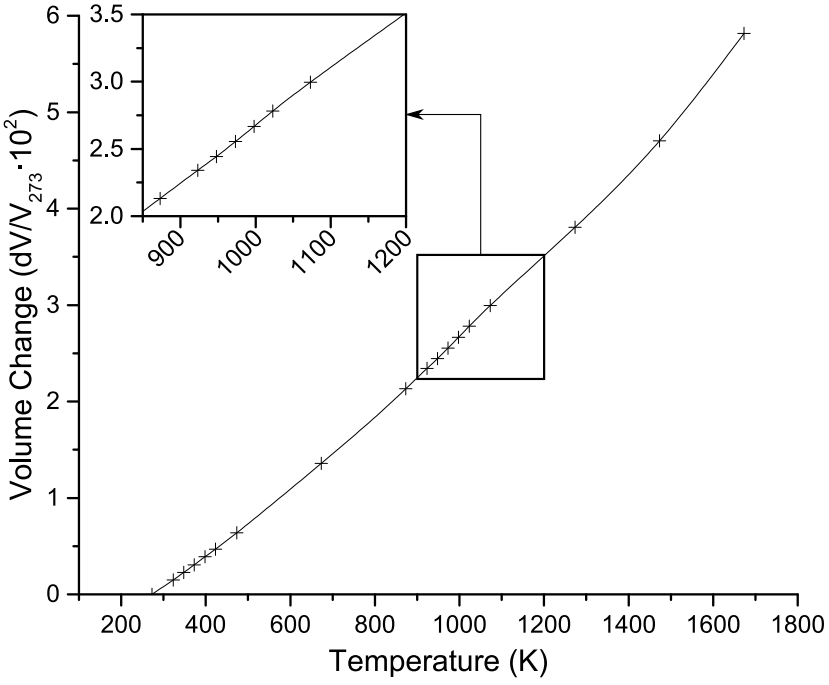

(b)

Figure 4.16: Calculated temperature dependencies of a) β-angle and b) volume change (w.r.t 273 K) of pristine Ba_2TiO_4, with 373-473 K region highlighted in the former and 850-1200 K region magnified in the latter.

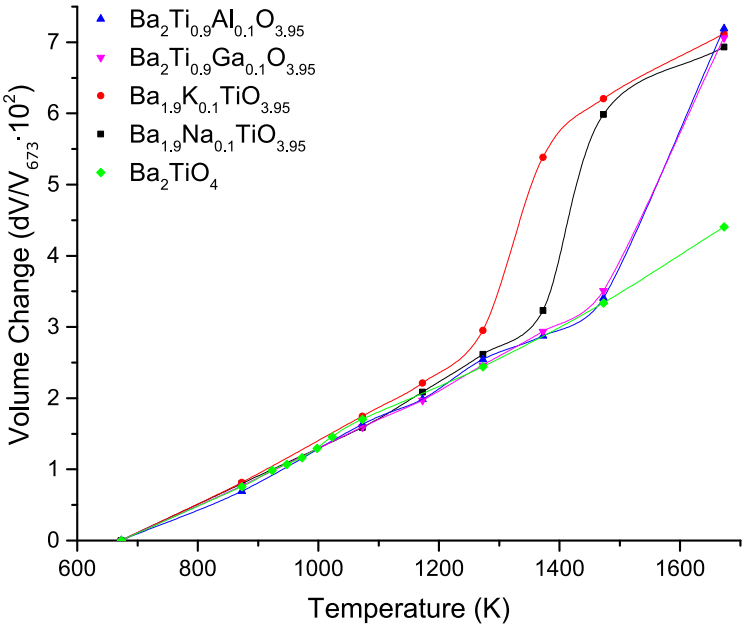

Figure 4.17: Volume change of pristine and doped Ba_2TiO_4 with respect to 673 K.

While pristine Ba_2TiO_4 maintains its phase up to the maximum simulated temperature (1673 K), the doped systems do not. Instead they undergo volume expansions of ∼2.7% and ∼2.2% in the trivalently and monovalently doped systems respectively, figure 4.17. With the exception of the Na^+ doped systems discussed next, the lattice angles remain unchanged throughout this volume expansion. Currently, further work is required to identify the origin and possible implications of this volume shift. However, changes in the mean squared displacements, discussed later, are found to be associated with the shift.

During simulations of the Ba_2TiO_4 systems it is found that those doped with Na^+ presented a somewhat unique "phase" behaviour. Unlike the other systems, which transform into and remain in the α′-phase, Na^+ doped systems initially shift to cells with β-angles under 90°. As the temperature is increased these systems slowly transform into the α′-phase as shown in figure 4.18a. Although, it is worth noting that the lattice angle β rapidly converges towards 90° during the volume expansion period. This behaviour is observed in all Na^+ doped systems tested, regardless of the dopant placement, dopant concentration or supercell size. However, the magnitude of the effect diminishes with decreasing dopant concentration, as seen from figure 4.18b. As this is observed in the Na^+ but not the K^+ doped systems it could be reasoned that the small size of the Na^+ ions, compared with the native Ba ions, may be responsible for this behaviour. However, further simulations will be required to verify the interatomic Na^+-O^{2-} potential, fully explore the effects of dopants on phase behaviour and to conclusively identify the precise causes of this behaviour in Ba_2TiO_4.

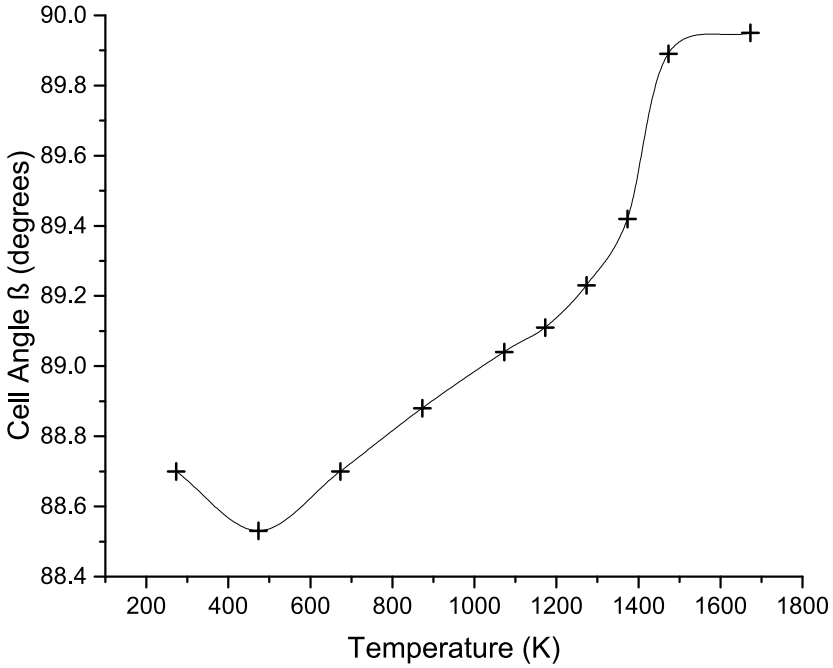

(a)

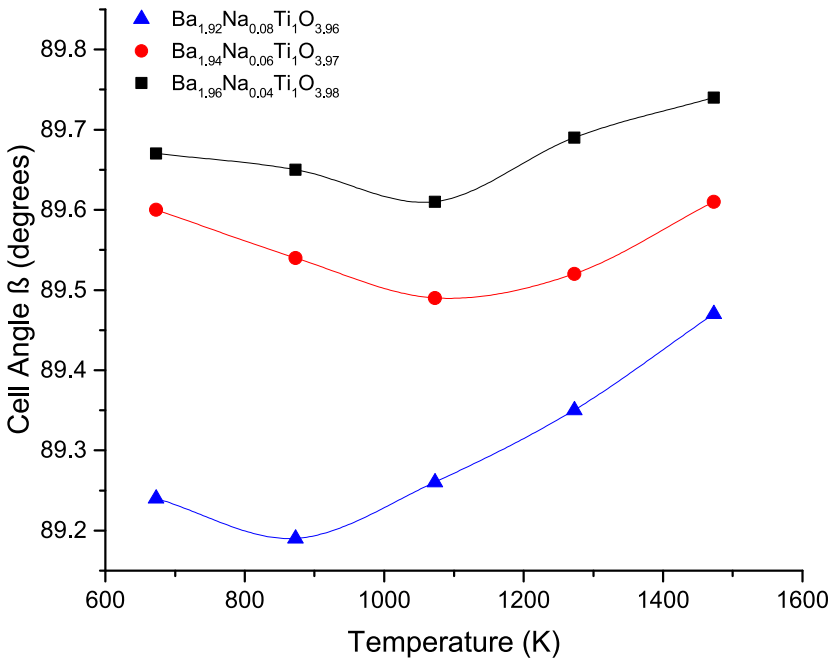

(b)

Figure 4.18: Temperature evolution of β-angle in a) 10% Na^+ doped Ba_2TiO_4 and b) the reduced 8%, 6% and 4% Na^+ doped variants.

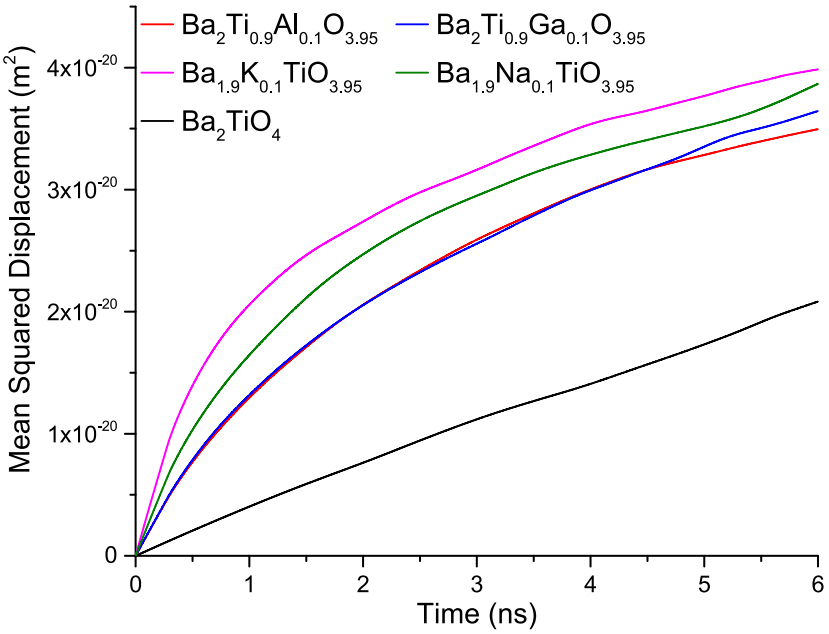

Figure 4.19: Smoothed oxygen MSDs for pristine and doped Ba_2TiO_4 at 1273 K.

The calculated mean squared displacements (MSDs) of the oxide ions at 1273 K in both the pristine and 10% doped Ba_2TiO_4 systems are plotted in figure 4.19. As mentioned earlier, the pristine systems are expected to be devoid of intrinsic oxide defects and should therefore exhibit minimal, if any measurable diffusion. However, this is contradicted by figure 4.19, which suggests this is not the case. Interrogation of the oxide ion positions duration the simulation showed, in agreement with the static lattice calculations, no evidence of oxygen Frenkel defect formation. Moreover, the oxide ions remain in their original starting TiO_4 tetrahedra, indicating the absence of true long-range migratory diffusion. The confinement of the oxide ions to their respective tetrahedra is visualised in the oxygen probability density maps in figure 4.20. This shows well defined and isolated oxygen sites, each corresponding to a natural lattice site. Therefore, the apparent diffusion, D = 5.38×10^{-9} cm^2 s^{-1} at 1273 K (table 4.9), in the pristine systems can only be attributed to the infrequent rotation of TiO_4 tetrahedra which results in the oxide ions swapping sites with one another.

Table 4.9: Calculated oxygen diffusion coefficients (D) for Ba_2TiO_4 systems at 1273 K.

System	D (cm^2 s^{-1})
Ba_2TiO_4	5.38×10^{-9}
$Ba_2Ti_{0.9}Al_{0.1}O_{3.95}$	4.94×10^{-9}
$Ba_2Ti_{0.9}Ga_{0.1}O_{3.95}$	6.00×10^{-9}
$Ba_{1.9}K_{0.1}TiO_{3.95}$	4.44×10^{-9}
$Ba_{1.9}Na_{0.1}TiO_{3.95}$	4.59×10^{-9}

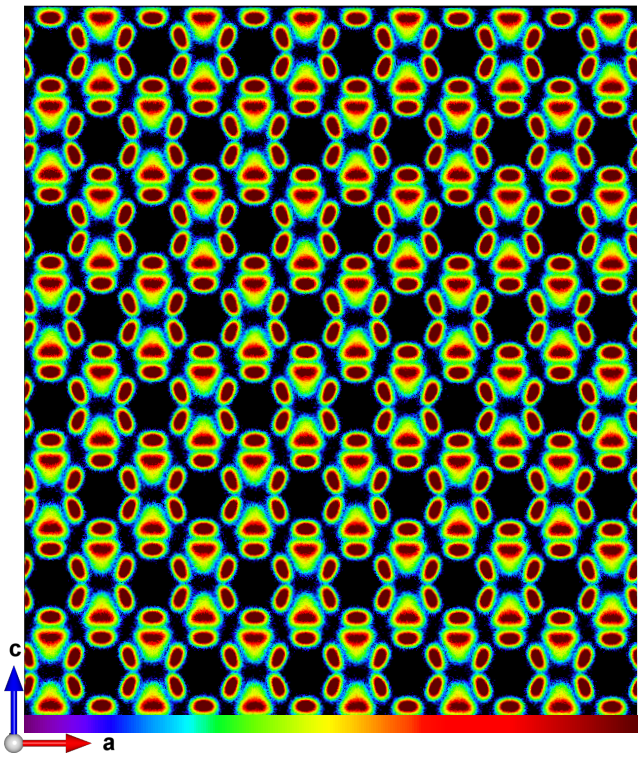

(a)

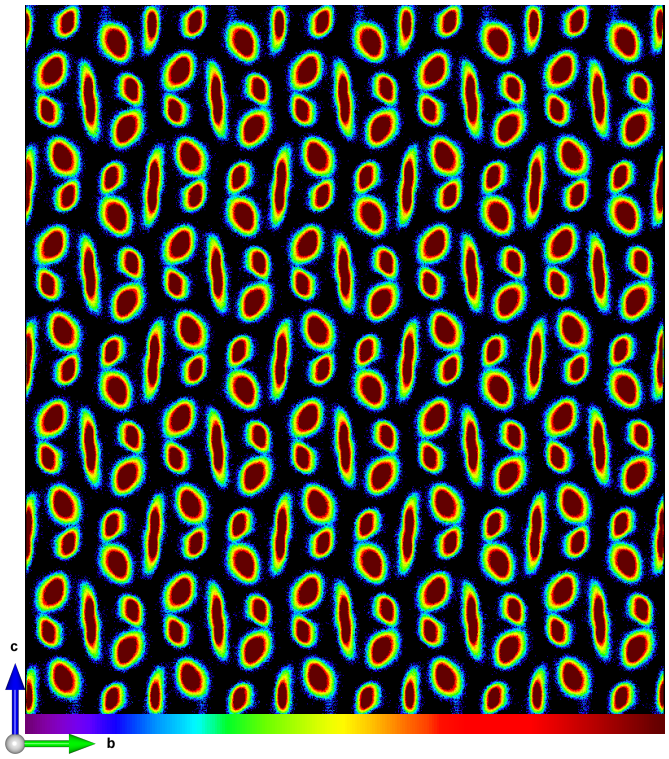

(b)

Figure 4.20: Oxygen probability density maps of pristine Ba_2TiO_4 at 1273K viewed orthogonal to the a) *ac* and b) *bc*-planes, colour scales, shown below each image, range from purple-lowest to red-highest with black indicating zero.

Unlike the pristine systems, the doped systems display significant ballistic and caging regimes. Therefore, simulations were extended to 6 ns in order to enable better equilibration. It can be seen in figure 4.19 that all of the doped systems take on a similar slope to the pristine system, indicating similar diffusivity. The oxide ion diffusion coefficients for the doped systems are indeed found to be similar to those of the pristine, listed in table 4.9. However, the oxygen density maps of trivalently and monovalently doped Ba_2TiO_4 systems, figures 4.22 and 4.21, show significant displacement of the oxide ions, particularly the O_I^{2-} sites which are distorted the most by the presence of oxide ion vacancies. The oxide ion vacancy defects, and therefore the oxide ions, are found to be somewhat mobile, but profoundly restricted to regions immediately neighbouring the dopant ions. The migration of oxide ion vacancies from one defect cluster to another is observed, if somewhat sporadically, during the simulations, but is almost immediately followed by the reverse migration. This trapping prevents the long range diffusion of oxide ions. As such, only the highly localised movements of the oxide ions about their defect clusters, seen in the oxygen density maps, and the tetrahedral rotation effects are significant contributors to the calculated diffusion coefficients, with the latter being identical to that discussed for the pristine Ba_2TiO_4 system.

Arrhenius plots for oxygen diffusivities in doped and undoped Ba_2TiO_4 systems are given in figures 4.23a-e on page 118. It can be seen that all systems, to a greater or lesser degree, experience high temperature curtailing of their diffusion coefficients. However, this effect is most pronounced in the monovalently doped systems, where a substantial drop is observed following the previously discussed volume shift. It is likely that the structural changes which accompany the volume shift affect the rotational flexibility of the tetrahedra, which cause a corresponding change in the measured diffusion coefficients. The temperatures at which the volume shifts occurred depended not only on dopant identity and concentration but the initial starting configuration. Suggesting that the dopant substructure does play a vital role in promoting the volume shifts. These shifts occur at slightly lower temperatures in the monovalently doped systems, which is to be expected given that Ba^{2+} site doping has a profound effect on the materials phase stability, as evident from experimental investigations.[215,216] However, currently no experimental information regarding the high temperature volume behaviour of doped Ba_2TiO_4 systems exist with which these results can be compared. Nevertheless, further examination of the high temperature phase behaviour is required.

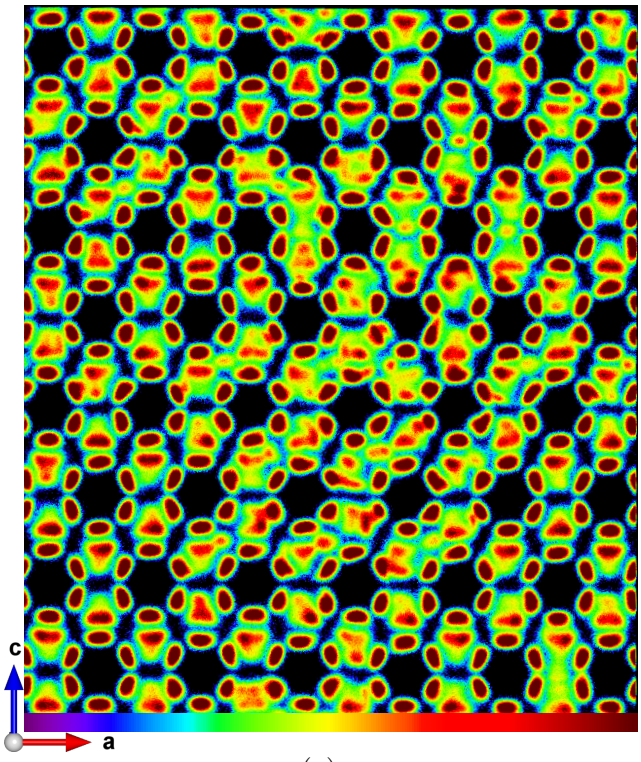

(a)

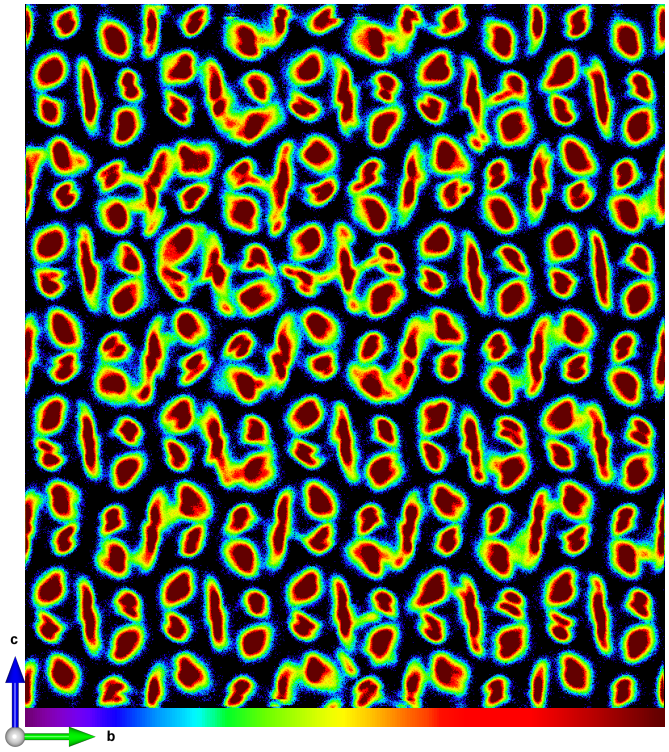

(b)

Figure 4.21: Oxygen probability density in $Ba_{1.9}K_{0.1}TiO_{3.95}$ at 1273K, viewed orthogonal to the a) *ac* and b) *bc*-planes, colour scales, shown below each image, range from purple-lowest to red-highest with black indicating zero.

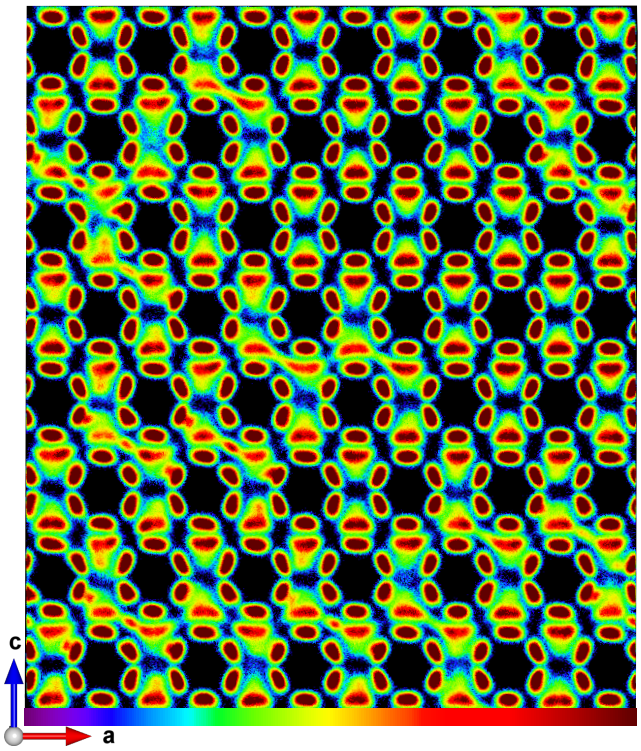

(a)

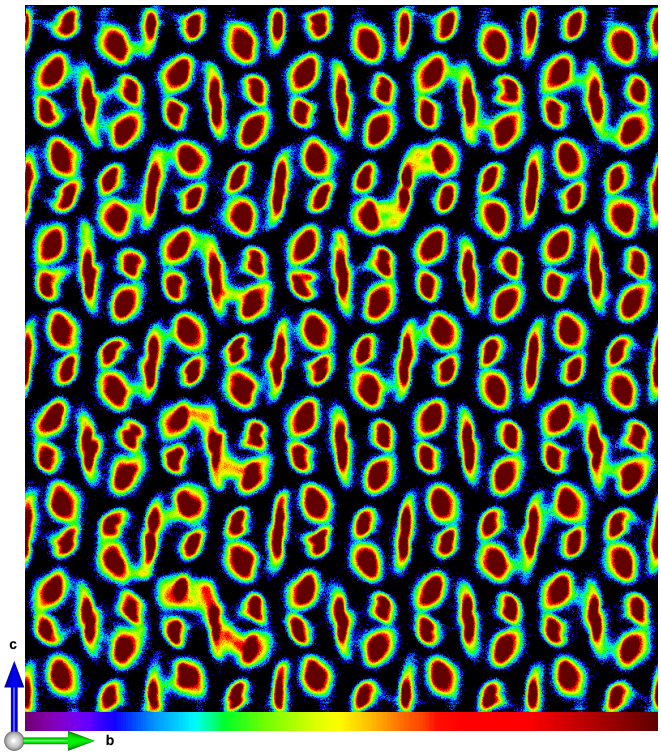

(b)

Figure 4.22: Oxygen probability density in $Ba_2Ti_{0.9}Al_{0.1}O_{3.95}$ at 1273K, viewed orthogonal to the a) *ac* and b) *bc*-planes, colour scales, shown below each image, range from purple-lowest to red-highest with black indicating zero.

It has been shown by Sansom *et al.*[245] that oxyapatites are one of the few materials capable of accommodating Ti^{4+} substituents on their tetrahedrally coordinated sites. As discussed in section 1.2.1, oxyapatites are known to be good oxide ion conductors, even prior to doping. However, in the aforementioned study it is shown that Ti^{4+} doping decreases the conductivity of both oxygen excess and deficient oxyapatites compared to their undoped counterparts. It is suggested therein that the decreased conductivities result from the trapping of the oxide defects by the Ti^{4+} ions.[245] It is possible that a similar effect is in part responsible for the poor oxide ion conductivities observed for Ba_2TiO_4 in this work. Furthermore, Al^{3+} doping of Ba_2TiO_4 has been found, in this work, to have no significant effect on oxide ion conductivity, which is in direct contrast to the oxyapatite materials.[66,69] However, not all materials which contain Ti^{4+} are poor oxide ion conductors, for example, perovskite like $Na_{0.5}Bi_{0.5}TiO_3$ based materials display significant levels of oxide ion conduction following small changes in their cation stoichiometry.[86] Another example would be the Ta^{5+} doped spinel-type material Zn_2TiO_4.[246] These materials differ from Ba_2TiO_4 and the Ti^{4+} doped oxyapatites as they accommodate Ti^{4+} in octahedral rather than tetrahedral sites.

While experimental measurements for the total conductivity of Ba_2TiO_4 samples were provided by Slater and Keenan[247], such values cannot be compared directly with those calculated in this work. This is because no oxide ion diffusion actually occurred in the pristine systems during the molecular dynamic simulations to which comparisons can be made, and because the type and number of defects responsible for conduction in the experimental "pristine" system are not known, preventing the extraction of a diffusion coefficient. However, activation energies for the total conductivity in pristine (1.08 eV) and La^{3+} doped (1.34 eV) Ba_2TiO_4 systems were extracted from the experimental data.[247]

To summarise, molecular dynamics simulations suggest that pristine Ba_2TiO_4 is a poor oxide ion conductor. Furthermore, neither monovalent or trivalent doping is found to noticeably enhance oxide ion conductivity despite having favourable solution energies. This is a consequence of defect trapping which effectively renders the oxide ion vacancies immobile. The β-α′-phase transformation is calculated to occur in the 373-398 K region, which supports the findings of Chen *et al.*[215]. Finally, both monovalent and trivalent dopants are found to induce a high temperature volume expansion, with Na^+ also impeding the transformation to the α′-phase.

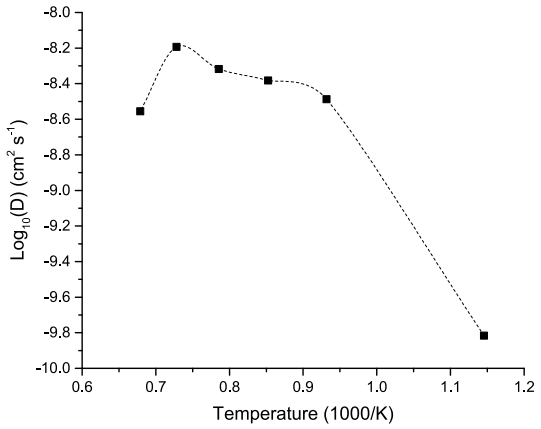

(a) $Ba_2Ti_{0.9}Al_{0.1}O_{3.95}$

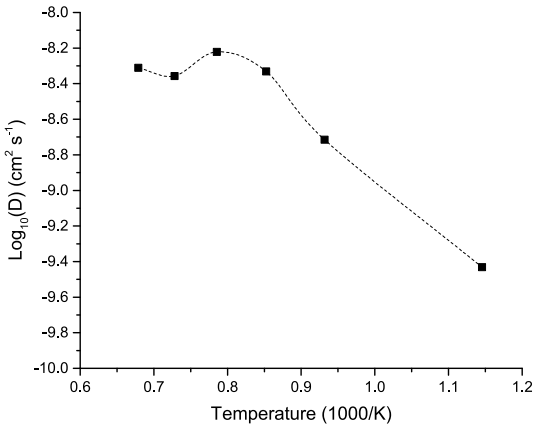

(b) $Ba_2Ti_{0.9}Ga_{0.1}O_{3.95}$

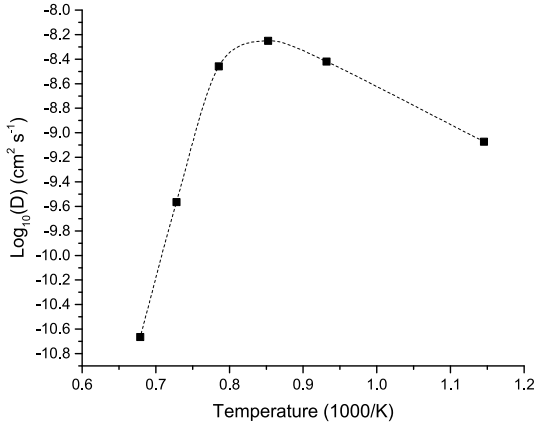

(c) $Ba_{1.9}K_{0.1}TiO_{3.95}$

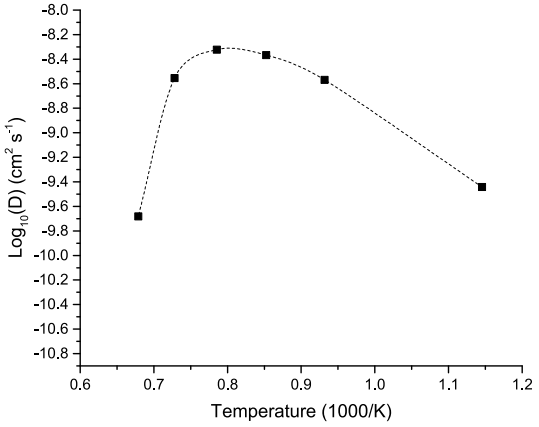

(d) $Ba_{1.9}Na_{0.1}TiO_{3.95}$

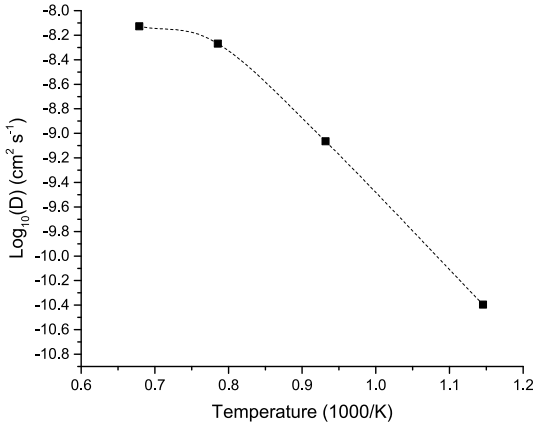

(e) Ba_2TiO_4

Figure 4.23: Plots showing the temperature dependencies of the oxygen diffusion coefficients (D) in pristine and doped Ba_2TiO_4 systems.

4.6 Summary and Conclusions

In this chapter, computational methods have been employed to study defects, dopants and oxide ion diffusion in Ba_2TiO_4. The main findings of this investigation have been summarised below.

A stable interatomic potential model capable of accurately reproducing both β and α′-phase structures of Ba_2TiO_4 has been successfully derived, alongside a modified interatomic potential for CO_3^{2-}.[236] Calculations suggest that carbonate defects are likely to be common impurities in both pristine and doped Ba_2TiO_4. Whereas those based on H_2O will only form in systems containing other supporting defects, such as oxide ion vacancies or interstitials. Although, both are likely to trap oxide ion defects. High Frenkel and Schottky defect formation energies mean that aliovalent doping is required to form oxide ion defects. Monovalent and trivalent dopants were found to induce oxide ion vacancy formation, however strong trapping effects rendered such vacancies practically immobile, resulting in negligible oxide ion conduction, as confirmed by molecular dynamic simulations.

In conclusion, monovalently and trivalently doped Ba_2TiO_4 systems are found to be extremely poor oxide ion conductors. This suggests, that unlike other materials with tetrahedra frameworks, Ba_2TiO_4 structured materials may not be capable of fast oxide ion conduction. In contrast to the olivine structured material Cd_2GeO_4, investigated in chapter 3, Ba_2TiO_4 currently has no viable use in the SOFC cathode or electrolyte fields. Finally, suggestions for further work into the Ba_2TiO_4 system have been made, and are detailed in chapter 6.

Chapter 5

Preliminary Investigation of Ba_2GeO_4

5.1 Introduction

Barium orthogermanate (Ba_2GeO_4) is a single phase material that crystallises with an orthorhombic low-K_2SO_4 type structure of space group *Pnma*.[248–250] It is therefore fairly similar in structure, but not identical, to Ba_2TiO_4, which was investigated in the previous chapter. A full description of the Ba_2GeO_4 structure can be found in the section following this introduction.

Within Ba_2GeO_4, there exists an isolated tetrahedral framework similar to that in Ba_2TiO_4, which was shown earlier to be a poor oxide ion conductor. However, unlike those in Ba_2TiO_4, these tetrahedra are germanium based. Germanium based frameworks such as these are known to facilitate fast oxide ion conduction in oxyapatite materials.[96] Therefore, they may serve the same purpose in Ba_2GeO_4.

In its pristine form, Ba_2GeO_4 is a poor conductor, which displays total conductivities of around 3×10^{-7} S cm^{-1} at 800 °C.[244] However, samples that have been doped with Ga^{3+} show a two order of magnitude increase in their conductivities.[244] This increase possibly results from the migration of oxide ion vacancy defects which form to charge balance the dopants. Both the pristine and doped materials display higher conductivities when placed in wet than dry environments.[244] This suggests the materials may possess some proton conducting abilities as well.

A computational investigation would not only explain the origins of the enhanced conductivities observed upon doping and exposure to water, but offer a mechanistic insight into the conduction mechanisms present in Ba_2GeO_4. Furthermore, by understanding defect behaviour in Ba_2GeO_4 and comparing it to that in Ba_2TiO_4 a better understanding of both systems can be achieved, which would aid subsequent investigations.

5.1.1 Structural Modelling

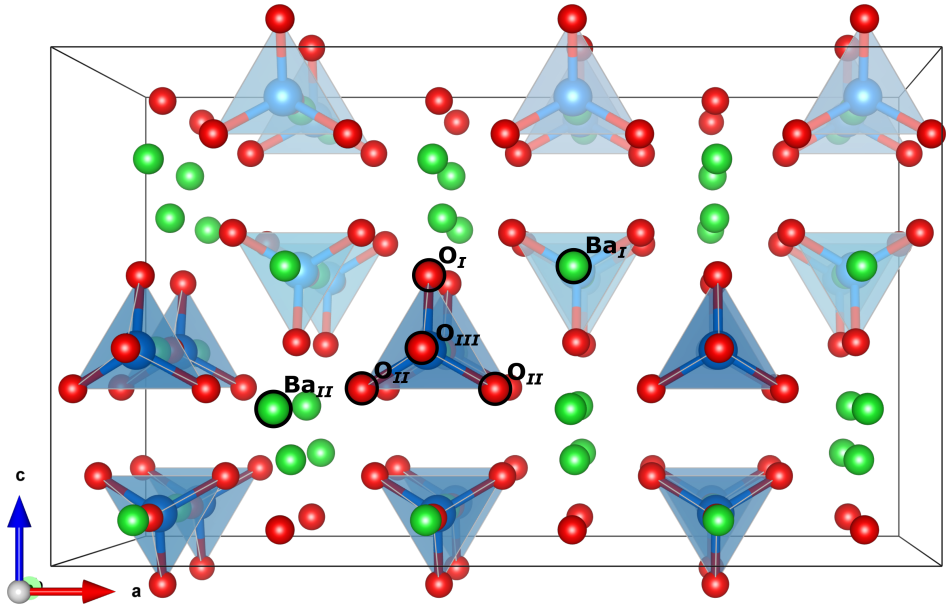

Figure 5.1: Crystal structure of Ba_2GeO_4 (3×2×1 supercell) as viewed down the *b*-axis, with the Ge, Ba and O ions represented as blue, green and red spheres respectively, and GeO_4 tetrahedra as blue polyhedra.

Having previously been misidentified as an olivine, investigations by Pieper *et al.*[248], Klockow and Eysel[251] and Corrie[244] showed Ba_2GeO_4 to be isostructural with its silicon counterpart which is a low-K_2SO_4 structured material. The structure of Ba_2GeO_4 is shown in figure 5.1 along with all site specific labels. In this structure, the germanium ions are surrounded by four oxide ions in a tetrahedral arrangement. The GeO_4 tetrahedra are isolated from one another by Ba_I sites down the *b*-axis. These *b*-axial Ba_I-GeO_4 channels then pack hexagonally around channels comprised of Ba_{II} sites.

As with previous investigations in this work, the first task is the identification of a suitable set of interatomic potentials with which to model Ba_2GeO_4. To be considered fit for use, a model must be stable in the material of interest and its binary oxide precursors and be in good agreement with the experimental structures of those materials.

Table 5.1: Comparison of experimental and DFT calculated Ba_2GeO_4 lattice parameters.

Parameter	Experimental[244]	DFT calculated	Change (%)
a (Å)	5.79 (5.97)[a]	6.05	4.50
b (Å)	7.57	7.71	1.95
c (Å)	10.41	10.72	3.02
$\alpha = \beta = \gamma$ (°)	90.00	90.00	0.00
Volume (Å^2)	470.16	500.47	6.45

[a] 2^{nd} and 3^{rd} digits swapped, see in-text discussion for information.

Numerous interatomic potentials for Ba^{2+}, Ge^{4+} and O^{2-} were taken from literature and scanned in different combinations to assess their suitability. Similar to Ba_2TiO_4, only models with Ba^{2+}-O^{2-} potentials based on that by Bush *et al.*[226] produced acceptable starting points from which the modelling process could begin. However, such a process is not trivial, and attempts to refine the interatomic potentials failed to identify a stable model that was within acceptable limits of the experimental structure of Ba_2GeO_4.[244]

Initially, a manual approach was taken to the model fitting process. In this, the Buckingham potential and shell model terms were iteratively adjusted by hand in an attempt to reproduce the experimentally determined lattice parameters and bond distances. In each attempt an impasse was reached, beyond which no further improvements could be achieved without significantly reducing the O^{2-} shell's spring constant or increasing its charge. However, such polarisability results in the emergence of imaginary phonon modes in Ba_2GeO_4 and/or GeO_2, furthermore it also causes the shells to detach during non-equilibrium calculations. Following this, a genetic approach was taken. Using a genetic algorithm, previously designed for Ba_2TiO_4, numerous starting models were taken and run for at least 8000 iterations. Again, the same impasse was encountered each time. Finally, a more brute force approach was employed. In this, the best models were chosen and their Buckingham A, ρ, and where required C parameters varied to generate an interatomic potential "surface". However, this again failed to locate a satisfactory set of interatomic potentials with which to model Ba_2GeO_4. Other than the lattice parameters the GeO_4 tetrahedral units were found to be a large source of error as they were often found to have at least a 45° rotational mismatch with the experimental structure and a ∼0.1 Å Ge^{4+}-O^{2-} bond contraction/expansion. Which, in turn, affected the Ba^{2+}-O^{2-} bond distances.

In table 5.1 it can be seen that the experimentally reported cell dimensions are not consistent with the reported volume ($5.79 \times 7.57 \times 10.41 \neq 470.16$ Å).[244] Comparing these values with a second set of experimental lattice parameters showed good agreement in all but the a-parameter.[248] Further examination suggests that the 2^{nd} and 3^{rd} digits in the a-value may have been switched as, an a-value of 5.97 Å is consistent with the reported volume and is a much better match for other reference sets.[248]

The Ba_2GeO_4 lattice was relaxed using density functional theory (DFT) in an attempt to aid the fitting process. Upon relaxation, the Ba_2GeO_4 cell underwent an expansion, particularly in the a-dimension, as evident from table 5.1. Despite this relaxation, fitting attempts still failed to yield a suitable interatomic potential model. It is perhaps interesting to note that the *materials project* computationally predicts five possible structures for Ba_2GeO_4, none of which are found to be isostructural with Ba_2SiO_4 as indicated by experiment.[252–254] They instead predict structures which are more comparable to Sr_2GeO_4 and Ba_2TiO_4.

Preliminary attempts made to fit to the "corrected" ($a = 5.97$ Å) experimental structure did not yield substantial improvements, however further work is still required. Falling this, further experimental measurements would be required to fully resolve and verify the Ba_2GeO_4 structure and to remove any possible impurity effects. A refined structure would either *i*) enable resumption of the current investigative methods or *ii*) confirm the accuracy of the experimental structure, in which case, less approximate computational methods would be required to continue the investigation.

Chapter 6

Concluding Comments and Further Work

6.1 Summary

In this thesis, interatomic potential based numerical modelling techniques have been employed to provide an atomic level insight into the defect behaviours and ion transport properties of three A_2BO_4-type oxide materials. The atomistic examination of these phenomena expands upon the current knowledge base in a way that is difficult to achieve by conventional means. The primary aim of this thesis was to assess the selected materials' applicability in solid oxide fuel cell applications. However, the information presented in this work was intended not only to aid in the development of advanced solid oxide fuel cell materials, but to provide a computational perspective on experimental observations. To conclude this thesis, an overview of the research conducted will now be given, followed by recommendations for further work.

In chapters 3 and 4, interatomic potential models for the A_2BO_4-type materials Cd_2GeO_4 and Ba_2TiO_4 were successfully developed. These models are in good agreement with experimental data and permit investigation of their respective material's defect properties. However, as discussed in chapter 5, these methods are unable to adequately model the third A_2BO_4-type material, Ba_2GeO_4.

Isolated point defect calculations were performed on Cd_2GeO_4 and both phases of Ba_2TiO_4. The results indicate intrinsic defect formation energies to be unfavourably high in both materials, suggesting that they are poor oxide ion conductors in their pristine states. A conclusion that is supported by the molecular dynamic simulations carried out as part of this work. Solution energies were calculated for a broad range of dopants and their incorporation mechanisms. These calculations indicate that oxide ion interstitial defects can be formed in Cd_2GeO_4 through trivalent doping, and oxide ion vacancy defects in Ba_2TiO_4 by monovalent or trivalent doping. However, only the Cd_2GeO_4 systems show enhanced oxide ion migration upon doping; the oxide ion vacancy defects in doped Ba_2TiO_4 systems being effectively immobile, even at high temperatures.

In Cd_2GeO_4, the oxide ions diffuse primarily along the *ac*-plane; *via* a "knock-on" mechanism down the *a*-axis and a stepwise mechanism along the *c*-axis, with calculated migration barriers of around 0.79 eV. However, defect trapping confines these interstitials to the dopant rich regions of the cell, reducing their mobility. Even at high temperatures, defect trapping substantially reduces Cd_2GeO_4's oxide ion conducting ability.

The low and negligible oxide ion conductivities encountered in doped Cd_2GeO_4 (10% Y^{3+} and Nd^{3+}) and Ba_2TiO_4 (10% Na^+, K^+ Al^{3+} and Ga^{3+}) systems respectively make them poor choices for IT-SOFC electrolyte applications. Furthermore, the negligible electrical conducting abilities of Cd_2GeO_4 and Ba_2TiO_4 also bars their use as SOFC cathode materials.

Molecular dynamic simulations of pristine Ba_2TiO_4 systems suggest β to α′-phase transformation temperatures closer to those reported by Chen *et al.*[215] than those by Lee *et al.*[216]. Calculations show most defects are lower in energy in the high temperature α′-phase, suggesting, in agreement with experiment, that many defects will stabilise the α′-phase.[215,216] Subsequent investigations revealed carbonate impurities are likely to be common in pristine and doped Ba_2TiO_4 systems alike, and that their presence will stabilise the α′-phase. This is supported by the experimental investigations of Trussov *et al.*[242] on the phase stabilising abilities of carbonaceous impurities. Such findings offer, in part, a possible explanation for the varied phase transformation temperatures reported in literature for Ba_2TiO_4. The hydroxide defects formed upon water incorporation are shown to be low in energy in Ba_2TiO_4 systems containing oxide ion vacancies or interstitials. Upon formation, hydroxide units trap the anion defects, reducing their mobility. Such behaviour is likely to be observed in related β-K_2SO_4 type materials.

The materials examined in this work were not found to measure up to current electrolytes in terms of their oxide ion conducting abilities. Nevertheless, a large and diverse array of A_2BO_4-type materials remain as yet uninvestigated, some of which may present fast oxide ion conducting abilities.[147] A report by Nalbandyan and Novikova[153] detailed a list of A_2BO_4-type structures that contain isolated tetrahedra. In that report, the structures were categorised by their coordination environments and ranked, amongst other things, by their packing densities. The oxide ion conducting ability of a material is strongly related to, but not solely dependent on, its structure. By investigating more A_2BO_4-type materials and, if possible, identifying the relationships that exist between them, their structures and their conducting abilities a broader understanding of oxide ion conduction within them can be acquired. Application of this knowledge could then be used to aid the materials selection process in subsequent investigations.

6.2 Further Work

Whipple *et al.*[183] showed that trivalently doped Cd_2GeO_4 samples synthesised under vacuum and kept in an O_2 free atmosphere are semiconductors. It was reported that dramatic drops in electrical conductivity occurred upon exposure to O_2, but could be reversed by placing the samples in a vacuum again. They attribute this behaviour to the chemisorption of oxygen. From this, it can be inferred that electronic and atomic forms of charge compensating defects will dominate at low and high oxygen partial pressures (P_O) respectively. It is possible that this behaviour could be leveraged to enhance the ORR capabilities of cathodes impregnated with Cd_2GeO_4. Further work into Cd_2GeO_4 should focus on assessing its viability as a catalyst for the ORR, and if possible improving it. The first step in such an investigation would be to identify the types of electronic defects present at low values of P_O. By calculating the relative stabilities of electronic and atomic defects as a function of P_O, the ability of Cd_2GeO_4 to facilitate the ORR can be evaluated. However, other methods such as density functional theory should be employed as electronic defects such as F-centres cannot be readily evaluated using the interatomic potential methods employed in this work. Examining surface and sub-surface defects would also help to further understanding of the Cd_2GeO_4 material and would aid in the above suggested investigation.

As the substitution of Ge^{4+} and Si^{4+} MO_4 sites with Ti^{4+} ions reduces the conductivities of oxyapatite materials, it is possible that Ge^{4+} or Si^{4+} doping of the Ti^{4+} sites in Ba_2TiO_4 may result in improved conductivities.[245] Investigating the effect of Ge^{4+} and Si^{4+} substituents on oxide ion conduction in Ba_2TiO_4 would help to further understanding of defect trapping in systems with titanium tetrahedra.

Experimental studies have suggested that oxide ion interstitials may be formed in Ba_2TiO_4 through the introduction of pentavalent dopants.[245] It is possible that oxide ion interstitials may be less aggressively trapped in Ba_2TiO_4 than their vacancy counterparts and so also warrant investigation.

While both carbonate and water based defects were considered in Ba_2TiO_4, they were done so separately. However, it is known that water accelerates the CO_2 based degradation of Ba_2TiO_4, as such it would be pertinent investigate the interactions between water and carbonate defects in the materials bulk.

The high temperature volume shifts observed in the doped Ba_2TiO_4 systems warrant further study and analysis in order to identify their origin. As does the phase retention behaviour of Na^+ doped systems. However, in the case of the latter, further verification of the Na-O interatomic potential is required to rule out the possibility of errors in the potential model.

Finally, further refinement of the Ba_2GeO_4 crystal structure is required before interatomic potential based methods can be employed to model it. Failing this, *ab initio* based techniques should be employed to aid the fitting process or to investigate the material through less biased computational methods.

References

[1] *BP Statistical Review of World Energy June 2016*, British petroleum company technical report, 2016.

[2] S. Shafiee and E. Topal, *Energy Policy*, 2009, **37**, 181–189.

[3] T. Nejat-Veziroglu, *Int. J. Hydrogen Energy*, 1987, **12**, 99–129.

[4] S. Solomon, K. Plattner, Gian, R. Knutti and P. Friedlingstein, *Proc. Natl. Acad. Sci.*, 2009, **106**, 1704–1709.

[5] C. Drechsel, Annual Electric Utilities Environmental Conference (2005) on Air Quality, Global Climate Change and Renewable Energy, Trinity Consultants, United States, 2006.

[6] N. MacDowell, N. Florin, A. Buchard, J. Hallett, A. Galindo, G. Jackson, C. S. Adjiman, C. K. Williams, N. Shah and P. Fennell, *Energy Environ. Sci.*, 2010, **3**, 1645.

[7] J. Mark Z, *Energy Environ. Sci*, 2009, **2**, 148–173.

[8] R. S. Haszeldine, *Science*, 2009, **325**, 1647–1652.

[9] C. Song, *Catal. Today*, 2006, **115**, 2–32.

[10] C. M. White, B. R. Strazisar, E. J. Granite, J. S. Hoffman and H. W. Pennline, *EM Air Waste Manag. Assoc. Mag. Environ. Manag.*, 2003, **53**, 29–34.

[11] J. Hill, E. Nelson, D. Tilman, S. Polasky and D. Tiffany, *Proc. Natl. Acad. Sci. U. S. A.*, 2006, **103**, 11206–10.

[12] T. D. Searchinger, *Environ. Res. Lett.*, 2010, **5**, 024007.

[13] L. Brennan and P. Owende, *Renew. Sustain. Energy Rev.*, 2010, **14**, 557–577.

[14] D. Pimentel, A. Marklein, M. A. Toth, M. N. Karpoff, G. S. Paul, R. McCormack, J. Kyriazis and T. Krueger, *Hum. Ecol.*, 2009, **37**, 1–12.

[15] S. Teleke, M. E. Baran, S. Bhattacharya and A. Q. Huang, *IEEE Trans. Sustain. Energy*, 2010, **1**, 117–124.

[16] M. Winter and R. J. Brodd, *Chem. Rev.*, 2004, **104**, 4245–4269.

[17] B. C. Steele and A. Heinzel, *Nature*, 2001, **414**, 345–352.

[18] A. Durmayaz, O. S. Sogut, B. Sahin and H. Yavuz, *Prog. Energy Combust. Sci.*, 2004, **30**, 175–217.

[19] N. Brandon, S. Skinner and B. Steele, *Annu. Rev. Mater. Res.*, 2003, **33**, 183–213.

[20] G. J. Snyder and S. M. Haile, *Adv. Mater. Energy Convers. II*, 2004, **51**, 33–41.

[21] N. Mahato, A. Banerjee, A. Gupta, S. Omar and K. Balani, *Prog. Mater. Sci.*, 2015, **72**, 141–337.

[22] L. Malavasi, C. A. J. Fisher and M. S. Islam, *Chem. Soc. Rev.*, 2010, **39**, 4370–4387.

[23] S. Mekhilef, R. Saidur and A. Safari, *Renew. Sustain. Energy Rev.*, 2012, **16**, 981–989.

[24] S. J. Eighambardoust, S. Rowshanzamir and M. Amjadi, *Int. J. Hydrogen Energy*, 2010, **35**, 9349–9384.

[25] J. Fleig, *Annu. Rev. Mater. Res.*, 2003, **33**, 361–382.

[26] M. Biswas and K. Sadanala, *Powder Metall. Min.*, 2013, 26–55.

[27] O. Z. Sharaf and M. F. Orhan, *Renew. Sustain. Energy Rev.*, 2014, **32**, 810–853.

[28] A. Kirubakaran, S. Jain and R. K. Nema, *Renew. Sustain. Energy Rev.*, 2009, **13**, 2430–2440.

[29] T. Elmer, M. Worall, S. Wu and S. B. Riffat, *Renew. Sustain. Energy Rev.*, 2015, **42**, 913–931.

[30] P. Devlin, G. Moreland and J. Christensen, *Fuel Cell Technologies*, `energy.gov/eere/fuelcells/comparison-fuel-cell-technologies`, (Accessed: January 2014).

[31] G. Merle, M. Wessling and K. Nijmeijer, *J. Membr. Sci.*, 2011, **377**, 1–35.

[32] Y. Wang, K. K. S. Chen, J. Mishler, S. C. S. Cho and X. C. X. Adroher, *Appl. Energy*, 2011, **88**, 981–1007.

[33] Ballard, *Fuel Cell electric buses, a solution for public transport?*, `ballard.com/power-products/motive-modules/bus/`, (Accessed: January 2015).

[34] C. Song, *Catal. Today*, 2002, **77**, 17–49.

[35] R. M. Ormerod, *Chem. Soc. Rev.*, 2003, **32**, 17–28.

[36] A. B. Stambouli and E. Traversa, *Renew. Sustain. Energy Rev.*, 2002, **6**, 433–455.

[37] T. Adams, J. Nease, D. Tucker and P. Barton, *Ind. Eng. Chem. Res.*, 2012, **52**, 3089–3111.

[38] S. Singhal, *Solid State Ionics*, 2000, **135**, 305–313.

[39] O. Yamamoto, *Electrochim. Acta*, 2000, **45**, 2423–2435.

[40] K. Eguchi, H. Kojo, T. Takeguchi, R. Kikuchi and K. Sasaki, *Solid State Ionics*, 2002, **152-153**, 411–416.

[41] N. Q. Minh, *Solid State Ionics*, 2004, **174**, 271–277.

[42] M. R. Walluk, J. Lin, M. G. Waller, D. F. Smith and T. A. Trabold, *Appl. Energy*, 2014, **130**, 94–102.

[43] J. Jeong, S.-W. Baek and J. Bae, *J. Power Sources*, 2014, **250**, 98–104.

[44] R. J. Kee, H. Zhu and D. G. Goodwin, *Proc. Combust. Inst.*, 2005, **30 II**, 2379–2404.

[45] S. C. Singhal, *Solid State Ionics*, 2002, **152-153**, 405–410.

[46] S. Das, D. Das and A. Patra, *Energy Procedia*, 2014, **54**, 439–447.

[47] F. Lefebvre-Joud, G. Gauthier and J. Mougin, *J. Appl. Electrochem.*, 2009, **39**, 535–543.

[48] D. Brett, a. Atkinson, N. Brandon and S. Skinner, *Chem. Soc. Rev.*, 2008, **37**, 1568–1578.

[49] Da Han, X. Liu, F. Zeng, J. Qian, T. Wu and Z. Zhan, *Sci. Rep.*, 2012, **2**, 1–5.

[50] E. Fabbri, A. Magrasó and D. Pergolesi, *MRS Bull.*, 2014, **39**, 792–797.

[51] B. Zhu, *J. Power Sources*, 2001, **93**, 82–86.

[52] E. Ivers-Tiffée, A. Weber and D. Herbstritt, *J. Eur. Ceram. Soc.*, 2001, **21**, 1805–1811.

[53] C. Sun, R. Hui and J. Roller, *J. Solid State Electrochem.*, 2010, **14**, 1125–1144.

[54] J. B. Goodenough, *Annu. Rev. Mater. Res.*, 2003, **33**, 91–128.

[55] S. P. S. Badwal and F. T. Ciacchi, *Ionics (Kiel).*, 2000, **6**, 1–21.

[56] Y. Lin and S. Beale, *Appl. Math. Model.*, 2006, **30**, 1485–1496.

[57] J. A. Kilner, *Solid State Ionics*, 2000, **129**, 13–23.

[58] J. E. H. Sansom, A. Najib and P. R. Slater, *Solid State Ionics*, 2004, **175**, 353–355.

[59] J. R. Tolchard, M. S. Islam and P. R. Slater, *J. Mater. Chem.*, 2003, **13**, 1956–1961.

[60] R. Devananthan, W. J. Weber, S. C. Singhal and J. D. Gale, *Solid State Ionics*, 2006, **177**, 1251–1258.

[61] D. W. Strickler and W. G. Carlson, *J. Am. Ceram. Soc.*, 1964, **47**, 122–127.

[62] P. Shuk, *Solid State Ionics*, 1996, **89**, 179–196.

[63] D. W. Jung, J. C. Nino, K. L. Duncan, S. R. Bishop and E. D. Wachsman, *Ionics (Kiel).*, 2010, **16**, 97–103.

[64] M. Dudek, M. Mosialek, G. Mordarski, R. Socha and A. Rapacz-Kmita, *Arch. Metall. Mater.*, 2011, **56**, 2874–2889.

[65] T. Ishihara, T. Shibayama, M. Honda, H. Nishiguchi and Y. Takita, *J. Electrochem. Soc.*, 2000, **147**, 1332.

[66] L. León-Reina, E. R. Losilla, M. Martínez-Lara, M. C. Martín-Sedeño, S. Bruque, P. Núñez, D. V. Sheptyakov and M. A. G. Aranda, *Chem. Mater.*, 2005, **17**, 596–600.

[67] P. Lacorre, F. Goutenoire, O. Bohnke, R. Retoux and Y. Laligant, *Nature*, 2000, **404**, 856–858.

[68] T. Wei, P. Singh, Y. Gong, J. B. Goodenough, Y. Huang and K. Huang, *Energy Environ. Sci.*, 2014, **7**, 1680–1684.

[69] A. L. Shaula, V. V. Kharton, J. C. Waerenborgh, D. P. Rojas and F. M. B. Marques, *J. Eur. Ceram. Soc.*, 2005, **25**, 2583–2586.

[70] M. Mogensen, D. Lybye, N. Bonanos, P. V. Hendriksen and F. W. Poulsen, *Solid State Ionics*, 2004, **174**, 279–286.

[71] K. Momma and F. Izumi, *J. Appl. Crystallogr.*, 2011, **44**, 1272–1276.

[72] H. G. Scott, *J. Mater. Sci.*, 1975, **10**, 1527–1535.

[73] S. J. Skinner and J. A. Kilner, *Mater. Today*, 2003, **6**, 30–37.

[74] T. S. Zhang, J. Ma, H. Cheng and S. H. Chan, *Mater. Res. Bull.*, 2006, **41**, 563–568.

[75] Z. Tianshu, P. Hing, H. Huang and J. Kilner, *Solid State Ionics*, 2002, **148**, 567–573.

[76] I. Maier, H. Pressures, S. Cole, C. T. Dioxide, D. E. Rase and R. Roy, *J. Phase Equilibria Diffus.*, 1975, **88**, 34–37.

[77] A. A. Yaremchenko, V. V. Kharton, E. N. Naumovich and A. A. Tonoyan, *Mater. Res. Bull.*, 2000, **35**, 515–520.

[78] D. W. Jung, *PhD thesis*, University of Florida, 2009.

[79] D. Hohnke, *Solid State Ionics*, 1981, **5**, 531–534.

[80] C. R. A. Catlow, Z. X. Guo, M. Miskufova, S. A. Shevlin, A. G. H. Smith, A. A. Sokol, A. Walsh, D. J. Wilson and S. M. Woodley, *Phil. Trans. R. Soc. A*, 2010, **368**, 3379–3456.

[81] F. M. L. Figueiredo and F. M. B. Marques, *Wiley Interdiscip. Rev. Energy Environ.*, 2013, **2**, 52–72.

[82] H. He, *Solid State Ionics*, 2000, **130**, 183–193.

[83] T. Ishihara, H. Matsuda and Y. Takita, *J. Am. Chem. Soc.*, 1994, **116**, 3801–3803.

[84] M. Morales, J. J. Roa, J. Tartaj and M. Segarra, *J. Eur. Ceram. Soc.*, 2016, **36**, 1–16.

[85] K. Huang, R. S. Tichy and J. B. Goodenough, *J. Am. Ceram. Soc.*, 2005, **81**, 2565–2575.

[86] M. Li, M. J. Pietrowski, R. a. De Souza, H. Zhang, I. M. Reaney, S. N. Cook, J. a. Kilner and D. C. Sinclair, *Nat. Mater.*, 2014, **13**, 31–5.

[87] S. Vasala and M. Karppinen, *Prog. Solid State Chem.*, 2015, **43**, 1–36.

[88] S. Speakman, J. Richardson, B. Mitchell and S. Misture, *Solid State Ionics*, 2002, **149**, 247–259.

[89] J. B. Goodenough, J. E. Ruiz-Diaz and Y. S. Zhen, *Solid State Ionics*, 1990, **44**, 21–31.

[90] K. Kakinuma, H. Yamamura, H. Haneda and T. Atake, *Solid State Ionics*, 2002, **154-155**, 571–576.

[91] a. Najib, J. E. H. Sansom, J. R. Tolchard, P. R. Slater and M. S. Islam, *Dalton Trans.*, 2004, 3106–3109.

[92] P. R. Slater, J. E. H. Sansom and J. R. Tolchard, *Chem. Rec.*, 2004, **4**, 373–384.

[93] M. S. Islam, J. R. Tolchard and P. R. Slater, *Chem. Commun.*, 2003, 1486.

[94] A. Jones, P. R. Slater and M. Saiful Islam, *Chem. Mater.*, 2008, **20**, 5055–5060.

[95] E. Kendrick, M. S. Islam and P. R. Slater, *Chem. Commun. (Camb).*, 2008, **33**, 715–717.

[96] E. Kendrick, M. S. Islam and P. R. Slater, *J. Mater. Chem.*, 2007, **17**, 3104–3111.

[97] J. R. Tolchard, P. R. Slater and M. S. Islam, *Adv. Funct. Mater.*, 2007, **17**, 2564–2571.

[98] A. Inoubli, M. Kahlaoui, I. Sobrados, S. Chefi, A. Madani, J. Sanz and A. Ben Haj Amara, *J. Power Sources*, 2014, **271**, 203–212.

[99] E. J. Abram, C. A. Kirk, D. C. Sinclair and A. R. West, *Solid State Ionics*, 2005, **176**, 1941–1947.

[100] S. Nakayama, Y. Higuchi, Y. Kondo and M. Sakamoto, *Solid State Ionics*, 2004, **170**, 219–223.

[101] P. Lacorre, *Solid State Sci.*, 2000, **2**, 755–758.

[102] S. Georges, F. Goutenoire, F. Altorfer, D. Sheptyakov, F. Fauth, E. Suard and P. Lacorre, *Solid State Ionics*, 2003, **161**, 231–241.

[103] D. Marrero-López, J. Peña-Martínez, J. C. Ruiz-Morales, D. Pérez-Coll, M. C. Martín-Sedeño and P. Núñez, *Solid State Ionics*, 2007, **178**, 1366–1378.

[104] D. Marrero-López, J. Canales-Vázquez, J. Ruiz-Morales, J. Irvine and P. Núñez, *Electrochim. Acta*, 2005, **50**, 4385–4395.

[105] P. Singh and J. B. Goodenough, *J. Am. Chem. Soc.*, 2013, **135**, 10149–10154.

[106] P. Singh and J. B. Goodenough, *Energy Environ. Sci.*, 2012, **5**, 9626–9631.

[107] P.-H. Chien, Y. Jee, C. Huang, R. Derviolu, I. Hung, Z. Gan, K. Huang and Y.-Y. Hu, *Chem. Sci.*, 2016, **7**, 3667–3675.

[108] R. D. Bayliss, S. N. Cook, S. Fearn, J. A. Kilner, C. Greaves and S. J. Skinner, *Energy Environ. Sci.*, 2014, **7**, 2999–3005.

[109] E. Kendrick, J. Kendrick, K. S. Knight, M. S. Islam and P. R. Slater, *Nat. Mater.*, 2007, **6**, 871–875.

[110] S. Li, F. Schönberger and P. Slater, *Chem. Commun. (Camb).*, 2003, **44**, 2694–2695.

[111] S. Carter, A. Selcuk, R. J. Chater, J. Kajda, J. A. Kilner and B. C. H. Steele, *Solid State Ionics*, 1992, **53-56**, 597–605.

[112] K. C. Wincewicz and J. S. Cooper, *J. Power Sources*, 2005, **140**, 280–296.

[113] B. Shri Prakash, S. Senthil Kumar and S. T. Aruna, *Renew. Sustain. Energy Rev.*, 2014, **36**, 149–179.

[114] Z. Gao, L. V. Mogni, E. C. Miller, J. G. Railsback and S. A. Barnett, *Energy Environ. Sci.*, 2016, **9**, 1602–1644.

[115] P. I. Cowin, C. T. G. Petit, R. Lan, J. T. S. Irvine and S. Tao, *Adv. Energy Mater.*, 2011, **1**, 314–332.

[116] S. E. Hou, A. Aguadero, J. A. Alonso and J. B. Goodenough, *J. Power Sources*, 2011, **196**, 5478–5484.

[117] J. B. Goodenough and Y.-H. Huang, *J. Power Sources*, 2007, **173**, 1–10.

[118] S. P. Jiang, *J. Mater. Sci.*, 2008, **43**, 6799–6833.

[119] E. Maguire, B. Gharbage, F. M. B. Marques and J. A. Labrincha, *Solid State Ionics*, 2000, **127**, 329–335.

[120] S. B. Adler, *Chem. Rev.*, 2004, **104**, 4791–4843.

[121] D. Ding, X. Li, S. Y. Lai, K. Gerdes and M. Liu, *Energy Environ. Sci.*, 2014, **7**, 552.

[122] X. Lou, S. Wang, Z. Liu, L. Yang and M. Liu, *Solid State Ionics*, 2009, **180**, 1285–1289.

[123] J. Richter, P. Holtappels, T. Graule, T. Nakamura and L. J. Gauckler, *Monatshefte fur Chemie*, 2009, **140**, 985–999.

[124] S. J. Skinner, *Int. J. Inorg. Mater.*, 2001, **3**, 113–121.

[125] G. S. Godoi and D. P. F. de Souza, *Mater. Sci. Eng. B Solid-State Mater. Adv. Technol.*, 2007, **140**, 90–97.

[126] J. D. Kim, G. D. Kim, J. W. Moon, Y. il Park, W. H. Lee, K. Kobayashi, M. Nagai and C. E. Kim, *Solid State Ionics*, 2001, **143**, 379–389.

[127] T. Klemensø, C. Chatzichristodoulou, J. Nielsen, F. Bozza, K. Thydén, R. Kiebach and S. Ramousse, *Solid State Ionics*, 2012, **224**, 21–31.

[128] M. Prestat, A. Infortuna, S. Korrodi, S. Rey-Mermet, P. Muralt and L. J. Gauckler, *J. Electroceramics*, 2007, **18**, 111–120.

[129] N. Simrick, A. Bieberle-Hütter, T. Ryll, J. Kilner, A. Atkinson and J. Rupp, *Solid State Ionics*, 2012, **206**, 7–16.

[130] Z. Liu, M. Liu, L. Yang and M. Liu, *J. Energy Chem.*, 2013, **22**, 555–559.

[131] J. Huang, F. Xie, C. Wang and Z. Mao, *Int. J. Hydrogen Energy*, 2012, **37**, 877–883.

[132] M. T. Fernández-Díaz, J. L. Martínez and J. Rodríguez-Carvajal, *Solid State Ionics*, 1993, **63-65**, 902–906.

[133] S. J. Skinner and J. A. Kilner, *Solid State Ionics*, 2000, **135**, 709–712.

[134] A. Chroneos, D. Parfitt, J. A. Kilner and R. W. Grimes, *J. Mater. Chem.*, 2010, **20**, 266–270.

[135] M. Yashima, M. Enoki, T. Wakita, R. Ali, Y. Matsushita, F. Izumi and T. Ishihara, *J. Am. Chem. Soc.*, 2008, **130**, 2762–2763.

[136] J. C. Grenier, F. Mauvy, C. Lalanne, J.-M. Bassat, F. Chauveau, J. Mougin, J. Dailly and M. Marrony, ECS Transactions, 2009, pp. 2537–2546.

[137] E. Boehm, J. M. Bassat, P. Dordor, F. Mauvy, J. C. Grenier and P. Stevens, *Solid State Ionics*, 2005, **176**, 2717–2725.

[138] A. P. Khandale, R. P. Lajurkar and S. S. Bhoga, *Int. J. Hydrogen Energy*, 2014, **39**, 19039–19050.

[139] H. Chaker, T. Roisnel, M. Potel and R. B. Hassen, *J. Solid State Chem.*, 2004, **177**, 4067–4072.

[140] M. Li, J. Cheng, Y. Gan, S. Li, B. He and W. Sun, *J. Power Sources*, 2015, **275**, 151–158.

[141] Q. Zhou, Y. Gao, F. Wang, D. An, Y. Li, Y. Zou, Z. Li and W. Wang, *Ceram. Int.*, 2014, **41**, 639–643.

[142] R. J. Woolley and S. J. Skinner, *Solid State Ionics*, 2014, **255**, 1–5.

[143] S. J. Lee, P. Muralidharan, S. H. Jo and D. K. Kim, *Electrochem. commun.*, 2010, **12**, 808–811.

[144] Q. Zhou, Y. Shi, J. Hu, T. Wei, Z. Li, Y. Li, X. Qi, W. Zhao and W. Zhang, *Ceram. Int.*, 2014, **40**, 13481–13485.

[145] Q. Zhou, Y. Shi, T. Wei, Z. Li, D. An, J. Hu, W. Zhao, W. Zhang, Z. Ji and J. Wang, *Int. J. Hydrogen Energy*, 2014, **39**, 10710–10717.

[146] M. West, C. Ortiz and A. Manthiram, *Int. J. Hydrogen Energy*, 2015, **40**, 1186–1194.

[147] H. Muller-Buschbaum, *J. Alloys Compd.*, 2003, **349**, 49–104.

[148] X. Kuang, M. A. Green, H. Niu, P. Zajdel, C. Dickinson, J. B. Claridge, L. Jantsky and M. J. Rosseinsky, *Nat. Mater.*, 2008, **7**, 498–504.

[149] M. Al Daroukh, V. V. Vashook, H. Ullmann, F. Tietz and I. Arual Raj, *Solid State Ionics*, 2003, **158**, 141–150.

[150] P. Batocchi, F. Mauvy, S. Fourcade and M. Parco, *Electrochim. Acta*, 2014, **145**, 1–10.

[151] J. Dailly, S. Fourcade, A. Largeteau, F. Mauvy, J. C. Grenier and M. Marrony, *Electrochim. Acta*, 2010, **55**, 5847–5853.

[152] P. M. Panchmatia, A. Orera, G. J. Rees, M. E. Smith, J. V. Hanna, P. R. Slater and M. S. Islam, *Angew. Chemie - Int. Ed.*, 2011, **50**, 9328–9333.

[153] V. Nalbandyan and A. Novikova, *Acta Crystallogr. B.*, 2012, **68**, 227–39.

[154] M. S. Islam, D. J. Driscoll, C. A. J. Fisher and P. R. Slater, *Chem. Mater.*, 2005, **17**, 5085–5092.

[155] J. D. Gale, *J. Chem. Soc. Faraday Trans.*, 1997, **93**, 629–637.

[156] J. D. Gale and a. L. Rohl, *Mol. Simul.*, 2003, **29**, 291–341.

[157] J. D. Gale, *General Utility Lattice Program User Manual*, 2012.

[158] W. Smith, T. Forester and I. Todorov, *The DL POLY Classic User Manual*, 2012.

[159] W. Smith and T. R. Forester, *J. Mol. Graph.*, 1996, **14**, 136–141.

[160] M. Born and E. Bormann, *Ann. Phys.*, 1920, **367**, 218–246.

[161] J. H. Harding, *Reports Prog. Phys.*, 1990, **53**, 1403–1466.

[162] P. P. Ewald, *Ann. Phys.*, 1921, **369**, 253–287.

[163] A. K. Cheetham and P. Day, in *Solid State Chemistry: Techniques*, ed. A. K. Cheetham and P. Day, Oxford University Press, Oxford, 1988, vol. 1, ch. 7, pp. 231–275.

[164] A. R. Leach, *Molecular modelling: Principles and applications*, Prentice Hall, Dorset, 2nd edn, 1997, vol. 21.

[165] C. M. Freeman, A. M. Gorman and J. M. Newsam, in *Computer Modeling in Inorganic Crystallography*, ed. R. Catlow, Academic Press, San Diego, 1997, ch. 5, pp. 117–150.

[166] R. A. Buckingham, *Proc. R. Soc. A Math. Phys. Eng. Sci.*, 1938, **168**, 264–283.

[167] P. Morse, *Phys. Rev.*, 1929, **34**, 57–64.

[168] B. G. Dick and A. W. Overhauser, *Phys. Rev.*, 1958, **112**, 90–103.

[169] N. F. Mott and M. J. Littleton, *Trans. Faraday Soc.*, 1938, **34**, 485.

[170] F. Kröger and H. Vink, in *Solid State Physics*, ed. S. Frederick and T. David, Academic Press, 1995, vol. Volume 3, pp. 307–435.

[171] M. Schie, R. Waser and R. A. De Souza, *J. Phys. Chem. C*, 2014, **118**, 15185–15192.

[172] B. Wang, R. J. Lewis and A. N. Cormack, *Acta Mater.*, 2011, **59**, 2035–2045.

[173] A. Shlyakhtina, D. Belov, A. Knotko, I. Kolbanev, A. Streletskii and L. Shcherbakova, *Solid State Ionics*, 2014, **262**, 543–547.

[174] T. Ishihara, Y. Yan, T. Sakai and S. Ida, *Solid State Ionics*, 2016, **288**, 262–265.

[175] A. V. Shlyakhtina, D. A. Belov, A. V. Knotko, M. Avdeev, I. V. Kolbanev, G. A. Vorobieva, O. K. Karyagina and L. G. Shcherbakova, *J. Alloys Compd.*, 2014, **603**, 274–281.

[176] L. Verlet, *Phys. Rev.*, 1967, **159**, 98–103.

[177] H. J. C. Berendsen, J. P. M. Postma, W. F. van Gunsteren, a. DiNola and J. R. Haak, *J. Chem. Phys.*, 1984, **81**, 3684–3690.

[178] W. G. Hoover, *Phys. Rev. A*, 1985, **31**, 1695–1697.

[179] P. H. Hünenberger, in *Advanced Computer Simulation: Approaches for Soft Matter Sciences*, ed. C. Holm and K. Kremer, Springer, Heidelberg, 2005, vol. 173, pp. 105–149.

[180] G. E. Murch, *Solid State Ionics*, 1982, **7**, 177–198.

[181] M. A. Simonov, E. L. Belokoneva and N. V. Belov, *J. Struct. Chem.*, 1981, **22**, 478–479.

[182] P. Tarte, *J. Inorg. Nucl. Chem.*, 1965, **27**, 1933–1938.

[183] E. R. Whipple, S. N. Subbarao and F. P. Koffyberg, *J. Solid State Chem.*, 1980, **34**, 231–239.

[184] J. H. W. De Wit, G. Van Unen and M. Lahey, *J. Phys. Chem. Solids*, 1977, **38**, 819–824.

[185] P. S. Clarke, J. W. Orton and A. J. Guest, *Phys. Rev. B*, 1978, **18**, 1813–1817.

[186] J. W. Orton and M. J. Powell, *Philos. Mag. Part B*, 1978, **38**, 491–501.

[187] P. M. Panchmatia, A. Orera, E. Kendrick, J. V. Hanna, M. E. Smith, P. R. Slater and M. S. Islam, *J. Mater. Chem.*, 2010, **20**, 2766–2772.

[188] W. M. Haynes, *CRC Handbook of Chemistry and Physics*, CRC Press, Boca Raton, 92nd edn, 2000.

[189] F. D. Hardcastle and S. Laffoon, *J. Ark. Acad. Sci.*, 2012, **66**, 87–93.

[190] N. E. Brese and M. O'Keeffe, *Acta Crystallogr. Sect. B*, 1991, **47**, 192–197.

[191] C. Fisher, M. Islam and R. Brook, *J. Solid State Chem.*, 1997, **128**, 137–141.

[192] A. M. Walker, K. Wright and B. Slater, *Phys. Chem. Miner.*, 2003, **30**, 536–545.

[193] A. M. Walker, S. M. Woodley, B. Slater and K. Wright, *Phys. Earth Planet. Inter.*, 2009, **172**, 20–27.

[194] Y. Jin, Y. Hu, R. Chen, Y. Fu, G. Ju, Z. Mu, J. Lin, Z. Wang, F. Xue and Q. Zhang, *J. Alloys Compd.*, 2015, **623**, 255–260.

[195] M. J. Akhtar, Z.-U.-N. Akhtar, R. A. Jackson and C. R. A. Catlow, *J. Am. Ceram. Soc.*, 1995, **78**, 421–428.

[196] A. J. McEvoy, *Solid State Ionics*, 2000, **135**, 331–336.

[197] A. F. Gualtieri and S. Bagni, *Period. di Mineral.*, 2001, **70**, 27–56.

[198] M. Marezio and J. P. Remeika, *J. Chem. Phys.*, 1967, **46**, 1862–1865.

[199] C. Earnest, in *Thermal Analysis in the Geosciences*, ed. W. Smykatz-Kloss and S. S. J. Warne, Springer-Verlag, Berlin, 1991, vol. 38, ch. 15, pp. 288–312.

[200] G. K. P. Dathar, D. Sheppard, K. J. Stevenson and G. Henkelman, *Chem. Mater.*, 2011, **23**, 4032–4037.

[201] M. Sebastian, in *Dielectric Materials for Wireless Communication*, ed. M. Sebastian, Elsevier Science, Amsterdam, 2008, ch. 3, pp. 49–82.

[202] S. Lee, C. A. Randall and Z. K. Liu, *J. Am. Ceram. Soc.*, 2007, **90**, 2589–2594.

[203] G. Pfaff, *J. Mater. Sci. Lett.*, 1991, **10**, 1059–1060.

[204] J. J. Ritter, R. S. Roth and J. E. Blendell, *J. Am. Ceram. Soc.*, 1986, **69**, 155–162.

[205] D. E. Rase and R. Roy, *J. Am. Ceram. Soc.*, 1955, **38**, 102–113.

[206] J. Bland, *Acta Crystallogr.*, 1961, **14**, 875–881.

[207] Y. Saito, H. Sato and Y. Sakabe, *J. Chem. Eng. Japan*, 2008, **41**, 441–446.

[208] Y. Saito and Y. Sakabe, *Fuel Cell*, 2005, **5**, 5–8.

[209] H. T. J. Reijers, G. D. Elzinga, P. D. Cobden, W. G. Haije and R. W. van den Brink, *Int. J. Greenh. Gas Control*, 2011, **5**, 531–537.

[210] I. Kumakiri, T. Okamoto, T. Murao, K. Tanaka and H. Kita, *Chem. Lett.*, 2015, **44**, 1016–1018.

[211] R. Inoue, S. Ueda, K. Wakuta, K. Sasaki and T. Ariyama, *ISIJ Int.*, 2010, **50**, 1532–1538.

[212] J. R. Gunter and G. B. Jameson, *Acta Crystallogr. Sect. C Cryst. Struct. Commun.*, 1984, **40**, 207–210.

[213] W. D. Parker and S. M. Nakhmanson, *Phys. Rev. B*, 2013, **88**, 245108.

[214] K. K. Wu and I. D. Brown, *Acta Crystallogr. Sect. B Struct. Sci.*, 1973, **29**, 2009–2012.

[215] B. Chen, F.-H. Liao, H. Jiao and X.-P. Jing, *Phase Transitions*, 2012, **86**, 380–390.

[216] S. J. Lee, M. D. Biegalski and W. M. Kriven, *J. Mater. Res.*, 1999, **14**, 3001–3006.

[217] T. Ahmad and A. K. Ganguli, *J. Mater. Res.*, 2004, **19**, 2905–2912.

[218] P. Ayyub, V. R. Palkar, S. Chattopadhyay and M. Multani, *Phys. Rev. B*, 1995, **51**, 6135–6138.

[219] O. Marks, J. R. Günter and F. Hofer, *React. Solids*, 1988, **6**, 217–230.

[220] G. H. Jonker and W. Kwestroo, *J. Am. Ceram. Soc.*, 1958, **41**, 390–394.

[221] K. H. Felgner, T. Muller, H. T. Langhammer and H. P. Abicht, *Mater. Lett.*, 2004, **58**, 1943–1947.

[222] V. Shanker, T. Ahmad and A. K. Ganguli, *Bull. Mater. Sci.*, 2004, **27**, 421–427.

[223] H. Marusawa and Y. Saito, *Key Eng. Mater.*, 2007, **350**, 143–146.

[224] P. Guo, B. Wang, M. Bauchy and G. Sant, *Cryst. Growth Des.*, 2016, **16**, 3124–3132.

[225] M. A. McCoy, R. W. Grimes and W. E. Lee, *Philos. Mag. A*, 1997, **75**, 833–846.

[226] T. S. Bush, J. D. Gale, C. R. a. Catlow and P. D. Battle, *J. Mater. Chem.*, 1994, **4**, 831.

[227] B. Jaffe, W. R. Cook and H. Jaffe, in *Piezoelectric Ceramics*, ed. B. Jaffe, W. R. Cook and H. Jaffe, Academic Press, London, 1971, vol. 3, ch. 5, pp. 53 – 114.

[228] K. Kreuer, *Annu. Rev. Mater. Res.*, 2003, **33**, 333–359.

[229] K. Wright, R. Freer and C. R. A. Catlow, *Phys. Chem. Miner.*, 1994, **20**, 500–503.

[230] M. Ahmadi, N. Phonthammachai, T. H. Shuan, T. J. White, N. Mathews and S. G. Mhaisalkar, *Org. Electron.*, 2010, **11**, 1660–1667.

[231] D. Lybye and N. Bonanos, *Solid State Ionics*, 1999, **125**, 339–344.

[232] J. Xiao, H. Zhang, Z. Yang, H. Wang, G. Ma and Z. Zhou, *J. Alloys Compd.*, 2012, **521**, 106–111.

[233] S. Peroos, Z. Du and N. H. De Leeuw, *Biomaterials*, 2006, **27**, 2150–2161.

[234] N. H. de Leeuw, J. R. Bowe and J. a. L. Rabone, *Faraday Discuss.*, 2007, **134**, 195–214; discussion 215–233, 415–419.

[235] J. Li, A. E. Smith, P. Jiang, J. K. Stalick, A. W. Sleight and M. A. Subramanian, *Inorg. Chem.*, 2015, **54**, 837–844.

[236] T. D. Archer, S. E. A. Birse, M. T. Dove, S. A. T. Redfern, J. D. Gale and R. T. Cygan, *Phys. Chem. Miner.*, 2003, **30**, 416–424.

[237] a. Pavese, M. Catti, S. C. Parker and a. Wall, *Phys. Chem. Miner.*, 1996, **23**, 89–93.

[238] M. Catti, A. Pavese and G. D. Price, *Phys. Chem. Miner.*, 1993, **19**, 472–479.

[239] T. D. Perry IV, R. T. Cygan and R. Mitchell, *Geochim. Cosmochim. Acta*, 2007, **71**, 5876–5887.

[240] C. D. Cappa and M. J. Elrod, *Phys. Chem. Chem. Phys.*, 2001, **3**, 2986–2994.

[241] S. Kerisit and S. C. Parker, *J. Am. Chem. Soc.*, 2004, **126**, 10152–10161.

[242] I. Trussov, A. Jarvis and P. R. Slater, *Experimental Investigations of Carbonaceous Defects in Barium Orthotitanate (unpublished)*, The university of birmingham technical report, 2017.

[243] R. D. Shannon, *Acta Crystallogr. Sect. A*, 1976, **32**, 751–767.

[244] B. Corrie, *PhD thesis*, University of Birmingham, 2015.

[245] J. Sansom, P. Sermon and P. Slater, *Solid State Ionics*, 2005, **176**, 1765–1768.

[246] T. Esaka, T. Ikebe and M. Kamata, *Solid State Ionics*, 1995, **76**, 237–242.

[247] P. R. Slater and P. Keenan, *Conductivity measurements of barium orthotitanate*, University of birmingham technical report, 2015.

[248] G. Pieper, W. Eysel and T. Hahn, *J. Am. Ceram. Soc.*, 1972, **55**, 619–622.

[249] J. P. Guha, *J. Mater. Sci.*, 1979, **14**, 1744–1748.

[250] R. Ropp, in *Encyclopedia of the Alkaline Earth Compounds*, ed. R. Ropp, Elsevier, Oxford, 2013, vol. 14, ch. 5, pp. 351–480.

[251] Klockow and W. Eysel, *JCPDS Grant-in-Aid Report*, Institut der universität heidelberg technical report, 1988.

[252] G. Hautier, C. Fischer, V. Ehrlacher, A. Jain and G. Ceder, *Inorg. Chem.*, 2011, **50**, 656–663.

[253] A. Jain, S. P. Ong, G. Hautier, W. Chen, W. D. Richards, S. Dacek, S. Cholia, D. Gunter, D. Skinner, G. Ceder and K. A. Persson, *APL Mater.*, 2013, **1**, 11002.

[254] A. Jain, *The Materials Project*, `www.materialsproject.org`, (Accessed: January 2016).

[255] D. J. Binks, *PhD thesis*, University of Surrey, 1994.

[256] G. V. Lewis and C. R. a. Catlow, *J. Phys. C Solid State Phys.*, 1985, **18**, 1149–1161.

[257] M. Cherry, M. Islam and C. Catlow, *J. Solid State Chem.*, 1995, **118**, 125–132.

[258] L. Minervini, M. O. Zacate and R. W. Grimes, *Solid State Ionics*, 1999, **116**, 339–349.

[259] L. Minervini, R. W. Grimes and K. E. Sickafus, *J. Am. Ceram. Soc.*, 2000, **83**, 1873–1878.

[260] M. R. Levy, *PhD thesis*, Imperial College London, 2005.

[261] C. R. A. Catlow, *J. Phys. Chem. Solids*, 1977, **38**, 1131–1136.

[262] T. B. Lee and M. L. McKee, *Inorg. Chem.*, 2011, **50**, 11412–11422.

[263] J. F. Paulson, in *Ion-Molecule Reactions*, ed. J. L. Franklin, Springer US, Boston, 1972, vol. 1, ch. 4, pp. 77–100.

[264] D. R. Bates, *Adv. At. Mol. Opt. Phys.*, 1990, **27**, 1–80.

[265] J. F. Hiller and M. L. Vestal, *J. Chem. Phys.*, 1980, **72**, 4713–4722.

[266] G. V. Lewis and C. R. A. Catlow, *J. Phys. Chem. Solids*, 1986, **47**, 89–97.

Appendix A

Cd_2GeO_4

A.1 Supplementary Information

Table A.1: Interatomic potential and shell model parameters for dopants in Cd_2GeO_4. Buckingham potentials are for M-O interactions. Binary oxide lattice energies and isolated point defect energies are included for each dopant.

Ion	Reference	E_{Latt} (eV)	M^n_{Ge} (eV)	$M^n_{Cd_I}$ (eV)	$M^n_{Cd_{II}}$ (eV)
K^+	[226]	-23.41	88.99	17.21	17.52
Li^+	[255]	-31.28	87.08	13.27	14.14
Na^+	[255]	-26.52	87.38	14.89	15.52
Rb^+	[97]	-21.22	90.74	19.61	19.75
Ba^{2+}	[256]	-31.23	77.91	7.43	6.69
Ca^{2+}	[256]	-36.05	72.34	1.41	1.24
Co^{2+}	[255]	-40.07	67.39	-2.10	-1.82
Fe^{2+}	[256]	-39.56	67.89	-1.69	-1.45
Mg^{2+}	[256]	-40.55	66.93	-2.46	-2.15
Mn^{2+}	[256]	-38.56	69.10	-0.91	-0.77
Ni^{2+}	[256]	-40.60	66.73	-2.46	-2.15
Sr^{2+}	[256]	-33.44	75.47	4.38	3.91
Zn^{2+}	[255]	-39.34	68.12	-1.25	-1.05
Al^{3+}	[256]	-161.00	33.61	-31.18	-31.14
Co^{3+}	[257]	-157.31	35.93	-29.83	-29.79
Fe^{3+}	[256]	-150.37	39.35	-26.91	-27.06
Ga^{3+}	[258]	-155.57	37.22	-29.20	-29.20
Gd^{3+}	[258]	-133.26	50.16	-18.73	-19.61
In^{3+}	[258]	-141.25	45.25	-22.70	-23.21
La^{3+}	[259]	-127.40	53.28	-15.94	-17.05
Nd^{3+}	[260]	-130.20	39.26	-17.49	-18.47

Table is continued on page 140

Continuation of table A.1 on page 139

Ion	Reference	E_{Latt} (eV)	M^n_{Ge} (eV)	$M^n_{Cd_I}$ (eV)	$M^n_{Cd_{II}}$ (eV)
Sc^{3+}	[260]	-145.66	42.85	-24.76	-25.10
Mn^{3+}	[257]	-151.46	39.26	-27.24	-27.37
Y^{3+}	[259]	-135.53	48.74	-19.90	-20.67
Pr^{3+}	[260]	-128.98	52.33	-16.82	-17.87
Eu^{3+}	[260]	-132.27	50.47	-18.46	-19.36
Ce^{3+}	[260]	-128.69	52.50	-16.66	-17.72
Sm^{3+}	[259]	-131.87	51.01	-17.99	-18.93
Ce^{4+}	[97]	-104.29	22.46	-44.27	-45.82
Mn^{4+}	[97]	-114.02	9.85	-54.80	-55.70
Pb^{4+}	[97]	-103.48	23.60	-43.32	-44.93
Si^{4+}	[97]	-128.68	-8.15	-68.72	-69.25
Sn^{4+}	[97]	-111.01	12.04	-52.03	-53.03
Ti^{4+}	[256]	-112.51	8.60	-53.53	-54.43
Zr^{4+}	[256]	-110.91	13.80	-51.48	-52.57

Table A.2: Solution energies (eV) for M^+ doping of Cd_2GeO_4 cation sites *via* the constant cation (CC) and constant oxygen (CO) mechanisms discussed in section 3.3.1.

Dopant	CC-Ge	CC-Cd_I	CC-Cd_{II}	CO-Ge	CO-Cd_I	CO-Cd_{II}
K^+	12.23	2.48	2.78	11.84	2.12	2.43
Li^+	14.25	2.47	3.33	13.87	2.12	2.98
Na^+	12.17	1.71	2.33	11.78	1.35	1.98
Rb^+	12.89	3.78	3.92	12.50	3.42	3.56

Table A.3: Solution energies (eV) for M^{2+} doping of Cd_2GeO_4 cation sites *via* the constant cation (*CC*), constant oxygen (*CO*) and isovalent (*Iso*) mechanisms discussed in section 3.3.2.

Dopant	*CC*-Ge	*CO*-Ge	*Iso*-Cd_I	*Iso*-Cd_{II}
Ba^{2+}	9.64	9.38	1.18	0.44
Ca^{2+}	8.88	8.63	-0.02	-0.20
Cd^{2+}	8.60	8.34	-	-
Co^{2+}	7.96	7.70	0.49	0.77
Cu^{2+}	8.77	8.51	1.67	2.31
Fe^{2+}	7.94	7.68	0.39	0.62
Mg^{2+}	7.98	7.72	0.60	0.92
Mn^{2+}	8.15	7.90	0.17	0.31
Ni^{2+}	7.83	7.57	0.67	0.98
Sr^{2+}	9.41	9.16	0.34	-0.13
Zn^{2+}	7.96	7.71	0.62	0.81

Table A.4: Solution energies (eV) for M^{3+} doping of Cd_2GeO_4 cation sites *via* the constant cation (*CC*) and constant oxygen (*CO*) mechanisms discussed in section 3.3.3.

Dopant	*CC*-Ge	*CC*-Cd_I	*CC*-Cd_{II}	*CO*-Ge	*CO*-Cd_I	*CO*-Cd_{II}
Al^{3+}	3.58	3.93	3.98	3.45	4.16	4.20
Co^{3+}	4.05	3.44	3.48	3.92	3.67	3.70
Fe^{3+}	4.01	2.89	2.73	3.88	3.12	2.96
Ga^{3+}	4.47	3.19	3.20	4.34	3.42	3.42
Gd^{3+}	6.25	2.51	1.63	6.13	2.74	1.86
In^{3+}	5.34	2.53	2.03	5.21	2.76	2.26
Pr^{3+}	6.28	2.28	1.24	6.15	2.51	1.46
Eu^{3+}	6.07	2.29	1.38	5.94	2.51	1.61
Ce^{3+}	6.31	2.29	1.24	6.18	2.52	1.47
Sm^{3+}	6.41	2.56	1.61	6.28	2.78	1.84
La^{3+}	6.45	2.37	1.26	6.32	2.60	1.48
Mn^{3+}	4.45	3.09	2.97	4.32	3.32	3.20
Nd^{3+}	6.15	2.22	1.23	6.03	2.45	1.46
Y^{3+}	5.98	2.48	1.70	5.85	2.70	1.93
Sc^{3+}	5.14	2.68	2.34	5.01	2.91	2.57

Table A.5: Solution energies (eV) for M^{4+} doping of Cd_2GeO_4 cation sites *via* the constant cation (*CC*), constant oxygen (*CO*) and isovalent (*Iso*) mechanisms discussed in section 3.3.4.

Dopant	*Iso*-Ge	*CC*-Cd_I	*CC*-Cd_{II}	*CO*-Cd_I	*CO*-Cd_{II}
Ce^{4+}	5.18	6.72	5.17	7.17	5.63
Ge^{4+}	-	5.43	4.92	5.89	5.37
Mn^{4+}	2.30	5.92	5.02	6.38	5.48
Pb^{4+}	5.51	6.86	5.25	7.32	5.71
Si^{4+}	-1.04	6.66	6.13	7.11	6.59
Sn^{4+}	1.48	5.68	4.67	6.14	5.13
Ti^{4+}	-0.46	5.68	4.78	6.14	5.24
Zr^{4+}	3.14	6.13	5.04	6.58	5.49

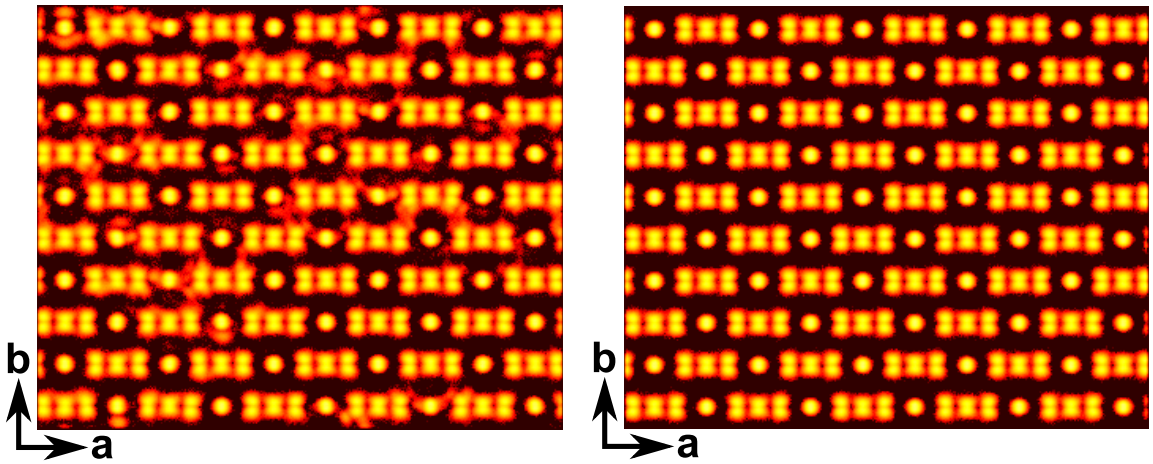

(a) (b)

Figure A.1: Oxygen density map of the a) $Cd_{1.9}Y_{0.1}GeO_{4.05}$ and b) Cd_2GeO_4 systems 1273 K viewed orthogonal to the *ab*-plane, with lighter shades indicating higher densities.

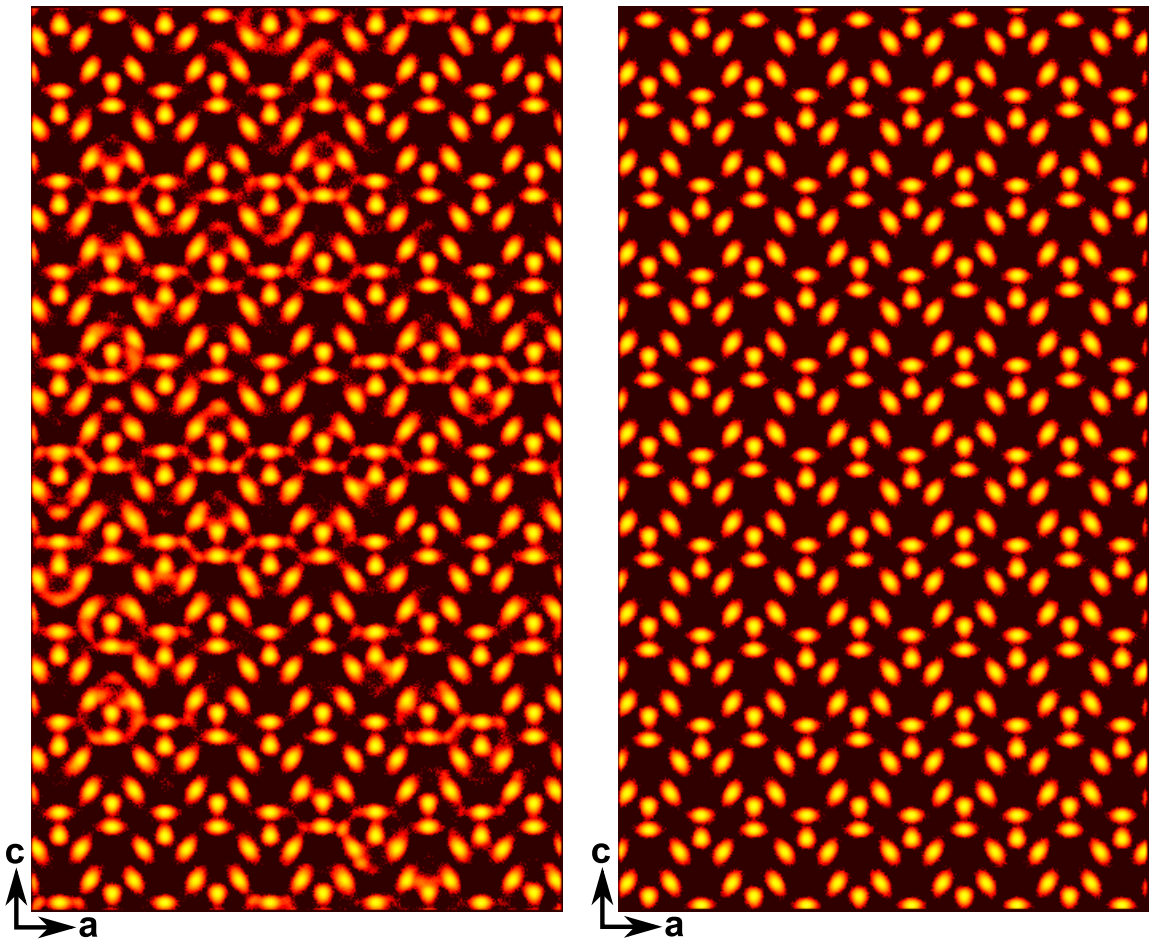

(a) (b)

Figure A.2: Oxygen density map of the a) $Cd_{1.9}Y_{0.1}GeO_{4.05}$ and b) Cd_2GeO_4 systems at 1273 K viewed orthogonal to the *ac*-plane, with lighter shades indicating higher densities.

Table A.6: Diffusion coefficients (D) calculated for oxygen in $Cd_{1.9}Y_{0.1}GeO_{4.05}$ and $Cd_{1.9}Nd_{0.1}GeO_{4.05}$.

Temperature (K)	D (cm^2 s^{-1})	
	$Cd_{1.9}Y_{0.1}GeO_{4.05}$	$Cd_{1.9}Nd_{0.1}GeO_{4.05}$
873	3.02×10^{-10}	$4.82\times10^{-10\dagger}$
1073	2.35×10^{-9}	2.87×10^{-9}
1273	1.03×10^{-8}	9.16×10^{-9}
1473	3.50×10^{-8}	2.34×10^{-8}

† Extrapolated from high temperature data.

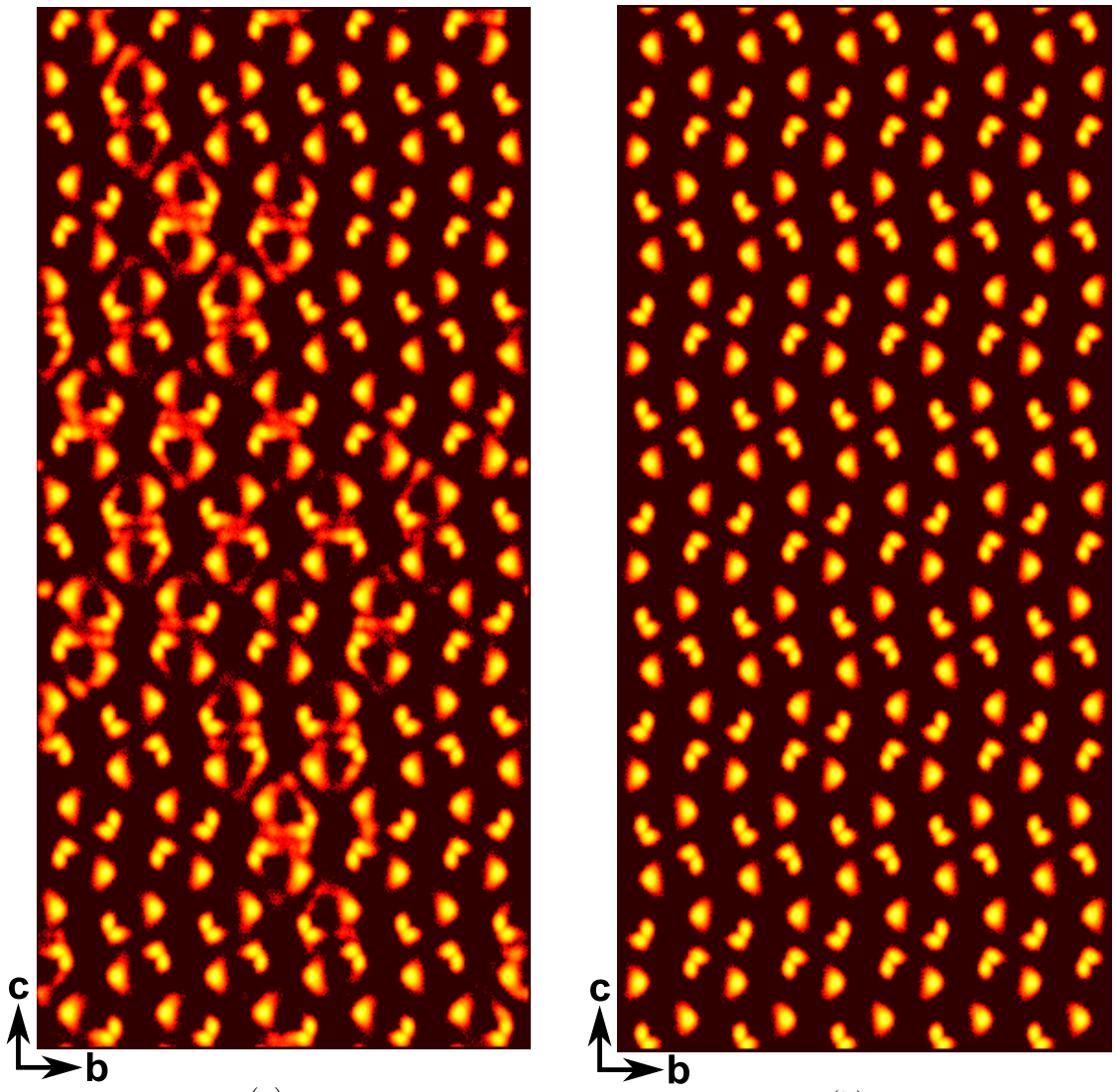

(a) (b)

Figure A.3: Oxygen density map of the a) $Cd_{1.9}Y_{0.1}GeO_{4.05}$ and b) Cd_2GeO_4 systems 1273 K viewed orthogonal to the *bc*-plane, with lighter shades indicating higher densities.

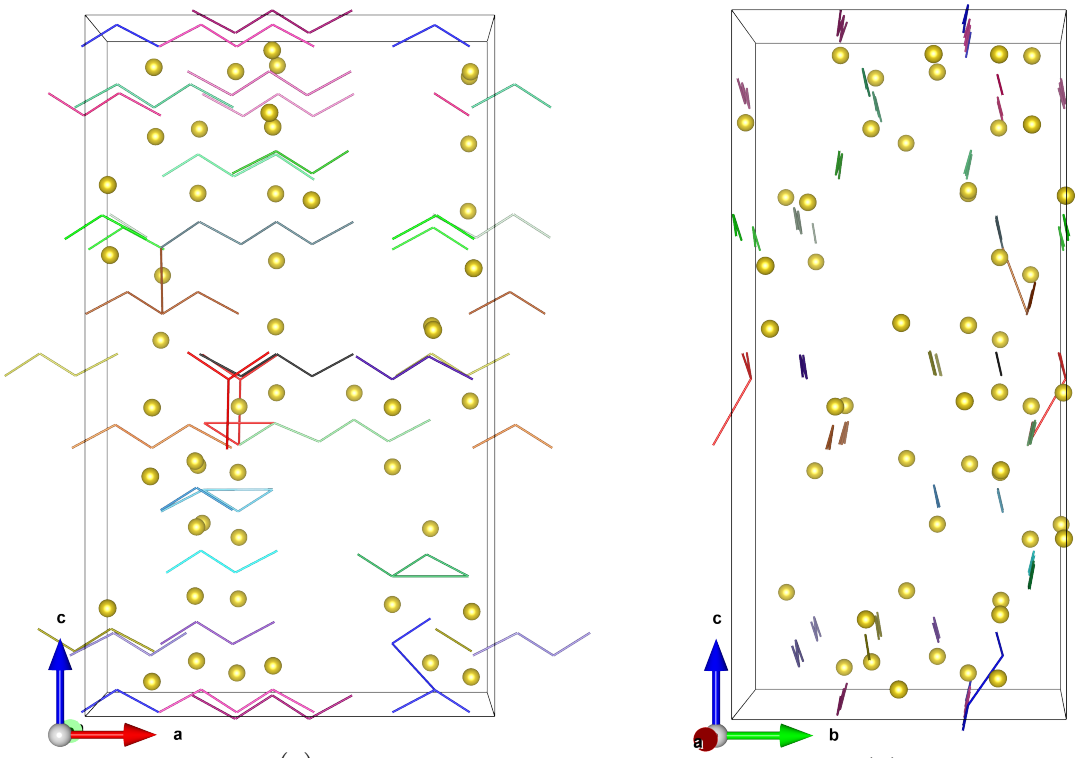

(a) (b)

Figure A.4: Schematic representation of oxygen defect migration during a 3 ns simulation of $Cd_{1.9}Y_{0.1}GeO_{4.05}$ at 1073 K as viewed down the a) *a*-axis and the b) *b*-axis. Coloured lines represent an oxide defect migrating from one tetrahedra to another and the gold spheres represent the Y ions. Colouring is used to separate the individual defects that were tracked.

Table A.7: Axial diffusion coefficients for oxygen in $Cd_{1.9}Y_{0.1}GeO_{4.05}$ at 1473 K.

Axis	D (cm^2 s^{-1})	Ratio
a	1.90×10^{-8}	4
b	4.89×10^{-9}	1
c	1.15×10^{-8}	2

Appendix B

Ba_2TiO_4

B.1 Derivation of E_{OT}

To ensure the energies calculated for CO_3^{2-} incorporation were accurate, a term (E_{OT}) was included to account for the energy of the $O^{2-}+CO_2 \rightarrow CO_3^{2-}$ reaction. Two pathways were generated to allow E_{OT} to be derived using literature values available at the time of study, the mechanisms of which are given below:

Pathway A

$$O^{2-} \rightarrow O^- + e^- \quad \text{(B.1)}$$
$$O^- + CO_2 \rightarrow CO_3^- \quad \text{(B.2)}$$
$$CO_3^- + e^- \rightarrow CO_3^{2-} \quad \text{(B.3)}$$

Pathway B

$$O^{2-} \rightarrow O^- + e^- \quad \text{(B.4)}$$
$$O^- \rightarrow O + e^- \quad \text{(B.5)}$$
$$O + CO_2 \rightarrow CO_3 \quad \text{(B.6)}$$
$$CO_3 + e^- \rightarrow CO_3^- \quad \text{(B.7)}$$
$$CO_3^- + e^- \rightarrow CO_3^{2-} \quad \text{(B.8)}$$

For brevity E_{ea}^1 and E_{ea}^2 denote 1^{st} and 2^{nd} electron affinities, and $D(CO_2\text{-}O)$ the bond dissociation energy of a C-O bond in CO_3. The following equations were used to calculate E_{OT} *via* pathways A and B:

Pathway A: E_{OT} = -E_{ea}^2(O) + -$D(CO_2\text{–}O^{2-})$ + $E_{ea}^2(CO_3)$ = -14.33
Pathway B: E_{OT} = -E_{ea}^2(O) + -E_{ea}^1(O) + -$D(CO_2\text{–}O)$ + $E_{ea}^1(CO_3)$ + $E_{ea}^2(CO_3)$ = -14.41

The average of these two values, -14.37 eV, was used in all carbonate calculations. E_{ea}^1(O) and E_{ea}^2(O) values of -1.46 and 8.27 eV were used respectively.[188,261] $E_{ea}^1(CO_3)$ and $E_{ea}^2(CO_3)$ values of -3.50 and -3.80 eV were taken from Lee and McKee[262] & Cappa and Elrod[240], with the former being an average. Using data from Paulson[263] & Bates[264] $D(CO_2\text{-}O)$ was calculated as 0.3 eV, a value of 2.26 eV for $D(CO_2\text{-}O^{2-})$ was used in accord with Hiller and Vestal[265].

B.2 Supplementary Information

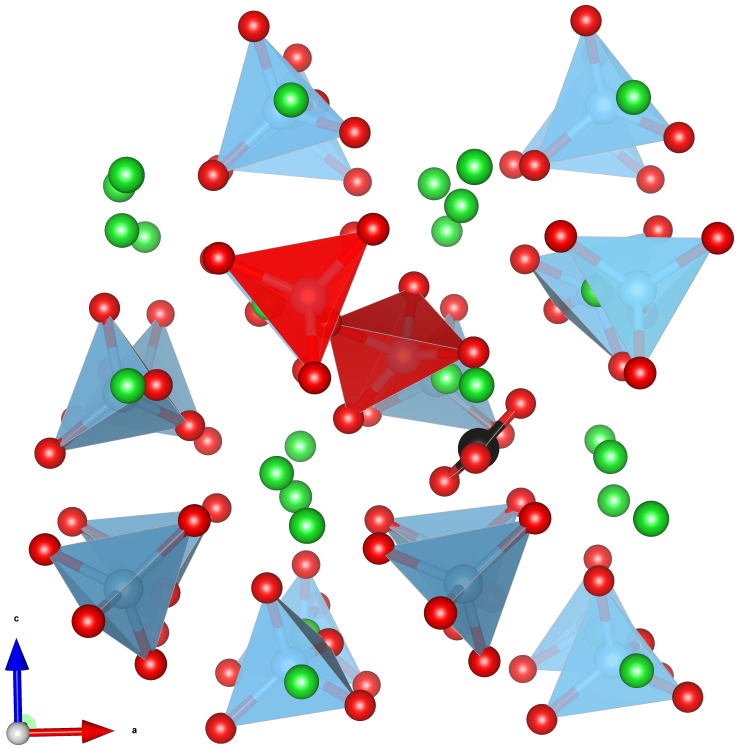

(a)

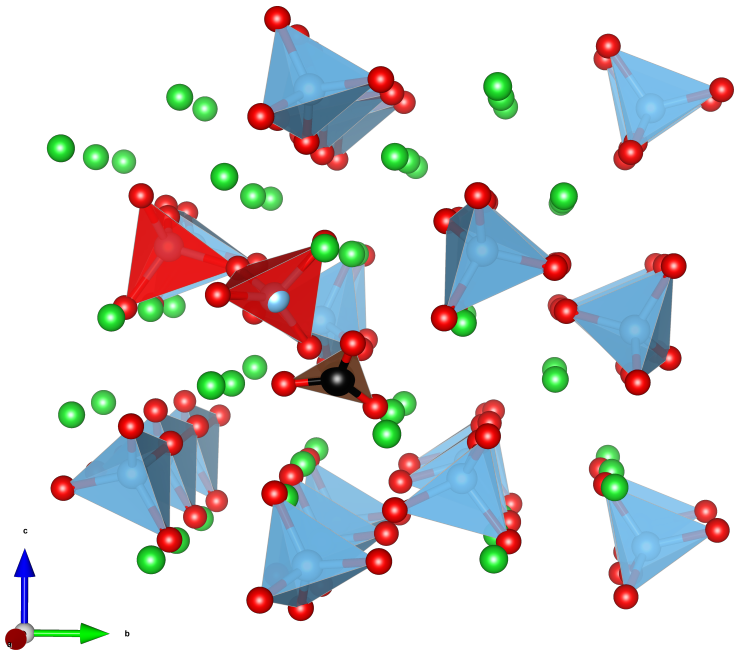

(b)

Figure B.1: $[(CO_3)_i'' + V_O^{\bullet\bullet}]$ defect in α′-Ba_2TiO_4 viewed down the a) b-axis and b) a-axis. Green, blue, red and black spheres indicate Ba, Ti, O and C ions respectively, and blue, red and brown polyhedra TiO_4, "Ti_2O_7" and CO_3 units.

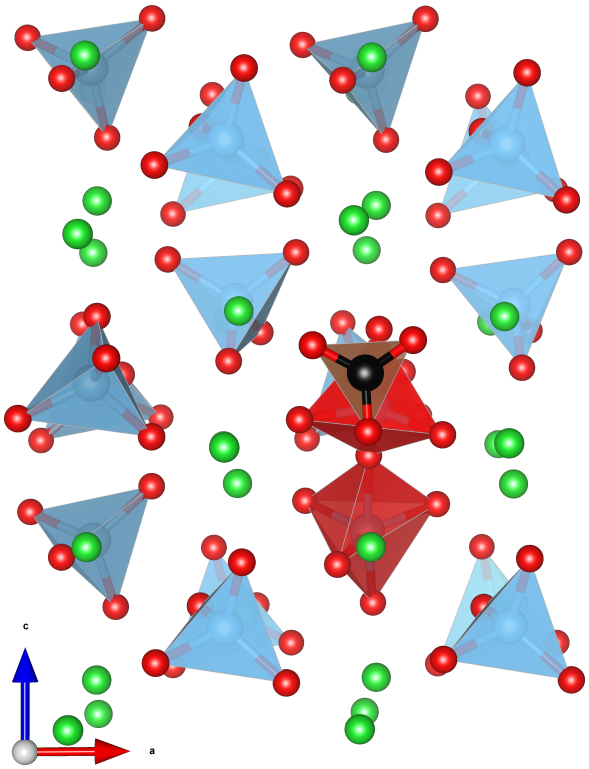

(a)

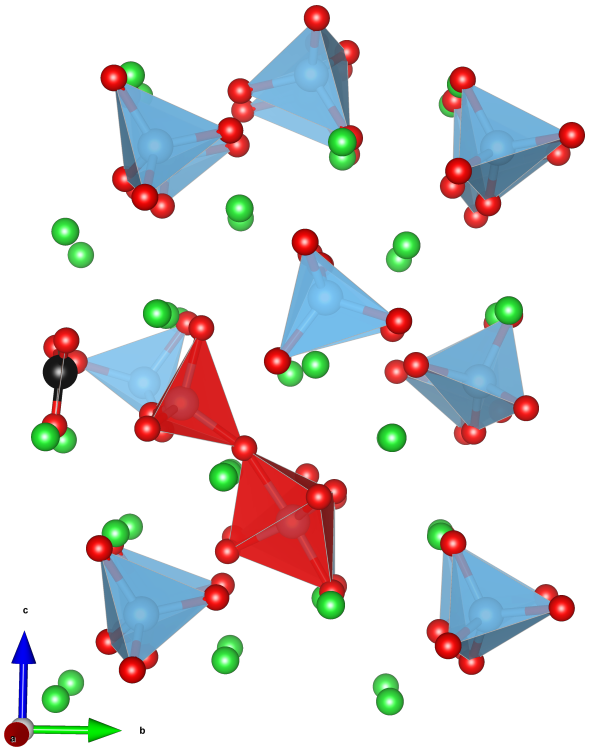

(b)

Figure B.2: Images of a $(CO_3)_i''$ defect in a α'-Ba_2TiO_4 lattice viewed down the a) b-axis and b) a-axis. Green, blue, red and black spheres indicate Ba, Ti, O and C ions respectively, and blue, red and brown polyhedra TiO_4, "Ti_2O_8" and CO_3 units.

Table B.1: Solution energies for M^+ doping of β-Ba_2TiO_4 cation sites *via* the constant cation and constant oxygen mechanisms discussed in section 4.4.1.

	Constant cation			Constant oxygen		
Dopants	Ba_I	Ba_{II}	Ti	Ba_I	Ba_{II}	Ti
Li^+	2.92	3.63	13.74	4.39	5.10	15.65
Na^+	2.17	2.66	13.70	3.64	4.12	15.62
K^+	1.88	2.49	14.70	3.35	3.96	16.62
Rb^+	2.03	2.72	15.21	3.50	4.19	17.13

Table B.2: Solution energies for M^+ doping of α′-Ba_2TiO_4 cation sites *via* the constant cation and constant oxygen mechanisms discussed in section 4.4.1.

	Constant cation solution energies (eV)								
Dopant	Ba_I	Ba_{II}	Ba_{III}	Ba_{IV}	Ba_V	Ba_{VI}	Ti_I	Ti_{II}	Ti_{III}
Li^+	3.29	3.17	3.20	3.51	3.62	3.39	12.03	12.52	12.42
Na^+	2.30	2.21	2.04	2.66	2.65	2.55	12.72	13.26	13.10
K^+	2.01	1.86	1.64	2.55	2.59	2.48	14.00	14.50	14.06
Rb^+	2.14	1.95	1.73	2.77	2.86	2.74	14.75	15.26	14.64

	Constant oxygen solution energies (eV)								
Dopant	Ba_I	Ba_{II}	Ba_{III}	Ba_{IV}	Ba_V	Ba_{VI}	Ti_I	Ti_{II}	Ti_{III}
Li^+	4.42	4.29	4.33	4.64	4.74	4.52	13.89	14.39	14.29
Na^+	3.43	3.34	3.16	3.79	3.78	3.68	14.59	15.13	14.96
K^+	3.14	2.98	2.77	3.68	3.71	3.61	15.87	16.37	15.93
Rb^+	3.27	3.08	2.85	3.90	3.99	3.86	16.61	17.13	16.50

Table B.3: Solution energies for M^{3+} doping of β-Ba_2TiO_4 cation sites *via* the constant cation and constant oxygen mechanisms discussed in section 4.4.2.

	Constant cation			Constant oxygen		
Dopants	Ba_I	Ba_{II}	Ti	Ba_I	Ba_{II}	Ti
Al^{3+}	7.53	8.22	3.37	7.36	8.05	4.01
Cr^{3+}	7.36	7.27	4.01	7.19	7.10	4.65
Ga^{3+}	5.37	8.66	4.06	5.20	8.49	4.70
Fe^{3+}	7.84	5.96	4.23	7.67	5.79	4.86
Sc^{3+}	7.39	7.63	4.75	7.22	7.46	5.39
In^{3+}	4.77	5.83	5.33	4.60	5.66	5.97
Y^{3+}	5.90	5.07	5.85	5.73	4.90	6.49
Gd^{3+}	4.69	4.61	6.81	4.52	4.44	7.44
Nd^{3+}	4.41	3.97	7.21	4.23	3.80	7.85
Pr^{3+}	3.68	3.39	7.23	3.50	3.22	7.87
Ce^{3+}	3.39	3.20	7.39	3.21	3.03	8.03
La^{3+}	3.34	3.06	7.45	3.17	2.89	8.09

Table B.4: Solution energies for M^{3+} doping of α'-Ba_2TiO_4 cation sites *via* the constant cation and constant oxygen mechanisms discussed in section 4.4.2.

	Constant cation solution energies (eV)								
Dopant	Ba_I	Ba_{II}	Ba_{III}	Ba_{IV}	Ba_V	Ba_{VI}	Ti_I	Ti_{II}	Ti_{III}
Al^{3+}	4.87	12.62	10.12	6.09	9.00	6.40	3.33	3.47	3.44
Cr^{3+}	5.71	7.01	4.75	5.74	7.77	6.08	3.98	4.08	4.01
Ga^{3+}	5.67	6.95	4.75	5.71	7.69	6.05	4.03	4.13	4.05
Fe^{3+}	5.55	6.44	4.75	6.15	7.39	5.98	4.20	4.28	4.20
Sc^{3+}	5.55	5.58	5.92	5.45	5.58	6.16	5.30	5.30	5.19
In^{3+}	4.89	4.81	4.83	4.66	5.29	5.23	5.80	5.77	5.63
Y^{3+}	4.41	3.96	4.26	3.89	4.19	4.29	6.56	6.59	6.42
Gd^{3+}	4.12	3.76	4.30	3.58	3.66	3.83	6.85	6.93	6.75
Nd^{3+}	3.40	3.14	3.47	2.82	2.91	3.15	6.80	6.90	6.75
Pr^{3+}	3.27	3.04	3.37	2.69	2.77	3.00	6.94	7.02	6.90
Ce^{3+}	3.21	3.00	3.33	2.63	2.71	2.93	6.99	7.07	6.97
La^{3+}	3.04	2.89	3.23	2.50	2.58	2.76	7.13	7.19	7.12

	Constant oxygen solution energies (eV)								
Dopant	Ba_I	Ba_{II}	Ba_{III}	Ba_{IV}	Ba_V	Ba_{VI}	Ti_I	Ti_{II}	Ti_{III}
Al^{3+}	4.66	12.41	9.91	5.87	8.78	6.19	3.95	4.09	4.06
Cr^{3+}	5.49	6.79	4.54	5.52	7.56	5.86	4.61	4.70	4.63
Ga^{3+}	5.46	6.73	4.54	5.50	7.47	5.84	4.66	4.75	4.68
Fe^{3+}	5.34	6.23	4.53	5.93	7.17	5.77	4.82	4.90	4.82
Sc^{3+}	5.34	5.36	5.70	5.23	5.37	5.95	5.92	5.92	5.81
In^{3+}	4.67	4.59	4.61	4.44	5.07	5.01	6.43	6.39	6.25
Y^{3+}	4.19	3.74	4.05	3.68	3.98	4.08	7.18	7.21	7.04
Gd^{3+}	3.90	3.54	4.09	3.36	3.44	3.62	7.47	7.55	7.37
Nd^{3+}	3.18	2.92	3.25	2.61	2.70	2.94	7.42	7.53	7.37
Pr^{3+}	3.05	2.82	3.16	2.47	2.56	2.78	7.56	7.65	7.53
Ce^{3+}	3.00	2.78	3.12	2.42	2.50	2.72	7.61	7.69	7.59
La^{3+}	2.82	2.68	3.01	2.28	2.36	2.55	7.75	7.81	7.75

Table B.5: References for the interatomic Buckingham potentials used for Ba_2TiO_4 dopants, combined with relevant calculated binary oxide lattice energies and isolated point defect energies.

Ion	Ref.	E_{Latt}	β-Phase Sites (eV)			α′-Phase Sites (eV)								
			M^n_{Ti}	$M^n_{Ba_I}$	$M^n_{Ba_{II}}$	$M^n_{Ti_I}$	$M^n_{Ti_{II}}$	$M^n_{Ti_{III}}$	$M^n_{Ba_I}$	$M^n_{Ba_{II}}$	$M^n_{Ba_{III}}$	$M^n_{Ba_{IV}}$	$M^n_{Ba_V}$	$M^n_{Ba_{VI}}$
Li^+	[266]	-29.09	95.54	11.02	11.73	93.81	94.30	94.20	11.39	11.26	11.29	11.60	11.71	11.49
Na^+	[266]	-24.90	97.61	12.36	12.85	96.60	97.14	96.97	12.49	12.40	12.22	12.85	12.83	12.74
K^+	[266]	-22.22	99.94	13.41	14.02	99.22	99.72	99.28	13.53	13.38	13.17	14.07	14.11	14.01
Rb^+	[266]	-21.23	100.95	14.06	14.75	100.46	100.98	100.35	14.16	13.98	13.75	14.79	14.88	14.76
Al^{3+}	[260]	-162.01	39.03	-34.00	-33.31	38.98	39.12	39.09	-36.52	-28.77	-31.27	-35.30	-32.39	-34.99
Cr^{3+}	[260]	-155.01	43.18	-30.67	-30.75	43.14	43.24	43.17	-32.18	-30.88	-33.13	-32.15	-30.11	-31.81
Ga^{3+}	[260]	-154.49	43.48	-32.40	-29.11	43.45	43.54	43.47	-31.96	-30.68	-32.88	-31.92	-29.94	-31.58
Fe^{3+}	[260]	-152.73	44.53	-29.05	-30.93	44.50	44.58	44.50	-31.19	-30.30	-32.00	-30.60	-29.36	-30.76
Ti^{3+}	[256]	-150.98	45.92	-28.62	-28.39	0.00	0.00	0.00	-68.37	-69.16	-72.34	-70.85	-70.10	-69.05
Sc^{3+}	[260]	-145.69	49.15	-28.60	-27.54	49.11	49.11	49.00	-27.68	-27.65	-27.31	-27.78	-27.65	-27.07
In^{3+}	[260]	-141.30	51.87	-25.27	-26.10	51.81	51.78	51.64	-26.14	-26.22	-26.20	-26.37	-25.74	-25.80
Y^{3+}	[260]	-135.24	55.86	-23.45	-23.53	55.60	55.63	55.46	-23.59	-24.04	-23.74	-24.11	-23.81	-23.71
Gd^{3+}	[260]	-133.43	57.16	-22.83	-23.27	56.79	56.88	56.69	-22.98	-23.34	-22.79	-23.52	-23.44	-23.27
Nd^{3+}	[260]	-130.18	58.81	-21.94	-22.22	58.37	58.47	58.31	-22.08	-22.34	-22.00	-22.65	-22.56	-22.32
Pr^{3+}	[260]	-129.16	59.48	-21.72	-21.91	59.02	59.11	58.98	-21.69	-21.93	-21.59	-22.28	-22.19	-21.96
Ce^{3+}	[260]	-128.71	59.77	-21.54	-21.81	59.30	59.38	59.27	-21.52	-21.74	-21.40	-22.10	-22.02	-21.80
La^{3+}	[260]	-127.53	61.20	-21.06	-21.36	60.02	60.08	60.02	-21.11	-21.26	-20.92	-21.65	-21.57	-21.38

Table B.6: Binding energies (eV) of the most clustered $2M'_{Ti}$:$V_O^{\bullet\bullet}$ conformations in Ba_2TiO_4, values for $V_O^{\bullet\bullet}$ at infinite separation also given.

Dopant Placement	Proximal $V_O^{\bullet\bullet}$		Isolated $V_O^{\bullet\bullet}$	
	Al	Ga	Al	Ga
1^{st} Nearest neighbours	-2.85	-3.25	0.33	0.36
2^{nd} Nearest neighbours	-2.63	-2.88	0.37	0.44
3^{rd} Nearest neighbours	-2.52	-2.44	0.39	0.41
4^{th} Nearest neighbours	-2.46	-2.57	0.42	0.43
5^{th} Nearest neighbours	-2.43	-2.57	0.41	0.43

Table B.7: Binding energies (eV) of the most clustered $2M'_{Ba_I}$:$V_O^{\bullet\bullet}$ conformations in Ba_2TiO_4, values for $V_O^{\bullet\bullet}$ at infinite separation also given.

Dopant Placement	Proximal $V_O^{\bullet\bullet}$			Isolated $V_O^{\bullet\bullet}$		
	Na^+	K^+	Rb^+	Na^+	K^+	Rb^+
1^{st} Nearest Neighbours	-1.75	-1.89	-2.05	0.53	0.41	0.36
2^{nd} Nearest Neighbours	-1.96	-2.02	-2.12	0.38	0.28	0.22
3^{rd} Nearest Neighbours	-1.60	-1.39	-1.50	0.35	0.32	0.31
4^{th} Nearest Neighbours	-1.66	-1.52	-1.68	0.40	0.44	0.45
5^{th} Nearest Neighbours	-1.90	-1.76	-1.83	0.33	0.34	0.33
6^{th} Nearest Neighbours	-2.15	-2.02	-1.98	0.41	0.43	0.43
7^{th} Nearest Neighbours	-1.88	-1.92	-1.97	0.29	0.35	0.38
8^{th} Nearest Neighbours	-1.58	-1.41	-1.46	0.38	0.43	0.45

PCCP

PAPER

View Article Online
View Journal | View Issue

Cite this: *Phys. Chem. Chem. Phys.*, 2016, **18**, 26284

A computational study of doped olivine structured Cd_2GeO_4: local defect trapping of interstitial oxide ions†

Adam J. McSloy,[a] Paul F. Kelly,[a] Peter R. Slater[b] and Pooja M. Panchmatia*[a]

Received 5th August 2016,
Accepted 2nd September 2016

DOI: 10.1039/c6cp05436f

www.rsc.org/pccp

Computational modelling techniques have been employed to investigate defects and ionic conductivity in Cd_2GeO_4. We show due to highly unfavourable intrinsic defect formation energies the ionic conducting ability of pristine Cd_2GeO_4 is extremely limited. The modelling results suggest trivalent doping on the Cd site as a viable means of promoting the formation of the oxygen interstitial defects. However, the defect cluster calculations for the first time explicitly suggest a strong association of the oxide defects to the dopant cations and tetrahedral units. Defect clustering is a complicated phenomenon and therefore not trivial to assess. In this study the trapping energies are explicitly quantified. The trends are further confirmed by molecular dynamic simulations. Despite this, the calculated diffusion coefficients do suggest an enhanced oxide ion mobility in the doped system compared to the pristine Cd_2GeO_4.

1 Introduction

In the search for new oxide ion conductors, perovskite, fluorite and apatite type materials have been the focus of most investigations due to their fast oxide ion conducting abilities.[1] Although such materials are promising, many different structural classes remain as yet uninvestigated. The oxygen-rich apatite-type conductors differ from most in that ionic conduction occurs *via* a faster interstitial mechanism rather than a vacancy mechanism.[2] Fast interstitial oxide conduction is often observed in oxygen excess materials which possess flexible tetrahedral frameworks, such as apatites or melilites.[2–6] As a result of this one could envisage that structures with similar frameworks capable of accommodating interstitial oxide ions may also present fast ionic conductivities. One such material is cadmium orthogermanate (Cd_2GeO_4) which is of interest due to its structural similarity to the apatites in that it possesses isolated tetrahedra and so may be prone to interstitial formation *via* either isolated interstitial oxide ion defects, or by increasing the coordination sphere of Ge, as in the apatite systems, and hence showing enhanced ionic conductivity. Its olivine structure is also of interest since Li-containing olivines have been shown to be good ionic conductors, albeit Li ions conductors *via* a vacancy mechanism.[7] Still, this material's open structure does warrant further investigation as a potential oxide ion conductor.

Cadmium orthogermanate, of the formula Cd_2GeO_4, crystallises with an orthorhombic olivine type *Pmcn* structure. As shown in Fig. 1 the Cd ions occupy two distinct lattice sites. The O ions coordinate octahedrally to the Cd ions and tetrahedrally to the Ge ions. The isolated GeO_4 groups form channels down the *b*-axis and are spaced both vertically and horizontally by channels of Cd_I and Cd_{II} ions. To date, there is no literature on the applications of Cd_2GeO_4 as a solid oxide fuel cell (SOFC) material, however Whipple *et al.* reported the semiconducting properties for Cd_2GeO_4 in the 80's.[8] They found that conductivity is enhanced when doping with trivalent metal ions for samples heated under a vacuum, where they suggested that the electrons originate from shallow donors with their mobility determined by

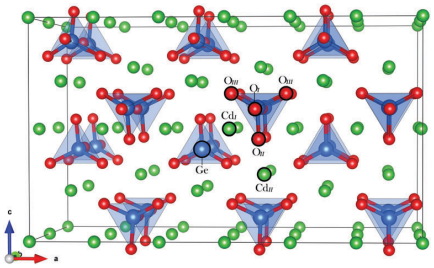

Fig. 1 Structure of Cd_2GeO_4 with Ge, Cd and O ions represented as blue, green and red spheres respectively and GeO_4 tetrahedra in blue.

[a] *Department of Chemistry, Loughborough University, Loughborough LE11 3TU, UK. E-mail: p.panchmatia@lboro.ac.uk*
[b] *School of Chemistry, The University of Birmingham, Edgbaston, Birmingham B15 2TT, UK*

† Electronic supplementary information (ESI) available. See DOI: 10.1039/c6cp05436f

a combination of large polaron formation and impurity scattering. They also reported a large drop in electrical conductivity is observed upon exposure to oxygen which is thought to originate from the reversible chemisorption of oxygen onto the surface of the grains.

2 Computational methodology

The simulation methods employed in this study are reviewed in brief here, but more comprehensive reviews can be found elsewhere.[9–11] Interatomic potential based energy minimisation calculations were performed using the general utility lattice program (GULP)[12,13] and molecular dynamics simulations using DL_POLY classic.[14] Images in this paper were generated using VESTA visualisation software.[15]

Calculations were based on the Born model for ionic solids where ionic interactions are described using a long range Coulombic term and an analytical function representing the short-range Pauli repulsion and attractive van der Waals interactions. In this work the short-range interactions were described with the Buckingham potential:[16]

$$\Phi_{ij}(r_{ij}) = A\exp\left(-\frac{r_{ij}}{\rho}\right) - \frac{C}{r_{ij}^{6}} \quad (1)$$

where Φ_{ij} is the potential energy resulting from the interaction between ions i and j at a distance of r. A, ρ and C are the empirically derived potential parameters specific to each interaction. Potentials from various literature sources were screened to identify a preliminary potential set. These potentials were then empirically fitted to the experimental structure with a high degree of agreement.[17] The interatomic potentials where then further vetted in their respective binary oxides. The final interatomic potentials are presented in Table 1. Potentials selected to model the dopants,[18,19] discussed later, were verified by testing them in their respective binary oxides with the oxide potential listed in Table 1a. The electronic polarisability of the ions, which is of particular importance when considering charged defects, was described using the Dick and Overhauser shell model.[20] Point defects were modelled using the Mott Littleton method.[21] This method partitions the area surrounding the defect into two spherical regions. Ions in the central region, which immediately surround the defect, are treated explicitly. While those in the outer region are handled more approximately by quasi-continuum methods.[21] For single-defect calculations the central region's radius was truncated at 12 Å, but this was increased appropriately for larger multi-defect systems. The aforementioned methods have, previously, been successfully employed to model defects in olivine-$(Fg/Mg)_2SiO_4$, $LiFePO_4$ and apatite structures.[5,7,22]

Molecular dynamic (MD) simulations were performed on $5 \times 5 \times 5$ supercells containing $\sim$3500 ions, at four temperatures 873, 1073, 1273 and 1473 K. Systems were equilibrated at zero kelvin before simulating for a further 3 ns under isothermal–isobaric (*NPT*) conditions. Final production runs were carried out under constant volume (*NVT*) conditions for 3 ns with a time step of 0.5 fs. Oxygen shells were included *via* the adiabatic shell model. Diffusion coefficients (D) were derived from the mean squared displacements (MSD), $\langle[\Delta\vec{r}(t)]^2\rangle$, using eqn (2). Migration activation energies were then extracted using the Arrhenius relation.

$$D = \frac{\text{MSD}}{6t} \quad (2)$$

3 Results and discussion

3.1 Structural modelling and intrinsic defects

Cd_2GeO_4, shown in Fig. 1, is an olivine *Pmcn* structured material comprised of Ge tetrahedra and two inequivalent Cd octahedra. In Cd_2GeO_4, the isolated tetrahedra are linked by corner and edge sharing Cd octahedra. These tetrahedra align to form columns down the *b*-axis.

A comparison of the calculated and experimental lattice parameters, Table 2a, indicates a good fit to within 1%.[17] Similarly, the interatomic distances, Table 2b, are also in reasonable agreement with the experimental data. Such agreement, between the simulated and experimental structures, supports the validity of the model employed in this work.

In materials such as $Ba_2In_2O_4$ the oxygen defects, pivotal to oxide ion conduction, form naturally though oxygen Frenkels.[25,26] However, the formation of Frenkel and Schottky defects in

Table 1 Interatomic potential and shell model parameters for Cd_2GeO_4

Interaction	A (eV)	ρ (Å)	C (eV Å^6)	Ref.
(a) Buckingham potential parameters[a]				
Cd^{2+}–O^{2-}	1207.70	0.327100	0.00	—
Ge^{4+}–O^{2-}	1497.40	0.325646	16.00	23
O^{2-}–O^{2-}	22764.30	0.149000	27.89	24
Ion	**Shell charge (e)**	**k (eV Å^{-2})**		**Ref.**
(b) Shell parameters				
O^{2-}	−2.86	74.92		24

[a] A short range potential cut-off of 12 Å was enforced in all static-lattice calculations.

Table 2 Calculated and experimental properties of Cd_2GeO_4[17]

Parameter	Calculated	Experimental	Difference (%)
(a) Lattice parameters			
a (Å)	6.528	6.584(3)	−0.056 (−0.86)
b (Å)	5.262	5.211(2)	−0.051 (−0.98)
c (Å)	11.177	11.160(4)	−0.017 (−0.16)
$\alpha = \beta = \gamma$ (°)	90.0	90.0	−0.0 (−0.00)
Bond	**Calculated**	**Experimental**	**Difference**
(b) Interatomic distances (Å)			
Cd_I–O_{II} (×2)	2.30	2.29	−0.00
Cd_I–O_I (×2)	2.26	2.30	−0.04
Cd_I–O_{III} (×2)	2.40	2.36	−0.04
Cd_{II}–O_{II}	2.23	2.25	−0.03
Cd_{II}–O_{III} (×2)	2.25	2.28	−0.03
Cd_{II}–O_I	2.44	2.36	−0.08
Cd_{II}–O_{III} (×2)	2.49	2.43	−0.06
Ge–O_I	1.73	1.76	−0.03
Ge–O_{III} (×2)	1.75	1.76	−0.01
Ge–O_{II}	1.77	1.77	−0.00

Cd_2GeO_4 is found to be energetically unfavourable therefore the concentration of these defects will be negligibly small even at higher temperatures, listed in Table 3. We are confident that the high intrinsic defect energies are not as a result of the interatomic potentials employed since the scrutiny employed to verify the potentials was stringent and included verifying the potentials against the respective binary oxides as well as the integrated properties of the crystal structure such as the interatomic distances and the coordination about each ion among others. As the spontaneous formation of oxygen defects in pristine Cd_2GeO_4 is unfavourable doping was employed to induce their formation.

3.2 Doping

Aliovalent doping is a well-known method of promoting oxygen defect formation in oxide materials.[1,27] During the course of investigation a broad range of mono, di, tri and tetravalent dopant ions on both cation sites were investigated. Considering both constant-cation and constant-oxygen based methods of charge-compensation. In constant-cation mechanisms, such as eqn (3) and (5), charge-compensation is achieved through the formation of oxygen interstitials or vacancies. While constant-oxygen mechanisms are charge balanced by cation vacancies or interstitials, as seen in eqn (4) and (6). The relative favourability of a particular dopant and its incorporation pathway can be established from its solution energy, which is calculated from its constituent isolated point defect energies and relevant lattice energies. Investigations concluded that constant-oxygen stoichiometry was favoured in all but the trivalent doping mechanisms. This suggests that mono, di, and tetravalent doping would primarily result in the formation of cation defects, rather than oxide defects. As these mechanisms do not offer a means to induce oxygen defect formation they are considered no further.

In this work four different trivalent doping mechanisms were considered. The first two, shown in eqn (3) and (4), represent trivalent doping of the Cd sites $\left(M_{Cd}^{\bullet}\right)$. With the charges in the former and latter compensated by O interstitial $\left(O_i''\right)$ and Cd vacancy $\left(V_{Cd}''\right)$ defects respectively. The oxygen vacancy $\left(V_O^{\bullet\bullet}\right)$ and Ge interstitially $\left(Ge_i^{\bullet\bullet\bullet\bullet}\right)$ compensated Ge site doping $\left(M'_{Ge}\right)$ mechanisms are represented in eqn (5) and (6) correspondingly.

$$\frac{1}{2}M_2O_3 + Cd_{Cd}^{\times} \rightarrow M_{Cd}^{\bullet} + \frac{1}{2}O_i'' + CdO \quad (3)$$

$$\frac{1}{2}M_2O_3 + \frac{3}{2}Cd_{Cd}^{\times} \rightarrow M_{Cd}^{\bullet} + \frac{1}{2}V_{Cd}'' + \frac{3}{2}CdO \quad (4)$$

$$\frac{1}{2}M_2O_3 + Ge_{Ge}^{\times} + \frac{1}{2}O_O^{\times} \rightarrow M'_{Ge} + \frac{1}{2}V_O^{\bullet\bullet} + GeO_2 \quad (5)$$

$$\frac{1}{2}M_2O_3 + Ge_{Ge}^{\times} \rightarrow M'_{Ge} + \frac{1}{4}Ge_i^{\bullet\bullet\bullet\bullet} + \frac{3}{4}GeO_2 \quad (6)$$

The calculated solution energies for the trivalent doping of Cd_2GeO_4 at the Cd_{II} and Ge sites, following eqn (3)–(6), are plotted in Fig. 2 as a function of dopant ionic radii. It should be noted that 6 coordinate radii have been used in Fig. 2 to aid comparison, and that radii for the high-spin states have been used where applicable. Results show Cd, specifically Cd_{II}, site substitution mechanisms are favoured by all but the smallest trivalent dopant ion tested (Al), which is consistent with experimental suggestions.[8,28] The larger dopants, such as La, are favoured as their ionic radii are closer to Cd (0.95 Å), making them more appropriate.[29] The results show that Ge based substitution are generally unfavourable, with high defect energies. Substitutions on the Cd site are predicted to be more favourable, with a small preference for constant-cation stoichiometry in which charge compensating oxygen interstitials form. This indicates that trivalent doping offers a potential method of forming oxygen interstitial defects.

3.3 Defect clustering

It is known that defects, particularly those of opposite charge, generally tend to associate with one another.[30] These defect–defect interactions, which are determined by Coulombic forces and lattice relaxations, can significantly affect defect mobility and could result in ion trapping.[31,32] Although in general one would expect that introducing a trivalent dopant on the Cd site

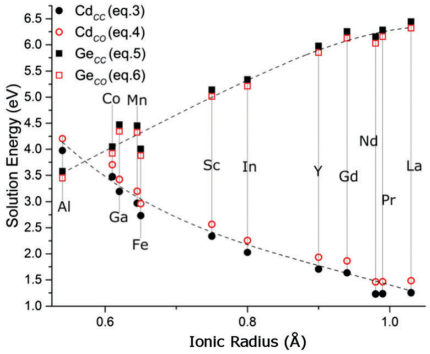

Fig. 2 Solution energies for M^{3+} doping of the Cd_{II}^{2+} and Ge^{4+} sites *via* mechanisms 3 (Cd_{CC}), 4 (Cd_{CO}), 5 (Ge_{CC}) and 6 (Ge_{CO}).

Table 3 Calculated Cd_2GeO_4 intrinsic defect energies

Defect	Defect equation[a]	Defect energy (eV)
Cd Frenkel	$Cd_{Cd}^{\times} \rightarrow V_{Cd}'' + Cd_i^{\bullet\bullet}$	6.00
Ge Frenkel	$Ge_{Ge}^{\times} \rightarrow V_{Ge}'''' + Ge_i^{\bullet\bullet\bullet\bullet}$	19.31
O Frenkel	$O_O^{\times} \rightarrow V_O^{\bullet\bullet} + O_i''$	6.25
Schottky	$2Cd_{Cd}^{\times} + Ge_{Ge}^{\times} + 4O_O^{\times} \rightarrow 2V_{Cd}'' + V_{Ge}'''' + 4V_O^{\bullet\bullet} + Cd_2GeO_4$	31.41

[a] Equations given in Kröger–Vink notation.

giving rise to donor defects of opposite charge should result in some level of clustering, it has been shown many a time that ionic conductivity is significantly enhanced in *e.g.* apatites and little of evidence of defect trapping is observed.[2,33] Therefore, an understanding of clustering behaviour will be important in understanding material stability, and offer insight into ionic conductivity thus aiding the dopant selection process. For this, $2M^{\bullet}_{Cd}{:}O''_i$ defect clusters, where M = Sc^{3+}, Y^{3+}, Nd^{3+}, $Pr^{3+}$and La^{3+}, were examined. The lanthanides were considered due to their large sizes and low incorporation energies. The two comparatively smaller dopants Y and Sc were also included to elucidate the effects of dopant size on defect clustering, and due to existence experimental data for the former.[8]

The identification of stable conformations is an important consideration during clustering analysis. The stability of a cluster can be determined from its binding energy $E_{Binding}$, which is the difference in energy between the cluster $E_{Cluster}$ and the sum of its constituent point defects E_{Defect}, as shown in eqn (7).

$$E_{Binding} = E_{Cluster} - \sum E_{Defect} \quad (7)$$

For example, the binding energy of a $2Nd^{\bullet}_{Cd}{:}O''_i$ cluster is calculated following eqn (8).

$$E_{Binding} = E\left(2Nd^{\bullet}_{Cd}O''_i\right) - E\left(O''_i\right) - 2E\left(Nd^{\bullet}_{Cd}\right) \quad (8)$$

A negative binding energy would indicate that the cluster is bound, and, is more favourable compared to the defects at infinite separation.

As previously discussed, an oxygen interstitial is formed for every two dopants in order to maintain charge neutrality. Therefore, the simplest charge neutral defect cluster would consist of a single oxygen interstitial and a pair of neighbouring dopant ions $\left(2M^{\bullet}_{Cd}{:}O''_i\right)$. Investigation of small $2M^{\bullet}_{Cd}{:}O''_i$ clusters can be conducted with relative ease due to the limited number of possible permutations ($\sim$4000). The complex nature of defect clustering means behaviours may differ in larger clusters. However investigation of larger clusters quickly becomes infeasible due to the vast number of possible conformations associated with them ($>1 \times 10^7$ for $4M^{\bullet}_{Cd}{:}2O''_i$ systems). As such, investigations have been restricted to $2M^{\bullet}_{Cd}{:}O''_i$ clusters. Any effects which may arise from further clustering will be captured during the molecular dynamics simulations where the random placements of clusters lead to finding some in proximity to one another. With the exception of Y, each dopant is found to present only a single stable $2M^{\bullet}_{Cd}{:}O''_i$ cluster conformation. The Sc and Y based clusters adopt "Ge_3O_{13}" based defect structures, as shown in Fig. 3a, in which the dopants, like the natural Cd ions, are six coordinate. However, the "GeO_5" structure shown in Fig. 3b is favoured by the three larger dopants, Nd, Pr and La, as it affords them a more preferable seven coordinate environment. The existence of interstitially bridged defects has been proposed in other materials such as "Ge_2O_9" groups in apatite.[2,33] However, currently, no reports of analogous "Ge_3O_{13}" type defect structures can be found.

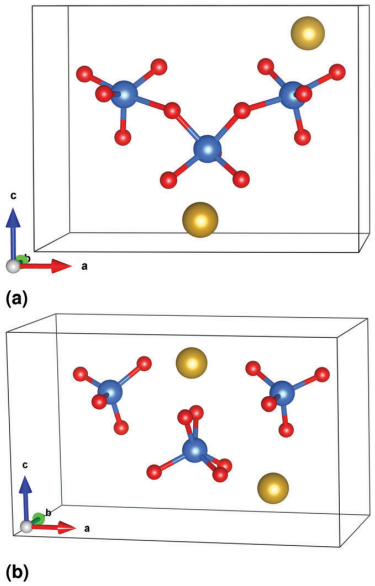

Fig. 3 (a) "Ge_3O_{13}" and (b) "GeO_5" $2M^{\bullet}_{Cd}{:}O''_i$ clusters, with O, Ge and M represented as red, blue and gold spheres respectively. Surrounding ions omitted for clarity.

The calculated binding energies for the stable $2M^{\bullet}_{Cd}{:}O''_i$ defect clusters are reported in Table S1 (ESI†) and are plotted against dopant size in Fig. 4a. Examination reveals defect clustering to be a highly favourable process. Therefore, the existence of isolated defects, particularly at non-trivial defect concentrations, is unlikely. Furthermore, the binding energy generally decreases as the dopant's radius deviates from the native Cd ion's (0.95 Å), which is due to the dopant size dependency of the lattice relaxation interactions (discussed later). As the previously discussed solution energies were calculated assuming infinite dilution they failed to take into account the additional stabilisation energy arising from defect–defect interactions. This results in an overestimation of the solution energies due to the non-trivial nature of such interactions. However, this can be corrected for by simply adding the binding energy to the solution energy. It can be seen from Table 4 that dopant incorporation is much more favourable once defect–defect stabilisation energy is factored in.

Although binding energies are an approximate indicator due to their complicated nature of the extent to which an oxygen interstitial may become trapped, it is more appropriate to consider interstitial separation energy. This represents the energy required to remove an oxygen interstitial from its cluster to infinity. The separation energy is calculated as the difference in binding energy between a cluster with and without its oxygen interstitial. The calculated interstitial separation energies for the $2M^{\bullet}_{Cd}{:}O''_i$ clusters are presented in Table S1 (ESI†) and Fig. 4b. Again, this shows increased separation energies for dopants notably larger or smaller than Cd. The larger the dopant ion the greater its preference for the seven coordinate

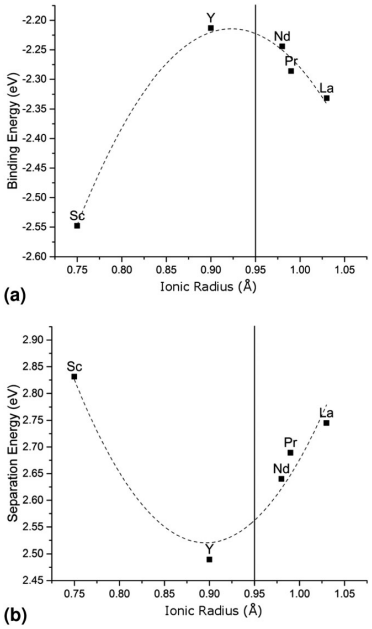

Fig. 4 (a) Binding and (b) interstitial separation energies of $2M^{\bullet}_{Cd}:O''_i$ clusters as a function of dopant radius with Cd's ionic radius indicated by the solid black line, trend line include as a guide only.

Table 4 Corrected solution energies for the trivalent doping of Cd_2GeO_4 *via* the mechanism detailed in eqn (3)

Dopant	Radii (Å)	$E_{Solution}$ (eV)
Sc	0.75	1.06
Y	0.9	0.60
Nd	0.98	0.11
Pr	0.99	0.09
La	1.03	0.09

environment provided by the oxygen interstitial. Small dopants, such as Sc, are a poor fit for the native Cd site. However, interstitial defects allow the oxygen ions to relax around to dopant to accommodate it better. As such, the energetic penalty for the movement of an oxygen interstitial away from its $2M^{\bullet}_{Cd}:O''_i$ cluster is likely to be greater for dopants notably larger or smaller then Cd. This suggests that ions closer in size to Cd are generally more appropriate dopants, as their lower trapping capability suggests increased oxide defect mobility. However, this is not conclusive as it fails to provide information on the short to medium range defect interactions. Further to this, molecular dynamic simulations were carried out to elucidate interstitial defect trapping at higher temperatures. This being said, the large binding and separation energies clearly show that interstitial diffusion will be heavy restricted by the dopants with a high trapping probability.

3.4 Diffusion

Molecular dynamic simulations were conducted on pristine and 10% doped Cd_2GeO_4 in order to assess the impact of doping on oxide ion conduction. Yttrium was selected as the primary dopant due to its reduced binding and separation energies. The starting structures for the doped systems were generated by randomly placing 25 $2M^{\bullet}_{Cd}:O''_i$ clusters in $5 \times 5 \times 5$ supercells.

The mean squared displacements (MSD) of the oxide ions, Fig. 5, clearly shows oxygen diffusion is only significant in doped systems. The diffusion coefficients for oxygen in $Cd_{1.9}Y_{0.1}GeO_{4.05}$, as calculated following eqn (2), are presented in Fig. 6 and Table S2 (ESI†). The MD results suggest that, although mobile, the oxide defects generally reside in the dopant rich regions of the cell, shown from the O–Y and O–Cd_{II} radial distribution functions presented in Fig. 7. This supports the earlier defect clustering analysis which indicated trapping of the interstitials by the dopants to be highly favourable. As previously discussed $2Y^{\bullet}_{Cd}:O''_i$ clusters assume "Ge_3O_{13}" based structures while larger ions such as Nd prefer to adopt "GeO_5" based clusters. To probe the effects of differing defect cluster structures on oxide diffusion a limited number of simulations were conducted on Nd doped Cd_2GeO_4 systems. The diffusion coefficients for the Nd doped systems were found to be comparable to those of Y doped systems, as indicated by the MSDs in Fig. 5. This suggests that the difference

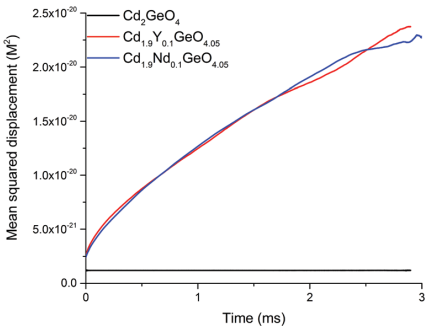

Fig. 5 Mean squared displacements for oxygen in Cd_2GeO_4 (black), $Cd_{1.9}Y_{0.1}GeO_{4.05}$ (red) and $Cd_{1.9}Nd_{0.1}GeO_{4.05}$ (blue) at 1273 K MD simulations.

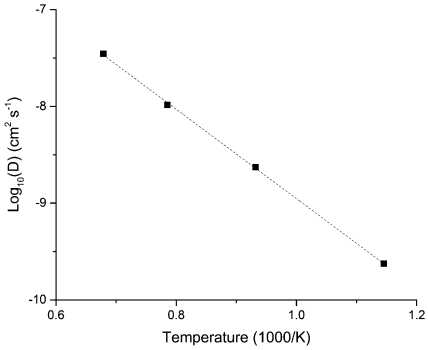

Fig. 6 Plot showing temperature dependency of oxygen diffusion in $Cd_{1.9}Y_{0.1}GeO_{4.05}$.

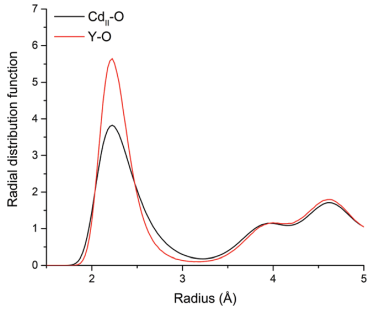

Fig. 7 Radial distribution functions for O about Cd_{II} and Y at 1473 K.

in interstitial trapping of the Y and Nd doped systems, calculated at high temperature, is negligible compared to their overall binding energies which were calculated at zero Kelvin.

The calculated diffusion coefficients are found to be several orders of magnitude higher than those of the common cathode material LSM-20 and on a par with composite cathode materials such as YSZ-40 wt% LSM which, at 1073 K, have diffusion coefficients of 1.3×10^{-12} and 1.0×10^{-9} cm^2 s^{-1} respectively.[34] However, many common electrolyte or advanced electrode materials present significantly higher diffusion coefficients, for example yttria stabilized zirconia (2.6×10^{-7} cm^2 s^{-1} at 1273 K) and lanthanum strontium cobalt ferrite (2.6×10^{-9} cm^2 s^{-1} at 773 K).[25,31]

The MD results suggest that oxide ions diffuse primarily in the *ac*-plane, which is shown by the axial MSDs (Fig. S1, ESI†), with a calculated activation energy of 0.92 eV, and that, like apatite germinates, all oxide ions are found to be mobile.[2] The oxide defects diffuse down the *a*-axis through the sequential formation of "Ge_3O_{13}" and intermediary "Ge_2O_9" defects between nearest neighbouring tetrahedra in a "knock-on" type mechanism. This mechanism, which is depicted in Fig. 8, forms diffusion channels along to the *a*-axis as represented in Fig. 9. This bears a striking resemblance to the oxygen vacancy diffusion mechanism reported in $La_{1-x}Ba_{1+x}GaO_{4-x/2}$.[35] Movement between these channels is permitted by the *c*-axial diffusion mechanism. This mechanism differs from the former in that it is stepwise and as oxide ions must unbind from their tetrahedra, traverse the Cd_{II} channel and rebind with another tetrahedra. The exact pathway of this mechanism is highly dependent on the local environment, specificity the presence of dopant or other interstitial ions.

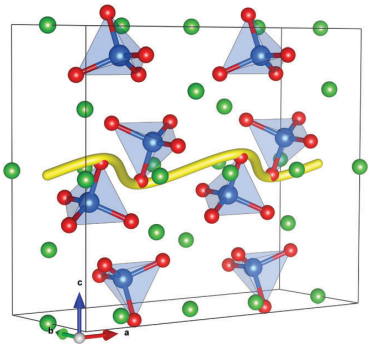

Fig. 9 Depiction of the primary *a*-axial diffusion pathway (yellow) elucidated from 1273 K MD simulations of $Cd_{1.9}Y_{0.1}GeO_{4.05}$. With Ge, Cd and O ions represented as blue, green and red spheres respectively.

Similar anisotropic diffusivity is predicted *via* static lattice methods for olivine (Mg_2SiO_4) itself. Such work reports *a*-axial diffusion is also favoured, with an activation energy of 0.97 eV.[22]

4 Conclusion

To summarise, in this work we predict that oxygen defect formation in olivine-type Cd_2GeO_4 can be promoted through trivalent doping which follows a constant-cation mechanism. Furthermore, the dopant ion, and the size thereof, is predicted to play a significant role in trapping the mobile defects (a complicated phenomenon to capture fully in a computational model). The oxide ion interstitial diffusion primarily occurs in the *ac*-plane *via* a "knock-on" mechanism along *a*-axis, in line with previous migration pathways reported in the Li-olivine structure and *via* a stepwise mechanism along the *c*-axis. However for the first time we explicitly show, that even at high temperatures the mobile oxide ions tend to stay within the dopant rich regions of the cell. Thus confirming the favourability of dopant trapping, which partially inhibits oxide ion transport. Finally, from our MD simulations we calculated migration barriers of 0.92 eV. In conclusion, whilst trivalent doping on the Cd site shows some promise, the oxide ion trapping capabilities of the dopant ions limit the use of Cd_2GeO_4 as an oxide ion conductor. Finally, we show the use of simulations to illustrate the potential of the olivine structure to accommodate

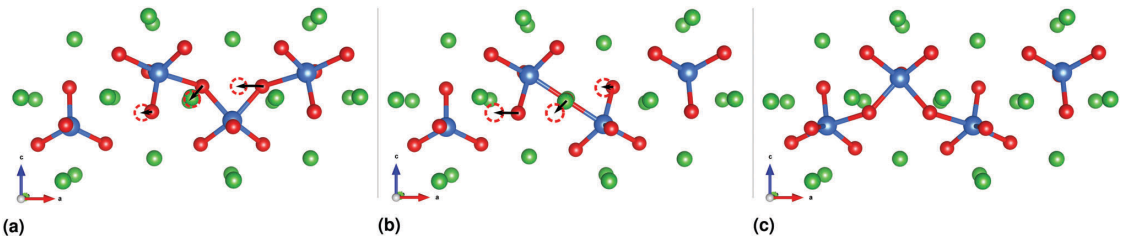

Fig. 8 Schematic representation of oxygen defect migration along the *a*-axis *via* the formation and breaking of an intermediary "Ge_2O_9" group. With Ge, Cd and O ions represented as blue, green and red spheres respectively.

interstitial oxide ions, and exclusively quantify the binding energies and, hence, the trapping of such mobile defects in this material. In addition to the relevance in the oxide ion conductor field, this work is also of relevance to the Li ion battery field, given the large interest in olivine-type $LiFePO_4$.

References

1 N. Mahato, A. Banerjee, A. Gupta, S. Omar and K. Balani, *Prog. Mater. Sci.*, 2015, **72**, 141–337.
2 E. Kendrick, M. S. Islam and P. R. Slater, *Chem. Commun.*, 2008, 715–717.
3 J. R. Tolchard, M. S. Islam and P. R. Slater, *J. Mater. Chem.*, 2003, **13**, 1956–1961.
4 P. R. Slater, J. E. H. Sansom and J. R. Tolchard, *Chem. Rec.*, 2004, **4**, 373–384.
5 P. M. Panchmatia, A. Orera, G. J. Rees, M. E. Smith, J. V. Hanna, P. R. Slater and M. S. Islam, *Angew. Chem., Int. Ed.*, 2011, **50**, 9328–9333.
6 X. Kuang, M. A. Green, H. Niu, P. Zajdel, C. Dickinson, J. B. Claridge, L. Jantsky and M. J. Rosseinsky, *Nat. Mater.*, 2008, **7**, 498–504.
7 M. S. Islam, D. J. Driscoll, C. A. J. Fisher and P. R. Slater, *Chem. Mater.*, 2005, **17**, 5085–5092.
8 E. Whipple, S. Subbarao and F. Koffyberg, *J. Solid State Chem.*, 1980, **34**, 231–239.
9 A. K. Cheetham and P. Day, *Solid State Chemistry: Techniques*, Clarendon Press, 1988.
10 A. R. Leach, *Molecular Modelling: Principles and Applications*, Prentice Hall, 2001.
11 C. R. A. Catlow, *Computer Modeling in Inorganic Crystallography*, Elsevier Science, 1997.
12 J. D. Gale, *J. Chem. Soc., Faraday Trans.*, 1997, **93**, 629–637.
13 J. D. Gale and A. L. Rohl, *Mol. Simul.*, 2003, **29**, 291–341.
14 W. Smith and T. R. Forester, *J. Mol. Graphics*, 1996, **14**, 136–141.
15 K. Momma and F. Izumi, *J. Appl. Crystallogr.*, 2011, **44**, 1272–1276.
16 R. A. Buckingham, *Proc. R. Soc. London, Ser. A*, 1938, **168**, 264–283.
17 M. A. Simonov, E. L. Belokoneva and N. V. Belov, *J. Struct. Chem.*, 1981, **22**, 478–479.
18 M. Levy, PhD thesis, Imperial College London, 2005.
19 L. Minervini, R. W. Grimes and K. E. Sickafus, *J. Am. Ceram. Soc.*, 2000, **83**, 1873–1878.
20 B. G. Dick and A. W. Overhauser, *Phys. Rev.*, 1958, **112**, 90–103.
21 N. F. Mott and M. J. Littleton, *Trans. Faraday Soc.*, 1938, **34**, 485–499.
22 A. M. Walker, K. Wright and B. Slater, *Phys. Chem. Miner.*, 2003, **30**, 536–545.
23 P. M. Panchmatia, A. Orera, E. Kendrick, J. V. Hanna, M. E. Smith, P. R. Slater and M. S. Islam, *J. Mater. Chem.*, 2010, **20**, 2766–2772.
24 J. R. Tolchard, P. R. Slater and M. S. Islam, *Adv. Funct. Mater.*, 2007, **17**, 2564–2571.
25 C. Sun, R. Hui and J. Roller, *J. Solid State Electrochem.*, 2010, **14**, 1125–1144.
26 C. Fisher, M. Islam and R. Brook, *J. Solid State Chem.*, 1997, **128**, 137–141.
27 S. J. Skinner and J. A. Kilner, *Mater. Today*, 2003, **6**, 30–37.
28 Y. Jin, Y. Hu, R. Chen, Y. Fu, G. Ju, Z. Mu, J. Lin, Z. Wang, F. Xue and Q. Zhang, *J. Alloys Compd.*, 2015, **623**, 255–260.
29 W. Haynes, *CRC handbook of chemistry and physics: a ready-reference book of chemical and physical data*, CRC Press, Boca Raton, FL, 2011.
30 B. Wang, R. J. Lewis and A. N. Cormack, *Acta Mater.*, 2011, **59**, 2035–2045.
31 R. Devanathan, W. J. Weber, S. C. Singhal and J. D. Gale, *Solid State Ionics*, 2006, **177**, 1251–1258.
32 M. Schie, R. Waser and R. A. De Souza, *J. Phys. Chem. C*, 2014, **118**, 15185–15192.
33 K. Imaizumi, K. Toyoura, A. Nakamura and K. Matsunaga, *Solid State Ionics*, 2014, **262**, 512–516.
34 S. Jiang, *J. Mater. Sci.*, 2008, **43**, 6799–6833.
35 E. Kendrick, J. Kendrick, K. S. Knight, M. S. Islam and P. R. Slater, *Nat. Mater.*, 2007, **6**, 871–875.